

Ignacio González Insua

Optical generation of mm-wave signals for use in
broadband radio over fiber systems

Beiträge aus der Informationstechnik

Ignacio González Insua

**Optical generation of mm-wave signals for use in
broadband radio over fiber systems**

 VOGT

Dresden 2010

Bibliografische Information der Deutschen Bibliothek
Die Deutsche Bibliothek verzeichnet diese Publikation in der Deutschen
Nationalbibliografie; detaillierte bibliografische Daten sind im Internet über
<http://dnb.ddb.de> abrufbar.

Bibliographic Information published by Die Deutsche Bibliothek
Die Deutsche Bibliothek lists this publication in the Deutsche Nationalbibliografie;
detailed bibliographic data is available in the internet at <http://dnb.ddb.de>.

Zugl.: Dresden, Techn. Univ., Diss., 2010

Die vorliegende Arbeit stimmt mit dem Original der Dissertation
„Optical generation of mm-wave signals for use in
broadband radio over fiber systems“ von Ignacio González Insua überein.

© Jörg Vogt Verlag 2010
Alle Rechte vorbehalten. All rights reserved.

Gesetzt vom Autor

ISBN 978-3-938860-40-3

Jörg Vogt Verlag
Niederwaldstr. 36
01277 Dresden
Germany

Phone: +49-(0)351-31403921
Telefax: +49-(0)351-31403918
e-mail: info@vogtverlag.de
Internet : www.vogtverlag.de

Technische Universität Dresden

**Optical generation of mm-wave signals for use in
broadband radio over fiber systems**

Ignacio González Insua

von der Fakultät Elektrotechnik und Informationstechnik der
Technischen Universität Dresden

zur Erlangung des akademischen Grades eines

Doktoringenieurs

(Dr.-Ing.)

genehmigte Dissertation

Vorsitzender: Prof. Dr.-Ing. E. Jorswieck

Tag der Einreichung

4. September 2009

Gutachter: Prof. Dr.-Ing. C.G. Schäffer

Prof. Dr. rer. nat. habil. D. Jäger

Tag der Verteidigung

4. Februar 2010

Table of Contents

1	Introduction	1
2	General system requirements for mobile broadband communication systems.....	5
2.1	Gigabit wireless communications	5
2.2	Millimetre wave propagation.....	7
2.2.1	Free space propagation.....	7
2.3	Channel capacity	9
2.4	Technical challenges	14
2.4.1	Channel propagation	14
2.4.2	Antenna technology	15
2.4.3	Integrated circuit technology.....	17
2.4.4	Modulation schemes.....	19
2.5	Signal transport schemes: radio over fiber architectures	21
2.5.1	Downlink transmission.....	21
2.5.2	Uplink transmission	24
3	Optical methods for microwave signal generation.....	27
3.1	Heterodyned laser techniques.....	27
3.1.1	Mode-locking	28
3.1.2	Injection-locking	29
3.1.3	Phase locked loops	29
3.2	External optical modulators.....	30
4	Propagation of mm-wave signals in optical waveguides.....	33
4.1	Chromatic dispersion.....	34
4.1.1	Chromatic dispersion impaired system	37
4.2	IM/DD fiber optic mm-wave links.....	41
4.2.1	Unmodulated mm-wave carrier.....	43
4.2.2	Modulated carrier with an intermediate frequency f_{IF}	47
4.3	Effects of transmitter chirp.....	51
4.3.1	Directly modulated IF links.....	51
4.3.2	Externally modulated IF links	54

4.4	Remote heterodyne detection fiber optic mm-wave links	57
4.5	Phased induced intensity noise	63
4.6	Polarization mode dispersion.....	65
5	Electrooptical upconversion methods.....	69
5.1	Mach-Zehnder modulator	69
5.1.1	Mach-Zehnder modulator biased at MIN	75
5.2	Fiber loop.....	82
5.2.1	Fiber loop with a phase modulator	84
5.2.2	Fiber loop with a semiconductor optical amplifier.....	96
6	Comparison of optical heterodyne receiver architectures.....	109
6.1	Amplitude shift keying (ASK).....	109
6.1.1	Receivers with coherent demodulation	113
6.1.2	Receivers with incoherent demodulation	115
6.2	Phase shift keying (PSK)	119
6.3	Linewidth effects	121
6.4	Overview	122
7	System experiments.....	125
7.1	Fiber loop setup.....	125
7.1.1	Fiber loop with phase modulator.....	125
7.1.2	Fiber loop with SOA	129
7.2	Broadband radio over fiber wireless access	133
7.2.1	Optical double sideband data modulation	134
7.2.2	Optical single sideband data modulation.....	141
7.2.3	Comparison ODSB vs OSSB	150
7.3	Heterodyned uncorrelated lasers.....	153
7.3.1	RF bandwidth.....	155
7.3.2	Laser linewidth.....	156
7.3.3	Simple remote heterodyne with diode detector	158
7.4	Overview	163
8	Summary.....	165

Literature	171
Acknowledgments.....	183
Appendix A Phase modulation index measurements of PM.....	187
Appendix B Phase modulation index measurement of SOAs.....	193
Appendix C SOA datasheets	199
Appendix D VPI simulation schematics.....	205
Curriculum Vitae	208

Constants

c	Light speed in vacuum	$299.79 \cdot 10^6$ m/s
h	Planck's constant	$6.62 \cdot 10^{-34}$ Ws ²
k_B	Boltzmann constant	$1.3807 \cdot 10^{-23}$ J/K
π	pi	3.1416
q	Electron charge	$1.6022 \cdot 10^{-19}$ As

Symbols

α	Fiber loss parameter
α_{eff}	Effective α -factor
α_{int}	SOA internal loss
α_{LE}	Linewidth enhancement factor
α_{MZM}	Chirp parameter of a Mach Zehnder modulator
a_0	Average optical intensity
β	Propagation constant
B	Bandwidth
B_n	Noise bandwidth
β_2	Group velocity dispersion parameter
B_j	Oscillator strength
C	Channel capacity
C/N_{pen}	Carrier to noise penalty
CS_{el}	Electrical carrier suppression
CS_{opt}	Optical carrier suppression
d	Distance (general)
d_0	Reference distance
δ	Dirac impulse
D	Dispersion parameter
D_M	Material dispersion
D_W	Waveguide dispersion
Δf	Frequency separation
$\Delta\phi$	Optical phase difference
$\Delta\phi_{FM,IM}$	Phase offset between frequency and intensity modulation
Δg	Gain variation
ΔL	Length difference
ΔL_0	Repetition length of transmission zeros
ΔL_{path}	Optical path length difference
Δn	Birefringence index
ΔP	Power variation
$\Delta\theta$	Electrical phase difference
ΔT	Pulse broadening
ΔT_N	Normalized pulse broadening
$\Delta\lambda$	Wavelength spectral width
$\Delta\tau$	Differential propagation delay
$\Delta\tau_{disp}$	Dispersion induced differential propagation delay
$\Delta\tau_{path}$	Path difference induced differential propagation delay

$\Delta\tau_{pmd}$	Polarization mode dispersion induced differential propagation delay
$\Delta\nu$	Signal linewidth (general)
$\Delta\omega$	Pulse spectral width
E	Electric field (general)
ER	Extinction ratio
ER_{pen}	Extinction ratio penalty
E_{sat}	Saturation energy in a SOA
f	Frequency (general)
f_c	Optical carrier frequency
f_{IF}	Intermediate frequency
f_{LO}	Local oscillator frequency
f_m	Modulation frequency
f_{opt}	Optical frequency
f_{RF}	RF frequency
FSR	Free spectral range
Γ	Mode confinement
Γ_n	n^{th} harmonic mixer conversion gain
G	Gain (general)
g_0	SOA gain per unit length
G_C	Combined antenna gain
G_{RX}	Receiver antenna gain
G_{TX}	Transmitter antenna gain
$H(f)$	Fiber low pass equivalent transfer function
η	Photodiode quantum efficiency
η_{conv}	Wavelength conversion efficiency
I	Current (general)
I_0	Mean pulse amplitude for a logical “zero”
I_1	Mean pulse amplitude for a logical “one”
I_{bias}	Bias current
I_d	Dark current
i_s	Shot noise current
i_T	Thermal noise current
IL	Implementation loss
φ	Phase (general)
Φ_k	Random phase
J	Current density
J_k	Bessel function of the k^{th} order
φ_d	Dispersion induced phase change
κ	Coupler splitting ratio
κ_{pol}	Polarization splitting ratio
λ	Wavelength (general)
λ_0	Zero dispersion wavelength
L	Length (general)
L_0	First transmission zero length
l_c	Coherence length
L_{shad}	Shadowing loss

LL	Link loss
m_a	Amplitude modulation index
m_f	Frequency modulation index
m_{ph}	Phase modulation index
n	Refraction index
N_{cd}	Carrier density in a SOA
n_{cd}	Carrier density perturbation
n_g	Group index
n_L	Refraction index in a laser cavity
n_p	Peak number of photons required per bit of information
n_{path}	Path loss exponent
n_{sp}	Spontaneous emission inversion parameter
$n_{x,y}$	Polarisation dependent refraction index
N_{power}	Noise power
NF_{amp}	Amplifier noise figure
NF_{RX}	Receiver noise figure
P_{el}	Electrical power (general)
P_{LO}	Local oscillator optical power
P_{opt}	Optical power (general)
P_{probe}	Probe optical power
P_{pump}	Pump optical power
P_s	Signal optical power
P_{sat}	SOA saturation power
Π	Instantaneous optical power
$PIIN$	Phase induced intensity noise
PL	Path loss
$PL_{freespace}$	Path loss in free space
P_{RX}	Received RF power
P_{TX}	Transmitted RF power
Q	Q factor
θ	Angle between the signal linearized polarization state and x polarization axis
R	Photodiode responsivity
r_{33}	Pockels coefficient
R_b	Bit rate
R_L	Load resistor
RIN	Relative intensity noise
S	Dispersion slope
SE	Spectral efficiency
SL	System loss factor
SNR	Signal to Noise Ratio
$S_f(f)$	Laser frequency fluctuation spectrum
$S_\phi(f)$	Phase fluctuation spectrum
σ_0	Standard deviation for a logical “zero”
σ_1	Standard deviation for a logical “one”
σ_n	Noise standard deviation
σ_s^2	Shot noise variance

σ_T^2	Thermal noise variance
σ_ϕ^2	Phase noise variance
T	Temperature (general)
T_b	Bit slot time
t_r	Rise/fall time at transmitter
T_s	Received rise/fall time
t	time (general)
t_m	Transmission factor
τ	Time delay
τ_c	Carrier lifetime
τ_s	Stimulated carrier lifetime
V	Voltage (general)
V_b	Bias voltage
V_{DC}	DC bias voltage
V_o	Offset voltage
V_π	Half-wave voltage
v_g	Group velocity
ω	Angular frequency
ω_j	Resonance angular frequency
Z_t	Overall transceiver impedance

Operators

j	Imaginary unit
x^*	Complex conjugation of x

Acronyms

10 GET	10 Gigabit Ethernet
ASE	Amplified Spontaneous Emission
ASK	Amplitude Shift Keying
A/V	Audio/video
AWGN	Additive White Gaussian Noise
BtB-Measurement	Back-to-Back-Measurement (Reference measurement for Bit Error Rate)
BER	Bit Error Rate
BERT	Bit Error Rate Tester
BiCMOS	Bipolar Complementary Metal Oxide Semiconductor
BPSK	Binary Phase Shift Keying
BS	Base Station
CATV	Community Antenna TeleVision
Ccw	Counter clockwise
CD	Chromatic Dispersion
C/N	Carrier to Noise
CR	Coupling Ratio
CS	Central Station
CS _{el}	Electrical Carrier Suppression
CS _{opt}	Optical Carrier Suppression

CMOS	Complementary Metal Oxide Semiconductor
CW	Continuous Wave
Cw	Clockwise
DCF	Dispersion Compensating Fiber
DFB	Distributed Feedback Laser
DPSK	Differential Phase Shift Keying
DQPSK	Differential Quadrature Phase Shift Keying
DSB-SC	Double Sideband with Suppressed Carrier
DSF	Dispersion Shifted Fiber
DWDM	Dense Wavelength Division Multiplex
EAM	Electro-Absorption Modulator
EAT	Electro-Absorption Transceiver
EBPF	Electrical BandPass Filter
ECL	External Cavity Laser
EDFA	Erbium Doped Fiber Amplifier
ELPF	Electrical Low Pass Filter
E/O	Electrical to Optical
ER	Extinction Ratio
ESA	Electrical Spectrum Analyzer
FBG	Fiber Bragg Grating
FDM	Frequency Division Multiplex
FLM	Fiber Loop Mirror
FM	Frequency Modulation
FSK	Frequency Shift Keying
FSR	Free spectral range
FTTH	Fiber to the Home
GaAs	Gallium Arsenide
GVD	Group Velocity Dispersion
HBT	Heterojunction Bipolar Transistor
HDTV	High Definition Television
HEMT	High Electron Mobility Transistor
IC	Integrated Circuit
IF	Intermediate Frequency
IL	Insertion Loss
IM	Intensity Modulation
IM/DD	Intensity Modulation / Direct Detection
InP	Indium Phosphide
ISI	InterSymbol Interference
ITU	International Telecommunication Union
LAN	Local area network
LD	Laser Diode
LFS	Linear Fit Slope
LiNbO ₃	Lithium Niobate
LNA	Low Noise Amplifier
LO	Local Oscillator
LOS	Line Of Sight
LPF	Low Pass Filter

MAX	MAXimum transmission bias point
MIN	MINimum transmission bias point
MMF	Multi Mode Fiber
MZI	Mach-Zehnder Interferometer
MZM	Mach-Zehnder Modulator
NLOS	Non Line Of Sight
NRZ-Format	Non-Return-to-Zero-Format
OBPF	Optical BandPass Filter
ODSB	Optical Double SideBand
O/E	Optical to Electrical
OFDM	Orthogonal Frequency Division Multiplex
ONU	Optical Network Unit
OOK	On-Off Keying
OSA	Optical Spectrum Analyzer
OSSB	Optical Single SideBand
PC	Polarization Controller
PD	Photodiode
PIIN	Phase Induced Intensity Noise
PLL	Phase Locked Loop
PM	Phase Modulation/Modulator
PMD	Polarization Mode Dispersion
PON	Passive Optical Network
PRBS	Pseudorandom Binary Sequence
PSK	Phase Shift Keying
PSTN	Public Switched Telephone Network
QAM	Quadrature Amplitude Modulation
QCSE	Quantum Confined Stark Effect
QPSK	Quadrature Phase Shift Keying
QUAD	QUADrature transmission bias point
RBW	Resolution BandWidth
RF	Radio Frequency
RHD	Remote Heteroyne Detection
RoF	Radio over Fiber
RSOA	Reflective Semiconductor Optical Amplifier
SiGe	Silicon Germanium
SMF	Single Mode Fiber
SNR	Signal to Noise Ratio
SOA	Semiconductor Optical Amplifier
SSB	Single SideBand
UWB	Ultra WideBand
VCO	Voltage Controlled Oscillator
xDSL	Digital Subscriber Line
XGM	Cross Gain Modulation
XPM	Cross Phase Modulation
WDM	Wavelength Division Multiplex
WLAN	Wireless local area network
WPAN	Wireless personal area network

1 Introduction

The demand for high data rates seems to keep growing as the integration of many services like internet telephony, high-definition TV (HDTV), audio/video (A/V) on demand, etc. push the existing connections bandwidth limits. Moreover, the end user would also like to access all these services while being mobile.

Commercial xDSL service providers offer peak data rates up to 50 Mbps (e.g. VDSL) to the end user and gigabit wired connections will be available in the near future. Nonetheless, there is a limit as to how much bandwidth can be transported over a twisted pair copper wire due to its low frequency cut-off. Therefore complex modulation schemes such as orthogonal frequency division multiplexing (OFDM) are used which require intensive digital post processing. While this modulation scheme is the principal driving force for xDSL services and the most popular one used up to date, the data rates are still not high enough to provide all the afore mentioned services with decent quality.

Fiber to the home (FTTH) is an emerging technology which offers the enormous bandwidth of optical fiber (in the THz range). Connections are being deployed in many countries (in USA by Verizon, in Germany by Deutsche Telekom, in France by France Telecom, etc) and future networks start looking as shown in Figure 1.1. The connection between the optical line terminal and the end user will be carried out through a passive optical network (PON) to provide broadband coverage of broadcast TV, internet traffic and public switched telephone network traffic (PSTN).

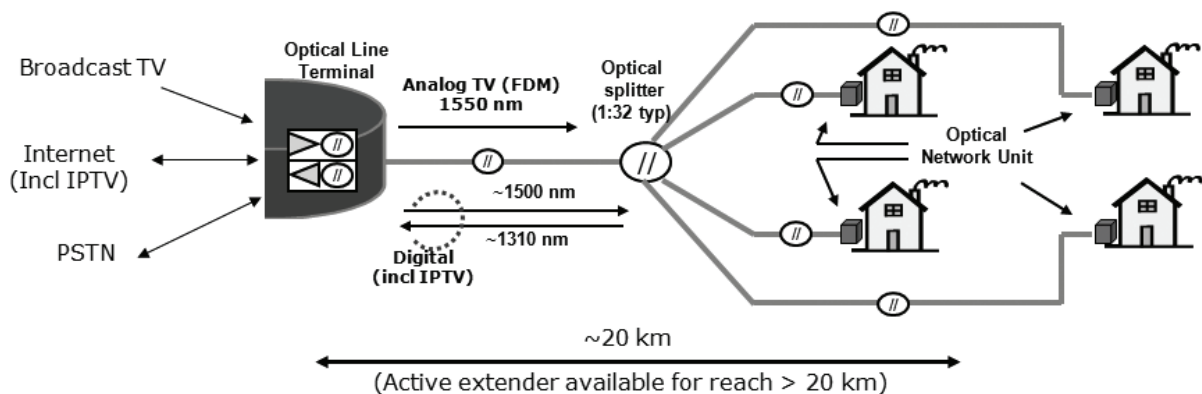


Figure 1.1: FTTH network architecture. FDM: Frequency Division Multiplex [1].

Each house will have an optical network unit (ONU) capable of routing all the traffic and distributing it inside the household. A typical home with a FTTH connection will appear as shown in Figure 1.2. The huge bandwidth can be then divided into the different users (i.e. rooms) in the house and be transported through low loss, electromagnetic immune optical fiber. Wired gigabit connections will be easily implemented such as already deployed 10 Gigabit Ethernet (10 GET) but that leaves the wireless transmission problem still unsolved for mobile devices.

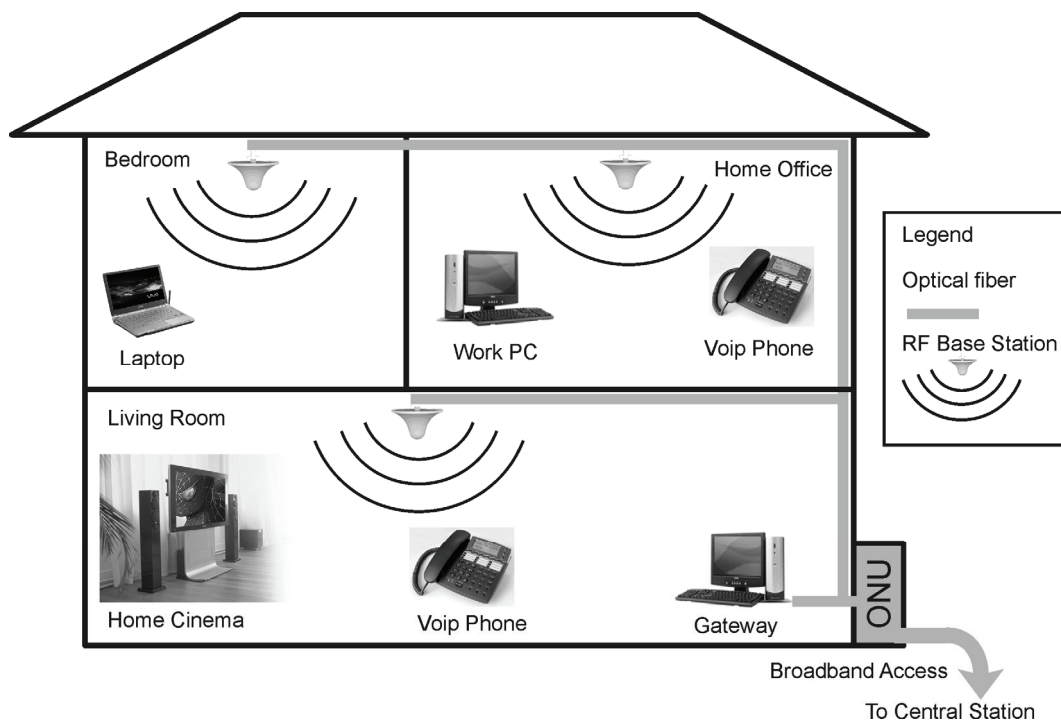


Figure 1.2: FTTH inhouse distribution. ONU: Optical network unit.

Millimeter wave Radio-over-Fiber (RoF) systems are a key enabler to realize gigabit speed broadband wireless services as there is a huge unlicensed bandwidth at these high frequencies (i.e. 60 GHz, 70 GHz and 90 GHz). The idea behind RoF systems is to centralize all the expensive components and control devices in the so called central station (CS) so as to simplify the distribution points, called base stations (BS), which are fed through optical fiber as seen in Figure 1.3. The enormous bandwidth offered by optical fiber allows the division of space in picocells or femtocells, depending on the cell size. Within each cell, a BS is in charge of distributing the data among its users through different intermediate frequencies. There are various proposed architectures, such as RoF without mm-wave generation, with sub mm-wave generation or with mm-wave generation (the special case depicted in Figure 1.3), which

will be discussed later. The BS is then an optical to electrical (O/E) converter which sends the broadband data on a mm-wave carrier and depending on the RoF architecture, is more or less complex. In this context, each base station (or in FTTH case, each room in the household) will have a small, compact and most importantly cheap O/E transceiver which would be connected via optical fiber to the central station via an optical network.

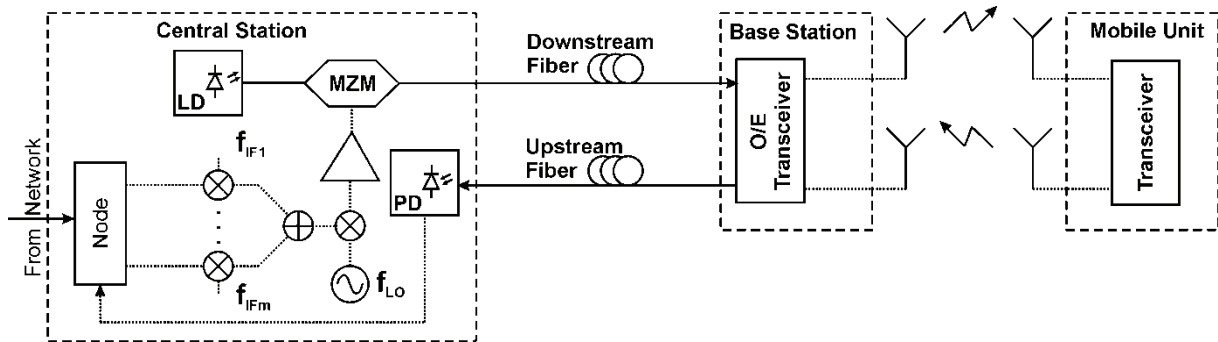


Figure 1.3: RoF basic architecture.

Moreover, future research concentrates on going one step further and giving up on the CS altogether by using directly the wired 10 GET connection in the household and a simple scheme to upconvert the broadband baseband signal. A simple solution would be to remotely heterodyne the 10 GET optical signal with a local oscillator separated by the desired mm-wave frequency. The critical system parameters as well as optimum receivers need to be further investigated for this application.

However, today the architecture of RoF systems is completely different and not compatible with FTTH architectures. In future access networks like wavelength division multiplex passive optical networks (WDM-PON) analog RoF and digital FTTH signals must co-exist in the same fiber infrastructure. If this will happen, seamless broadband access services could be readily put into the field. In the second generation FTTH system splitting ratio up to 1:64 (or even more) and fiber lengths greater than 50 km are under discussion. Moreover, the bit error rate (BER) requirements are as high as $BER = 10^{-9}$, either for wired or wireless systems. This results in rather high values for the power budget of the analog RoF systems and a good immunity against the chromatic dispersion of the fiber.

The outline of this work is as follows. Chapter 2 will discuss the requirements for broadband wireless access services in terms of channel capacity, free space propagation and fading effects while also taking into account the most important technical challenges still ahead.

Chapter 3 gives an overview of the most common optical mm-wave generation methods whereas chapter 4 discusses the effects of the different RoF architectures with regard to propagation in a dispersive medium (i.e. optical fiber) and the penalties incurred therein. Chapter 5 first characterizes the generation of mm-wave signals with a Mach-Zehnder modulator under different conditions. Moreover, a novel generation method via an optical fiber loop mirror with different configurations is proposed and is one of the main topics of this thesis. In chapter 6 an evaluation of the different receiver architectures for the mobile unit is developed, taking special interest in sensitivity, implementation loss and bit error rate performance for the different setups. The maximum attainable capacities of each receiver are also calculated. In chapter 7 the results of the broadband wireless experiments are presented and discussed in detail. Finally, chapter 8 provides a summary of the most important results achieved throughout this work.

2 General system requirements for mobile broadband communication systems

In this section a general overview of the requirements for mobile broadband communication systems will be addressed, and the basic ideas and applications will be described.

2.1 Gigabit wireless communications

The adoption of each successive generation of Ethernet technology has been driven by economics, performance demand, and the rate at which the price of the new generation has approached that of the old. As the cost of 100 Mbps Ethernet decreased and approached the previous cost of 10 Mbps Ethernet, users rapidly moved to the higher performance standard. Additionally, gigabit Ethernet became economic (e.g. below €200) for server connections and desktop gigabit connections have come within €10 or less of the cost of 100 Mbps technology. Consequently, gigabit Ethernet has become the standard for servers, and systems are now ordered with gigabit Network interface cards. Mirroring events in the wired world, as the prices of wireless gigabit links approach the prices of 100 Mbps links, users are switching to the higher-performance product, both for traditional wireless applications (e.g. voice), as well as for applications that only become practical at gigabit speeds (e.g. HDTV streaming).

Wireless communications are directed towards the need for gigabit speeds and longer-range connectivity as the applications emerge for home A/V networks, high-quality multimedia, voice and data services. Current wireless local area networks (WLANs) offer peak rates of 54 Mbps, with 200–540 Mbps, such as IEEE 802.11n, becoming available soon. However, even 500 Mbps is inadequate when faced with the demand for higher access speed from rich media content and competition from 10 Gbps wired LANs. In addition, future home A/V networks will require a Gbps data rate to support multiple high-speed, HDTV streams (e.g. carrying an uncompressed high-definition video at resolutions of up to 1920×1080 progressive scans, with latencies ranging from 5 to 15 ms, and 30 bit per channel and a frame rate of 90 fps will require a data rate as high as 5 Gbps) [2].

Some approaches, such as IEEE 802.11n, are improving data rates by evolving the existing WLANs standards to increase the data rate; to up to 10 times faster than IEEE 802.11a or 802.11g, but still less than 1 Gbps. Others, such as the ultra-wideband (UWB) are pursuing much more aggressive strategies, such as sharing spectra with other users. However, the

typical 480 Mbps bandwidth of UWB cannot fully support broadcast video and therefore the data packets need to be recompressed. This forces manufacturers to utilize expensive encoders and more memory into their systems, in effect losing video content and adding latency in the process. Another approach will be moving to higher, unused and unregulated millimeter wave frequencies. Millimetre wave technology can be classified as occupying the electro magnetic spectrum that spans between 30 and 300 GHz, which corresponds to wavelengths from 10 to 1 mm. An interesting application band at 60 GHz offers various advantages over current communications systems in the L band. One of the deciding factors that make 60 GHz technology attractive is the establishment of huge unlicensed bandwidths (up to 9 GHz) that are available worldwide. The spectrum allocations vary for different regions and are listed in Table 2.1 [3].

Region	Unlicensed BW (GHz)	Max Tx Power (mW)	Max antenna gain (dBi)
Europe	9 GHz (57–66)	20	37
Japan	7 GHz (59–66)	10	47
USA	7 GHz (57–64)	500	Not specified
Korea	7 GHz (57–64)	10	To be decided
Australia	3.5 GHz (59.4–62.9)	10	Not specified

Table 2.1: The 60 GHz band allocation around the world [3].

While this is comparable to the unlicensed bandwidth allocated for ultra-wideband purposes (~2–10 GHz), the 60 GHz band is continuous and less restricted in terms of power limits (also there are less existing users). This is due to the fact that the UWB system is an overlay system and thus subject to different considerations and very strict regulation. This huge bandwidth offers potential in terms of capacity and flexibility and makes 60 GHz technology particularly attractive for gigabit wireless applications. The main use of the bandwidth will be in the downlink as broadcast for distribution of high definition multimedia content whereas the uplink can be realized with about 100 MHz for user data upload. Although 60 GHz regulations allow much higher transmit power compared to other existing wireless local area networks (e.g. maximum 100 mW for IEEE802.11 a/b/g) and wireless personal area network (WPAN) systems, the higher transmit power is necessary to overcome the higher path loss at

60 GHz. While the high path loss seems to be a disadvantage at 60 GHz, it does however confine the 60 GHz power and system operation in an indoor environment. Hence, the effective interference levels for 60 GHz are less severe than those systems located in the congested 2-2.5 GHz and 5-5.8 GHz regions. In addition, higher frequency re-use can also be achieved over a very short distance in an indoor environment, thus allowing a very high throughput network. The compact size of the 60 GHz radio also permits multiple antenna solutions at the user terminal that are otherwise difficult, if not impossible, at lower frequencies. Compared to a 5 GHz system, the form factor of millimetre wave systems is approximately 140 times smaller and thus the antennas can be conveniently integrated into consumer electronic products, but it will require new design methodologies to meet modern communication needs.

2.2 Millimetre wave propagation

In this section propagation of mm-wave signals in free space will be modeled to recognize limiting factors and common impairments. The carrier frequency at $f_{RF} = 60$ GHz provides the following advantages:

- Broadband unlicensed bandwidth (7 GHz).
- Due to high path losses and oxygen absorption the transmission is confined to very small local areas (i.e a room) with no wall transmission. This provides highly secure, virtually interference-free links with the possibility of frequency re-use within a small geographic region.
- Small antenna size capable of distributed antenna array configurations and on-chip integration.

But due to limitations in our lab equipment, the proof of concept system experiments for gigabit wireless transmission in later sections was carried out at $f_{RF} = 33$ GHz. Therefore, the theory will be developed for these two carrier frequencies.

2.2.1 Free space propagation

Due to the spherical propagation of radio waves in free space, the path loss decays with the square of f_{RF} , mathematically in dB,

$$PL_{freespace} = 20 \cdot \log_{10} \left(\frac{4\pi \cdot d \cdot f_{RF}}{c} \right) \quad (2.1)$$

where d is the link distance and c the speed of light in vacuum. The path loss as a function of link distance is plotted in Figure 2.1 for different carrier frequencies f_{RF} . The initial loss is quite high, but then increasing the distance reaches a plateau. The path loss at $f_{RF} = 60$ GHz for the first meter ($d = 1$ m) is around 68 dB and 62.8 dB for $f_{RF} = 33$ GHz.

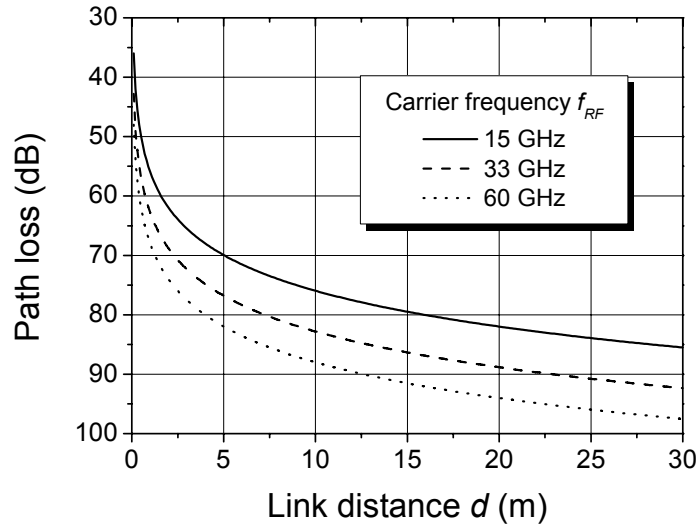


Figure 2.1: Path loss as a function of link distance d with carrier frequency f_{RF} as a parameter.

The free space path loss can be mitigated by using high gain, albeit directional, antennas. A more detailed expression for line-of-sight (LOS) links was given by Friis accounting for other system parameters such as antenna gain and system losses. The general equation relates the received power P_{RX} to the transmitted power P_{TX} by [4]

$$\frac{P_{RX}}{P_{TX}} = \frac{G_{TX} \cdot G_{RX} \cdot c^2}{16 \cdot \pi^2 \cdot d^2 \cdot f_{RF}^2 \cdot SL} \quad (2.2)$$

Here G_{TX} and G_{RX} are the transmitter antenna and receiver antenna gain respectively and SL is a system loss factor ($SL > 1$) to account for extra effects such as implementation loss and human shadowing losses. Besides free space path losses which are already quite high at mm-wave frequencies, the atmosphere presents a couple of additional impairments such as

- Water vapour and oxygen absorption.
- Precipitation attenuation due to rain.
- Foliage blockage.
- Scattering effects.

- Diffraction (i.e. bending).

Studies about these effects are well known in the literature and as an example, the atmospheric absorption for two different geographical scenarios were researched in [5]. The results are plotted in Figure 2.2. At 60 GHz there is a strong absorption due to resonance with oxygen molecules. Although oxygen absorption is quite an impediment at 60 GHz compared to lower frequencies, the extra attenuation of 10 dB/km when used in indoor scenarios (i.e. $d < 20$ m) results in only a 0.2 dB penalty. Working at $f_{RF} = 33$ GHz has the low extra attenuation value of 0.1 dB/km, which can be safely neglected for indoor short range scenarios.

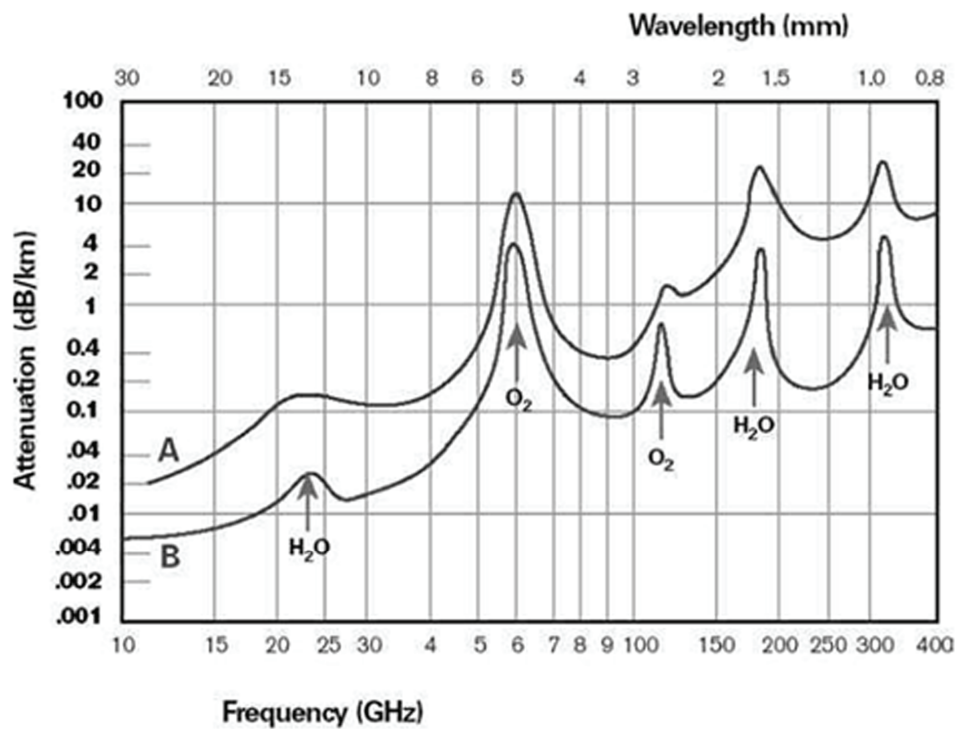


Figure 2.2: Average atmospheric absorption of mm-waves for two different scenarios [5]. Scenario A: Sea level and scenario B: 4 km elevation.

2.3 Channel capacity

Claude Shannon established the theoretical basis of digital communication with two well-known theorems: source coding and channel coding. The first established the minimum bit error rate (BER) required to reproduce a source signal within a given degree of accuracy. Shannon's channel coding theorem on the other hand establishes the maximum rate at which

transmission is achievable with arbitrarily high accuracy. This channel capacity C in presence of additive white Gaussian noise (AWGN) takes the form [6]

$$C = B_n \cdot \log_2 \left(1 + \frac{P_{RX}}{B_n \cdot N_{power}} \right) = B_n \cdot \log_2 (1 + SNR) \quad (2.3)$$

where B_n is the systems noise bandwidth, P_{RX} the received power, N_{power} the noise power and SNR the signal to noise ratio. This establishes an upper bound to channel capacity. While simple techniques for reaching within about 30% to 50% of channel capacity have been known and employed for at least 30 years, only within the last few years has a composite technique involving iterative soft decoding of parallel or serial concatenated codes, known as “turbo decoding”, shown that efficiencies above 80% of channel capacity are practically achievable, provided sufficient long decoding delays can be tolerated.

The main challenges of wireless propagation at 60 GHz are

- High loss from the Friis equation in Eq. (2.2).
- Human shadowing.
- Non-negligible Doppler shift.
- Non line-of-sight (NLOS) propagation which causes random fluctuations in the signal level known as multipath fading.
- Noise.

Although high powers are allocated for the 60 GHz band, Eq. (2.2) denotes the importance of the antenna gains. The SNR at the receiver can be calculated from Friis equation in dB form adding other loss and noise factors as

$$SNR = P_{TX} + G_{TX} + G_{RX} - PL(d) - L_{shad} - IL - (10 \cdot \log_{10}(k_B T B_n) + NF_{RX}) \quad (2.4)$$

where L_{shad} stands for human shadowing losses, IL denotes an implementation loss factor, k_B is Boltzmann’s constant, T is the absolute operating temperature in °K and NF_{RX} the noise figure of the receiver. $PL(d)$ is the path loss defined as

$$PL(d) = PL(d_0) + 10 \cdot n_{path} \cdot \log \left(\frac{d}{d_0} \right) \quad (2.5)$$

for the link distance d and reference distance d_0 . The exponent n_{path} in Eq.(2.5) is useful to later depict several transmission scenarios, such as line of sight (LOS) or non-line of sight (NLOS) in home or office environments. Ignoring human shadowing losses, meaning there is a direct LOS between transmitter and receiver (i.e. $L_{shad} = 0$) the following parameters were used to simulate a millimeter wireless link operating at $f_{RF} = 33$ and 60 GHz with $P_{TX} = 10$ dBm, $NF_{RX} = 10$ dB, $IL = 6$ dB, $B_n = 7$ GHz and $d = 10$ m. The channel capacity C was evaluated from Eq. (2.3) for different combined antenna gains G_C (i.e. $G_C = G_{TX} + G_{RX}$ in dB) varying the transmitted power P_{TX} in Figure 2.3a and Figure 2.3c whereas the channel bandwidth B_n is swept in Figure 2.3b and Figure 2.3d.

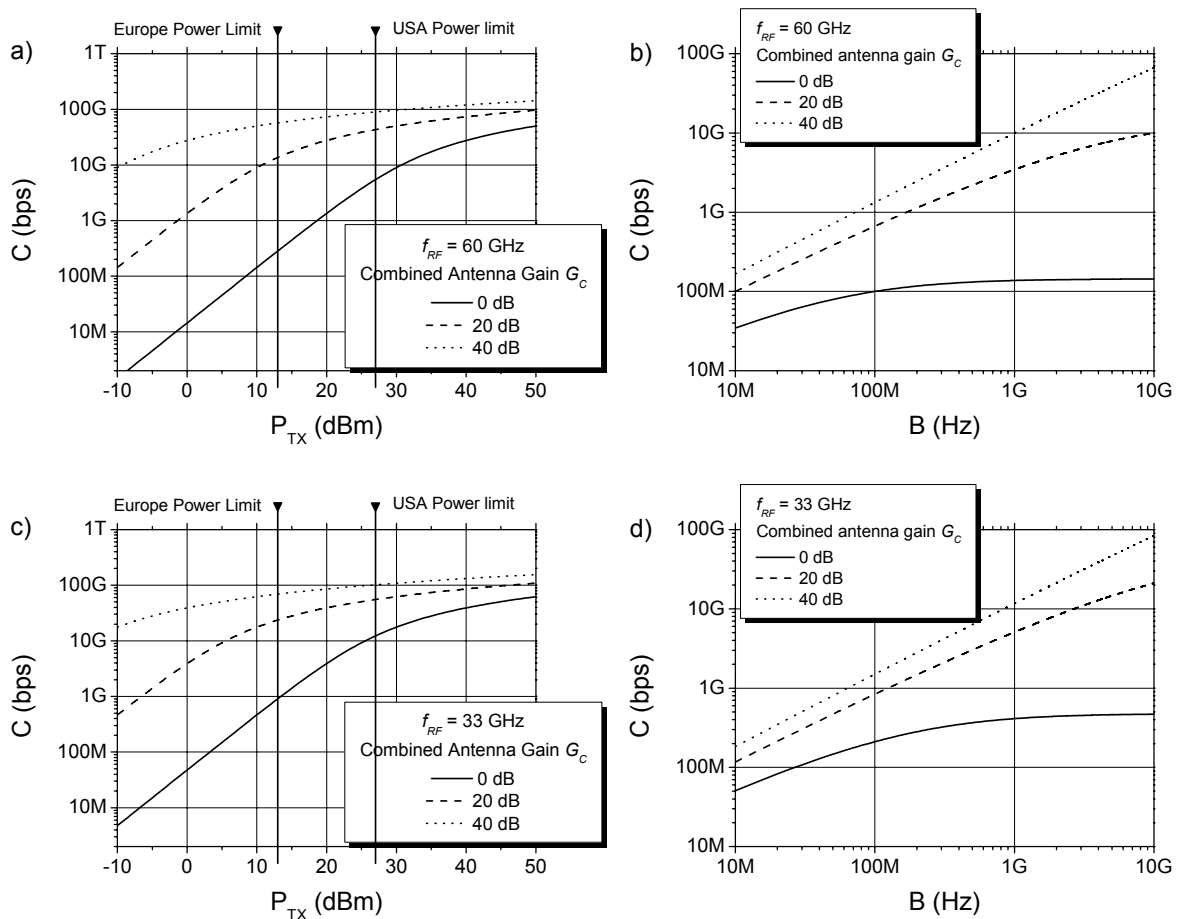


Figure 2.3: Shannon's maximum channel capacity C as a function of transmitted power (a and c) and system bandwidth (b and d) for a 33 GHz (c and d) and 60 GHz (a and b) wireless link.

One important result from these curves is that using omnidirectional antennas (i.e. $G_C = 0$ dB) no gigabit wireless channel can be obtained with the limits for $P_{TX} = 13$ dBm and $B = 7$ GHz

imposed in Europe. Only in USA with $P_{TX} = 27$ dBm can a real gigabit wireless connection be implemented, but that is a huge amount of power used. Another problem with omnidirectional antennas is that power is wasted in the backscattered directions, so future antennas for gigabit wireless communications will have to have high gain and be extremely directive to minimize power loss in unused directions while providing some sort of beam steering to adjust the propagation direction.

Different scenarios for gigabit wireless indoor links arise, basically LOS or NLOS. The basic parameters are described in Table 2.2. In NLOS links the path loss due to scattering exceeds the square law for free space links. This path loss exponent can vary from $n_{path} = 1.55$ in LOS corridors due to a guided wave effect, to $n_{path} = 2$ (LOS in free space) up to $n_{path} = 5$ in extreme NLOS links. The path loss exponent n_{path} is explained in detail in [7].

Environment	n_{path}	Shadowing	Reference
Home 5-10m (LOS/NLOS)	1.55/2.44	1.5/6.2	[7]
Conf. Room 20 m (LOS/NLOS)	1.77/3.83	6/7.6	[8]

Table 2.2: Gigabit wireless links scenarios parameters [3].

Calculating the capacity as a function of link distance d for these various scenarios gives rise to the results in Figure 2.4a for $f_{RF} = 60$ GHz.

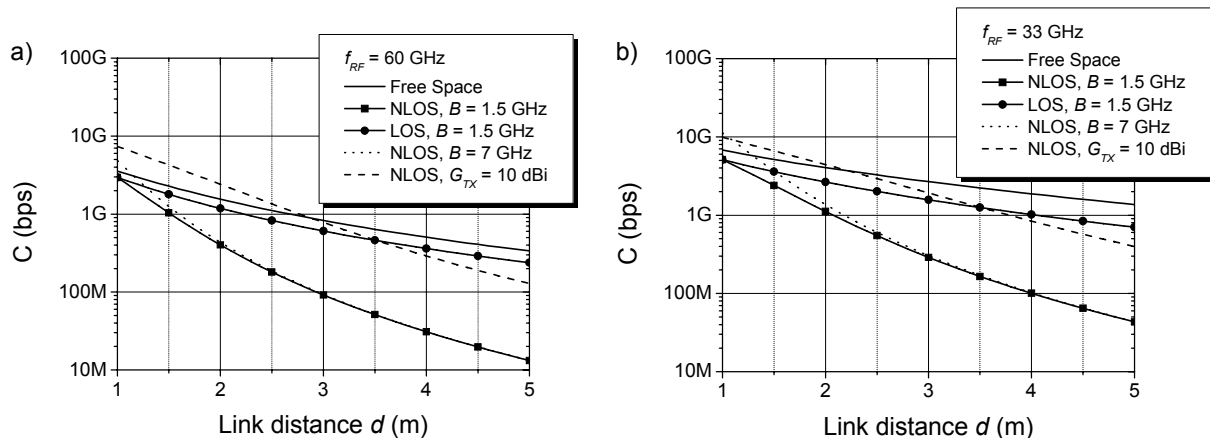


Figure 2.4: Capacity C as a function of link distance d for a) $f_{RF} = 60$ GHz and b) $f_{RF} = 33$ GHz.

The first curve of interest is the free space path loss which already shows that for omnidirectional antennas with zero gain, a true gigabit wireless link is limited to a couple of

metres. Considering the office LOS scenario with $n_{path} = 1.77$ and a $B_n = 1.5$ GHz has a lower performance than free space due to shadowing losses plus the guided wave effect which are taken into account. The NLOS case with $n_{path} = 3.83$ proves to be the worst case scenario for omnidirectional antennas, as not even 100 kbps can be realized at 20 m distance by increasing the bandwidth. The increase in bandwidth from 1.5 GHz to 7 GHz only improves the performance in the first meters. The same general observations can be obtained from Figure 2.4b for $f_{RF} = 33$ GHz whereas due to less link loss, the wireless reach is somewhat extended.

The critical point is then the gain of the antennas and later, the frequency dependence of such gain. A curve considering a transmitter antenna with $G_{TX} = 10$ dB shows a considerable improvement and a gigabit wireless link can be theoretically implemented up to a distance of $d = 2.7$ m for 60 GHz links and $d = 3.7$ m for a 33 GHz link. As the combined gain of the antennas seems to greatly increase the capacity of the link, plotting the capacity versus gain in Figure 2.5 can help design links accordingly.

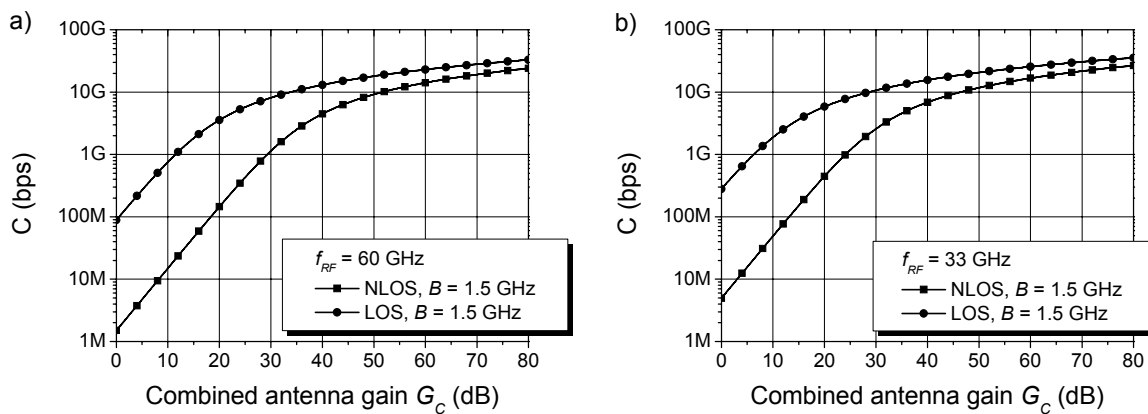


Figure 2.5: Capacity C as a function of combined antenna gain G_C for a) $f_{RF} = 60$ GHz and b) $f_{RF} = 33$ GHz.

The case of interest is NLOS (i.e. $n_{path} = 3.83$), which with $G_C = 30$ dB achieves a gigabit link with a distance of 20 m (indoor office scenario) in Figure 2.5 for both RF frequencies. If higher data rates were to be implemented, like 10 Gbps, then either extreme high gain antennas with $G_C = 50$ dB would have to be used plus an spectral efficient modulation format like M-ary phase shift keying (PSK). However, if the bandwidth B is increased to 7 GHz, then simple amplitude modulation formats like amplitude shift keying (ASK) could be employed.

For a single antenna element with antenna gain more than 20 dBi, a reliable communication link is difficult to establish even in LOS condition at 60 GHz. This is due to the human blockage which can easily block and attenuate such a narrowbeam signal. To overcome this problem, a switched beam antenna array or adaptive antenna array is required to search and beamform to the available signal path. The array is subsequently required to track the signal path periodically and establish the best path available (which could be NLOS if human shadowing is high).

As far as the proof of concept system is concerned, using $f_{RF} = 33$ GHz instead of 60 GHz provides only a 5.2 dB path loss difference at reference distance $d_0 = 1$ m. The challenge resides in the relative bandwidth of the system. Working with ASK signals at data rates as high as 10 Gbps at a carrier frequency of 33 GHz means that a system with a relative bandwidth of 30% must be realized. Usually, the relative bandwidth doesn't surpass 10% so as to have good quality RF components (i.e. filters, amplifiers, etc.).

2.4 Technical challenges

Even though 60 GHz technologies offer certain advantages over lower frequency systems, there are still numerous challenges that need to be addressed. In this section an overview of these open points in 4 main categories (channel propagation, antenna technology, integrated circuit technology and modulation schemes) will be described.

2.4.1 Channel propagation

Due to the high popularity of cellular networks, WLANs and the emerging massification of WiMax, there are plenty of channel models and measurements in the lower frequency channel range (5 GHz for WLAN [9]-[10] and 3-10 GHz in the UWB band [11]-[13]). However, the 60 GHz band lacks of many channel modeling and even less measurements are consistently made. Moreover, the few models available are radio channel models which include the antennas [14]. A propagation channel model would be necessary for general use. Therefore, a mm-wave propagation channel characterization for short range wireless communications was develop in [15] for 60 GHz links for various indoor scenarios. Furthermore, the reflection and transmission behavior of building materials at 60 GHz is reported in [16]. The higher losses at 60 GHz mean that material penetration is extremely difficult (or even impossible) and that the 60 GHz radio signal will be effectively confined to single rooms. While this is

advantageous for security reasons, it also means that to provide coverage in a wide area, the need of repeaters or some kind of distribution system for femtocellular networks is imperative.

2.4.2 Antenna technology

Many types of antenna structures are considered not suitable for 60 GHz WPAN/WLAN applications due to the requirements for low cost, small size, light weight, and high gain. In addition, 60 GHz antennas also require to be operated with approximately constant gain and high efficiency over the broad frequency range (57–66 GHz). The beamforming at 60 GHz can be achieved by either switched beam arrays or phase arrays. Switched beam arrays have multiple fixed beams that can be selected to cover a given service area. It can be implemented much easier compared to the phase arrays which require the capability of continuously varying the progressive phase shift between the elements. The complexity of phase arrays at 60 GHz typically limits the number of elements. A 2x2 beam steering antenna was developed in [17] at 61 GHz with circular polarization and 14 dB gain. A third solution called photonic beamforming is a hybrid electrical/optical approach. Using new photonic lightwave circuits in silica technology the phase of multiple antenna elements can be easily adjusted [18]. More information on this subject can be found in [19]-[20].

The implementation of larger phase arrays, however, presents some technical challenges such as requirement for higher feed network loss, more complex phase control network, stronger coupling between antennas as well as feedlines, and so forth. These challenges make the design and fabrication of the larger phase arrays become more complex and expensive.

For later system experiments and as a proof of concept to cope with the equipment in our lab, a wireless link at $f_{RF} = 33$ GHz was implemented. The broadband data reached data rates as high as $R_b = 10$ Gbps, therefore the realisation of a system with a relative bandwidth $> 30\%$ was quite challenging. For this reason, a wireless link with $f_{RF} = 33$ GHz will be characterized. Figure 2.6a shows the calculated free space path loss for a wireless link with the transmission distance d as a parameter according to Eq. (2.1). For the case $d = 1$ m, at $f_{RF} = 33$ GHz, the free space path loss was calculated to be $PL_{freespace} = 62.8$ dB. The ideal channel transfer function exhibits a loss tilt which varies ± 2.5 dB inside the bandwidth of interest (24-40 GHz).

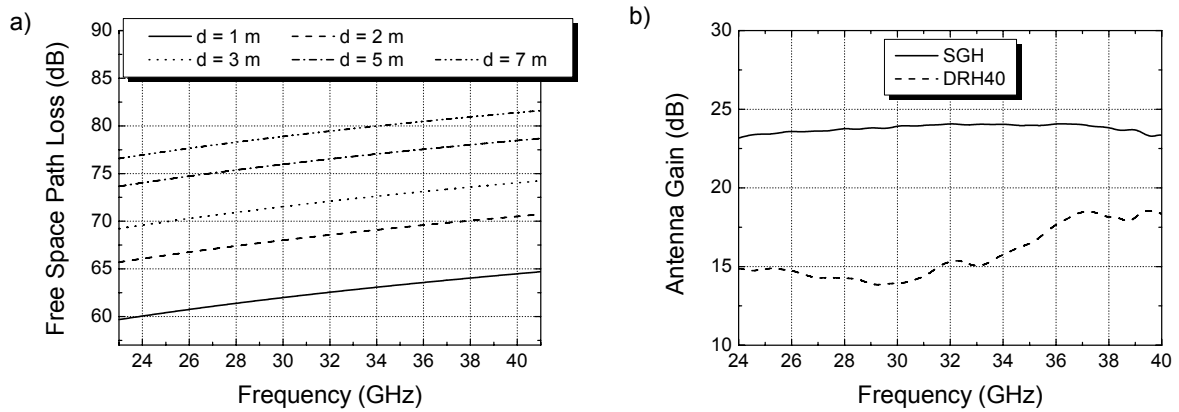


Figure 2.6: a) Free space path loss as a function of frequency for a wireless link with the transmission distance d as a parameter and b) antenna gain response.

A more general equation to calculate the link loss was developed by Friis [4]

$$LL = \frac{P_{RX}}{P_{TX}} = \frac{G_{TX} G_{RX} \lambda^2}{16\pi^2 d^2 SL} \quad (2.6)$$

where P_{TX} and P_{RX} are the transmitter and receiver power respectively, G_{TX} and G_{RX} are the transmitter and receiver antenna gain respectively, λ is the wavelength, d the link distance and SL is a system loss factor ($SL \geq 1$ which includes shadowing and other losses). For the system experiments two antenna sets were available:

- Vivaldi DRH40: Vivaldi type antennas with a frequency response from 4 to 40 GHz and a nominal gain $G_{vivaldi} = 15$ dB. The gain response in the frequency range of interest is shown in Figure 2.6b.
- SGH 2640: standard gain horn antennas with a frequency range from 26 to 40 GHz and a nominal gain $G_{horn} = 24$ dB. Its gain response is also depicted in Figure 2.6b.

The link loss of our channel was measured in an anechoic chamber setting the antennas $d = 3.1$ m apart. The results are shown in Figure 2.7 for different antenna combinations. This case corresponds to the free space case as the chamber guarantees no multipath or reflection paths. A certain tilt in the response can still be observed, being 1.6 dB for the Horn-Horn and 2.8 dB for the Horn-Vivaldi case in the systems bandwidth of interest. These two cases can be tolerated but using two Vivaldi antennas exhibit a tilt of 7.55 dB which is unacceptable, as a signal using the whole available bandwidth (i.e. 9 GHz) will surely be distorted.

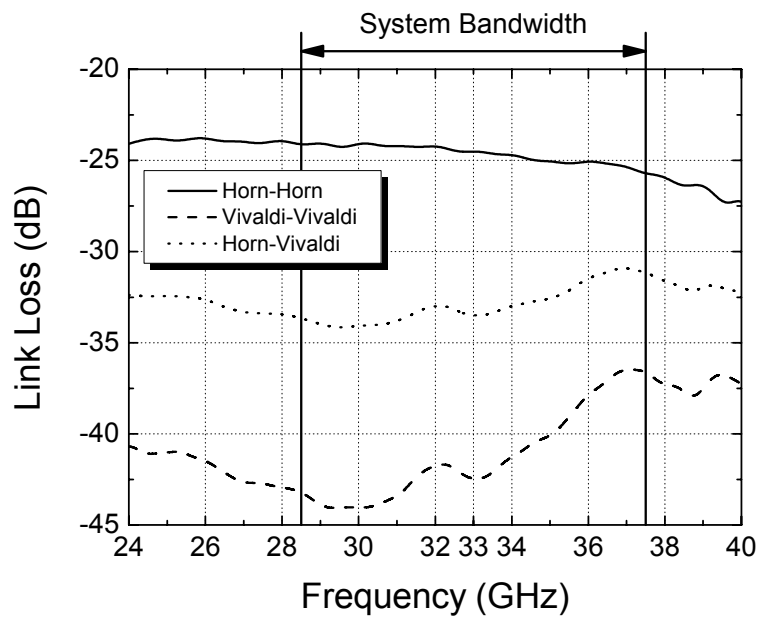


Figure 2.7: Link loss as a function of frequency for a wireless link for $d = 3.1$ m and different antenna combinations.

The antennas directional diagram for the E-plane and H-plane can be seen in Figure 2.8a for a Horn antenna and Figure 2.8b for a Vivaldi antenna. The Horn antenna is clearly more directive, thus providing more gain (10 dB more than the Vivaldi).

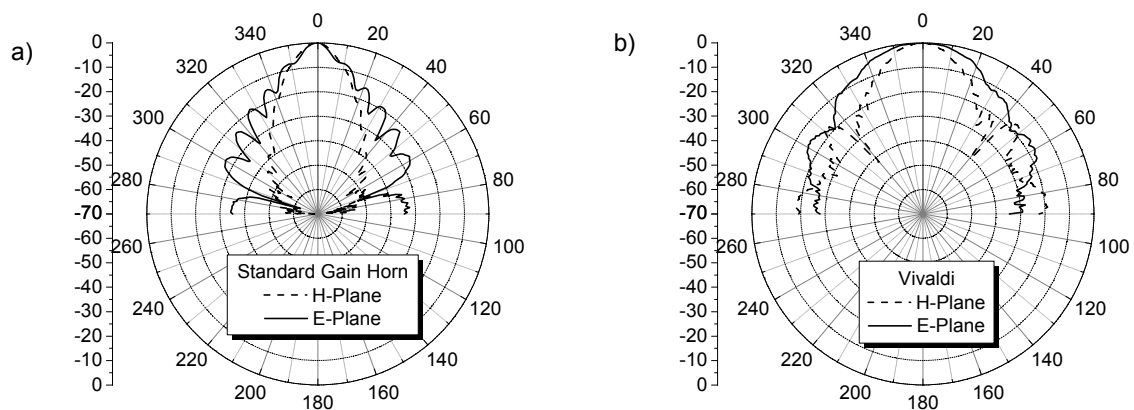


Figure 2.8: Antennas directional diagrams with $f_{RF} = 33$ GHz for a) Horn antenna and b) Vivaldi antenna.

2.4.3 Integrated circuit technology

To exploit the wireless market it seems the key aspects that decide a technology's success are the size and cost. By using integrated circuit (IC) technology the size of the devices is reduced and mass production is feasible, allowing a reduction in cost. At mm-wave there are three

competing IC technologies: group III and IV semiconductor technology such as gallium arsenide (GaAs) and indium phosphide (InP); silicon germanium (SiGe) technology such as HBT and BiCMOS; and silicon technology such as CMOS and BiCMOS. There is, up to now, no single technology that can meet all the objectives and system requirements. Therefore, the choice of IC technology will depend on the application. For example, GaAs technology allows fast, high gain, and low noise implementation but suffers poor integration and expensive implementation. On the other hand, SiGe technology is a cheaper alternative to the GaAs with comparable performance. A comparison of the costs of different semiconductor technologies normalized to the cost of InP is shown in Figure 2.9 for the year 2005 [21]. All of these technologies can work at 60 GHz being InP the most expensive to develop. GaAs technology in both its high electron mobility transistor (HEMT) variants: metamorphic HEMT or pseudomorphic HEMT, offers around a 60% of the InP cost. Most impressive is the reduction in cost when using SiGe, with only a mere 8% of the InP costs.

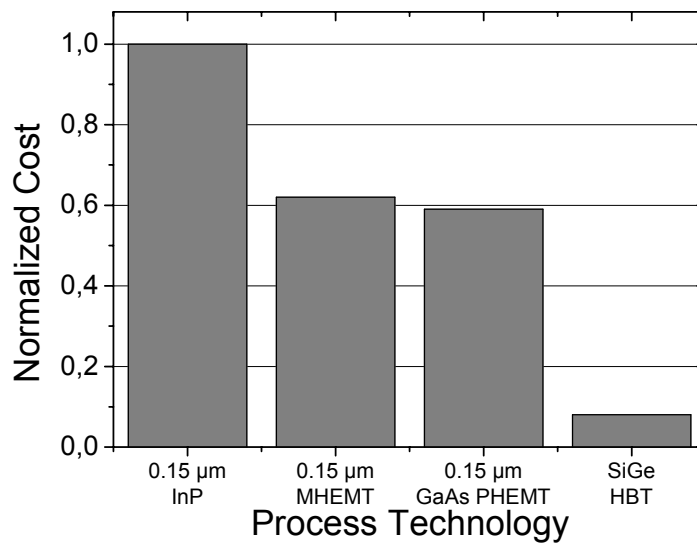


Figure 2.9: Relative cost, per unit area, for semiconductor technologies normalized to InP [21].

In [22], the first mm-wave fully antenna integrated SiGe chip has been demonstrated. In reduced size and mass production, CMOS technology appears to be the leading candidate as it provides low-cost and high integration solutions compared to the others at the expense of performance degradation such as low gain, linearity constraint, poor noise, lower transit frequency, and lower maximum oscillation frequency. Recent advances in CMOS technology [23] have demonstrated the feasibility of bulk CMOS process at 130 nm for 60 GHz RF

building blocks, active and passive elements. More future research and investigations in developing a fully integrated CMOS chip solution have to be performed.

2.4.4 Modulation schemes

The choice of the modulation format at 60 GHz will be highly dependent on the wireless channel, the use of high gain antennas or arrays of them and the limitations of the RF technology. For example, if the delay spread of the propagation channel is high, then orthogonal frequency division multiplex (OFDM) will be the obvious choice due to its flat fading capabilities. On the other hand, high directive antennas could be used to minimize the effects of multipath fading.

Regarding CMOS technology, the lower power and high linearity requirements of the amplifiers make the use of OFDM complicated. Moreover, the poor phase noise performance limits higher modulation formats to less than 16 quadrature amplitude modulation (16QAM), 16 phase shift keying (16PSK) or 16 frequency shift keying (16FSK). The use of simple modulation formats such as amplitude shift keying (ASK) or differential phase shift keying (DPSK) are motivated by the huge unlicensed bandwidth available in the 60 GHz band. Therefore, the choice of the modulation format is a tradeoff of a number of issues which need to be further studied.

A comparison of different attributes of the most common modulation formats is summarized in Table 2.3. For later system experiments, ASK was selected as the modulation format to be used. Though relatively spectral inefficient, ASK offers several advantages such as simplicity of implementation, potential ultra-high data rate capabilities (i.e. 10 Gbps), relative insensitivity to amplifier non-linearity and oscillator phase noise and most of all, ease of interfacing to wire or fiber data networks [24].

2 General system requirements for mobile broadband communication systems

Mod. Scheme	Mod. Circuitry, Relative Complexity	Demod. Circuitry, Relative Complexity	Clock Recovery Required	IF Circuitry, Relative Complexity	Data Rate @ 1 GHz BW (Gbps)	Relative SNR Improvement (dB)
ASK/OOK – Envelope	Low	Lowest	No	Lowest	0.8	0 (Ref)
ASK/OOK - Coherent	Low	Medium	Yes	Lowest	0.8	-1
FSK – Coherent	Medium	High	Yes	Lowest	0.8	-4.7
BPSK	Low	Medium	Yes	Lowest	0.8	-6.1
DPSK - Downconvert	Low	Low	No	Low	0.8	-5.1
QPSK	Medium	High	Yes	Low	1.9	-6.1

Table 2.3: Comparison of modulation schemes/architectures [25].

The spectral efficiency can be defined as the channel capacity divided by the bandwidth used. Shannon's theorem puts a limit on the maximum spectral efficiency SE that can be achieved, and rearranging terms from Eq. (2.3) it takes the form

$$SE(\text{bps} / \text{Hz}) = \frac{C}{B} = \log_2(1 + SNR). \quad (2.7)$$

Simulations for different modulation formats with optimum coding are shown in Figure 2.10 including Shannon's fundamental limit as a function of the SNR . Each modulation reaches the maximum spectral efficiency determined by the logarithm of the number of constellation points in the format (i.e. $SE_{max} = \log_2(M)$, being M the number of constellation points). It is clear that increasing M results in a more spectral efficient format which approaches Shannon's limit for the case of the phase modulation formats. The case of ASK is similar to BPSK but with lower sensitivity, being one of the most spectral inefficient modulation formats which requires relatively high SNR to achieve a modest spectral efficiency of 1 bps/Hz. At the expense of system complexity, higher capacities can be obtained with higher order modulation formats for the same SNR . Quadrature amplitude modulation (QAM) proves to be the best approach as it requires the lowest SNR to reach its optimum spectral efficiency.

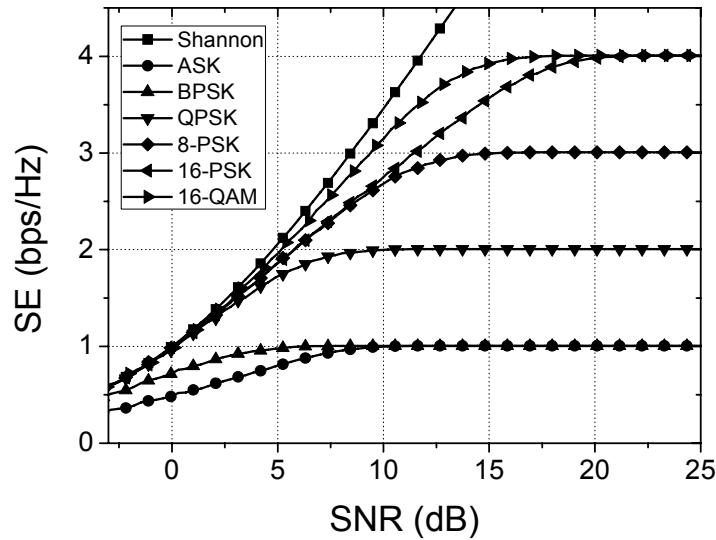


Figure 2.10: Spectral efficiency SE as a function of SNR for different modulation formats.

2.5 Signal transport schemes: radio over fiber architectures

The technical challenges described in section 2.4 concentrated mainly on physical aspects of gigabit wireless communications such as the components required for actual transmission from base station (BS) to the end user. The transport of these broadband signals to and from the BS will be briefly described in this section, taking into account both down- and uplink architectures.

2.5.1 Downlink transmission

For the downlink three basic architectures are available: RF over fiber, IF over fiber and baseband over fiber. The basic principle of transmitting an RF signal with broadband data is carried out by all of them. However, each differentiates itself mainly in the way the complexity of the system is divided. Schematics of these three approaches can be seen in Figure 2.11.

The most straightforward approach to interconnecting remote antenna base stations in a fiber radio system is via an optical fiber feed network which can transport the wireless signals directly over the fiber at the RF transmission frequency without the need for any subsequent frequency up- or down-conversion at the base stations. This signal transport scheme is known as ‘RF over fiber’ (RoF) and a schematic depicting the architecture is shown in Figure 2.11a. Such a configuration is attractive in microcellular and picocellular networks operating in the mm-wave frequency region where a large number of cheap and simple BSs are required to

provide wide geographical coverage. However, a critical issue is the need of high speed optical modulation techniques able to generate mm-wave signals and consequently high speed photodiodes able to convert the optical signals back to the mm-wave range in the electrical domain. Various methods are available for mm-wave generation and will be discussed later in chapter 3. Moreover, depending on the kind of modulation technique, the RF signal will suffer more or less fiber chromatic dispersion induced power fading. This analysis is thoroughly investigated in chapter 4.

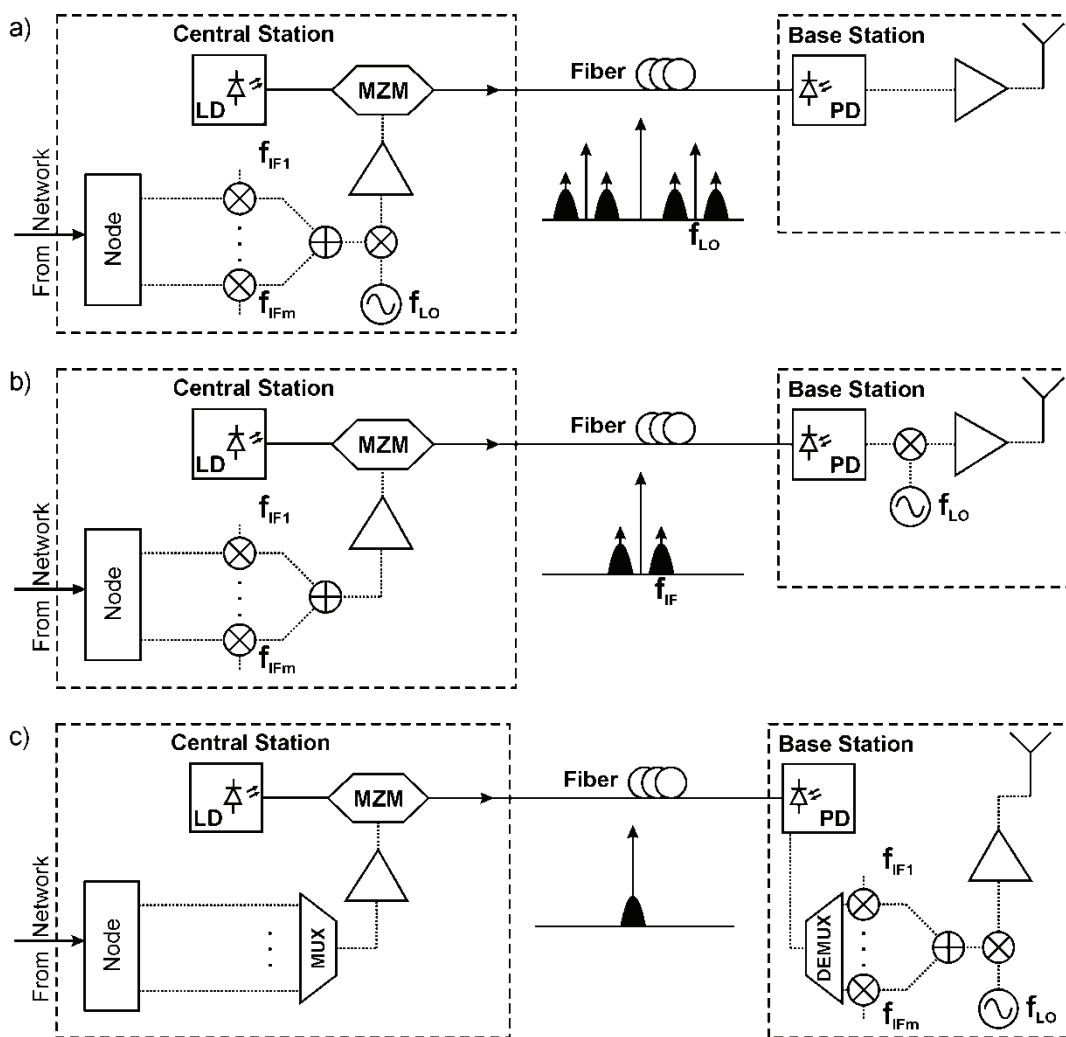


Figure 2.11: Signal transport schemes for the downlink. a) RF over fiber, b) IF over fiber and c) baseband over fiber.

By shifting the complexity a little bit into the BS, the transmission of ‘IF over fiber’ is shown in Figure 2.11b. In this case, IF frequency generally refers to intermediate frequencies in the L band (1-2 GHz). By reducing the frequency transmitted through the fiber the effects of fiber

chromatic dispersion are significantly diminished. Moreover, systems working directly at L band frequencies (e.g. WLAN) will not need up-conversion and the requirement on high speed optoelectronic components is reduced. However for systems working in the higher mm-wave range, the frequency up-conversion is carried out directly at the BS with a local oscillator (LO), increasing its complexity and cost.

To benefit from a mature technology such as baseband optical digital communications, the third approach ‘baseband over fiber’ was developed and is depicted in Figure 2.11c. Now the signal is time multiplexed and directly sent at baseband to the BS where the frequency upconversion is takes place. Therefore, the requirement on the optoelectronic components is the lowest and the effects of fiber chromatic dispersion are very low. In addition, many of the digital signal processing techniques can also be implemented. On the other hand, the BS is now a complex and costly unit, capable of up-converting different channels with different IFs.

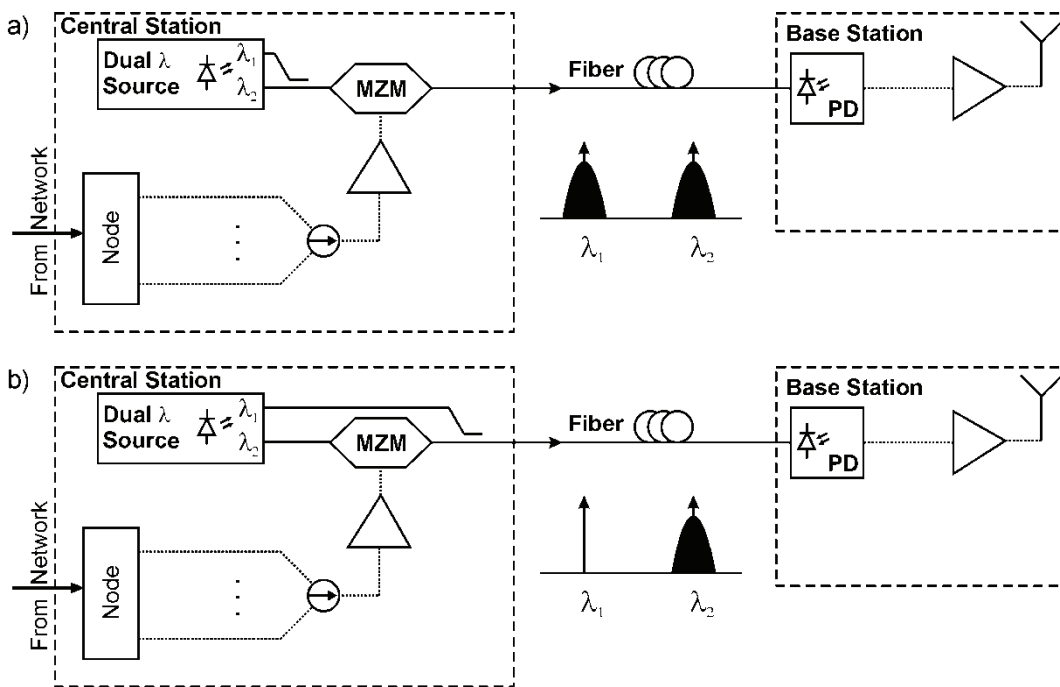


Figure 2.12: RHD signal transport schemes for the downlink. a) ODSB and b) OSSB.

The previous three approaches employ intermediate frequencies (IFs) which limit the bandwidth available for data transmission. To reach multi-gigabit data rates either some complex multi-level format is needed or the broadband data needs to be directly modulated onto the optical carrier. The latter procedure is known as remote heterodyne detection (RHD)

and offers two possibilities: optical double sideband (ODSB) and optical single sideband (OSSB) which are shown in Figure 2.12a and Figure 2.12b, respectively.

For this approach a dual wavelength source is needed which provides the two optical spectral lines. Coherence and correlation between these lines will be studied later in chapter 4. The main difference between both approaches resides in if the two optical lines are modulated with the broadband data or only one of them is. The base station architecture is the same for both cases, as the heterodyning to produce the RF frequencies takes place in the broadband photodiode. In this way, larger bandwidth is available, meaning that increased data rates can be transmitted.

2.5.2 Uplink transmission

There are many proposals for the downlink architecture but not so many for the uplink. The main issues are the need of a laser source in the BS and the modulation of this optical carrier with the uplink data. Some schematics can be seen in Figure 2.13.

The most straightforward approach would be to mimic the CS architecture, shown in Figure 2.13a. The uplink signal is modulated onto a laser diode through an external modulator. The main disadvantage of this approach is the need of high speed electro-optical components to accommodate the RF signal. In addition, the uplink signal will suffer from chromatic dispersion induced power fading.

Another solution would be to downconvert the uplink signal to intermediate frequencies, shown in Figure 2.13b. Now the laser diode can be directly modulated, saving the cost of a high speed external modulator. Furthermore, this approach benefits of the maturity of IF demodulation techniques. However, the need of an LO source in the BS increases its complexity and cost. Nonetheless, the LO can be distributed through the downlink and recovered in the BS through electrical filtering.

The last approach would be to use a device which receives the downlink data at one wavelength and modulates the uplink signal onto another optical carrier. This can be realized with an electro absorption transceiver (EAT) which acts as a detector for the downlink and as an electro absorption modulator (EAM) for the uplink. The corresponding schematic is shown in Figure 2.13c. The EAT can be thought of as a 4-port device with optical in/out and RF in/out ports. Realisations of such a structure can be found in [26]-[27].

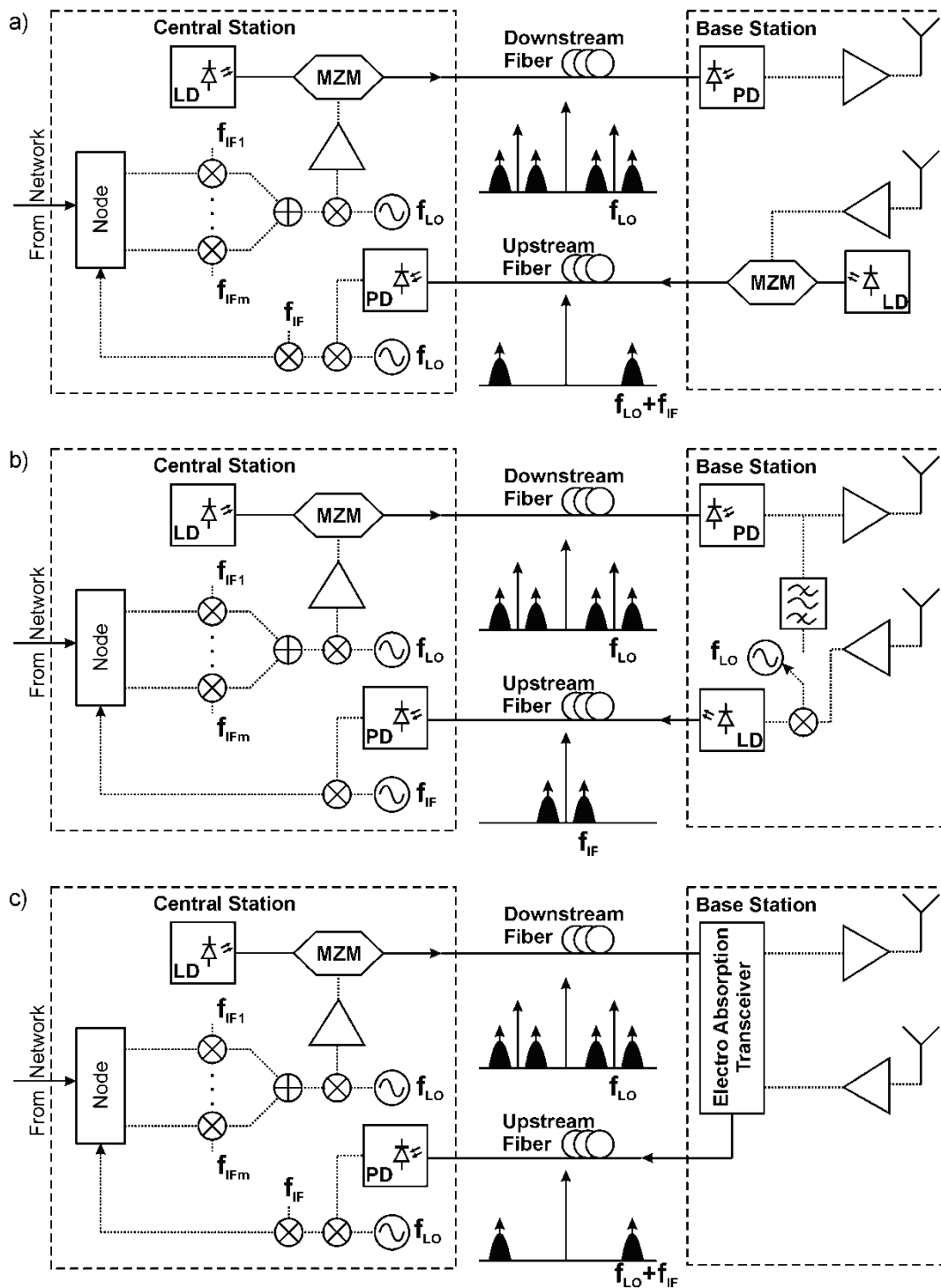


Figure 2.13: Signal transport schemes for the uplink. a) RF over fiber, b) IF over fiber and c) Electro Absorption Transceiver (EAT).

Another variant for the EAT is using reflecting semiconductor optical amplifiers (RSOA). Research done in [28] shows that the modulation on an optical carrier can be deleted and the original optical carrier can thus be remodulated with the new data stream. Direct modulation

of the RSOA bias current was achieved for 1.25 Gbps signals in [29], saving the optical modulator for the uplink. Data rates as high as 10 Gbps in WDM-PON were demonstrated in [30] after electronic equalization.

3 Optical methods for microwave signal generation

The generation of the mm-wave carriers can be achieved electrically, but optical heterodyne techniques offer definitive advantages. First of all, the ability to generate the mm-wave signals remotely due to the low loss of the fiber. Secondly, optical fiber provides immunity to electromagnetic interference. Thirdly, the mechanical flexibility and low weight provide ease of deployment. And finally, some optical upconversion methods are capable of generating multiples of a reference oscillator, providing saving costs due to frequency multiplication. Several optical methods are used to generate electrical local oscillator (LO) signals in the 30 to 300 GHz range. All of them involve the heterodyne mixing of two or more laser spectral lines (separated at the desired mm-wave frequency f_{LO}) in a photodiode to generate the electrical beat signals. The laser spectral lines can be obtained from a single laser source or two phase-correlated lasers, or even two uncorrelated lasers. Due to the mixing, generally in a broadband photodiode, the resulting signals provide low-phase noise in accordance to the electrical reference source used. While many methods rely on generating two phase correlated spectral lines, some can use “white noise” sources such as the amplified spontaneous emission (ASE) from an erbium doped fiber amplifier (EDFA). However, the coherence of the optical fields is a major issue. In the next sections, the most common methods are briefly explained.

3.1 Heterodyned laser techniques

Heterodyning two laser modes that are offset from each other by f_{LO} is the most commonly used and, subjectively, the simplest method for efficiently producing optical LO signals. The modes can originate from the same laser cavity, called mode-locking. The drawback in this case is that for a certain laser, this results in a fixed microwave frequency, as the laser modes are a solution to the propagation equations in a laser cavity. However, the modes can come from two independent optical sources that either electrically/optically phase locked or injection locked together. In either case, the optical LO signal intensity can be generally expressed as

$$P_{LO}(t) = a_0 + a_1 \cdot \sin(2\pi f_{LO}t + \varphi). \quad (3.1)$$

where $a_0 = (P_1 + P_2)/2$ is the average optical intensity of the two combined modes, $a_1 = \sqrt{P_1 P_2}$ and f_{LO} is the offset frequency of the two laser modes. For comparison purposes, a

mixer conversion gain will be defined as the ratio of the detected power at $nf_{LO}+f_{RF}$ to the detected electrical power at f_{RF} , which is given by [31]

$$\Gamma_n = \frac{a_n^2}{4a_0^2} \quad (3.2)$$

where n represents the n^{th} harmonic of f_{LO} used for the upconversion.

Ideally, the electrical fields for the individual laser modes are perfectly aligned, the intensities of each mode are equal, and the offset frequency is well stabilized. In this case, 100% optical modulation is achieved, $a_0 = a_1$, and the differential conversion gain is $\Gamma_1 = -6$ dB. Conventional electronic mixers have conversion losses of more than 6 dB, so this is quite a good result, although in this scenario, no link loss has been assumed.

3.1.1 Mode-locking

Inside a laser cavity many independent longitudinal modes are present. They are usually independent from each other, meaning that their phase noise is uncorrelated. The frequency separation Δf of the modes is given by the length of the cavity L , the refraction index n_L and the velocity of light c in the following form

$$\Delta f = \frac{c}{2n_L L}. \quad (3.3)$$

By mixing in a photodiode, all spectral lines contribute to generate electrical signals in the frequencies $n \cdot \Delta f$ ($n = 1, 2, \dots$). As all the modes in the laser cavity are uncorrelated, the generated electrical signal is unstable and very noisy.

With precise modulation of the laser with a signal with frequency f_m , which approximates the frequency separation Δf , these uncorrelated longitudinal modes can be coupled and thus stop being independent. This approach is called active Mode-Locking. Passive Mode-Locking can be achieved by using saturated absorbers. Passive Mode-Locking is easier to achieve in practice but lacks tuning capabilities. By heterodyne mixing in a photodetector, the resulting signal at $f_{LO} = n\Delta f$ is very stable and, as the longitudinal modes are now correlated, its phase noise is very low [32].

For the generation of mm-wave signals the use of semiconductor lasers is very popular. They are very compact and have mode separations Δf in the GHz region. Nonetheless, they have to

be specially designed for this purpose, with a section that allows active or passive mode-coupling. Many examples can be found in the literature, namely [33]-[39].

One main drawback of this technique is the broad spectrum of the laser source which makes the use in WDM systems quite inefficient. As many modes contribute to the mm-wave signal generation, this method is especially subtle to fiber dispersion. By optical filtering, two modes can be selected with a frequency separation of f_{LO} . This provides a dispersion tolerant signal at cost of power efficiency [40].

Special devices can be manufactured with optical filters inside the laser cavity which hinder the propagation of undesired modes so that only the two modes used for the mm-wave signal generation leave the laser cavity [41]. This results in a compact, efficient device but lacks tunability of the mm-wave frequency and a complex fabrication process.

3.1.2 Injection-locking

In contrast to mode-locking, where two or more laser modes are coupled by an external electrical modulation signal, in the case of Injection-Locking the coupling is produced by an optical signal. A laser (called Master laser) is modulated with the desired mm-wave LO signal so that the emission spectrum shows the corresponding modulation sidebands. Also subharmonics are possible, as seen in [42]. When this signal is “injected” into another laser (called Slave laser) then one modulation sideband of the Master laser couples the emission of the slave laser, so that both lasers transmit a correlated signal with the desired mm-wave separation.

Several configurations for this approach can be found in the literature [43]-[48]. The biggest disadvantage is the need of at least two lasers and other optical components (i.e. isolators, fiber couplers, etc). However, locking two or more slaves to one master laser provides multichannel capability and optical spectra with 1 Hz linewidth have been generated [49].

3.1.3 Phase locked loops

The most straightforward method to generate mm-wave signals is the heterodyne method where two lasers, which are separated by the desired frequency f_{LO} in the optical domain, combine in a photodiode to generate the mm-wave signal. This method can be achieved by using two completely uncorrelated laser sources but the frequency stability and phase noise are very poor. Normally an active phase-locked loop with a microwave source is needed to

couple both laser sources in phase and thus achieve stable mm-wave signals [50]-[58]. Due to the high spectral linewidth of semiconductor lasers (a couple of MHz) the control loop time constant has to be relatively small (typically < 1 ns). It is therefore very difficult to achieve this for a single phase-locked loop, which is why hybrid solutions with phase-locking and injection-locking are proposed [59]. Nonetheless they require complex optical and electrical configurations.

3.2 External optical modulators

The basic principle behind external optical modulators is to maintain the laser working in a continuous wave mode and modulate the optical field via diverse electrooptical effects, for example, the electrooptic effect in crystals. Basically, when light propagates in a crystal, two possible linearly polarized modes exist: the so called rays of propagation. Each mode possesses a unique direction of polarization and a corresponding index of refraction n_x and n_y (i.e. a velocity of propagation). The existence of two orthogonal fields with different indices of refraction ($n_x \neq n_y$) is called birefringence. The linear electrooptic effect is the change in the indices n_x and n_y that is caused and is proportional to an applied electric field which in turn will lead to a change in phase. When an interferometric structure is used, such as a Mach-Zehnder structure, the phase modulation is converted to intensity modulation. The electrooptic effect is found in crystals such as lithium niobate (LiNbO_3), III-V semiconductors such as gallium arsenide (GaAs) or indium phosphide (InP) as well as poled polymers.

The most common optical modulators work using the Pockels effect (or linear electrooptic effect) of LiNbO_3 which achieves high Pockels coefficients (e.g. $r_{33} = 31$ pm/V). The one disadvantage of LiNbO_3 as a material is that it cannot be integrated with the laser diode source. That is why special interest was pursued in the use of III-V semiconductor materials such as gallium arsenide and indium phosphide. The possibility of monolithic integration with CW lasers is the main advantage of these kind of materials even though the Pockels effect is weaker than that in lithium niobate and there tends to be a poor overlap between the optical mode and the applied electric field. Furthermore, the refractive index of InP is relatively higher ($n = 3.5$) than silica fiber leading to increased fiber-to-fiber insertion loss (typically 10 dB). However, integrated photonic devices based on GaAs and InP are becoming an interesting option to integrate multiple functions in chips. A low drive voltage (0.45 V) GaAs Mach-Zehnder modulator with 50 GHz bandwidth is demonstrated in [60]. InP is used in

high-power and high-frequency electronics because of its superior electron velocity with respect to the more common semiconductors silicon and GaAs. In [61] an 80 Gbps InP modulator with loaded capacitive electrodes is presented. InP also has a direct bandgap, making it useful for optoelectronics devices like laser diodes and is also used as a substrate for epitaxial indium gallium arsenide based opto-electronic devices.

In addition to being able to exploit the electrooptic effect in semiconductor materials it is also possible to use the electro-absorption effect. Electro-absorption can occur in both bulk semiconductors and quantum well structures; for the former it is referred to as the Franz Keldysh effect while in the latter it is called the quantum confined Stark effect (QCSE) [62]. With this in mind, compact electro absorption modulators (EAMs) can be built. However, there is a shift of absorption spectra with varying bias occurring over a relatively narrow window of wavelengths, thus precise alignment between the wavelength of the CW source laser and the EAM is required. EAMs have been successfully demonstrated at frequencies as high as 60 GHz [63], and the envisioned application here would be 60 GHz fibre radio picocells. The fact that EAMs can be monolithically integrated with lasers indicates the possibility of low cost manufacturing, although it should be pointed out that packaging issues still need to be resolved as does sensitivity to changes in temperature and/or bias voltage.

Efficient generation of optical LO signals can therefore also be obtained using a single laser source and a Mach Zehnder amplitude or phase modulator, using modulation sidebands of an externally modulated fiber link. Modulators with high bandwidths (up to 30 GHz with LiNbO_3) are now common optical components and if the mm-wave requirements aren't too high, they can be pretty inexpensive. Moreover, the generation of LO signals directly at f_{LO} or harmonic signals at nf_{LO} can be obtained. By adjusting the modulator bias point and RF drive power to the modulator introducing the low frequency reference signal at f_{LO} , efficient frequency multiplication to generate mm-wave signals upon detection can be achieved. Many setups are proposed and researched in the literature [64]-[67]. In contrast to direct modulated lasers, external modulation provides frequency stability, low chirp and by harmonic generation the effective bandwidth can be improved by several orders of magnitude. Moreover, there is a complete control over the modulation and schemes such as optical single sideband (OSSB) can be achieved. There is a distinction in whether the information signal is already modulated onto the optical signal and the external modulator is in charge of only

“upconverting” this signal into the mm-wave range [68]-[69], or if both the information and the mm-wave are inserted by the same external modulator [70].

4 Propagation of mm-wave signals in optical waveguides

The propagation of signals through optical waveguides is well described in the literature (for more details refer to [71]). The focus in this chapter will be on the properties and impairments of mm-wave signals which propagate in optical fibers. In this field, two distinct approaches can be distinguished: intensity modulation/direct detection (IM/DD) links or remote heterodyne detection (RHD) techniques. In IM/DD links, a single laser is modulated in its intensity with the mm-wave signals plus the data signal. After transmission through optical fiber, the mm-wave signal is recovered in a broadband photodiode by direct detection. This approach is very straightforward but requires high bandwidth devices. Depending on the type of system and the RF frequency employed, the laser spectral line could be modulated up to 60 GHz or higher. Directly modulated lasers are out of this range due to linearity problems and even external modulation can only achieve 40 GHz bandwidth (with LiNbO₃ MZMs for example). On the other hand, RHD are based on the transmission of two phase correlated optical carriers with a frequency offset equal to the desired mm-wave frequency. One of the carriers is modulated with the information and the mm-wave signal is recovered after heterodyning in a photodiode. Now the bandwidth requirement is defined by the information signals bandwidth, which can be as high as 7 GHz for a 10 Gbps ASK signal. However, this approach usually needs special care not to lose the phase correlation of the optical spectral lines. In both approaches, chromatic dispersion in optical fibers is a limiting factor for the transmission distance which can be achieved in this kind of fiber optic links when the microwave signals are in the above 20 GHz region.

For IM/DD mm-wave links, chromatic dispersion poses a carrier to noise (C/N) penalty due to differential phase changes in the modulation sidebands relative to the carrier of the optical signal. In RHD links it results in both a C/N penalty as well as an increase in phase noise on the mm-wave signal, both due to decorrelation of the two transmitted optical carriers. Also for high data rates (10 Gbps and above), fiber chromatic dispersion introduces a significant pulse broadening of the baseband information data which results in intersymbol interference (ISI) thus leading to higher error rates and transmission distance limitations.

4.1 Chromatic dispersion

Chromatic dispersion (CD) causes light pulses in optical fibers to spread, thus introducing intersymbol interference (ISI) and limits the transmission distance specially when operating with bit rates of 10 Gbps and higher. The group velocity of the fundamental mode in single mode fibers (SMF) is frequency dependent because of CD. As a result, the different spectral components which form an optical pulse travel at slightly different group velocities, and therefore, the pulse broadens. Thus, this effect is also referred to as group velocity dispersion or simply fiber dispersion.

Consider a single mode fiber of length L . A specific spectral component of the optical signal at the angular frequency ω would arrive at the output end of the fiber after a time delay $T = L/v_g$, where v_g is the group velocity, defined as [72]

$$v_g = \frac{d\omega}{d\beta}. \quad (4.1)$$

By using $\beta = nk_0 = n\omega/c$ in (4.1), then $v_g = c/n_g$, where n_g is the group index given by

$$n_g = n + \omega(dn/d\omega). \quad (4.2)$$

The frequency dependence of the group velocity leads to pulse broadening simply because different spectral components of the pulse disperse during propagation and do not arrive at the same time at the fiber end. If $\Delta\omega$ is the spectral width of the pulse, the extent of pulse broadening for a fiber length L is described by

$$\Delta T = \frac{dT}{d\omega} \Delta\omega = \frac{d}{d\omega} \left(\frac{L}{v_g} \right) \Delta\omega = L\beta_2 \Delta\omega, \quad (4.3)$$

Where $\beta_2 = d^2\beta/d\omega^2$ is known as the group velocity dispersion (GVD) parameter and determines how much an optical pulse would broaden on propagation inside the fiber. Expressing Eq. (4.3) as a function of the wavelength spectral width $\Delta\lambda$ results in

$$\Delta T = \frac{d}{d\lambda} \left(\frac{L}{v_g} \right) \Delta\omega = DL\Delta\lambda, \quad (4.4)$$

where

$$D = \frac{d}{d\lambda} \left(\frac{1}{v_g} \right) = -\frac{2\pi c}{\lambda^2} \beta_2. \quad (4.5)$$

D is called the dispersion parameter and is expressed in units of ps/nm·km being β_2 the propagation constant. As D depends on the transmission wavelength, then in WDM systems each channel will be affected by a different dispersion parameter.

The pulse spreading ΔT can be approximately related to the bitrate R_b in binary systems, by intuitively making the pulse broadening smaller than the allocated bit slot ($T_b = 1/R_b$). Although many details are needed for a precise relation of R_b and ΔT , an order of magnitude estimate can be obtained from the condition $R_b \Delta T < 1$ and therefore from Eq. (4.4) the following fundamental dispersion rule of thumb limit is obtained for non-return-to-zero (NRZ) modulation

$$R_b L |D| \Delta \lambda < 1. \quad (4.6)$$

Using single mode semiconductor lasers one can reduce $\Delta \lambda$ to less than 1 nm and obtain a $R_b L$ product of more than 1 Tbps·km. Taking $D = 17$ ps/nm·km for SMF around $\lambda = 1550$ nm, this would mean that for a data rate $R_b = 10$ Gbps, a maximum transmission length $L_{10} \approx 60$ km is obtained. This value is reduced to $L_{40} \approx 4$ km for $R_b = 40$ Gbps. It is evident that the higher the data rate R_b the more impaired the system is with respect to fiber dispersion.

The wavelength dependence of D is governed by the frequency dependence of the mode index n . From Eq. (4.5) and Eq. (4.2), D can be rewritten as

$$D = -\frac{2\pi c}{\lambda^2} \frac{d}{d\omega} \left(\frac{1}{v_g} \right) = -\frac{2\pi}{\lambda^2} \left(2 \frac{dn}{d\omega} + \omega \frac{d^2 n}{d\omega^2} \right) = D_M + D_W. \quad (4.7)$$

Clearly, fiber dispersion D has two main contributions: the so called material dispersion D_M and waveguide dispersion D_W . Material dispersion D_M takes the form [73]

$$D_M = \frac{1}{c} \frac{dn_g}{d\lambda} = -\frac{\lambda}{c} \frac{d^2 n}{d\lambda^2}. \quad (4.8)$$

Material dispersion occurs because the refractive index of silica, the material used for fiber fabrication, changes with the optical frequency ω . The origin of material dispersion is related to the characteristic resonance frequencies at which the material absorbs electromagnetic

radiation. The refractive index $n(\omega)$ is approximated for both cladding and core by the Sellmeier equation [74]

$$n^2(\omega) = 1 + \sum_{j=1}^M \frac{B_j \omega_j^2}{\omega_j^2 - \omega^2}, \quad (4.9)$$

where ω_j is the resonance frequency and B_j is the oscillator strength. These values are obtained empirically by fitting the measured curves to Eq. (4.9) with $M = 3$ [75]. Then with Eq. (4.8) the material dispersion D_M can be calculated.

Waveguide dispersion, on the other hand, depends on the relative powers transmitted in the core and the cladding, which depends on the geometry of the fiber, especially the spot size w_d . From [73] the wavelength variation of D_W is given by

$$D_W = \frac{\lambda}{2\pi^2 c n_{core}} \frac{d(\lambda/w_d^2)}{d\lambda}. \quad (4.10)$$

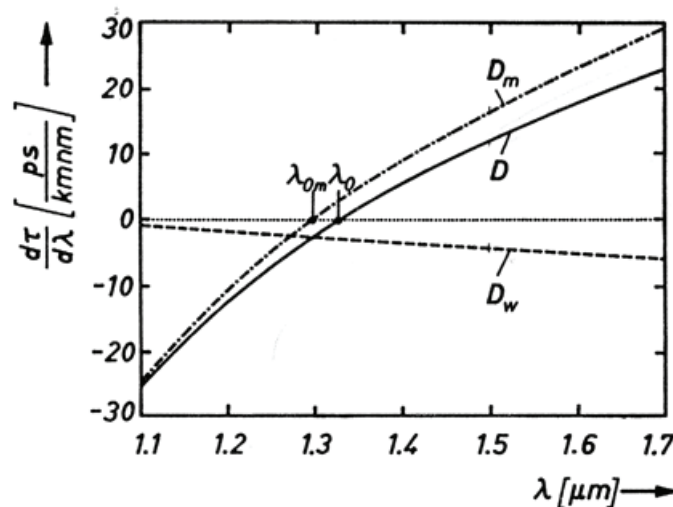


Figure 4.1: Total dispersion D and relative contributions of material dispersion D_M and waveguide dispersion D_W for a conventional single-mode fiber [73].

Figure 4.1 shows the wavelength dependency of the total dispersion D and the contributions of material dispersion D_M and waveguide dispersion D_W for standard single-mode fibers. The zero dispersion wavelength λ_0 is defined as the wavelength where the total dispersion D is zero. For standard SMF this occurs for $\lambda_0 \approx 1300$ nm. As the waveguide dispersion D_W can be tailored, different kind of fibers can be obtained where the material dispersion is totally

compensated (dispersion flattened fibers) or λ_0 is shifted to the long-haul telecommunication wavelength of 1550 nm (dispersion shifted fibers or DSF).

Working at the zero dispersion wavelength λ_0 would seem to solve the dispersion problem. However, optical pulses still experience broadening due to higher order dispersive effects. This is caused because D cannot be made zero at all wavelengths contained within the pulse spectrum. Therefore, the wavelength dependence of D plays an important role, especially in dispersion shifted fibers. The dispersion slope S can be then defined as [71]

$$S = \frac{\partial D}{\partial \lambda} = \left(\frac{2\pi c}{\lambda^2} \right)^2 \beta_3 + \left(\frac{4\pi c}{\lambda^3} \right) \beta_2, \quad (4.11)$$

where $\beta_3 = d\beta_2/d\omega = d^3\beta_2/d\omega^3$. At $\lambda = \lambda_0$, $\beta_2 = 0$ and S is proportional to β_3 . For a source of spectral width $\Delta\lambda$, the effective value of the dispersion parameter becomes $D = S\Delta\lambda$. The limiting bit rate distance product can be estimated by replacing this value of D in Eq. (4.6)

$$R_b L |S| (\Delta\lambda)^2 < 1. \quad (4.12)$$

Taking $S = 0.08$ ps/nm²·km for a dispersion shifted fiber around $\lambda_0 = 1550$ nm and a spectral width $\Delta\lambda = 1$ nm, then the $R_b L$ product approaches 12.5 Tbps·km, much higher than the dispersion limited $R_b L$ product. Consequently, the effects of dispersion slope will be neglected for the remainder of this work.

4.1.1 Chromatic dispersion impaired system

In this section the effects of chromatic dispersion pulse broadening for baseband data transmission under direct detection will be studied. As a model, a trapezoidal pulse shape is assumed for simplification purposes, with a bit period T_b and original rise/fall times tr (normalized to T_b) and no fiber attenuation is considered. According to Eq. (4.4) each pulse will spread by an amount ΔT , so we define the normalized pulse broadening as

$$\Delta T_N = \frac{\Delta T}{T_b} = \frac{D \cdot \Delta\lambda \cdot L}{T_b}. \quad (4.13)$$

At the receiver, the rise/fall time of the received pulse T_s is affected by the pulse broadening as well, and is changed to

$$T_s = \sqrt{tr^2 + \Delta T_N^2}. \quad (4.14)$$

Considering no power loss, the area of the transmitted trapezoidal pulse remains constant. The amplitude of the logical level 0 is zero, while the amplitude of the logical level 1 can be written as

$$I'_{1,0} = \frac{I_{1,0}}{1 + \Delta T_N} \quad (4.15)$$

where I_1 , I_0 and I'_1 , I'_0 are the mean pulse amplitudes of level 1,0 at the transmitter and receiver respectively. The receiver Q factor can be defined as

$$Q = \frac{I'_1 - I'_0}{\sigma_1 + \sigma_0} \quad (4.16)$$

where σ_1 and σ_0 are the standard deviation of amplitudes of level 1 and 0 respectively. They depend mainly on two noise contributors in the receiver, shot noise and thermal noise. Shot noise is a manifestation of the fact that the electric current consists of a stream of electrons that are generated at random times. On the other hand, thermal noise generates when at a finite temperature, electrons move randomly in any conductor. Random thermal motion of electrons in a resistor manifests as a fluctuating current even in the absence of applied voltage. Thus the photodiode current generated in response to a constant optical signal can be written as

$$I(t) = I_p + I_d + i_s(t) + i_T(t) \quad (4.17)$$

where $I_p = RP_{in}$ is the average current dependent on the responsivity R of the photodiode and the incident optical power P_{in} , I_d is the dark current and $i_s(t)$ and $i_T(t)$ are the contributions from shot and thermal noise respectively. Shot noise is mathematically a stationary random process with Poisson statistics, but can be approximated by Gaussian statistics. The variance is given by [71]

$$\sigma_s^2 = 2q(I_p + I_d)B_n \quad (4.18)$$

where B_n is the effective noise bandwidth of the receiver and q the electron charge.

Thermal noise is indeed a stationary random process with Gaussian statistics that is frequency independent up to $f \approx 1$ THz (nearly white noise) and its variance is given by [71]

$$\sigma_T^2 = \frac{4k_B T}{R_L} NF_{amp} B_n \quad (4.19)$$

where k_B is Boltzmann's constant, T is the absolute temperature in °K, R_L is the load resistor and NF_{amp} the amplifier noise figure. An important difference between both noise contributions is that shot noise depends on the generated photocurrent whereas thermal noise does not.

The total current noise for each level can be obtained by adding the contributions of shot and thermal noise. Since both are independent random processes with approximately Gaussian statistics, the total variance of the current fluctuations can be obtained by simply adding individual variances. The result is

$$\sigma_{1,0}^2 = \sigma_s^2 + \sigma_T^2 = 2q(I_{p_{1,0}} + I_d)B_n + \frac{4k_B T}{R_L} NF_{amp} B_n. \quad (4.20)$$

Figure 4.2 shows a histogram simulation of the voltage at the receiver for a dispersion impaired system. The crosstalk between the values of logical 0 and 1 can be clearly distinguished. Two Gaussian fits are drawn for comparison.

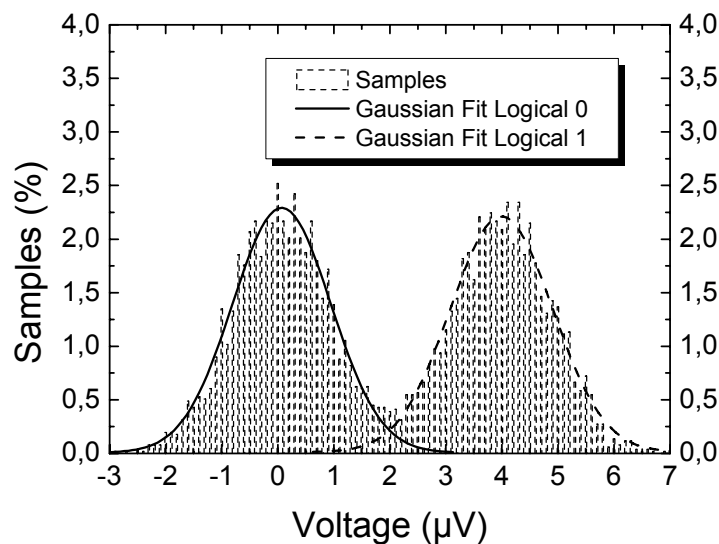


Figure 4.2: Histogram of the voltage at the receiver and the corresponding Gaussian fit for each logical level.

From Eq. (4.13)-(4.15) and [76] the expression of the bit error rate (BER) of a CD-impaired system can be found to be

$$BER(Q, p, \Delta T_N) = \left\{ \begin{array}{l} \frac{1}{16} \operatorname{erfc} \left(\frac{Q(1-p\Delta T_N)}{\sqrt{2}(1+\Delta T_N)} \right) + \frac{1}{8} \operatorname{erfc} \left(\frac{Q \cdot (g^{med}(1+p) - p(1+\Delta T_N))}{\sqrt{2}(1+\Delta T_N)} \right) \\ + \frac{1}{16} \operatorname{erfc} \left(\frac{Q \cdot (g^{inf}(1+p) - p(1+\Delta T_N))}{\sqrt{2}(1+\Delta T_N)} \right) + \frac{1}{8} \operatorname{erfc} \left(\frac{Q}{\sqrt{2}} \right) \\ + \frac{1}{8} \operatorname{erfc} \left(\frac{Q \cdot (g^{med}(1+p) - p\Delta T_N - 1)}{p\sqrt{2}(1+\Delta T_N)} \right) \\ + \frac{1}{16} \operatorname{erfc} \left(\frac{Q \cdot (g^{inf}(1+p) - p\Delta T_N - 1)}{p\sqrt{2}(1+\Delta T_N)} \right) \end{array} \right\} \quad (4.21)$$

where erfc is the complementary error function, $p = \sigma_0/\sigma_1$ and g^{med} and g^{inf} are given by

$$g^{med}(\Delta T_N, T_s) = \begin{cases} 1 & 1 - T_s \geq \Delta T_N \\ 1 - \frac{\Delta T_N + T_s - 1}{4T_s} & 1 + T_s \geq \Delta T_N \geq 1 - T_s \\ 0.5 & \Delta T_N \geq 1 + T_s \end{cases} \quad (4.22)$$

$$g^{inf}(\Delta T_N, T_s) = \begin{cases} 1 & 1 - T_s \geq \Delta T_N \\ 1 - \frac{\Delta T_N + T_s - 1}{2T_s} & 1 + T_s \geq \Delta T_N \geq 1 - T_s \\ 0.5 & \Delta T_N \geq 1 + T_s \end{cases}$$

Using Eq. (4.16) and Eq. (4.20) the variations of Q versus received optical power can be calculated for different transmission distances L , i.e. different pulse spreading values ΔT_N . Simulations were carried out with the following parameters: $R_b = 10$ Gbps with a Mach-Zehnder modulator with an extinction ratio $ER = 30$ dB, using a $p-i-n$ photodiode with responsivity $R = 1$ A/W and zero dark current $I_d = 0$, $\lambda_c = 1550$ nm, spectral linewidth $\Delta\lambda = 0.12$ nm, $P_{opt} = -35$ to -5 dBm and $D = 17$ ps/nm·km. The noise bandwidth is limited by a low pass filter to $B_n = 7.5$ GHz. The thermal noise is simulated with a thermal noise power density of $N_{th} = 10$ pA/ $\sqrt{\text{Hz}}$, corresponding to an effective temperature of $T_{eff} = 90^\circ\text{K}$. No system amplifier was used, so $NF_{amp} = 0$ dB over a load resistor $R_L = 50 \Omega$, thus $\sigma_T \approx 0.9 \mu\text{A}$.

As a result of fiber dispersion (attenuation is neglected), the Q factor decreases significantly as shown in Figure 4.3a when the fiber length is increased. Nonetheless, with Eq. (4.21) the BER can be evaluated and the results are shown in Figure 4.3b.

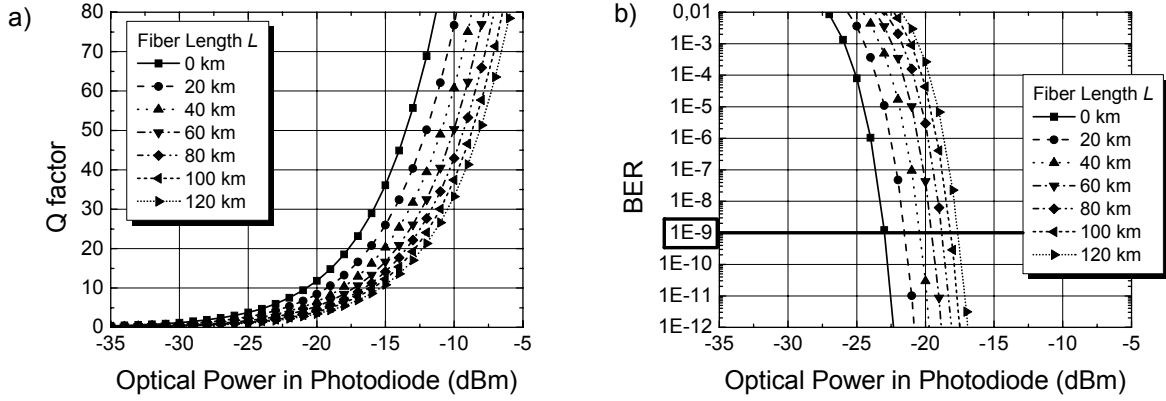


Figure 4.3: Simulated a) Q curves and b) BER curves for a system working with $R_b = 10$ Gbps as a function of received optical power in a $p-i-n$ photodiode.

Dispersion induced broadening affects the BER performance in two ways. First, a part of the pulse energy spreads beyond the allocated bit slot and leads to intersymbol interference thus for sufficient long fiber spans an error floor is reached independently of the optical power. Second, the pulse energy within the bit slot is reduced and thus the signal to noise ratio (SNR) is reduced at the decision circuit. Since the SNR should remain constant to maintain system performance, the receiver requires more average power. This is usually called dispersion-induced power penalty. For example, between $L = 0$ km and $L = 60$ km, there is a penalty of 3.5 dB for $BER = 10^{-9}$.

4.2 IM/DD fiber optic mm-wave links

Chromatic dispersion has a significant influence on the transmission distance in IM/DD mm-wave links for high RF frequencies ($f_{RF} > 20$ GHz). A typical link setup is shown in Figure 4.4, where $x_{in}(t)$ is the input mm-wave signal that is modulated on the optical carrier by electro-optic intensity modulation (E/O IM). The resulting optical signal, $y_{in}(t)$ is transmitted through optical fiber to the receiver. The mm-wave signal is here recovered by opto-electric direct detection (O/E DD), such as a photodiode, resulting in the signal $x_{out}(t)$.

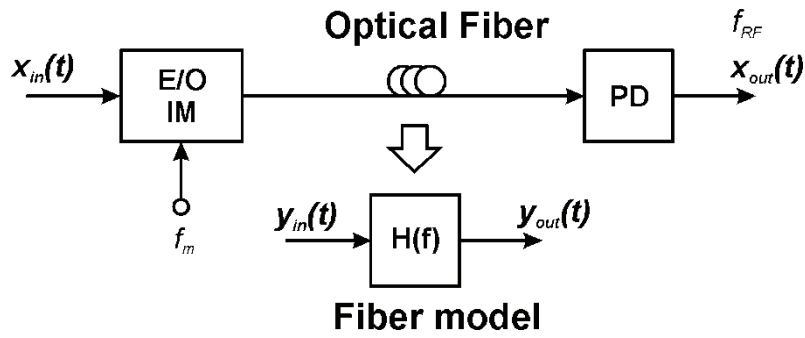


Figure 4.4: IM/DD fiber optic mm-wave link.

In this kind of links, the mm-wave signal is carried as a lower and an upper sideband around the optical carrier. Due to fiber dispersion and the mm-wave frequency offset ($f_m = f_{RF}$) between the sidebands and the optical carrier, the phase of each of the spectral components suffers a differential change. This produces either constructive or destructive interference. After detection, the destructive interference case results in a power reduction of the recovered mm-wave signal $x_{out}(t)$ known as dispersion power fading.

The fiber can be modeled as a band-pass filter with flat amplitude response and linear group delay. Although optical fiber exhibits a certain loss profile over the wavelength, the region used for mm-wave links is considered as narrow optical bandwidth ($< 1\text{nm}$) and the amplitude response therein can be considered constant. To evaluate the effects of fiber dispersion alone, the attenuation will be set to zero (i.e. no power losses). The low-pass equivalent transfer function of the fiber is given by [77]

$$H(f) = \exp^{-j\phi(f)} = \exp^{-j\delta f_m^2} \quad (4.23)$$

where

$$\delta = \frac{\pi D \lambda^2 L}{c} \quad (4.24)$$

and $f_m = f_{RF}$ is the mm-wave frequency, D is the chromatic dispersion, λ is the optical wavelength, c is the speed of light in vacuum and L is the length of the fiber. The optical signal after fiber transmission $y_{out}(t)$ results in

$$Y_{out}(f) = Y_{in}(f)H(f) \quad (4.25)$$

where $Y_{out}(f)$ and $Y_{in}(f)$ are the Fourier transforms of $y_{out}(t)$ and $y_{in}(t)$ respectively, obtained from

$$\begin{aligned} Y_{out}(f) &= \int_{-\infty}^{\infty} y_{out}(t) \exp^{-j2\pi ft} dt \\ Y_{in}(f) &= \int_{-\infty}^{\infty} y_{in}(t) \exp^{-j2\pi ft} dt. \end{aligned} \quad (4.26)$$

The receiver recovers the mm-wave signal by square law photodetection, then

$$x_{out}(t) = |y_{out}(t)|^2 \quad (4.27)$$

with a spectrum given by its Fourier transform

$$X_{out}(f) = \int_{-\infty}^{\infty} x_{out}(t) \exp^{-j2\pi ft} dt. \quad (4.28)$$

The dispersion induced C/N penalty on the recovered mm-wave signal is found by comparing the signal power of $X_{out}(f_{RF})$ with and without fiber transmission. Mathematically,

$$C / N_{pen} = 10 \log \left| \frac{X_{out}(f_m)_{nofiber}}{X_{out}(f_m)_{fiber}} \right|^2. \quad (4.29)$$

The C/N penalty takes different forms depending on the type of mm-wave signal that is to be transmitted. This will be detailed in the next few sections.

4.2.1 Unmodulated mm-wave carrier

For an unmodulated mm-wave carrier, the model representation is

$$x_{in}(t) = \sin(2\pi f_m t). \quad (4.30)$$

After E/O conversion, the resulting optical signal has an electric field given by

$$y_{in}(t) = \sqrt{1 + \sin(2\pi f_m t)} \exp^{j2\pi f_c t} \quad (4.31)$$

where f_c is the frequency of the optical carrier. A schematic for this kind of link is represented in Figure 4.5. The optical carrier in the form of a laser diode (LD) is modulated in its intensity with the electrical mm-wave carrier at f_m . If the optical Mach Zehnder Modulator (MZM) is biased at quadrature for maximum linearity and with a moderate modulation index m_a (i.e.

$m_a < 0.8 \cdot V_\pi$), then the output signal consists of the optical carrier plus two sidebands $f_c \pm f_m$. Mathematically, the electric field is represented by

$$E(t) = E_0 \left[e^{j\omega_c t} + A_{+1} \cdot e^{j(\omega_c + \omega_m)t} + A_{-1} \cdot e^{j(\omega_c - \omega_m)t} \right] \quad (4.32)$$

where E_0 is the input field amplitude, $A_{\pm 1}$ the amplitude of the respective sidebands, $\omega_c = 2\pi f_c$ the optical carrier angular frequency and $\omega_m = 2\pi f_m$ the mm-wave carrier angular frequency.

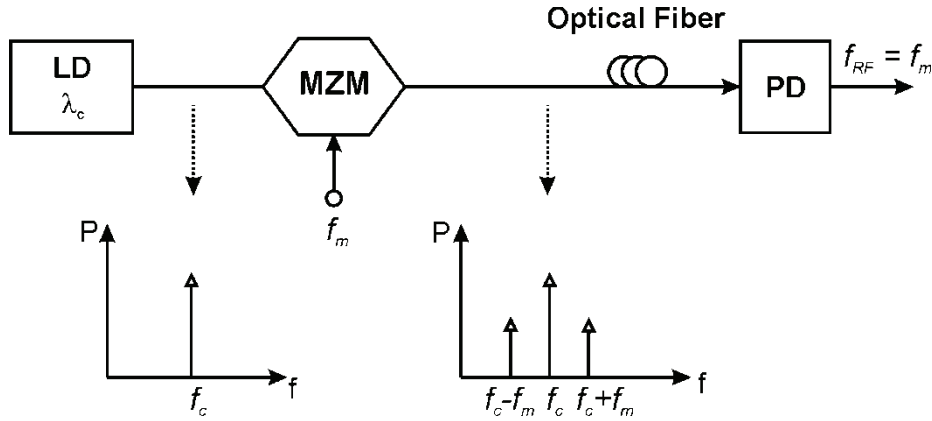


Figure 4.5: IM/DD fiber optic mm-wave link with unmodulated mm-wave carrier at f_m . LD: Laser Diode, MZM: Mach Zehnder Modulator, PD: Photodiode.

From the ideal model for an optical waveguide in Eq. (4.23), transmission in a dispersive medium imposes an additional phase change of the sidebands relative to the optical carrier given by

$$\varphi_d(f_m) = \delta f_m^2 = \frac{\pi DL \lambda_c^2 f_m^2}{c}. \quad (4.33)$$

Then the electric field arriving at the receiver has the form

$$E_{rec}(t) \sim E_0 \left[e^{j\omega_c t} + A_{+1} \cdot e^{j(\omega_c + \omega_m)t + \varphi_d(\omega_m)} + A_{-1} \cdot e^{j(\omega_c - \omega_m)t - \varphi_d(\omega_m)} \right]. \quad (4.34)$$

At the receiver, usually a photodiode (PD), all spectral components mix heterodynally and according to the proportionality of the photo current to the detected optical power, we have

$$I_{PD}(t) \sim P_{rec}(t) \sim |E_{rec}(t)|^2 = E_{rec}(t) \cdot E_{rec}^*(t). \quad (4.35)$$

For the special case at quadrature in which $A_{+1} = A_{-1}$, then the electrical power dependency on the dispersion induced phase shift is [78]

$$P_{el}(t) \sim I_{PD}^2(t) \sim \cos^2[\varphi_d(\omega_m)] = \cos^2\left[\pi cDL(f_m / f_c)^2\right]. \quad (4.36)$$

Using Eq. (4.36) and Eq. (4.29) the C/N penalty due to chromatic dispersion can be numerically calculated. As the interest in this chapter is to study the penalties caused by chromatic dispersion, fiber attenuation will be neglected for all the analyses from now on unless specifically stated otherwise. Figure 4.6 shows the C/N penalty for a mm-wave carrier at different RF frequencies as a function of transmission distance considering transmission over single mode fiber (SMF) with $D = 17$ ps/nm·km and a center wavelength of $\lambda_c = 1550$ nm. Even after a few km of SMF the C/N is so huge that the transmission distance is severely limited.

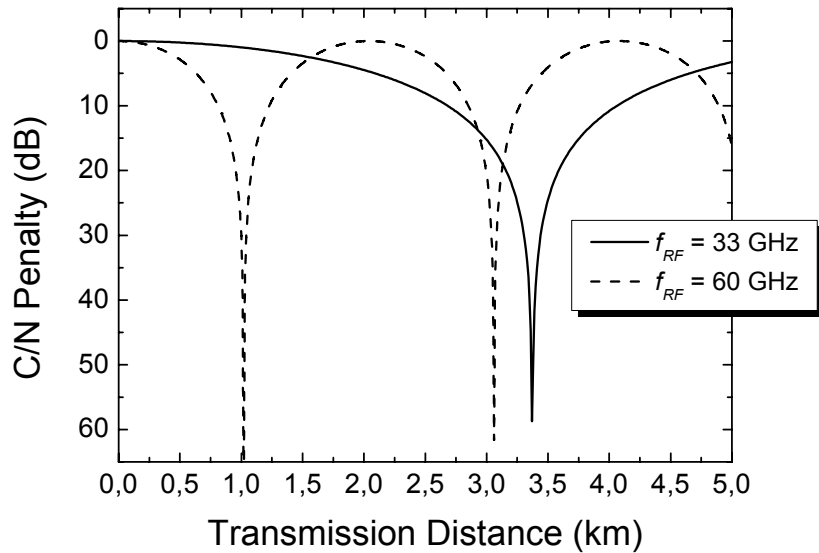


Figure 4.6: Dispersion induced C/N penalty as a function of transmission distance. Calculations for $f_{RF} = 33$ and 60 GHz, $D = 17$ ps/nm·km and $\lambda_c = 1550$ nm.

A complete extinction of the mm-wave carrier occurs when the phases of the lower and upper sidebands are π out of phase and multiples. That is when the phase of $H(f)$ in Eq. (4.23) has introduced a change of $\pi/2$ on each sideband relative to the optical carrier. From Eq. (4.33) the transmission distance for the first complete extinction can be obtained as

$$L_0 = \frac{c}{2D\lambda_c^2 f_m^2} \text{ for } \varphi_d = \frac{\pi}{2}. \quad (4.37)$$

For the above example of $f_m = f_{RF} = 33$ GHz, $\lambda_c = 1550$ nm and a fiber dispersion of $D = 17$ ps/nm·km this occurs at $L_0 = 3.37$ km. This behavior is cyclic in nature, and the period of repetition can be also derived from Eq. (4.24) as

$$\Delta L_0 = \frac{c}{D\lambda_c^2 f_m^2} \text{ for } \varphi_d = \pi. \quad (4.38)$$

This periodicity can be used to measure chromatic dispersion in optical fibers with decent accuracy [79]. Even though dispersion power fading occurs, that is critical at definite transmission distances. Careful planning of a network can be devised to avoid these critical points and obtain good performances. Some ideas can be found in the literature [80].

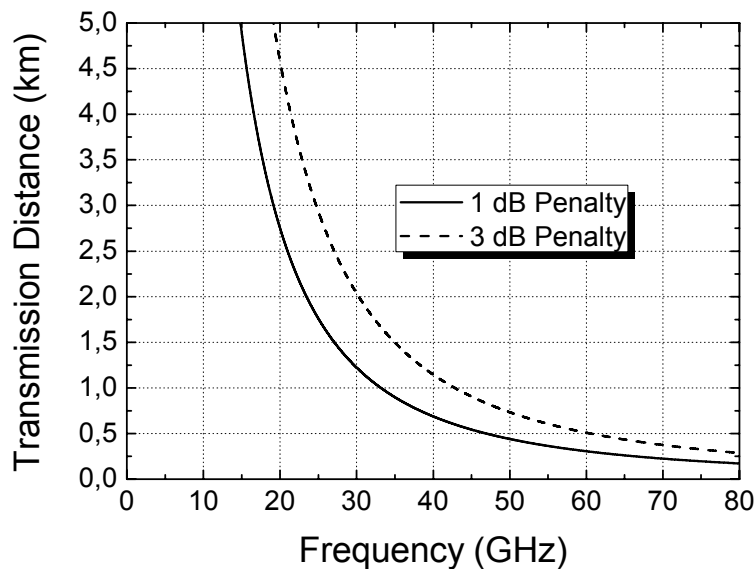


Figure 4.7: Transmission distance for 1 dB or 3 dB compression point as a function of f_{RF} . Calculations with $D = 17$ ps/nm·km and $\lambda_c = 1550$ nm.

In a system point of view, it is more interesting to predict when the signal enters the 1 dB or 3 dB penalty points as to know the extinction length of the mm-wave signal. This means, when the signal is attenuated 1 dB or 3 dB from the ideal case of no dispersion. The results from Eq. (4.36) for 1 dB and 3 dB respectively are shown in Figure 4.7 as a function of the RF frequency f_{RF} . It is evident that moving to higher frequencies limits greatly the transmission distance, not even reaching 500 m transmission for $f_{RF} = 60$ GHz.

4.2.2 Modulated carrier with an intermediate frequency f_{IF}

Interesting is the case of electrooptical upconversion of an intermediate frequency f_{IF} . In this method the laser diode is directly or externally modulated with an intermediate frequency f_{IF} of some couple of GHz. Then the broad bandwidth MZM is in charge of upconverting this signal into the mm-wave range [81]. A schematic of this kind of approach is shown in Figure 4.8.

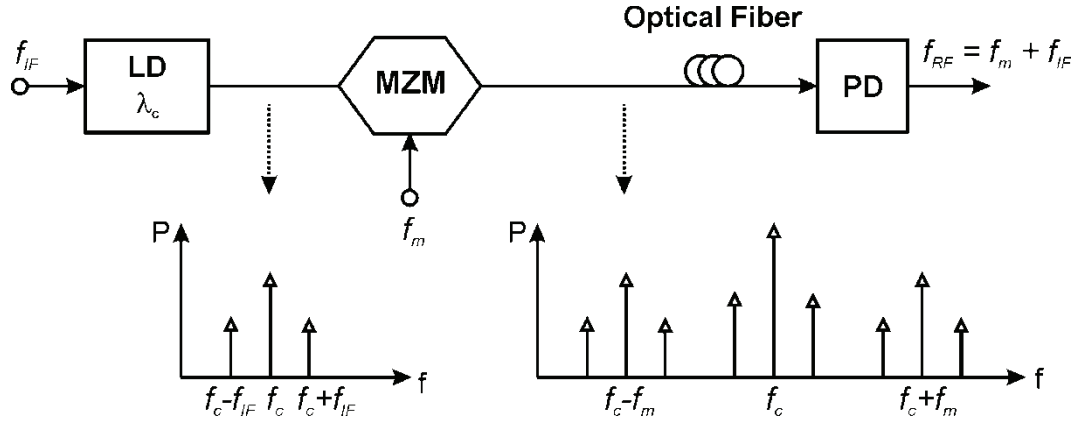


Figure 4.8: IM/DD fiber optic mm-wave link with a modulated mm-wave carrier at f_m . LD: Laser Diode, MZM: Mach Zehnder Modulator, PD: Photodiode.

By modulating the laser in its intensity with an adequate RF drive power at f_{IF} , only the ± 1 sidebands will be present. The same has to be ensured for the MZM so that the optical spectrum has the form depicted in Figure 4.8. Mathematically the received signal influenced by fiber chromatic dispersion before the photodiode is represented by

$$\frac{E_{rec}(t)}{E_0} \sim \left\{ \begin{array}{l} e^{j\omega_c t} + A \cdot e^{j(\omega_c t + \omega_{IF} t + \phi_d(\omega_{IF}))} + A \cdot e^{j(\omega_c t - \omega_{IF} t + \phi_d(\omega_{IF}))} \\ + B \cdot e^{j(\omega_c t + \omega_m t + \phi_d(\omega_m))} + B \cdot e^{j(\omega_c t - \omega_m t + \phi_d(\omega_m))} \\ + A \cdot B \cdot e^{j(\omega_c t + \omega_m t + \omega_{IF} t + \phi_d(\omega_m + \omega_{IF}))} \\ + A \cdot B \cdot e^{j(\omega_c t + \omega_m t - \omega_{IF} t + \phi_d(\omega_m - \omega_{IF}))} \\ + A \cdot B \cdot e^{j(\omega_c t - \omega_m t + \omega_{IF} t + \phi_d(\omega_m - \omega_{IF}))} \\ + A \cdot B \cdot e^{j(\omega_c t - \omega_m t - \omega_{IF} t + \phi_d(\omega_m + \omega_{IF}))} \end{array} \right\} \quad (4.39)$$

being A and B the amplitude of the sidebands of the intermediate frequency modulation (f_{IF}) and upconversion modulation (f_m) respectively and considering the same amplitude of the upper and lower sidebands in each modulation process. Mixing in a photodiode produces numerous frequency components (all the possible cross products between f_c , f_m and f_{IF}) being the only one of interest the one in $f_{RF} = f_m + f_{IF}$, given by

$$P_{rec}(t) \sim \cos(\omega_m t + \omega_{IF} t) \cdot \left\{ \cos[\varphi_d(\omega_m + \omega_{IF})] + \cos[\varphi_d(\omega_m) - \varphi_d(\omega_{IF})] \right\}. \quad (4.40)$$

The corresponding electrical signal is obtained in the same way as in Eq. (4.36) by squaring the generated current in the photodiode (i.e. $P_{el}(t) \sim I_{PD}^2 \sim P_{rec}^2(t)$).

Simulations are shown in Figure 4.9 for different intermediate frequencies f_{IF} but a resulting $f_{RF} = 33$ GHz kept constant. Similar strong dispersion limited effects as in section 4.2.1 are evident and changing f_{IF} has only a small deviation from the unmodulated case from Figure 4.6. The electrical power exhibits the same behavior as in section 4.2.1, so that the first extinction of the mm-wave signal can then again be derived from Eq. (4.40) and is given by

$$L_0 = \frac{c}{2D\lambda_c^2 f_m f_{RF}} \quad (4.41)$$

and the periodicity is then

$$\Delta L_0 = \frac{c}{D\lambda_c^2 f_m f_{RF}}. \quad (4.42)$$

By replacing $f_{RF} = f_m$, the same result as in Eq. (4.37) and Eq. (4.38) is obtained. This explains the subtle variations from the unmodulated case, as for small values of f_{IF} , then $f_{RF} \approx f_m$.

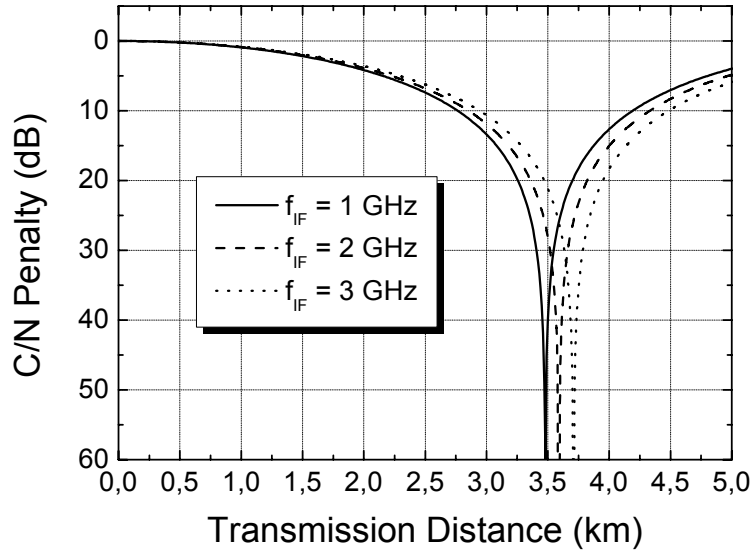


Figure 4.9: Dispersion induced C/N penalty as a function of transmission distance with f_{IF} as parameter. Calculations with $D = 17$ ps/nm·km, $\lambda_c = 1550$ nm and $f_{RF} = 33$ GHz.

Nonetheless, the transmission of this kind of signals is extremely limited by fiber chromatic dispersion to only a couple of km at best. Methods to extend the transmission distance are based on eliminating one of the redundant optical spectral lines (e.g. by optical filtering or special driving configurations of the MZM), so that the resulting RF signal comes from the beating of only two optical spectral lines. In this category we can distinguish two methods: double sideband with suppressed carrier (DSB-SC) [68] and optical single sideband (OSSB) modulation [82]. Both approaches provide the same optical spectrum: two sidebands separated by $2f_m$ where each sideband is modulated by the intermediate frequency f_{IF} .

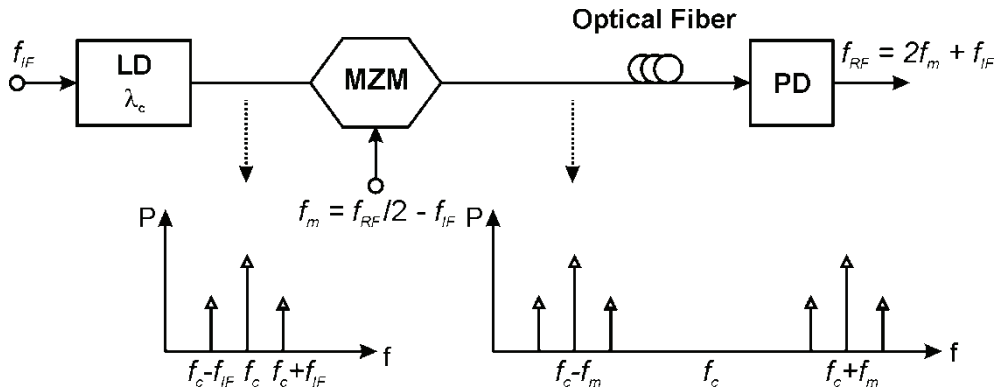


Figure 4.10: IM/DD fiber optic mm-wave link with DSB-SC modulation at $f_m = f_{RF}/2 - f_{IF}$. LD: Laser Diode, MZM: Mach Zehnder Modulator, PD: Photodiode.

By biasing a MZM at its minimum transmission point, the optical carrier is theoretically completely suppressed (DSB-SC method). The resulting spectrum is depicted in Figure 4.10. Notice that now the MZM is driven by approximately half the desired mm-wave frequency $f_m = f_{RF}/2 - f_{IF}$ as after photodetection an effective doubling of the frequency occurs. The received signal is now reduced from Eq. (4.39) to

$$\frac{E_{rec}(t)}{E_0} \sim \left\{ \begin{array}{l} A \cdot e^{j\left(\omega_c t + \frac{\omega_m}{2} t + \varphi_d\left(\frac{\omega_m}{2}\right)\right)} + A \cdot e^{j\left(\omega_c t - \frac{\omega_m}{2} t + \varphi_d\left(\frac{\omega_m}{2}\right)\right)} \\ + A \cdot B \cdot e^{j\left(\omega_c t + \frac{\omega_m}{2} t + \omega_{IF} t + \varphi_d\left(\frac{\omega_m}{2} + \omega_{IF}\right)\right)} \\ + A \cdot B \cdot e^{j\left(\omega_c t + \frac{\omega_m}{2} t - \omega_{IF} t + \varphi_d\left(\frac{\omega_m}{2} - \omega_{IF}\right)\right)} \\ + A \cdot B \cdot e^{j\left(\omega_c t - \frac{\omega_m}{2} t + \omega_{IF} t + \varphi_d\left(\frac{\omega_m}{2} - \omega_{IF}\right)\right)} \\ + A \cdot B \cdot e^{j\left(\omega_c t - \frac{\omega_m}{2} t - \omega_{IF} t + \varphi_d\left(\frac{\omega_m}{2} + \omega_{IF}\right)\right)} \end{array} \right\}. \quad (4.43)$$

And the resulting power for the received signal at $f_{RF} = 2f_m + f_{IF}$ is then given by [83]

$$P_{rec}(t) \sim \cos(\omega_m t + \omega_{IF} t) \cdot \cos \left[\varphi_d \left(\frac{\omega_m}{2} + \omega_{IF} \right) - \varphi_d \left(\frac{\omega_m}{2} \right) \right]. \quad (4.44)$$

Again the signal is generated from the beating of two optical spectral lines, so that they are still not completely immune to fiber dispersion power fading effects. Nonetheless these effects are much more benign, and thus is this method of electrooptical upconversion described as dispersion tolerant. Calculating the electrical power as $P_{el}(t) \sim P_{rec}^2(t)$, gives rise to the curves in Figure 4.11 for $f_{RF} = 33$ GHz. Now the intermediate frequency f_{IF} does indeed play a preponderant role in the achievable transmission length, as the curves vary greatly for the same resulting f_{RF} . Nevertheless, as opposed to the previous method, the transmission distance is increased in tenths of kms depending on the selection of the intermediate frequency f_{IF} and the system could be then power limited and not dispersion limited.

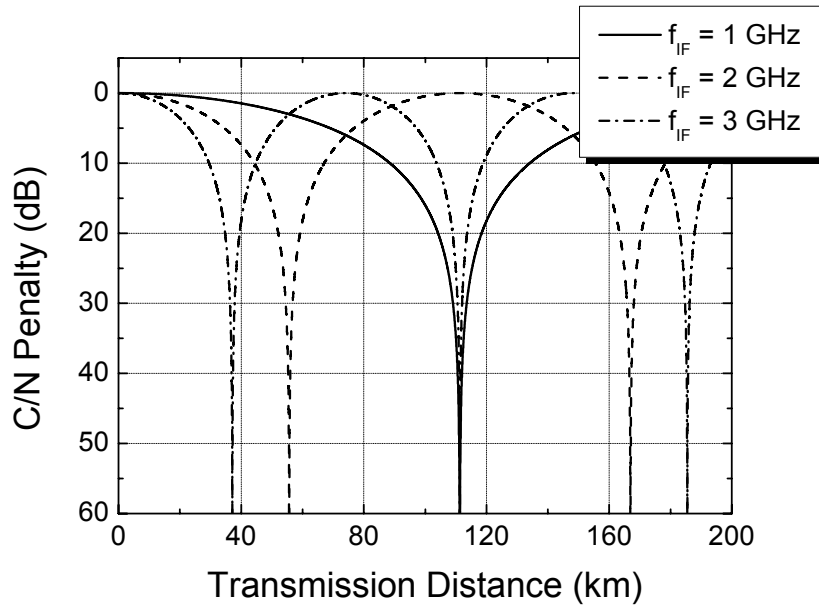


Figure 4.11: Dispersion induced C/N penalty as a function of transmission distance with f_{IF} as parameter for DSB-SC method. Calculations with $D = 17$ ps/nm·km, $\lambda_c = 1550$ nm and $f_{RF} = 33$ GHz.

The transmission distance at which the signal fades completely can be calculated from Eq. (4.44) and is given by

$$L_0 = \frac{c}{2D\lambda_c^2 f_{IF} f_{RF}} \quad (4.45)$$

and the periodicity is now

$$\Delta L_0 = \frac{c}{D\lambda_c^2 f_{IF} f_{RF}}. \quad (4.46)$$

From Eq. (4.45) the improvement in transmission distance is evident. The difference from the previous cases in Eq. (4.41) and Eq. (4.37) shows that now f_{IF} is indeed a key parameter and as it is quite small compared to f_{RF} , it shifts the incidence of the first transmission zero to some tenths of kms.

4.3 Effects of transmitter chirp

The previous results were calculated without considering transmitter chirp. Chirp is the inherent frequency modulation (FM) which accompanies intensity modulation (IM) in directly modulated optical lasers. This effect cannot be neglected, especially when working with intermediate frequencies as described in section 4.2.2. Laser chirp is a natural effect in directly modulated laser and can be minimally controlled [84]. To avoid laser chirp, external modulators are usually used. By operating the laser in continuous wave (CW) mode, the frequency modulation can be totally suppressed. But sometimes some chirp is beneficial, so by choosing the bias conditions carefully, the chirp parameter can be freely adjusted in external modulators [85].

The effects of transmitter chirp will then be briefly explained for the case of optical upconversion with DSB-SC method, as this scheme is the most dispersion tolerant. Both directly modulated lasers and externally modulated links will be studied.

4.3.1 Directly modulated IF links

This case corresponds to the previously described setup shown in Figure 4.10. An expression linking the instantaneous angular frequency deviation $\Delta\omega$ in relation to the power variation was derived in [86] for sinusoidal small signal modulation as

$$\frac{\Delta\omega}{\Delta P} = -\frac{\alpha_{LE}}{2P_0}(\omega_m - j\omega_g). \quad (4.47)$$

Here α_{LE} is the laser linewidth enhancement factor, ω_g is an output power dependent frequency at the intercept of the transient and adiabatic chirp [84], P_0 is the output power of the laser and ΔP is the power variation due to intensity modulation. More interesting is the

relation between the FM index $m_f = |\Delta\omega/\omega_m|$ and the IM index $m_a = |\Delta P/P_0|$ which can be derived from the absolute value from Eq. (4.47) as [87]

$$\frac{m_f}{m_a} = \frac{|\alpha_{LE}|}{2} \sqrt{1 + \left(\frac{\omega_g}{\omega_m}\right)^2}. \quad (4.48)$$

Independent measurements of m_f and m_a can lead to the determination of α_{LE} and ω_g but with some uncertainty as usually laser diodes have a frequency dependent phase offset between FM and IM. This phase offset is given by

$$\Delta\varphi_{FM,IM} = \arctan\left(-\frac{\omega_g}{\omega_m}\right). \quad (4.49)$$

However, a simple estimate of the chirp is sufficient to characterize the electro-optical upconversion system behavior [88] and $\Delta\varphi_{FM-IM} = 0$ will be considered first (i.e. pure blue-shift). An approximation for small signal modulation (i.e. $m_a < 0.5$ and $m_f < 1$) taking into account the effects of laser chirp was developed in [88] for blue-shift chirp, then the received electrical power at $f_{RF} = 2f_m + f_{IF}$ is now

$$P_{el} \sim \left[\begin{array}{l} \frac{m_a}{4} \left([J_0(m_f)]^2 + 2[J_1(m_f)]^2 \right) \cos(\varphi_d(f_m + f_{IF}) - \varphi_d(f_m)) \\ -J_0(m_f)J_1(m_f) \left(\frac{m_a^2}{8} - 1 \right) \sin(\varphi_d(f_m + f_{IF}) - \varphi_d(f_m)) \end{array} \right]^2 \quad (4.50)$$

where φ_d is the same expression as derived in Eq. (4.33). The results of varying the FM index m_f and IM index m_a are represented in Figure 4.12a and Figure 4.12b respectively. Changes in the FM index m_f result in strong variations of the normalized power as seen in Figure 4.12a. It is surprising that even higher powers are obtained with little chirp (i.e. more power than the initial launch power). The 3 dB length L_{3dB} is defined as the fiber length where the response drops 3 dB from the $L = 0$ case. Even some little chirp duplicates L_{3dB} , as $m_f = 0.2$ produces $L_{3dB} = 64$ km. It would seem that increasing even further the FM index would extend the transmission distance even more. However, for higher values of m_f , the approximation in Eq. (4.50) is no longer valid. A more exact solution can be found in [81] where it was demonstrated that for $m_f > 2$ a local minimum starts producing a loss of power around the original zero power length L_0 for the chirpless case.

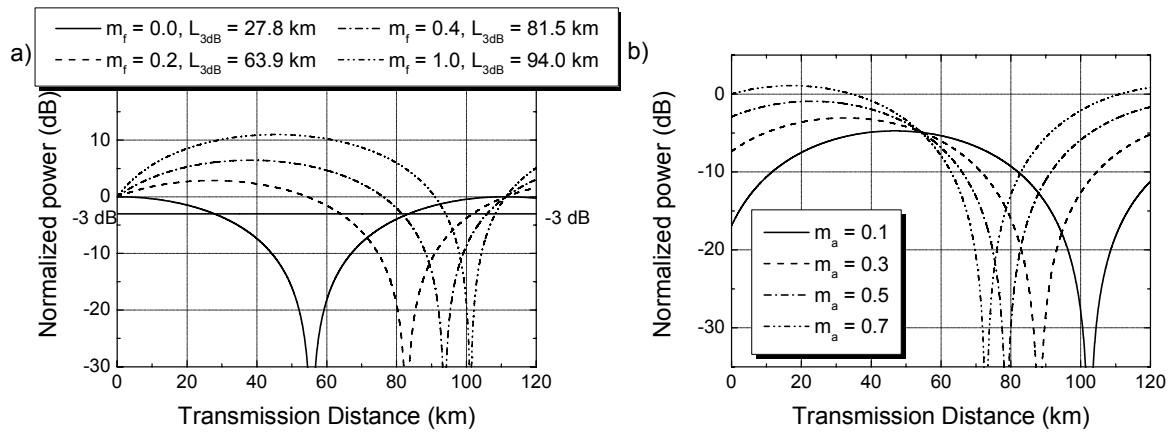


Figure 4.12: Normalized power as a function of transmission distance with transmitter chirp. a) Variation of m_f with $m_a = 0.4$ and b) variation of m_a with $m_f = 0.2$. Calculations with $D = 17$ ps/nm·km, $\lambda_c = 1550$ nm, $f_{IF} = 2$ GHz and $f_{RF} = 33$ GHz.

Figure 4.12b shows the dependency on the IM modulation index m_a when $m_f = 0.2$. Here the variations are not so drastical as the previous case, nonetheless a shift in L_0 is observed as m_a decreases. Although this would seem advantageous, the resulting RF power for lower m_a s is significantly lower than for higher m_a s. Therefore the choice of m_a is a compromise solution between RF power and reach.

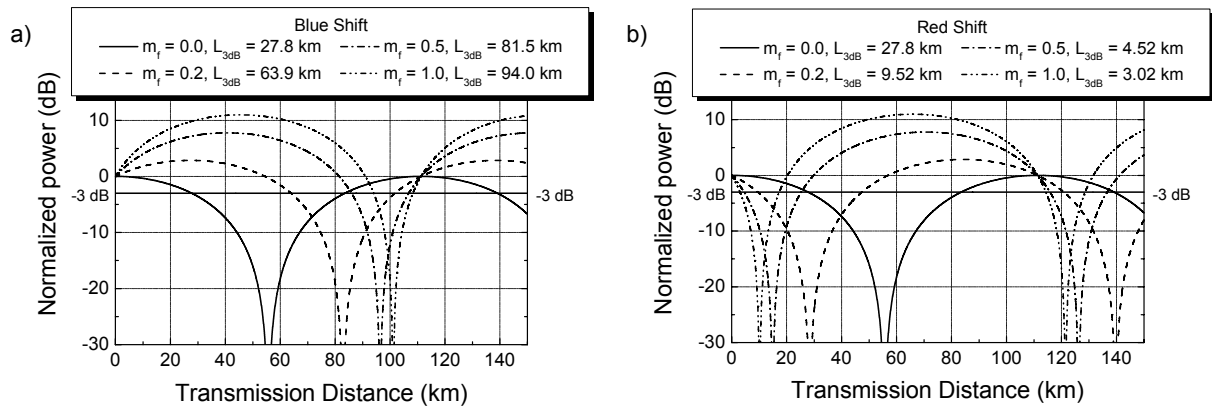


Figure 4.13: Normalized power as a function of transmission distance with transmitter chirp. a) Blue shift and b) red shift. Calculations with $m_a = 0.4$, $D = 17$ ps/nm·km, $\lambda_c = 1550$ nm, $f_{IF} = 2$ GHz and $f_{RF} = 33$ GHz.

The previous results were obtained considering pure blue-shift. In Figure 4.13 a comparison between both types of chirp is shown for different values of the FM index m_f . There is a symmetrical behavior between both cases, the main disadvantage being for the red shift case as the power drops abruptly in the first kms depending on the FM index m_f . For this case,

much shorter L_{3dB} are encountered in comparison to the chirpless case. In real deployed systems, laser diodes show no pure blue-shift ($\Delta\varphi_{FM,IM} = 0$) or red shift ($\Delta\varphi_{FM,IM} = \pi$) but a phase shift $\Delta\varphi_{FM,IM}$ between these two values. However, it is known that the typical chirp behavior of telecomm laser diodes is $\Delta f/\Delta P > 0$, hence a tendency to blue-shift is observed [84].

4.3.2 Externally modulated IF links

Instead of modulating directly a laser diode, an external modulator can be employed to have full control of the chirp of the laser spectral line [89]. Ideally, as the laser is operated in CW mode, an external modulated signal is considered chirpless. But when optimized for low switch voltage, it is inevitable to have some residual chirp, especially in integrated modulators [90]. Moreover, in some cases, designing a modulator with some negative chirp reduces the system power penalty over the chirp-free version [91]. An example of such a system is depicted in Figure 4.14.

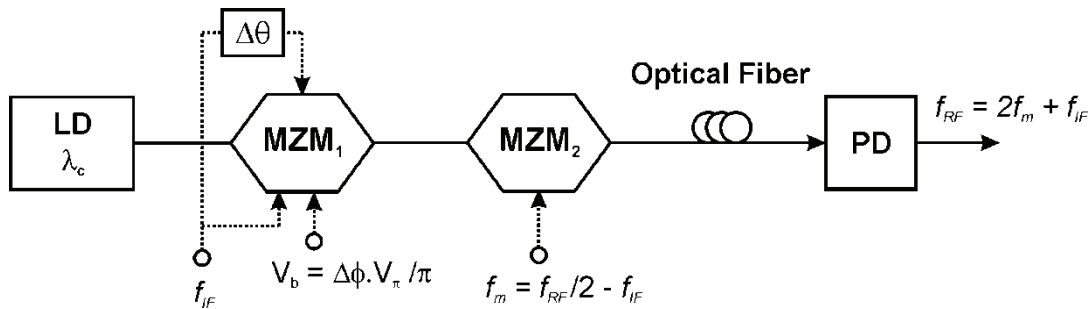


Figure 4.14: IM/DD fiber optic externally modulated mm-wave link with DSB-SC modulation. LD: Laser Diode, MZM: Mach Zehnder Modulator, PD: Photodiode.

The intermediate signal f_{IF} is now inserted via a dual-drive MZM (MZM₁ in Figure 4.14) which means that the drive signal is fed into both arms of MZM₁. In this way, some interesting cases can be achieved by adjusting the phase difference $\Delta\theta$ of the IF drive signals and the bias point of MZM₁ (through the arms phase difference $\Delta\phi$). Three cases are of special interest:

- a) $\Delta\phi = 0$ and $\Delta\theta = 0$ corresponds to pure phase modulation, which in reality should be simply achieved by a single phase modulator.
- b) $\Delta\phi = \pi/2$ and $\Delta\theta = \pi$ is the most common intensity modulation case with two sidebands plus carrier.

c) $\Delta\phi = \pi/2$ and $\Delta\theta = \pi/2$ is called single sideband modulation (SSB), as only one sideband is produced.

The results of each case are drawn in Figure 4.15 for $f_{RF} = 33$ GHz, $f_{IF} = 2$ GHz, $\lambda_c = 1550$ nm and $D = 17$ ps/nm·km. Intensity modulation is the same case previously calculated in Figure 4.11 as no modulator chirp is yet considered. The case of phase modulation proves the concept of phase modulation to intensity (PM-IM) conversion thanks to fiber dispersion [92]. The detected RF power for short lengths of fiber is minimal, but after some kms it increases, having a maximum where IM has its minimum. The 6 dB maximum power difference between PM and IM is due to the different bias point in which they work. As IM employs a MZM biased at quadrature, 3 dB optical power is lost, thus resulting in the 6 dB electrical power difference. The most interesting case is OSSB which has a constant RF power independent of fiber dispersion and proves to be the most dispersion tolerant method up to date [82]. It should be mentioned that no fiber attenuation was considered for all calculations.

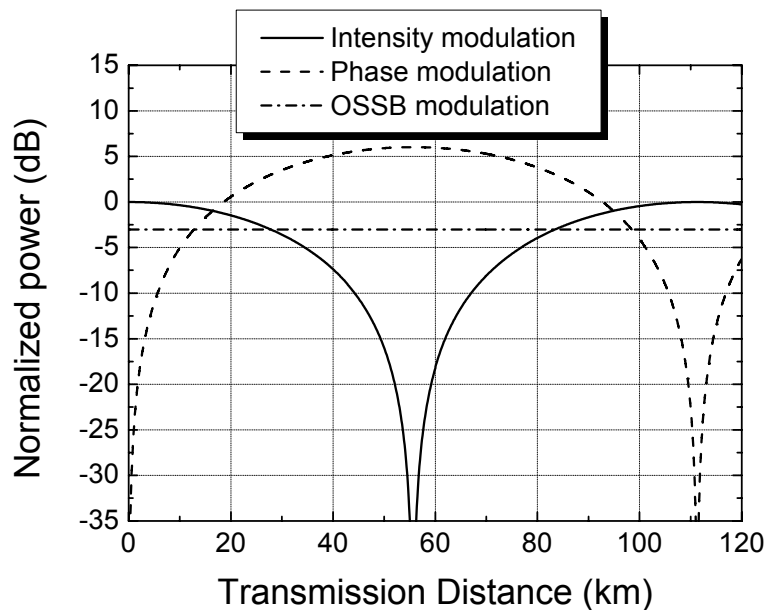


Figure 4.15: Normalized power as a function of transmission distance for different modulation schemes. Calculations with $D = 17$ ps/nm·km, $\lambda_c = 1550$ nm, $f_{IF} = 2$ GHz and $f_{RF} = 33$ GHz.

A dual-drive MZM with access to electrodes in both arms (as shown in Figure 5.3a) enables a variable chirp parameter. For such a MZM, the chirp parameter α_{MZM} is as a function of the modulation index and bias point is defined by [93]

$$\alpha_{MZM} = v \cdot \tan\left(\frac{\pi}{2} \cdot \frac{V_b - V_o - V_\pi}{V_\pi}\right) \quad (4.51)$$

with V_b being the bias voltage, V_o the offset voltage corresponding to the phase retardation in absence of electric field and

$$v = \frac{V_1 + V_2}{V_1 - V_2}. \quad (4.52)$$

V_1 and V_2 are the RF drive voltages applied to first and second arm of the MZM, respectively. Eq. (4.51) demonstrates the tunability of the chirp parameter α_{MZM} . As the chirp parameter influences the phase of the generated spectral components after the modulator, the chromatic dispersion effects studied in section 4.2 will also be affected. The fiber distance at which the RF beat signals after the photodiode exhibit a π phase difference was calculated Eq. (4.37) for a DSB with carrier signal and can now be rewritten taking the modulator chirp into account as [94]

$$L_0 = \frac{c}{2D\lambda_c^2 f_{RF}^2} \left(1 - \frac{2}{\pi} \arctan(\alpha_{MZM})\right). \quad (4.53)$$

By having a large and negative chirp the fiber distance can be actually extended. The RF power as a function of link distance is proportional to [95]

$$P_{RF} \propto \cos\left(\frac{\pi LD\lambda_c^2 f_{RF}^2}{c \left(1 - \frac{2}{\pi} \arctan(\alpha_{MZM})\right)}\right). \quad (4.54)$$

Eq. (4.54) is calculated in Figure 4.16 for $f_{RF} = 33$ GHz with the modulator chirp α_{MZM} as a parameter. As already demonstrated in section 4.2, the power degradation has a periodic behavior and the increase in link distance is evident for an IM/DD link. The case of $\alpha_{MZM} = 0$ is the same as that obtained in Figure 4.6. By using a negative chirp, the extinction distance can be almost doubled. Nonetheless, chirp produces spectral broadening which is significant in multigigabit systems, so adjusting the chirp must be a compromise solution between reach and spectral broadening issues.

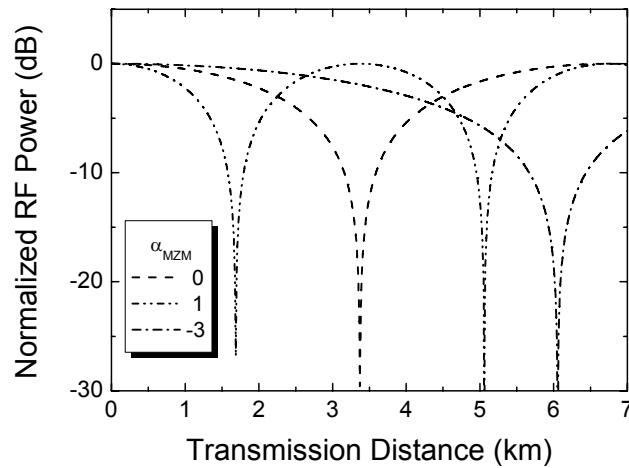


Figure 4.16: Calculated RF power versus transmission distance for $f_{RF} = 33$ GHz with the modulator chirp α_{MZM} as a parameter.

4.4 Remote heterodyne detection fiber optic mm-wave links

Remote heterodyne detection (RHD) techniques are based on the fiber optic transmission of two phase-correlated optical signals which are separated at the desired mm-wave frequency f_{RF} .

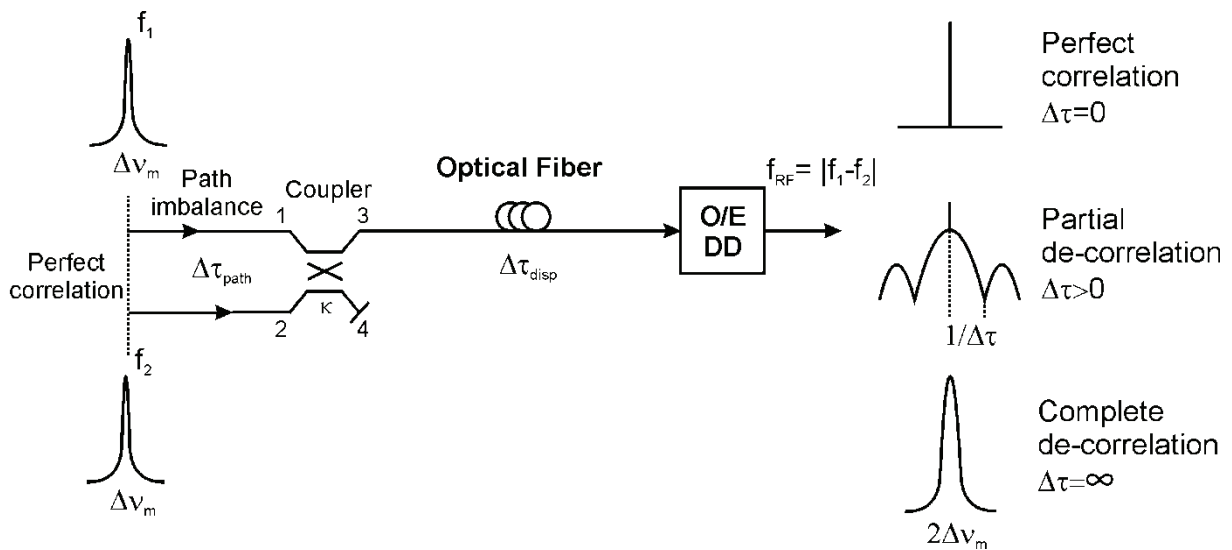


Figure 4.17: Principle of operation of RHD fiber optic mm-wave links.

A typical configuration of the RHD-technique is shown in Figure 4.17. Here the two phase-correlated signals part from perfect phase correlation, but usually they don't travel the same optical path. Therefore, when they are reunited to be transmitted over a single fiber link to the receiver, the difference in paths traveled produces a differential propagation delay, $\Delta\tau_{path}$.

Moreover, as both optical carriers travel through the optical fiber, they further suffer another differential propagation delay, $\Delta\tau_{disp}$, due to chromatic dispersion. Arriving at the receiver, the overall differential propagation delay is given by

$$\Delta\tau = \left| \Delta\tau_{path} + \Delta\tau_{disp} \right| \quad (4.55)$$

which results in a state of partial phase decorrelation. The amount of phase decorrelation depends on the introduced amount of differential delay. The first part of the differential delay in Eq. (4.55) is caused by the path imbalance and can be calculated to be

$$\Delta\tau_{path} = \pm \frac{\Delta L_{path} \cdot n}{c} \quad (4.56)$$

where ΔL_{path} is the difference in path length and n is the refractive index of the optical waveguide. The sign of the path imbalance depends on whether it works in the same or opposite direction as the dispersion induced delay $\Delta\tau_{disp}$, which is always considered positive and is given by

$$\Delta\tau_{disp} = D \cdot L \cdot \frac{\lambda_c^2}{c} \cdot f_{RF} \quad (4.57)$$

Therefore, the path imbalance induced delay could compensate a certain combination of mm-wave frequency f_{RF} and transmission distance L limitation due to fiber dispersion [96].

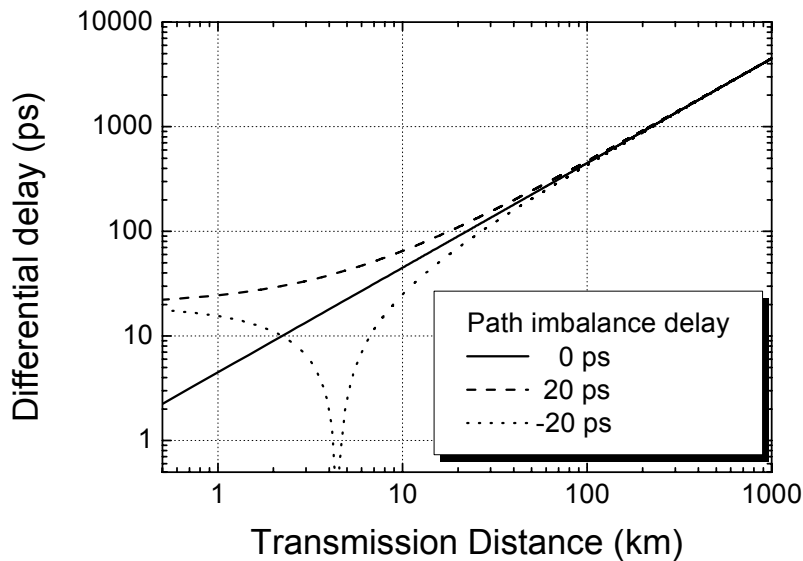


Figure 4.18: Differential delay as a function of transmission distance for $f_{RF} = 33$ GHz with $\Delta\tau_{path}$ as a parameter. Calculations done for $\lambda_c = 1550$ nm and $D = 17$ ps/nm·km.

Figure 4.18 shows the sum differential delay as a function of the transmission distance L for $f_{RF} = 33$ GHz with the path imbalance delay $\Delta\tau_{path}$ as a parameter. It can be observed that for $L = 4.4$ km, the sum differential delay is zero when the path imbalance poses a negative delay. From Eq. (4.56) and Eq. (4.57) this occurs for

$$\Delta L_{path} = D \cdot L \cdot \frac{\lambda_c^2}{n} \cdot f_{RF}. \quad (4.58)$$

On the contrary, when the path imbalance has the same sign as the dispersion induced delay, it contributes to a differential delay floor. When the paths are equal, a linear dependence is observed. Nonetheless, for large transmission distances, all cases converge to the delay induced by fiber dispersion.

Assuming that the master laser has a Lorentzian shaped power spectrum, the single sideband power spectral density of the mm-wave signal at the output of the O/E detector is given by [97]-[98]

$$S_f(f) = \delta(f) \exp(-2\pi\Delta\nu_m\Delta\tau) + \frac{\Delta\nu_m}{\pi(\Delta\nu_m^2 + f^2)} \cdot \left[1 - \exp(-2\pi\Delta\nu_m\Delta\tau) \cdot \left(\cos(2\pi f\Delta\tau) + \frac{\Delta\nu_m}{f} \sin(2\pi f\Delta\tau) \right) \right] \quad (4.59)$$

Where f is the offset from the mm-wave carrier and $\Delta\nu_m$ is the linewidth of the power spectrum of the master laser. Small depictions of the power spectrum can be seen at the right side of Figure 4.17. For a small differential delay ($\Delta\tau \approx 0$), the two optical signals remain correlated and the result spectrum is a delta function given by the first term in Eq. (4.59). On the other hand, for extreme large delays ($\Delta\tau \approx \infty$) the two signals become completely uncorrelated. The resulting mm-wave spectrum becomes Lorentzian shaped with a linewidth of $2\Delta\nu_m$. For intermediate values of $\Delta\tau$, the spectrum is a combination of the delta function and a sinc with spectral zeros spaced by $1/\Delta\tau$. With sufficient RF spectral resolution, the zero spacings of the partial decorrelated mm-wave signal spectrum give information on the total differential delay.

From Eq. (4.59) two effects can be distinguished. The first term corresponds to a decrease in C/N while the second term contributes to an increase of the phase noise. Following the law of conservation of energy, this means that the decrease in signal power (and also C/N) is due to

an increase of phase noise power at all offset frequencies. Nonetheless, both effects pose limitations on the maximum transmission distance and must be treated separately.

The delay induced C/N penalty is found from the first term in Eq. (4.59) as

$$C / N_{pen} = 10 \cdot \log \left(\frac{1}{\exp(-2\pi\Delta\nu_m\Delta\tau)} \right). \quad (4.60)$$

Figure 4.19 shows the C/N penalty from Eq. (4.60) with the master laser linewidth $\Delta\nu_m$ as a parameter. Only a small C/N penalty is observed even for large differential delays and wide linewidths, meaning this approach is quite tolerant to fiber dispersion in this aspect. The transmission distance is calculated for $f_{RF} = 33$ GHz for the special case where $\Delta\tau_{path} = 0$ ps, i.e. the differential delay is only introduced by the fiber dispersion. For standard DFB lasers, the linewidth is in the 5-10 MHz region, meaning transmission distances of 1000 km can be reached before a 3 dB C/N due to chromatic dispersion is reached. That is three orders of magnitude better than with the IM/DD method and thus fiber attenuation will be the transmission limiting factor in this case. Although the differential delay introduced by fiber dispersion $\Delta\tau_{disp}$ can be compensated with the path imbalance delay $\Delta\tau_{path}$, the penalty is so negligible that surely other factors will limit system performance (e.g. fiber attenuation or fiber dispersion on the baseband data).

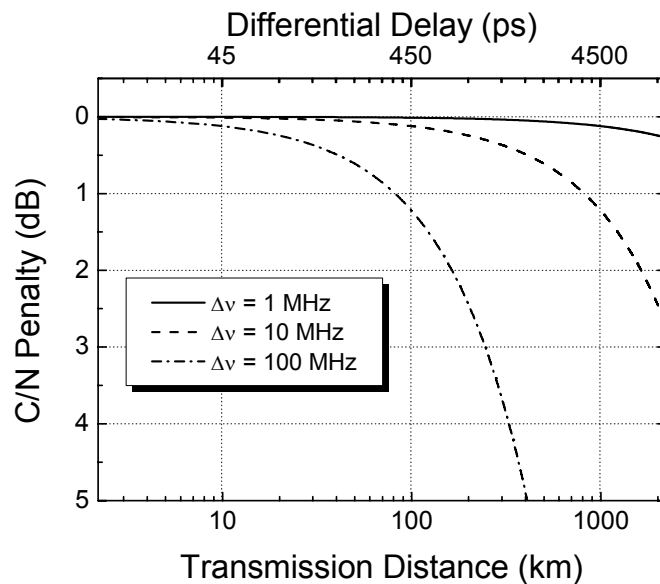


Figure 4.19: Dispersion induced C/N penalty as a function of differential delay with $\Delta\nu_m$ as parameter. The transmission distance is calculated for $f_{RF} = 33$ GHz, $\lambda_c = 1550$ nm and $D = 17$ ps/nm·km.

To analyze the phase noise variation, the phase fluctuation spectrum, $S_\phi(f)$, is best suited than the power spectrum from Eq. (4.59). From the master laser frequency fluctuation, $S_f(f)_m$, the phase fluctuations can be calculated as [99]

$$S_\phi(f)_{delay} = 2 \cdot \frac{S_f(f)_m}{f^2} \cdot [1 - \cos(2\pi f \Delta\tau)]. \quad (4.61)$$

The spectrum is shown in Figure 4.20 as a function of frequency offset from the carrier with the differential delay as a parameter. For infinite delays, the Lorentzian shape with a $1/f^2$ dependence can be clearly seen. For intermediate values of $\Delta\tau$ the sinc shape is observed, with its zero spacing. For low values of $\Delta\tau$ ($\Delta\tau < 1$ ps) then the zero spacings are so large, that the distribution of the phase noise is quite uniform, meaning that a significant amount of the delay induced phase noise will be removed by the filtering performed in the mm-wave receiver [100].

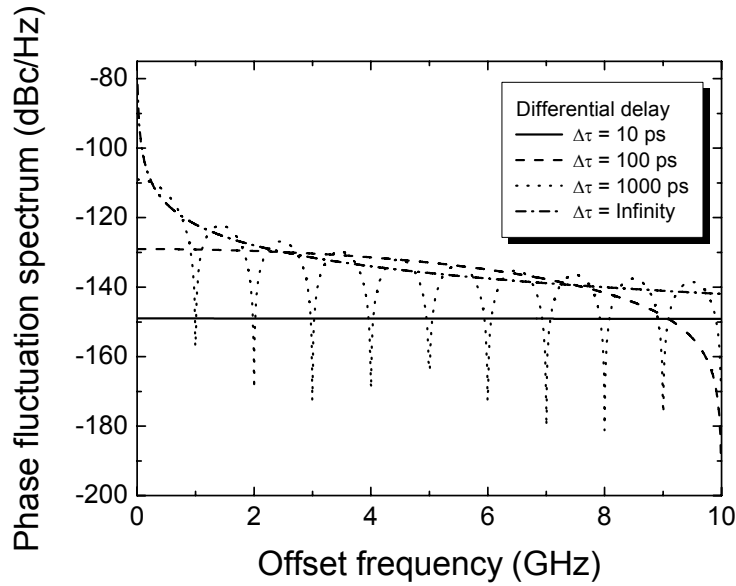


Figure 4.20: Phase fluctuation spectral density.

The phase noise is expressed as rms phase error σ_ϕ or as phase variance $(\sigma_\phi)^2$ given by

$$\begin{aligned} (\sigma_\phi)_{delay}^2 &= \int_0^{B_n} \frac{2\Delta v_m}{\pi f^2} \cdot [1 - \cos(2\pi f \Delta\tau)] df \\ &\approx 2\pi\Delta v_m B_n (\Delta\tau)^2 \text{ for } B_n \ll \frac{1}{\Delta\tau} \end{aligned} \quad (4.62)$$

where B_n is the mm-wave receiver noise bandwidth. Figure 4.21 shows the calculated rms phase error from Eq. (4.62) as a function of the differential delay with the master laser linewidth $\Delta\nu_m$ times the receiver noise bandwidth B_n as a parameter. It is clear that the rms phase error increases as the differential delay is bigger. Furthermore, an increase in master laser linewidth or receiver noise bandwidth also causes an increase in rms phase error.

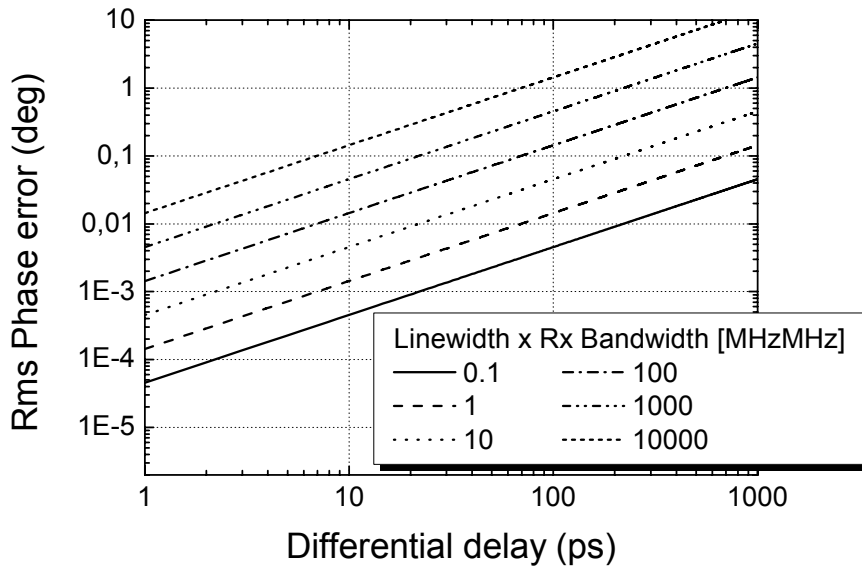


Figure 4.21: Delay induced rms phase error as a function of the differential delay with the master laser linewidth $\Delta\nu_m$ times the receiver noise bandwidth B_n as parameter.

The rms phase error is a limiting factor for phase modulation formats such as Binary Phase Shift Keying (BPSK), Quaternary PSK (QPSK) and higher order PSKs where the information is carried by the phase of the optical signal. Deviations in the phase states lead to an increase in the Bit Error Rates (BER). Table 4.1 shows the allowable rms phase error for different modulation formats. The values are taken from the Intelsat specifications for a QPSK system [101].

Modulation Format	1 dB Penalty at BER = 10^{-9}	Typical	10% of Typical
BPSK	11.4°	8.2°	0.82°
QPSK	3.9°	2.8°	0.28°
8PSK	1.8°	1.3°	0.13°
16PSK	1.2°	0.9°	0.09°

Table 4.1: Allowable rms phase error for different modulation formats [101].

With the help of Table 4.1 and Eq. (4.62), the maximum allowable transmission distance for $f_{RF} = 33$ GHz can be calculated for each different modulation format. The results are shown in Figure 4.22 for no path imbalance delay, i.e. the delay is only induced by chromatic dispersion in the fiber.

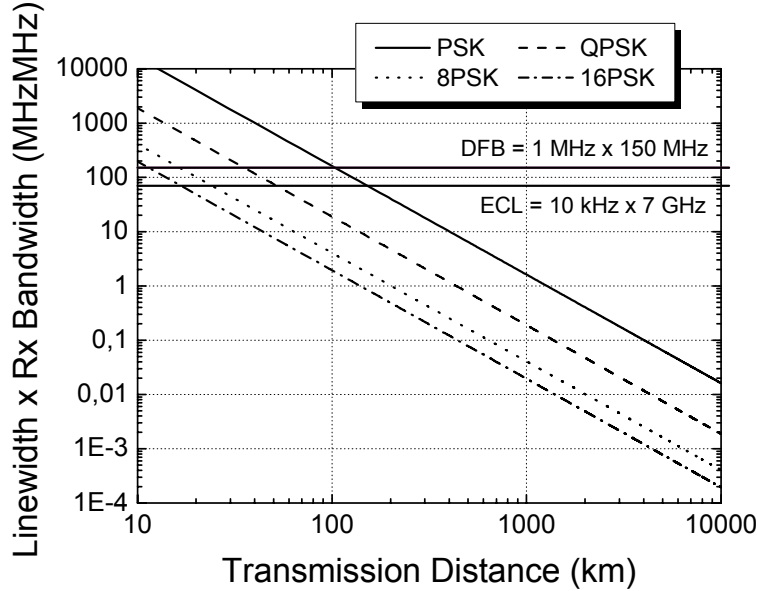


Figure 4.22: Master laser linewidth $\Delta\nu_m$ times the receiver noise bandwidth B_n as a function of the transmission distance for different system types. Calculated for $f_{RF} = 33$ GHz, $\lambda_c = 1550$ nm and $D = 17$ ps/km·nm.

From the above it is seen that, for bandwidths $B_n < 150$ MHz systems at this high carrier frequency, it is possible to transmit over long fiber distances with RHD-links using master laser with linewidths in the 1-10 MHz range (top horizontal line calculated with $\Delta\nu_m = 1$ MHz, typical values for DFB lasers). However, moving to higher data rates will require larger bandwidths. If $B_n = 7$ GHz, then laser linewidths in the order 10-100 kHz will be required to transmit phase modulation formats over decent distances (bottom horizontal line calculated with $\Delta\nu_m = 10$ kHz, which is representative for ECL lasers).

4.5 Phased induced intensity noise

Another point of interest is that the laser phase noise will be converted to intensity noise as investigated in [102]. The laser phase induced intensity noise (PIIN) is defined in [103] as

$$PIIN = 4\pi\Delta\nu_m \left(D \cdot \frac{\lambda_c^2}{c} L \cdot f_{RF} \right)^2 \quad (4.63)$$

where $\Delta\nu_m$ represents the spectral laser linewidth, λ_c the laser center wavelength, D is the fiber dispersion in ps/nm·km, c is the speed of light, L the fiber link length and f_{RF} the desired mm-wave frequency. Eq. (4.63) suggests that PIIN will strongly occur in optical mm-wave systems operating at high frequencies and/or long fiber link lengths. A plot of the several noise sources in an optical amplified mm-wave fiber link is shown in Figure 4.23. The calculations are based on a DFB laser with $\Delta\nu_m = 5$ MHz and a $RIN = -140$ dB/Hz operating at $\lambda_c = 1550$ nm. The optical signal is amplified by an EDFA with gain $G = 22$ dB, an ideal noise figure $NF = 3$ dB and the ASE bandwidth is limited to $B = 1$ nm via a fiber Bragg grating (FBG). The optical power is set to $P_{opt} = 0$ dBm and the mm-wave frequency is used is $f_{RF} = 33$ GHz. The photodiode used is a *pin* diode with $R_1 = 0.05$ A/W and $R_2 = 0.5$ A/W to show the difference in a higher current environment.

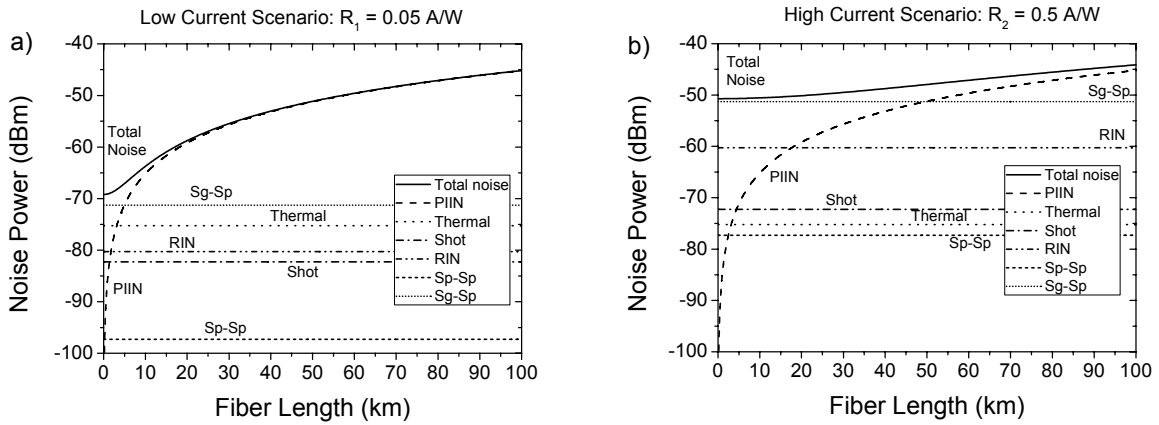


Figure 4.23: Contributions to total noise in mm-wave fiber links for $f_{RF} = 33$ GHz with fiber length L as a parameter in a 7.5 GHz bandwidth for a) $R_1 = 0.05$ A/W and b) $R_2 = 0.5$ A/W.

Clearly PIIN becomes the dominant source of noise at longer fiber lengths. In the example previously proposed, the effects of PIIN start dominating at $L_1 = 5$ km and $L_2 = 50$ km depending on the photodiode responsivity. Nonetheless, in optically amplified systems, generally the biggest contribution comes from the signal-spontaneous beat noise (i.e. Sg-Sp) which is dominant for higher responsivities R .

Although from a noise perspective PIIN is the major contributor, the C/N penalty was calculated in [102] for a QPSK signal with a receiver bandwidth of 33 MHz over $L = 30$ km as a function of carrier frequency and for different laser linewidths. The results indicate that

even at high RF frequencies such as $f_{RF} = 60$ GHz and large laser linewidths $\Delta\nu_m = 20$ MHz, there is only a penalty of 12 dB in the carrier to noise ratio.

Another study in [104] shows that to keep the power penalty below 0.5 dB for $BER = 10^{-11}$, the requirement on the laser linewidth becomes strict around 5 Gbps ($\Delta\nu_m < 2$ MHz). However, as a consequence of the saturation of the noise power in the higher bit rate range, the linewidth requirement is the same for tens of Gbps.

The impact of PIIN is the dominant noise mechanism which will reduce the mm-wave signal quality, but does not significantly restrict the overall system performance. With mainstream distributed feedback (DFB) lasers improving exhibiting laser linewidths around $\Delta\nu_m = 5$ MHz are not uncommon, and external cavity lasers (ECL) with $\Delta\nu_m = 100$ kHz would allow to neglect the contributions of PIIN to system degradations. Also using high responsivity photodiodes would shift the influence of PIIN to tens of km. Therefore, the contributions of PIIN can be safely neglected and the main contributor is, as usual, the signal-spontaneous beat noise from the optical amplifier.

4.6 Polarization mode dispersion

It is well known from the literature that polarization mode dispersion (PMD) is a limiting factor in high speed, long haul fiber optic systems [105]-[106]. In these systems where chromatic dispersion is either very small or compensated, PMD plays an important role as it imposes a delay between the two principal polarization modes that coexist in a fiber. In a similar way that chromatic dispersion induces a time delay $\Delta\tau_{disp}$ between two optical spectral lines, PMD causes a delay $\Delta\tau_{pmd}$ between the two principal states of polarization. This produces again a power penalty which leads to increase of the BER [107].

The optical field vectors of two light waves with the same arbitrary linearly polarization at angular frequency ω_i in an optical fiber can be mathematically written as

$$\vec{E}_i^{in}(t) = A_i \cdot e^{j\omega_i t} \begin{pmatrix} \cos \theta \\ \sin \theta \end{pmatrix} \text{ for } i = 1, 2 \quad (4.64)$$

where θ is the angle between the linear polarized field vectors and the x-axis of the orthogonal principle axis of the optical fiber, and A_i the field amplitude.

The fiber link represents an anisotropic medium with birefringence $\Delta n = n_x - n_y$ where $n_{x,y}$ is the refractive index at the orthogonal principal axis x and y of the fiber, respectively. The transformation matrix of the fiber link can be expressed as

$$T_i = \begin{pmatrix} e^{-j\delta_i^x} & 0 \\ 0 & e^{-j\delta_i^y} \end{pmatrix} \quad (4.65)$$

where the phase components are $\delta_i^{x,y} = 2\pi n_{x,y}L/\lambda_i$ being L the fiber length. The transmission through optical fiber results in the electrical field at the receiver taking the form

$$\vec{E}_i^{out}(t) = T_i \cdot \vec{E}_i^{in}(t). \quad (4.66)$$

The resulting optical power at the photodetector is then

$$P_{rec} = \left| \vec{E}_1^{out} + \vec{E}_2^{out} \right|^2. \quad (4.67)$$

At the photodiode, heterodyne mixing takes place and the resulting beat frequency $f_{RF} = f_1 - f_2$ has an electrical power P_{RF} which changes with the square of P_{rec} . The power penalty ΔP due to a PMD induced delay $\Delta\tau_{pmd}$ is given by [108]

$$\Delta P = -10 \cdot \log \left(\frac{1 + f(\kappa_{pol}) + \cos^2(\pi \cdot f_{RF} \cdot \Delta\tau_{pmd} \cdot L) \cdot (1 - f(\kappa_{pol}))}{2} \right) \quad (4.68)$$

for $\Delta\tau_{pmd} \geq 0, L \geq 0$ and $0 \leq \kappa_{pol} \leq 1$. Here $f(\kappa_{pol}) = \cos \left[4 \cdot \arccos \left(\sqrt{\kappa_{pol}} \right) \right]$, where κ_{pol} represents the splitting ratio of the signal with respect to the principal polarization axis, and L is the fiber length. Using the splitting ratio κ_{pol} as a parameter results in the curves shown in Figure 4.24. It is evident from the graphs and Eq. (4.68) that the worst case scenario is when $\kappa_{pol} = 0.5$, corresponding to $\theta = 45^\circ$, i.e. the signal is launched into the fiber with a linear polarization state with an angle of 45° with the principal polarization axes. For this worst case, Eq. (4.68) can be reduced to the form in [107]

$$\Delta P_{wc} = -20 \cdot \log \left(\cos(\pi \cdot f_{RF} \cdot \Delta\tau_{pmd} \cdot L) \right). \quad (4.69)$$

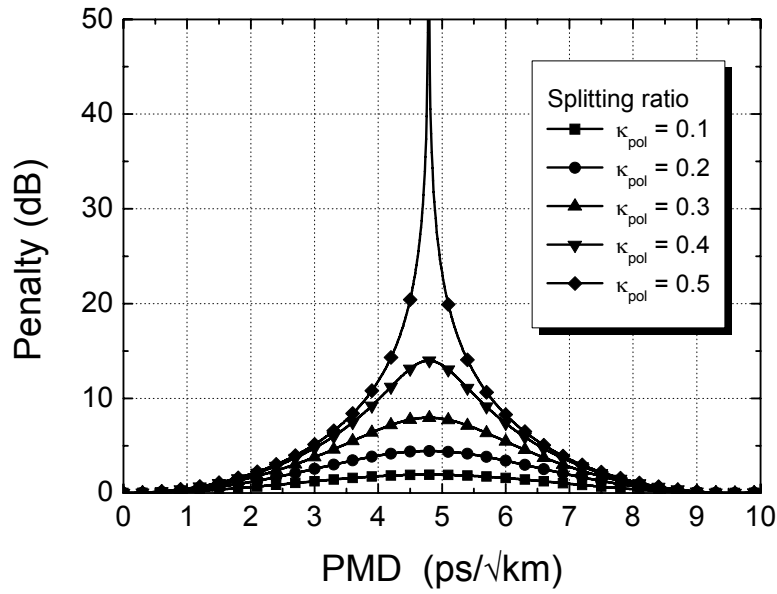


Figure 4.24: Power penalty for $f_{RF} = 33$ GHz due to PMD induced delay $\Delta\tau_{pmd}$ with the power splitting ratio κ_{pol} as a parameter and $L = 10$ km.

Although PMD is a statistical process, for special cases when the transmission distances are smaller than the beat length, it can be approximated linearly with the fiber length L . But when the fiber length is longer than the beat length, it usually follows with the square root of L [109]. We have then

$$\Delta\tau'_{pmd} = \Delta\tau_{pmd} \cdot \sqrt{L} \quad (4.70)$$

and so Eq. (4.69) results into

$$\Delta P_{wc} = -20 \cdot \log\left(\cos(\pi \cdot f_{RF} \cdot \Delta\tau'_{pmd} \cdot \sqrt{L})\right). \quad (4.71)$$

Figure 4.25 shows the power penalty as a function of the transmission distance L for two different fiber types. One is an old already deployed SMF fiber with $\Delta\tau'_{pmd} = 0.8$ ps/√km whereas the other one is a modern fiber with a much lower $\Delta\tau'_{pmd} = 0.1$ ps/√km. For older fibers the effects of PMD for $f_{RF} = 33$ GHz produce a power fading around $L = 355$ km. For modern fibers with low $\Delta\tau'_{pmd}$ the effects of PMD power fading are negligible even after long transmission distances in the order of thousands of kilometers.

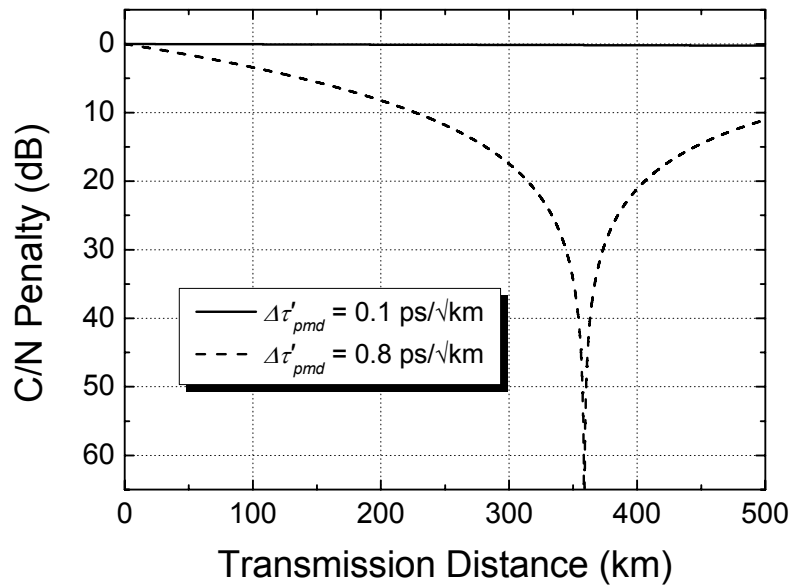


Figure 4.25: Power penalty for $f_{RF} = 33$ GHz due to PMD induced delay $\Delta\tau'_{pmd}$ for two different fibers with the $\Delta\tau'_{pmd}$ as a parameter.

The length where the mm-wave signal first vanishes can be again derived from Eq. (4.71) and is

$$L_0 = \left(\frac{1}{2f_{RF}\Delta\tau'_{pmd}} \right)^2. \quad (4.72)$$

This means that both optical fields' polarization states are orthogonal to each other and effectively cancel in the photodiode. Nonetheless, PMD penalties are much lower than the IM/DD case and for modern fibers also small compared to the RHD technique. Therefore for the subsequent applications in the next chapter the influence of PMD can be neglected.

5 Electrooptical upconversion methods

In order to reduce the requirements of high frequency RF sources in the central station, different optical frequency upconversion methods can be used. They consist in shifting lower frequencies in the electrical domain to higher frequency ranges by using different forms of the electrooptical effect (for example, the linear Pockels effect, the quadratic Kerr effect, etc.). Most of them consist in creating high order harmonics (i.e. multiples) of an input modulation frequency f_m and then filter out the undesired components, such that by heterodyning in a photodiode only the higher frequencies are generated. The following sections describe in detail the methods investigated in this thesis and the parameters that characterize them in terms of efficiency and RF frequencies achieved.

5.1 Mach-Zehnder modulator

One of the most popular ways of upconverting electrical signals is using an optical Mach-Zehnder modulator (MZM) at certain bias points to generate the required high order harmonics [109]. A schematic of a basic MZM is shown in Figure 5.1 with its most common bias or working points.

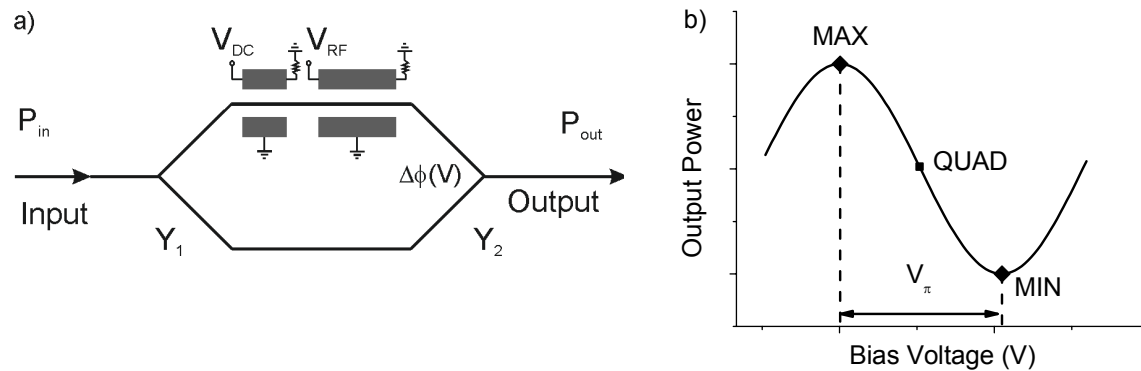


Figure 5.1: a) Basic Mach-Zehnder Modulator and b) its most common bias points.

Optical power P_{in} enters through a single mode dielectric optical waveguide which splits into two singlemode waveguides at the input waveguide Y branch. The input Y (Y_1) branch splits the power into upper and lower arms. The optical phase difference is shifted with respect to the unchanged state by an amount $\Delta\phi(V)=\phi_{RF}+\phi_{DC}$. This phase modulation is accomplished by

placing electrodes around the waveguides in each arm. In this example, the upper arm has two electrodes (one for the RF signal and the other for a DC signal) whereas the lower arm remains unchanged. Then the two waveguides have their powers recombined at the output Y branch (Y_2). The relative phase of the light from the two arms is determined by the phase modulator. If the light is in phase (i.e. $\Delta\phi=0$), it adds to form the fundamental mode of the output waveguide, and the output power P_{out} is at a maximum. If the light from the two arms is out of phase (i.e. $\Delta\phi=\pi$), it adds in Y_2 to form the second order mode of the output waveguide; this mode is not guided by the singlemode waveguide, so the power is radiated into the substrate and the output power is at a minimum. For the case where there is a transmission factor of t_m and both Y_1 and Y_2 provide equal splits, then

$$P_{out} = t_m \cdot \frac{P_{in}}{2} [1 + \cos(\Delta\phi(t))] = t_m \cdot P_{in} \cdot \cos^2\left(\frac{\Delta\phi(t)}{2}\right). \quad (5.1)$$

Being

$$\Delta\phi(t) = \pi \cdot \frac{V_{DC} + V_{RF}(t)}{V_\pi} = \pi \cdot \frac{V_{mod}(t)}{V_\pi} \quad (5.2)$$

where V_π is called the half-wave voltage and is the voltage swing needed to go from maximum to minimum transmission point (see Figure 5.1b). If V_{mod} is a mm-wave signal of the form $V_{mod}(t) = V_{DC} + V_{RF} \cdot \cos(\omega_{RF}t)$ then the output power becomes

$$P_{out}(t) = t_m \cdot \frac{P_{in}}{2} [1 + \cos(\pi\gamma + \pi m_a \cos(\omega_{RF}t))] \quad (5.3)$$

where $\gamma = V_{DC}/V_\pi$ is the normalized bias and $m_a = V_{RF}/V_\pi$ the amplitude modulation index driving the MZM. Figure 5.1b shows the most common bias points of operation of a MZM. The optimal DC Bias for linear operation is when $V_{DC} = V_\pi/2 + iV_\pi$ for $i = 0, 1, 2, \dots$. The case $i = 0$ is called quadrature (QUAD corresponding to $\gamma = 0.5$) and the output optical intensity can be expressed from Eq. (5.3) by Bessel-function expansion neglecting insertion losses (i.e. $t_m = 1$) as

$$P_{QUADout}(t) = \frac{P_{in}}{2} - P_{in} \sum_{k=-\infty}^{\infty} (-1)^k J_{2k+1}(m_a\pi) \cos((2k+1)\omega_{RF}t). \quad (5.4)$$

This corresponds to an optical carrier plus the odd-order sidebands (represented by the $2k+1$ term in the Bessel series). A schematic of a sample spectrum can be seen in Figure 5.2a. The same analysis can be done for the two other bias points of interest such as maximum power transmission (MAX where $\gamma = 0$) or minimum power transmission (MIN corresponding to $\gamma = 1$). The corresponding intensities are

$$P_{MAXout}(t) = \frac{P_{in}}{2}(1 - J_0(m_a\pi)) + P_{in} \sum_{k=-\infty}^{\infty} (-1)^k J_{2k}(m_a\pi) \cos(2k\omega_{RF}t) \quad (5.5)$$

and

$$P_{MINout}(t) = -P_{in} \sum_{k=-\infty}^{\infty} (-1)^k J_{2k+1}(m_a\pi) \cos((2k+1)\omega_{RF}t). \quad (5.6)$$

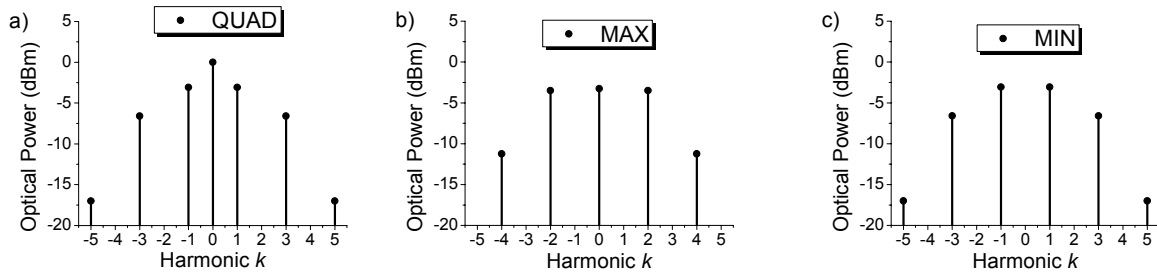


Figure 5.2: Spectra at the output of the MZM for $P_{in} = 1$ mW, $t_m = 1$ and $m_a = 0.8$ under a) QUAD bias, b) MAX bias and c) MIN bias.

For the MAX case, the spectrum is composed of an optical carrier plus the even order sidebands (Figure 5.2b). However, for the MIN case (Figure 5.2c), the optical carrier is ideally completely suppressed and only the odd-order sidebands are present. This case is of special interest, as after detection in a squaring device such as a photodiode, an effective doubling of the RF frequency can be achieved. The same could be obtained for the MAX bias point, but in this case there are two components in charge of generating the mm-wave signal (carrier and ± 2 harmonic), and thus this scheme is more susceptible to fiber dispersion (as explained in Section 4.2).

The modulator described in Figure 5.1 is usually called single-drive MZM, as only one RF and bias (DC) signal are used. Other interesting MZM architectures are depicted in Figure 5.3. A dual-drive MZM (shown in Figure 5.3a) has two electrodes in each arm of the MZM to achieve complete freedom over the relative optical phase and chirp parameter (see section

4.3.2). In this way, the voltage swing to produce a modulation index m_a can be reduced in half by carefully feeding of the RF signal in both arms (i.e. each arm is fed $m_a \cdot V_\pi/2$). Another interesting topology is the dual-nested MZM, where two MZMs are placed inside a MZM “superstructure”, depicted in Figure 5.3b. This type of modulator is mainly used to generate complex optical modulation formats such as differential quadrature phase shift keying (RZ-DQPSK) [110] but can also be used to generate a double sideband with suppressed carrier (DSB-SC) signal [111].

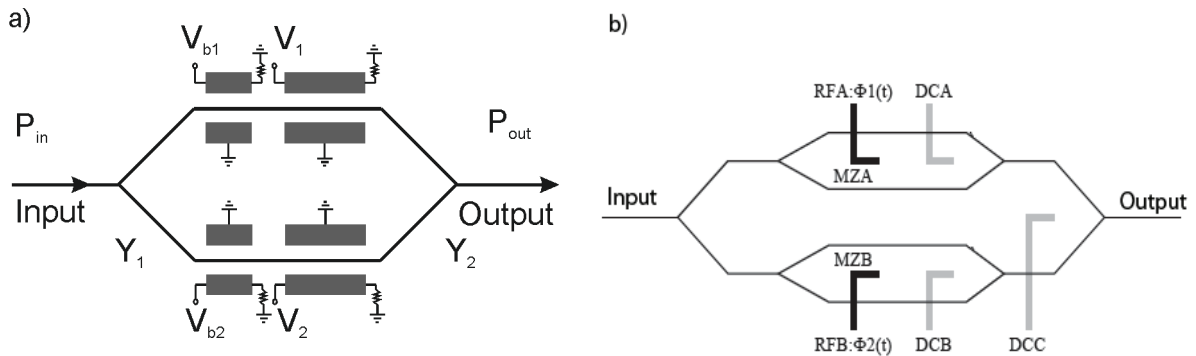


Figure 5.3: a) Dual-drive and b) dual-nested Mach-Zehnder modulators.

Through the course of this work both single-drive and dual-drive MZMs models were used. Nonetheless, both electrodes in one arm of the dual-drive MZM were grounded using it as a single-drive MZM. Therefore, the following analysis will focus only on single-drive MZMs.

The optical intensity in the MZM for sinusoidal drive can be also modeled as a Fourier expansion in the time domain

$$\begin{aligned}
 P(t) &= t_m P_0 \left(1 + \cos \left(\frac{\pi}{V_\pi} [A \sin(\omega_{RF} t) + V_b] \right) \right) \\
 &= t_m P_0 \left\{ \begin{aligned} & \left[1 + \cos \left(\frac{\pi V_b}{V_\pi} \right) J_0(m_a \pi) \right] - 2 \left[\sin \left(\frac{\pi V_b}{V_\pi} \right) J_1(m_a \pi) \right] \sin(\omega_{RF} t) \\ & + 2 \left[\cos \left(\frac{\pi V_b}{V_\pi} \right) J_2(m_a \pi) \right] \sin \left(2\omega_{RF} t + \frac{\pi}{2} \right) \\ & + 2 \left[\sin \left(\frac{\pi V_b}{V_\pi} \right) J_3(m_a \pi) \right] \sin(3\omega_{RF} t) + \dots \end{aligned} \right\} \quad (5.7)
 \end{aligned}$$

where m_a is the modulation index, $2P_0$ is the power incident on the modulator, t_m is the modulator transmission factor (<1 also known as insertion loss), V_b is the modulator bias voltage in units of V_π and A is the modulator RF driving amplitude. Usually the modulation index m_a is also referred to as modulation depth. For example, biasing the modulator at QUAD and modulating with $m_a = 1$ means going from the MAX to the MIN transmission point. Values of m_a higher than 1 usually involve overmodulation and the generation of higher order harmonics.

For example, working on either the maximum or minimum transmission point (i.e. $V_b = 0, V_\pi, 2V_\pi, \dots$) then only the even order harmonics are generated. The calculated harmonic content of the detector output as a function of the input RF drive power at f_{RF} for a MZM biased at minimum transmission for harmonics $n = 2, n = 4$ and $n = 6$ is shown in Figure 5.4.

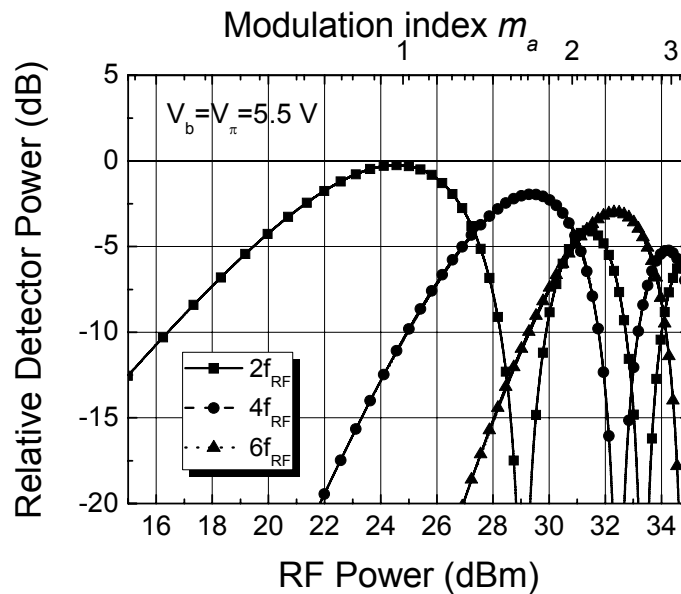


Figure 5.4: Simulated MZM photonic link response versus input RF drive power with minimum biasing of the modulator with no insertion loss (i.e. $t_m = 1$).

This simulation shows efficient frequency conversion to any of the even harmonics for specified RF drive powers. In this case a perfect MZM with no insertion loss (i.e. $t_m = 1$) is considered. One interesting case corresponds to $n = 4$. With a modulation index for this harmonic generation of $m_a = 1.635$ the second harmonic ($n = 2$) is cancelled, and theoretically a clean spectrum up to the 4th harmonic is obtained. The 6th is still present but 4 dB attenuated and if f_{RF} is sufficiently high, out of the band of interest. Table 5.1 summarizes the optimum

modulation indices m_a for different harmonic generation for a MZM biased at minimum with an insertion loss of 4.5 dB ($t_m = 0.35$).

$n =$	2	4	6	8	10
$m_a =$	0.97	1.7	2.4	3.1	3.7

Table 5.1: Optimal modulation indices m_a for n^{th} harmonic generation.

The previous discussion corresponds to a MZM with an infinite extinction ratio. The extinction ratio (ER) is defined as the difference in optical power from the maximum and minimum transmission points. Mathematically,

$$ER = \frac{P_{MAX}}{P_{MIN}}. \quad (5.8)$$

An infinite ER would mean that the minimum transmission point produces zero optical power and thus maximum signal swing. That is rarely the case, as some residual power is left during a logical “zero”. The power penalty in BER performance produced by a non-infinite ER was derived in [71] for *pin* receivers in digital communications and is given by

$$ER_{pen} = 10 \cdot \log\left(\frac{ER + 1}{ER - 1}\right). \quad (5.9)$$

Figure 5.5 shows how the power penalty decreases with increasing ER. Usually, MZM have $ER > 15$ dB, being the power penalties under 0.3 dB and thus can be considered negligible.

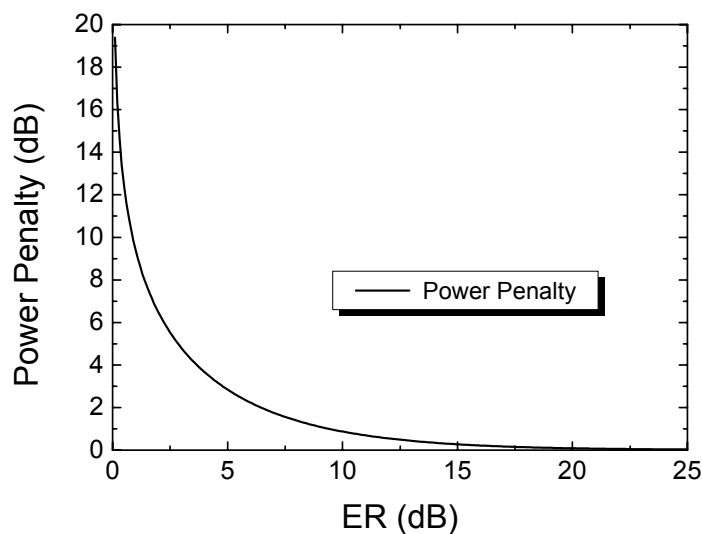


Figure 5.5: Power penalty degradation due to extinction ratio (ER).

Concerning mm-wave generation (i.e sinusoidal modulation), the effect of a finite ER is mainly affecting how much the carrier can be suppressed in the MIN bias point. Ideally from Eq. (5.6) and Figure 5.2c, the optical carrier should be non existent but that is rarely the case. In the next section the setup and experimental properties of a MZM biased at minimum transmission for the generation of mm-wave signals will be described.

5.1.1 Mach-Zehnder modulator biased at MIN

The case depicted in Figure 5.2c is for an ideal MZM with an infinite extinction ratio. Imperfections in the manufacturing process of MZMs lead to misalignments in the polarization of both arms, which result in a far from perfect suppression of the carrier. Therefore, a remnant of the optical carrier is still present and consequently, interfering mm-wave signals at different RF frequencies are generated.

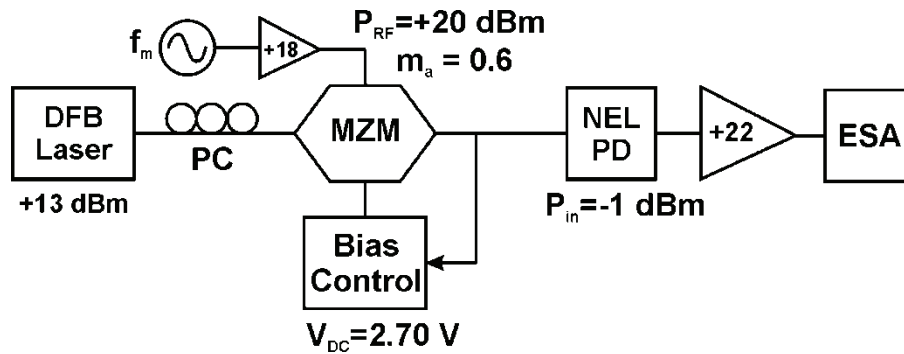


Figure 5.6: Setup for DSB-SC using a Mach-Zehnder modulator biased at MIN.

Figure 5.6 shows the basic setup to generate a Double Sideband with Suppressed Carrier (DSB-SC) signal by using a MZM biased at the minimum transmission point (MIN). The setup consists of a DFB laser with output power $P_{opt} = +13$ dBm, a polarization controller (PC) to align the polarization entering the MZM to achieve optimum modulation, an RF generator operating at f_m with its corresponding amplifier to set the modulation index $m_a = 0.6$ (a higher m_a could not be achieved with the amplifier available, so giving importance to linearity, this lower m_a was chosen) and a bias control circuit to set and maintain the bias point at MIN. The bias control unit operates on the principle of low frequency dithering [112] and a simple schematic is shown in Figure 5.7.

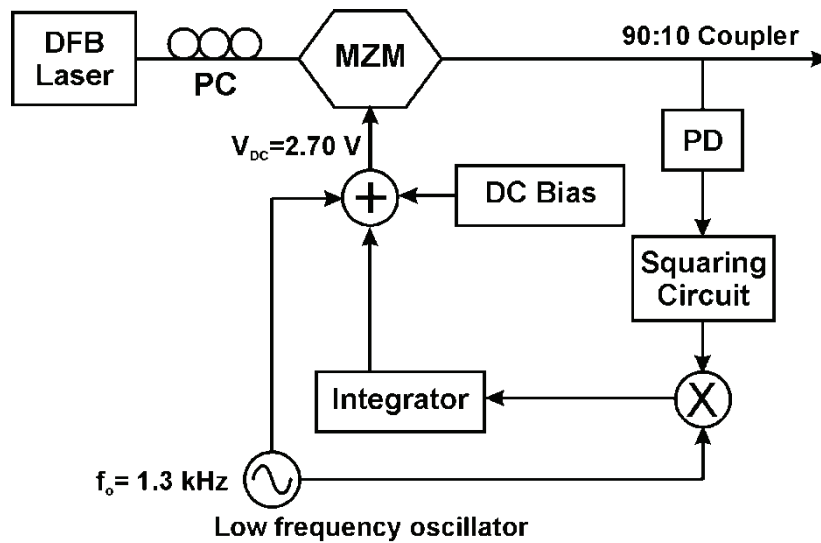


Figure 5.7: Bias control unit schematic.

The MZM is a 10 Gbps OC-192 compliant MZM from JDSU. Although it is specified for 10 Gbps operation, good results can still be obtained for higher modulation frequencies f_m . Its V_π is 5.5 V at 1 GHz and the insertion loss is 5 dB. The resulting optical spectrum at the output of the MZM is depicted in Figure 5.8a for $f_m = 16.5$ GHz. At this high frequency V_π was measured to be 6 V. Usually this kind of MZM are designed for multigbit data modulation so that with $V_{DC} \approx 0$ V they are biased at quadrature. Therefore, to reach the MIN transmission point $V_{DC} \approx V_\pi/2 \approx 2.75$ V. After generating the optical DSB-SC signal, the mm-wave signal is obtained by heterodyning in a broadband photodiode (NEL $B > 100$ GHz, $P_{max} = 0$ dBm, $R = 0.9$ A/W). The RF spectrum after amplification is plotted in an Electrical Spectrum Analyzer (ESA, R&S FSEK30) and is shown in Figure 5.8b. The increase in the noise floor at 26 GHz is due to the change in frequency range internally by the ESA. Simulations were carried out in the commercial software VPI Transmissionmaker 8.0 with the parameters which best fit the devices used in the experiments. There is a good agreement of the measurements with the obtained simulations in the optical as well as the electrical domain. Up to the first harmonics the overlap is perfect, but then the second harmonics have 5 dB variations. Nonetheless the values for the component at $2f_m$ and the remnant carrier match the measurements.

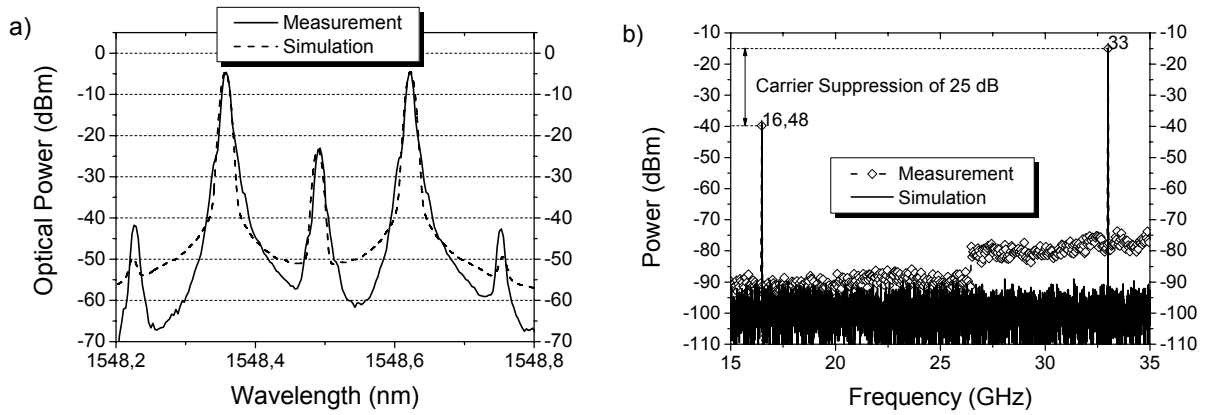


Figure 5.8: DSB-SC with MZM: a) Optical (10 pm RBW) and b) electrical spectrum (100 Hz RBW) for $f_m=16.5$ GHz and $m_a=0.6$.

By working on the MIN bias point the optical powers achieved are quite small (being -5 dBm the power of the ± 1 harmonics) requiring the use of optical amplification such as an erbium doped fiber amplifier (EDFA) or a semiconductor optical amplifier (SOA). Also it can evidently be seen that the carrier is not fully suppressed. For comparison purposes, the carrier suppression is defined as

$$CS_{opt} = \frac{P_{harm1}}{P_{carrier}} \quad (5.10)$$

where P_{harm1} is the power in the first harmonic and $P_{carrier}$ the power of the optical carrier. This is valid for the optical domain as well as the electrical domain. For the case in Figure 5.8a we obtain an optical carrier suppression $CS_{opt} = 19.67$ dB. However, the electrical carrier suppression is approximately $CS_{el} = 25$ dB. The remnant carrier beats with both the ± 1 harmonics and thus generates an RF component at f_m which reduces the available bandwidth of the system. Several methods can be used to extend the optical carrier suppression to acceptable values ($CS_{opt} > 25$ dB so that the carrier is suppressed more than 99.7% and its contribution can be neglected). Two of them will be described in more detail.

As one of the main causes of the imperfect cancelling of the carrier is the cross-polarization products happening in the MZM, the use of a polarizer at the output of the setup helps to reduce the carrier [113]. The modified setup is shown in Figure 5.9. An EDFA is used to amplify the optical signals, then a Fiber Bragg Grating (FBG) with bandwidth $B = 1$ nm works as a passband filter to reduce the amplified spontaneous emission (ASE) of the EDFA

which contributes to overall system noise. A second polarization controller (PC 2) is in charge of aligning the input signal to the fixed polarizer. The electrical receiver is the same used in the previous setup. The power of the EDFA is set so that we have $P_{opt} = -1$ dBm at the photodiode to match the previous case.

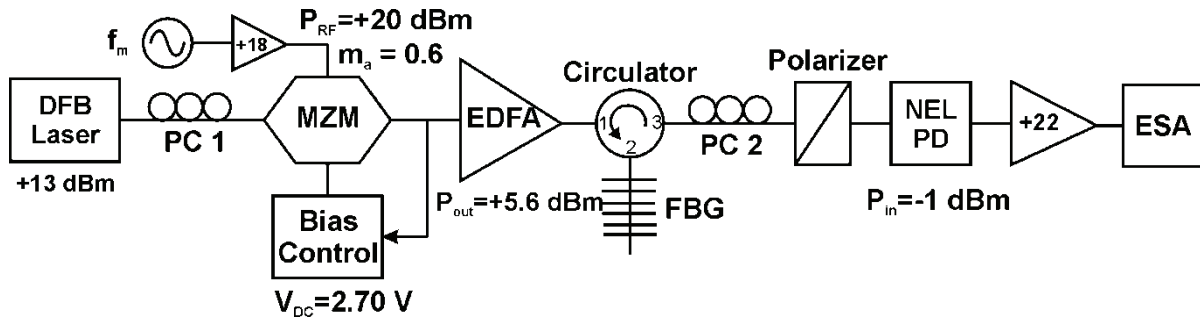


Figure 5.9: Setup for DSB-SC with output polarizer.

From the resulting optical spectrum shown in Figure 5.10a, a $CS_{opt} = 41.4$ dB is measured. The improvement is quite noticeable but the setup requires fine tuning of both polarization controllers (PC 1 and PC 2) to achieve decent results. The electrical spectrum in Figure 5.10b shows a $CS_{el} = 32$ dB. There is only a minimal improvement in the electrical carrier suppression (7 dB), indicating that the higher order harmonics (± 2 harmonic and so on) also contribute to the generation of the component at f_m .

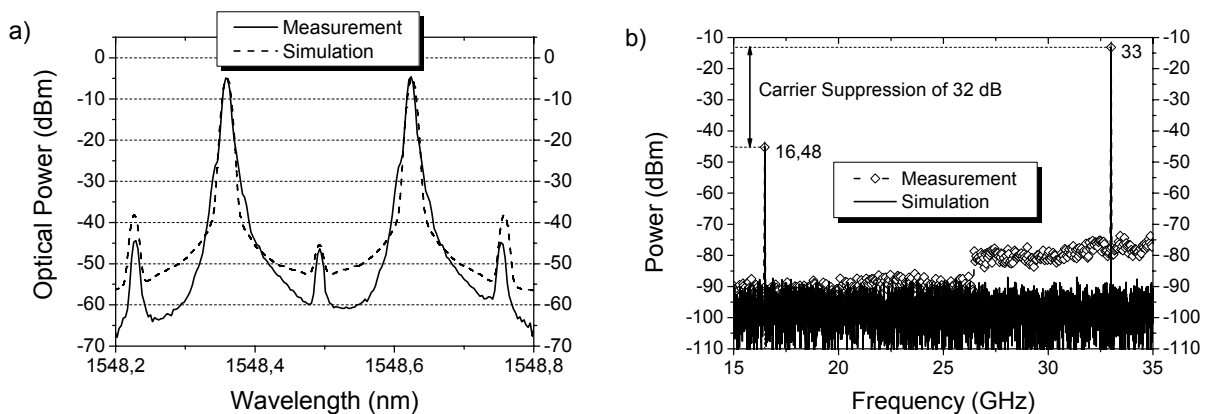


Figure 5.10: DSB-SC with MZM and polarizer: a) Optical (10 pm RBW) and b) electrical spectrum (100 Hz RBW) for $f_m = 16.5$ GHz and $m_a = 0.6$.

In order to test the frequency dependent properties of this scheme, the setup with a MZM alone (Figure 5.6) was used, but with lower RF powers (electrical power $P_m = -2$ dBm) to

prevent damage to the photodiode at lower modulation frequencies. The results of the frequency sweep are plotted in Figure 5.11. The electrical carrier suppression remains well over 20 dB over most of the frequency range. The power of the generated component at $2f_m$ has an evident slope, meaning the modulation index decreases at higher frequencies. Nonetheless, this modulator can still be used with good enough efficiency at higher frequencies than the specified on the datasheet. The 3 dB point of the modulator used is found to be at $f_m = 12.5$ GHz. The carrier suppression has variations as high as 20 dB attributed to the sensitivity of this scheme towards the bias point of the MZM. As seen in Figure 5.11, the power of the unwanted component at f_m fluctuates strongly, mainly due to small deviations in the MZM bias point adjustment.

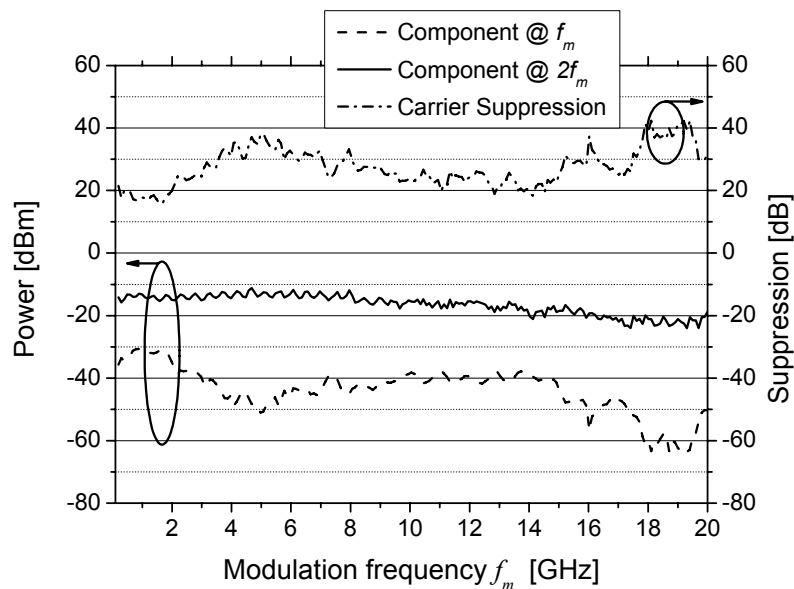


Figure 5.11: Frequency sweep of the MZM setup ($P_m = -2$ dBm).

The same test can be easily performed for the setup with the polarizer (see Figure 5.9) as no narrow band optical filters are used. For this measurement the FBG and circulator were taken out. The results are then depicted in Figure 5.12. The use of an EDFA allows more optical power so that the power of the harmonics is higher. Here the polarization changes and instabilities play a significant role in the measurements. During the sweep, the value of the optical carrier varied, although optically non-evident, electrically it was quite noticeable. The setup was tuned at a fixed frequency (namely $f_m = 10$ GHz) and then the sweep was run. As can be seen, the electrical carrier suppression is better than the previous case, being higher

than 40 dB for most of the frequency range. In practice, for a fixed frequency the setup can be tuned and optical carrier suppressions of up to 60 dB were achieved. Nonetheless, small changes in the bias voltage and polarization states produce interfering components at f_m . The introduction of the EDFA also contributes to the noise of the system and instabilities. Therefore, for a system where the modulation frequency is fixed, then the best option is to filter out the carrier optically. In this way the carrier is completely removed and small changes in the bias voltage do no affect in any way the systems performance.

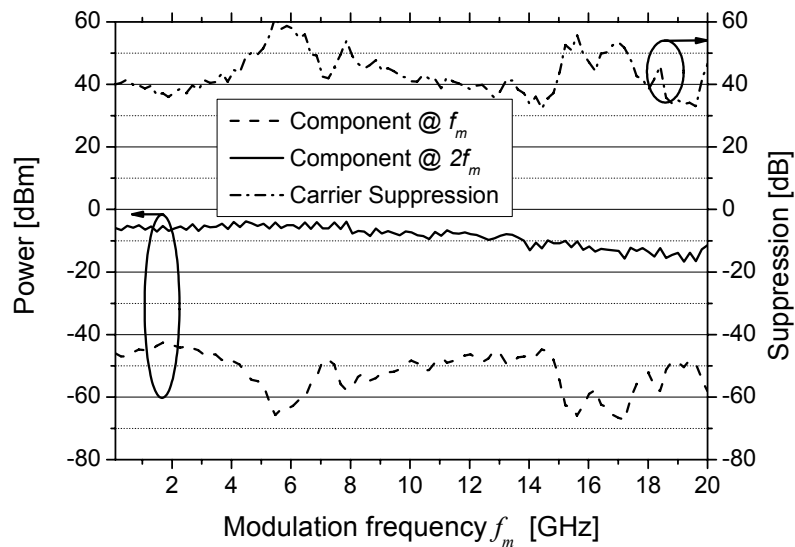


Figure 5.12: Frequency sweep of the MZM polarizer setup ($P_m = -2$ dBm, EDFA = 9 dBm).

One method to directly filter out the remnant carrier is by placing an optical filter such as a Fiber Bragg Grating (FBG) in the transmission path. In this way, optical carrier suppressions of more than 50 dB can be easily obtained. By designing an FBG with a bandwidth $B = 33$ GHz and a rejection of 60 dB, a $CS_{opt} = 57.75$ dB was achieved with the setup shown in Figure 5.13. The FBG must be tuned in the frequency to match the optical carrier and not suppress the sidebands. This tuning is realized by straining the FBG and changing its period and consequently its resonance wavelength [114].

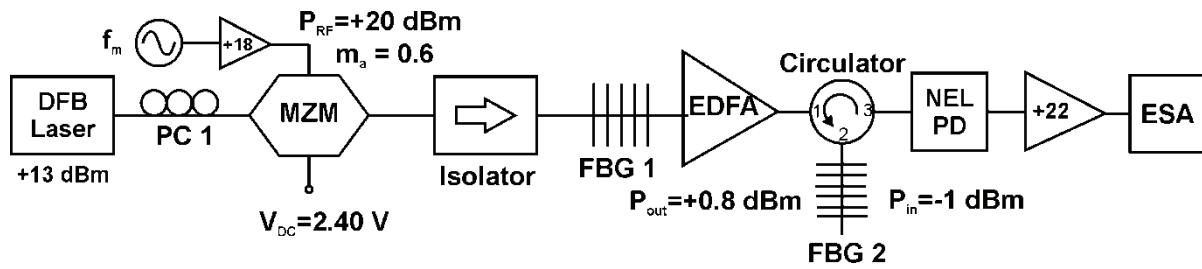


Figure 5.13: Setup for DSB-SC with output FBGs.

This last method offers a simple configuration and tuning, providing the highest carrier suppression and stability. Moreover, now the bias point stabilization is more relaxed, as FBG 1 attenuates the carrier by 60 dB, so that the bias control unit can be replaced by a simple manually tunable DC source. Also the bias point can be tuned to minimize the higher order harmonics ($V_{DC} = 2.4$ V instead of 2.7 V used in the other cases) and thus achieve a higher electrical carrier suppression. Figure 5.14 plots both the optical and respective RF spectra. The simulations predict no carrier present, however a remnant of the carrier is still observed in the measurements, attributed mainly to the beating of the ± 1 harmonic with the ± 2 harmonics (their frequency difference is $f_m = 16.5$ GHz). Nonetheless, an electrical suppression of $CS_{el} \approx 70$ dB was obtained, roughly a 40 dB improvement over the polarizer setup.

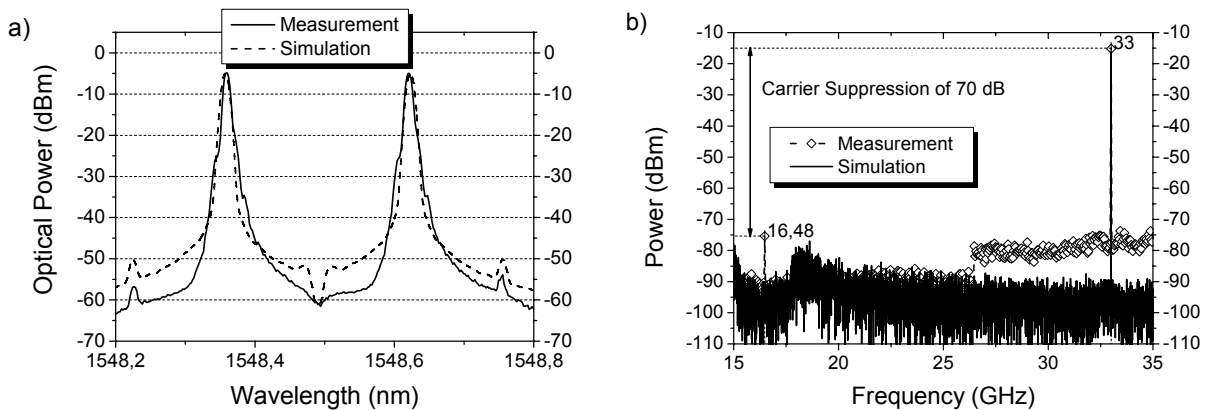


Figure 5.14: DSB-SC with MZM and FBG: a) Optical (10 pm RBW) and b) electrical spectrum (100 Hz RBW) for $f_m = 16.5$ GHz and $m_a = 0.6$.

Even though the setup with an FBG provides the best optical carrier suppression, the tunability of this scheme with respect to the modulation frequency f_m is very difficult, as the bandwidth of the FBG should be varied, or an extremely narrow bandwidth FBG must be

employed. The higher the modulation frequency f_m the less critical the requirements on the FBG bandwidth are. Recent techniques in our lab could produce FBGs with a bandwidth as small as $B = 12$ GHz but with lower rejection. Narrower FBGs are either difficult to produce or the rejection is lower than 60 dB. Therefore there is an inherent trade-off between bandwidth and rejection in FBGs [114].

As a performance benchmark, the phase noise of the generated mm-wave signal was measured after a single mode fiber (SMF) link of length L . The results are shown in Figure 5.15. For a frequency multiplication scheme, theory predicts that the phase noise of the resulting signal should be increased by a factor of $20 \cdot \log N$, where N is the multiplication factor [115]. For our case of frequency doubling, $N = 2$ and thus a theoretical phase noise increase of 6 dB is to be expected [116]. There is no significant change even after $L = 40$ km of SMF. As a reference, the phase noise of the mm-wave signal generator (WILTRON 68347B) is also plotted. The 6 dB theoretical increase is evident, but no further penalty is introduced in the system even after long transmission distances such as $L = 40$ km.

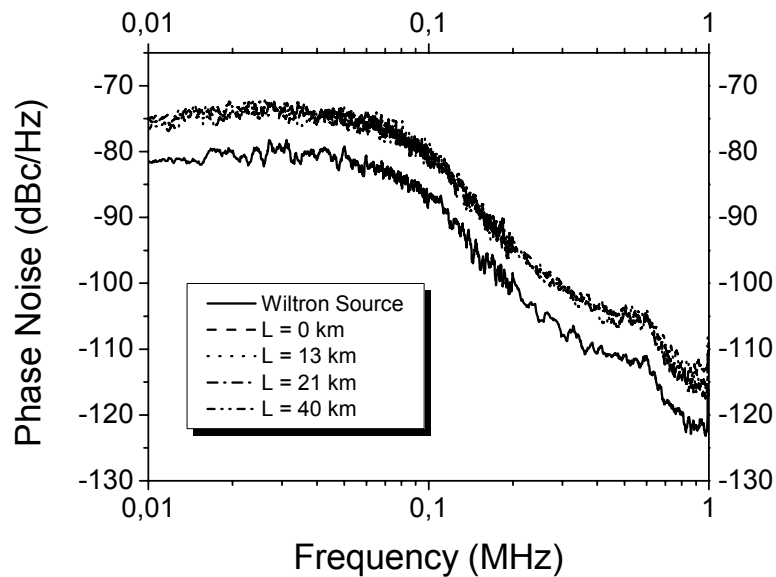


Figure 5.15: Phase noise for the doubling scheme using a MZM and FBG vs fiber length L .

5.2 Fiber loop

A similar approach as the one described in the previous section can be devised with help of a fiber loop mirror as depicted in Figure 5.16.

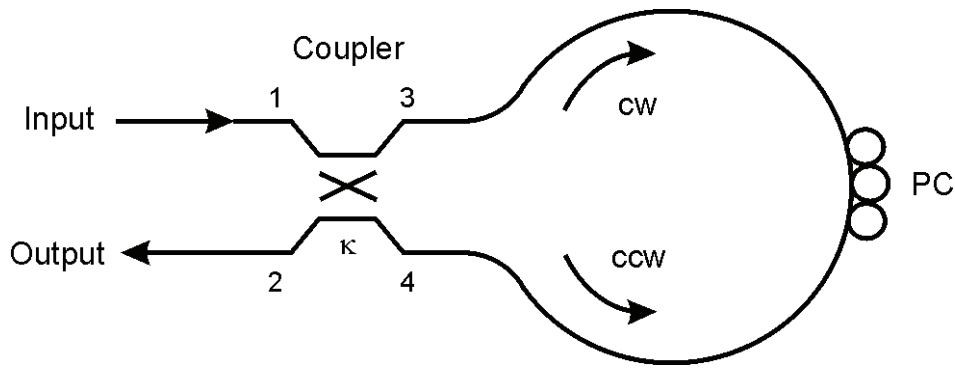


Figure 5.16: Fiber loop mirror. PC: Polarization controller, κ : couplers coupling ratio.

A fiber loop mirror (FLM) consists of a fused fiber coupler whose output ports are spliced together or simply connected by a short single mode fiber link [117]. An input signal into the coupler will be splitted in two counter-propagating waves: one traveling in the clockwise direction (cw) and other in the counterclockwise direction (ccw)

$$\begin{aligned} E_{cw}(t) &= S_{31} \cdot E_0 \cdot e^{j\omega_c t} \\ E_{ccw}(t) &= S_{41} \cdot E_0 \cdot e^{j\omega_c t} \end{aligned} \quad (5.11)$$

where ω_c is the optical carrier frequency, E_0 its amplitude and S_{ij} are the couplers scattering parameters. For a coupling ratio κ the scattering parameters are

$$\begin{aligned} S_{31} &= \sqrt{\kappa} \\ S_{41} &= j\sqrt{1-\kappa} \end{aligned} \quad (5.12)$$

meaning the cross transmission (i.e. S_{41}) has a $\pi/2$ phase shift with respect to the through transmission (i.e. S_{31}).

After traveling through the same fiber they recombine in the same coupler to provide the following outputs at each input port

$$\begin{aligned} E_{out,1}(t) &= S_{13} \cdot E_{ccw}(t) + S_{14} \cdot E_{cw}(t) \\ E_{out,2}(t) &= S_{23} \cdot E_{cw}(t) + S_{24} \cdot E_{ccw}(t) \end{aligned} \quad (5.13)$$

For a 50% symmetrical fiber coupler (i.e. $\kappa=0.5$ and $S_{ij}=S_{ji}$) then all the input optical power will be reflected back to port 1 of the fiber coupler. This theoretical condition is very difficult to achieve in practice, as small polarization misalignments of the counterpropagating waves

occur limiting the suppression. By controlling the polarization states of the signals inside the loop, a variable optical reflector can be realised [117].

Another interesting application which will be described in the next sections is the introduction of a phase changing element inside the loop.

5.2.1 Fiber loop with a phase modulator

Perhaps the most straight-forward and easy way of inducing a phase change is by using the electrooptical Pockels effect. A change in the refractive index of the material used makes the light travel slower and thus produces a phase change. Lithium Niobate (LiNbO_3) materials provide an efficient way of changing the phase using this linear electrooptical effect. For our research a LiNbO_3 phase modulator (PM) UDT PM-1.5-8.0 was used which limits the modulation frequency to approximately 8 GHz. Its V_π is specified to be 14 V but applying this RF drive power the maximum phase change reached was only 0.7π at low frequencies and even less at higher frequencies like 8 GHz (see Appendix A).

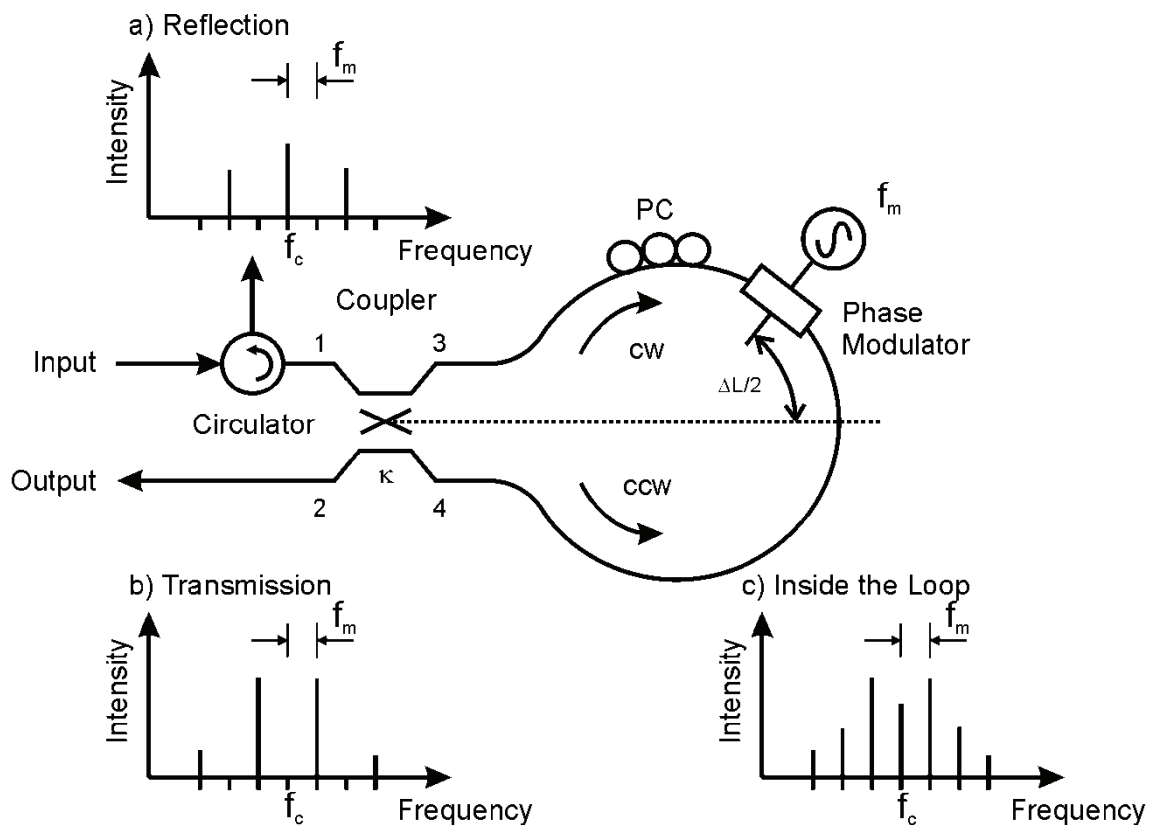


Figure 5.17: Unbalanced fiber loop mirror with phase modulator. Optical intensity spectra a) reflected at the input b) transmitted to the output and c) inside the loop. PC: Polarization controller

By inserting the PM inside the loop as shown in Figure 5.17, the phase of the counterpropagating waves will be modulated at different times, depending on the position of the phase modulator relative to the symmetry axis of the fiber loop [118]. For this case, Eq. (5.11) turns into

$$\begin{aligned} E_{cw}(t) &= S_{31} \cdot E_0 \cdot e^{j[\omega_c t + \pi \cdot m_{ph}^{cw} \cos(\omega_m(t-\tau))]} \\ E_{ccw}(t) &= S_{41} \cdot E_0 \cdot e^{j[\omega_c t + \pi \cdot m_{ph}^{ccw} \cos(\omega_m(t+\tau))]} \end{aligned} \quad (5.14)$$

assuming sinusoidal phase modulation. Here $m_{ph} = V_{RF}/V_\pi$ represents the phase modulation index of the phase modulator for each wave, V_π is the modulators half wave voltage, ω_m is the modulation angular frequency and τ is the half-time delay between the two counterpropagating waves defined by

$$\tau = \frac{n \cdot \Delta L}{2 \cdot c} \quad (5.15)$$

being n the refractive index of the fiber, c the speed of light and $\Delta L/2$ the distance from the symmetry axis of the loop where the modulator is placed.

The right hand part of the exponential in Eq. (5.14) describes an angle modulated signal, which can be expanded in a series of Bessel functions of the first kind of order k . Therefore, we have the Fourier series for the complex exponential as follows

$$e^{j \cdot \pi \cdot m_{ph} \cdot \sin(\omega_m(t \pm \tau))} = \sum_{k=-\infty}^{\infty} J_k(\pi \cdot m_{ph}) e^{\pm jk\omega_m \tau} e^{jk\omega_m t} \quad (5.16)$$

Now the output at port 2 of the fiber coupler changes into a series of the form

$$E_{out,2}(t) = E_0 \cdot \sum_{k=-\infty}^{\infty} A(\omega_m, k) \cdot e^{j(\omega_c + k\omega_m)t} \quad (5.17)$$

with

$$A(\omega_m, k) = S_{23} S_{41} \cdot J_k(\pi \cdot m_{ph}^{ccw}(\omega_m)) \cdot e^{jk\omega_m \tau} + S_{24} S_{31} \cdot J_k(\pi \cdot m_{ph}^{cw}(\omega_m)) \cdot e^{-jk\omega_m \tau} \quad (5.18)$$

The output signal contains all frequency components of the form $f_c \pm kf_m$ for $k=0,1,2\dots$ as described in Eq. (5.17). The amplitude of the sidebands is then proportional to $|A(\omega_m, k)|$ being the amplitude of the optical carrier

$$|A(\omega_m, 0)| = \left| S_{23}S_{41}J_0(\pi \cdot m_{ph}^{ccw}) + S_{24}S_{31}J_0(\pi \cdot m_{ph}^{cw}) \right|. \quad (5.19)$$

Assuming an ideal bidirectional phase modulator (i.e. $m_{ph}^{cw} = m_{ph}^{ccw} = m_{ph}$) and a symmetric fiber coupler (i.e. $S_{24} = S_{31}$ and $S_{23} = S_{41} = j \cdot S_{24}$), then the optical carrier is completely suppressed and Eq. (5.18) turns into

$$A(\omega_m, k) = \frac{J_k(\pi \cdot m_{ph}(\omega_m))}{2} (e^{-jk\omega_m\tau} - e^{jk\omega_m\tau}) \quad (5.20)$$

being

$$|A(\omega_m, k)| \approx 2 \cdot (S_{24})^2 \cdot J_k(\pi \cdot m_{ph}) \cdot \sin(k\omega_m\tau). \quad (5.21)$$

As seen in Eq. (5.21), when $\omega_m\tau = \pi/2$ then the odd spectral components of the frequency spectrum appear at port 2 of the fiber coupler and the even order ones are reflected back to port 1 as depicted in the insets in Figure 5.17.

High speed LiNbO₃ phase modulators usually have long travelling wave electrodes to achieve a near velocity match between the RF microwave and the optical wave [119]-[120]. This is also true for optical MZMs. Therefore they are not suitable for bidirectional operation. In the loop mirror the optical waves are propagating in the same (cw) and in the opposite direction (ccw) as the microwave signal in the modulator resulting in different modulation efficiencies for each optical wave for higher frequencies.

A sample measurement of the forward (cw) and backward (ccw) response of our UDT PM-1.5-8.0 is shown in Figure 5.18. As expected, a huge variation in the phase modulation indices is observed and different slopes are shown through a linear fit slope function (LFS). For frequencies higher than 1 GHz the slope of the modulation index of the ccw propagation is approximately 3.2 times that of the cw direction. From 4 GHz, the modulation index for the ccw direction can be considered to be practically zero. More measurements of the phase modulation index m_{ph} can be found in Appendix A.

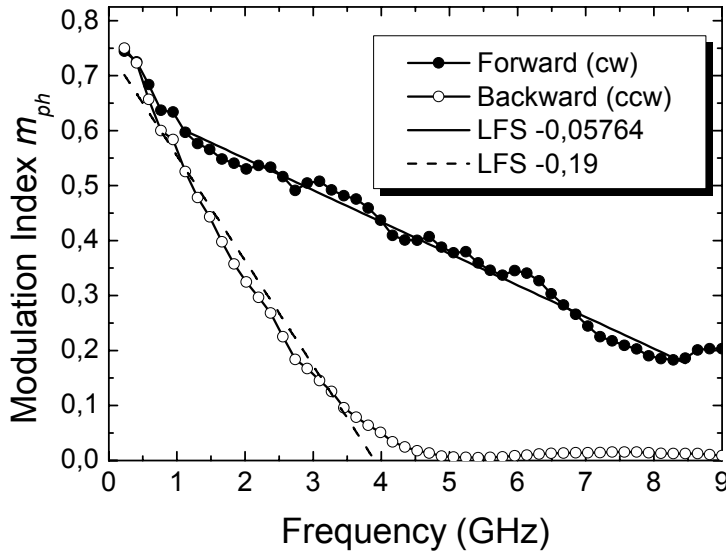


Figure 5.18: Measured modulation index m_{ph} for the cw and ccw waves versus modulation frequency f_m ($P_m = 26$ dBm, $V_\pi = 14$ V, LFS: Linear Fit Slope).

If the phase modulation indices differ for the cw and ccw waves, then the optical carrier in Eq. (5.19) can not be fully suppressed with a 50% fiber coupler (i.e. $\kappa = 0.5$). By replacing Eq. (5.12) in Eq. (5.19) we have a carrier suppression dependency on the couplers coupling ratio κ as follows

$$|A(\omega_m, 0)| = \left| \kappa J_0(\pi \cdot m_{ph}^{cw}) - (1 - \kappa) J_0(\pi \cdot m_{ph}^{ccw}) \right|. \quad (5.22)$$

Figure 5.19a plots the optical carrier versus coupling ratio κ according to Eq. (5.22). For an asymmetrical phase modulator the optical carrier is not completely suppressed by a $\kappa = 0.5$ coupler but the minimum is shifted dependent on the relationship between the cw and ccw phase modulation indices. Taking the data in Figure 5.18, for example, for $f_m = 4$ GHz and $\Delta L = 2$ cm, then the values for the modulation indices are $m_{ph}^{cw} = 0.43$ and $m_{ph}^{ccw} = 0.05$ approximately. For this case the optimal coupling ratio should be $\kappa = 0.626$ (as shown in Figure 5.19a). Figure 5.19b now plots the carrier suppression with respect to the first harmonic which is calculated as follows

$$CS = \frac{|A(\omega_m, 1)|}{|A(\omega_m, 0)|} = \frac{\left| \kappa J_1(\pi \cdot m_{ph}^{cw}) \cdot e^{-j\omega_m \tau} - (1 - \kappa) J_1(\pi \cdot m_{ph}^{ccw}) \cdot e^{j\omega_m \tau} \right|}{\left| \kappa J_0(\pi \cdot m_{ph}^{cw}) - (1 - \kappa) J_0(\pi \cdot m_{ph}^{ccw}) \right|}. \quad (5.23)$$

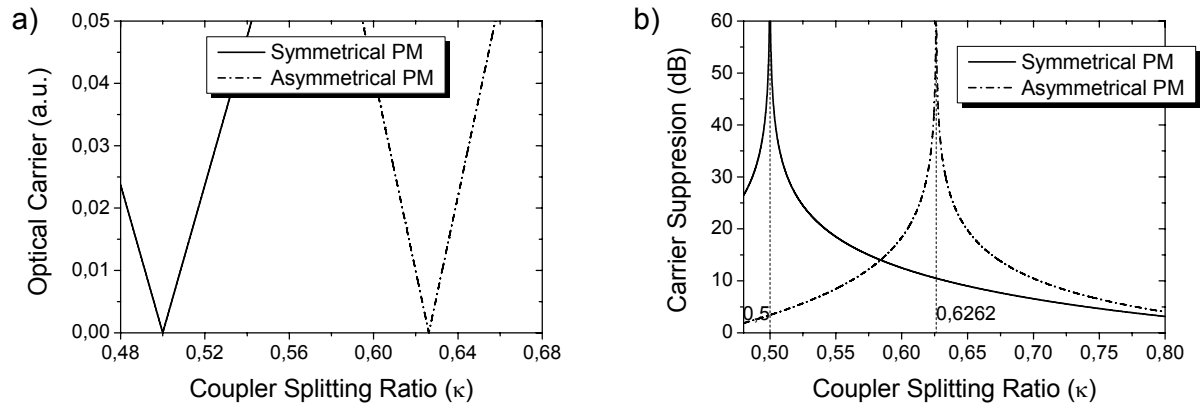


Figure 5.19: a) Optical carrier power and b) carrier suppression versus coupling ratio κ of the coupler for a symmetrical phase modulator ($m_{ph}^{cw} = m_{ph}^{ccw} = 0.43$) and an asymmetrical one ($m_{ph}^{cw} = 0.43$ and $m_{ph}^{ccw} = 0.05$) for a fixed $f_m = 4$ GHz and $\Delta L = 2$ cm.

The variation in coupling ratio is quite significant, 12.6% for our example. Therefore a tuning of the coupling ratio κ of the coupler should compensate the phase modulators lack of bidirectionality and achieve complete carrier suppression.

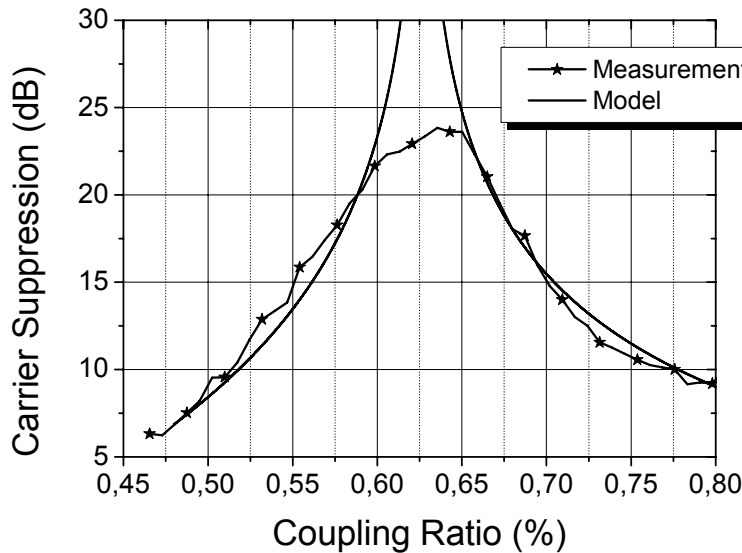


Figure 5.20: Measured electrical carrier suppression CS_{el} versus coupling ratio CR (modulation power $P_m = 26$ dBm, $\Delta L = 2$ cm, $f_m = 4$ GHz).

A temperature controlled tunable coupler was used to make a fiber loop and compare the results from the theory in Figure 5.19b. The phase modulator was placed at $\Delta L = 2$ cm and the

frequency chosen was $f_m = 4$ GHz, so that $m_{ph}^{cw} = 0.43$ and $m_{ph}^{ccw} = 0.05$. The results of the electrical carrier suppression (CS_{el}) from the model and measurements are shown in Figure 5.20. A good agreement from theory and measurements is observed.

Assuming a perfect phase modulator with $m_{ph}^{cw} = m_{ph}^{ccw} = m_{ph}$, the instantaneous phase shift $\Delta\varphi(t)$ between the two optical waves propagating in opposite directions in the fiber loop can be calculated as

$$\Delta\varphi(t) = \pi \cdot m_{ph} \cdot \left\{ \sin(\omega_m(t + \tau)) - \sin(\omega_m(t - \tau)) \right\} = -2 \cdot \pi \cdot m_{ph} \cdot \sin(\omega_m\tau) \cdot \cos(\omega_m t). \quad (5.24)$$

With a coupling ratio of $\kappa = 0.5$ of the fiber coupler, the intensity transmission ($T(t)$) at the output and reflection ($R(t)$) at the input of the loop mirror are given by

$$\begin{aligned} T(t) &= \frac{1}{2} \cdot [1 - \cos(\Delta\varphi(t))] = \frac{1}{2} \cdot [1 - \cos(\Delta\phi_m \cdot \cos(\omega_m t))] \\ R(t) &= \frac{1}{2} \cdot [1 + \cos(\Delta\varphi(t))] = \frac{1}{2} \cdot [1 + \cos(\Delta\phi_m \cdot \cos(\omega_m t))] \end{aligned} \quad (5.25)$$

with $\Delta\phi_m = 2 \cdot \pi \cdot m_{ph} \cdot \sin(\omega_m\tau)$.

Expanding Eq. (5.25) in a series of Bessel functions results in

$$\begin{aligned} T(t) &= \frac{1 - J_0(\Delta\phi_m)}{2} - \sum_{k=1}^{\infty} (-1)^k J_{2k}(\Delta\phi_m) \cdot \cos(2k\omega_m t) \\ R(t) &= \frac{1 + J_0(\Delta\phi_m)}{2} + \sum_{k=1}^{\infty} (-1)^k J_{2k}(\Delta\phi_m) \cdot \cos(2k\omega_m t). \end{aligned} \quad (5.26)$$

The output signal intensity contains spectral components with frequencies of $2kf_m$ with $k = 1, 2, \dots$. For that reason at the output of the loop mirror a DSB-SC signal with sidebands at $f_c \pm kf_m$ is generated. This optical signal is tolerant to the chromatic dispersion of the fiber and a low phase noise microwave signal at the base station can be generated because the optical sidebands are correlated [121].

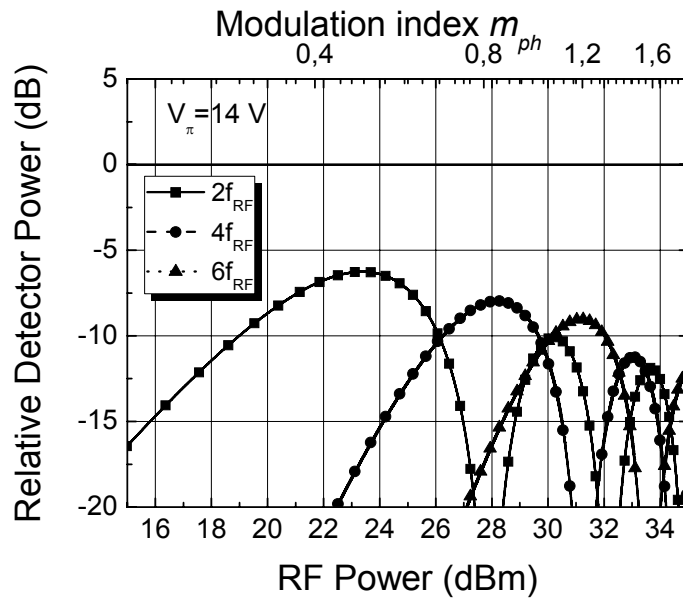


Figure 5.21: Simulated photonic link response of the fiber loop with a phase modulator versus input RF drive power ($V_\pi = 14$ V, $f_m = 1$ GHz, $\Delta L = 1$ cm).

Figure 5.21 shows the calculated photonic link response for the harmonics $n = 2, 4$ and 6 for a perfect fiber loop mirror with a phase modulator and no insertion loss for the coupler and phase modulator. The modulation frequency is chosen to be $f_m = 1$ GHz and the phase modulator is placed with $\Delta L = 1$ cm inside the loop so that $\omega_m \tau \approx \pi/2$. From the datasheet of the phase modulator V_π is reported to be 14 V. The response is similar to the MZM case described in section 5.1.1 but with lower efficiency. The optimum RF drive powers vary greatly with the half-wave voltage V_π of the phase modulator and as shown in Figure 5.18 the modulation index, and consequently the V_π of the phase modulator, are not constant over the whole operating frequency range for constant RF drive power. The optimum $\Delta\phi_m$ can be calculated from Eq. (5.26) and are displayed in Table 5.2 for different harmonics generation. For the case where $\omega_m \tau \approx \pi/2$, then $m_{ph} = \Delta\phi_m/2\pi$, providing the lowest phase modulation index possible.

$n =$	2	4	6	8	10
$\Delta\phi_m =$	3.08	5.34	7.54	9.68	11.75
m_{ph}	0.49	0.85	1.2	1.54	1.87

Table 5.2: Optimal $\Delta\phi_m$ for n^{th} harmonic generation and m_{ph} for $\omega_m \tau \approx \pi/2$.

Comparing the values of m_a in Table 5.1 with m_{ph} proves that this method is more efficient if both modulators have the same V_π for the case $\omega_m \tau \approx \pi/2$. The modulation index required for the fiber loop method is half the one required for the MZM approach. This originates in the argument of the Bessel functions in Eq. (5.7) and Eq. (5.26). Nonetheless, the relative detector power for this method is 6 dB lower than that of the MZM case. Also this analysis doesn't take into account the variations of V_π with modulation frequency f_m and the most important issue shown in Figure 5.18 which is the poor bidirectionality of high speed LiNbO₃ phase modulators.

This whole analysis is also valid for uncorrelated optical source signals when the optical path length differences are less than the coherence length of these signals. An amplified spontaneous emission (ASE) source, like the power spectrum of an erbium doped fiber amplifier (EDFA) with no input signal can be described through a Fourier decomposition of each noise term [122]. Considering an amplifier with unity coupling efficiency, uniform gain G and bandwidth B centered around ω_c , the electric field can be written as a sum of cosine terms spaced δf apart in frequency

$$E_{sp}(t) = \sum_{k=(-B/2\delta f)}^{B/2\delta f} \sqrt{2n_{sp}(G-1)hf_{opt}\delta f} \cos((\omega_c + 2\pi k\delta f)t + \Phi_k), \quad (5.27)$$

where n_{sp} is the inversion parameter and Φ_k is a random phase for each component of spontaneous emission. The bandwidth of the ASE at the output of an EDFA is approximately $\Delta\lambda = 30$ nm. Therefore the coherence length of the field is $l_c = 79$ μm assuming a rectangular intensity spectral density. Thus ASE light can interfere coherently if the distance l_c is much greater than all optical path differences encountered. As both cw and ccw waves travel *exactly* the same optical path in the fiber loop, heterodyning of ASE in a photodiode is possible [123]. The complex amplitudes of the counter propagating waves now take the form

$$E_N^{cw}(t) = S_{31} \cdot E_0 \cdot \sum_{k=-M}^M \cos\left[(\omega_c + 2\pi k\delta\nu)t + \Delta\phi_m^{cw} \cdot \sin(\omega_m(t - \tau)) + \Phi_k\right] \quad (5.28)$$

and

$$E_N^{ccw}(t) = S_{41} \cdot E_0 \cdot \sum_{k=-M}^M \cos\left[(\omega_c + 2\pi k\delta\nu)t + \Delta\phi_m^{ccw} \cdot \sin(\omega_m(t + \tau)) + \Phi_k\right], \quad (5.29)$$

where $M = B_0 / 2\delta\nu$.

The output current $i(t)$ from the photodetector is proportional to the intensity

$$i(t) = \frac{q}{hf_{opt}} \left[E_N^{cw}(t) + E_N^{ccw}(t) \right]^2, \quad (5.30)$$

averaging over all optical frequencies. Here q is the electron charge, h planck's constant and f_{opt} the optical frequency.

Due to the fact that the optical path length differences in the loop and all other components are less than the coherence length for this signals, the output current contains spectral components with frequencies of kf_m with $k = 1, 2, \dots$. Not only the generation of a microwave signal with the fundamental frequency f_m is possible, but also the upconversion by using higher order spectral components.

For experimental verification various fiber loops with different length differences ΔL were realized. By sweeping the modulation frequency f_m a periodical behavior of the amplitude of the harmonics in dependency of $\omega_m\tau$ (and thus ΔL , the position of the phase modulator inside the loop) is obtained according to Eq. (5.21). The maxima and minima of this function are placed at

$$f_{\min} = k \cdot \frac{c}{n\Delta L} \quad (5.31)$$

$$f_{\max} = \left(k + \frac{1}{2} \right) \cdot \frac{c}{n\Delta L} \quad (5.32)$$

for $k = 0, 1, 2, \dots$

Figure 5.22 shows the transfer function in transmission of the fiber loop for the generated mm-wave signal at $2f_m$ for two fiber loops, one with $\Delta L = 83$ cm and another one with $\Delta L = 25$ cm. Simulations were carried out according to Eq. (5.26) using a constant modulation index $m_{ph} = 0.32$. The measurements pose a good agreement with the simulations except for the efficiency drop for higher modulation frequencies. This is mainly caused by the phase modulation index drop from the phase modulator itself, but also due to the different phase modulation indices in the cw and ccw propagation direction (see Figure 5.18).

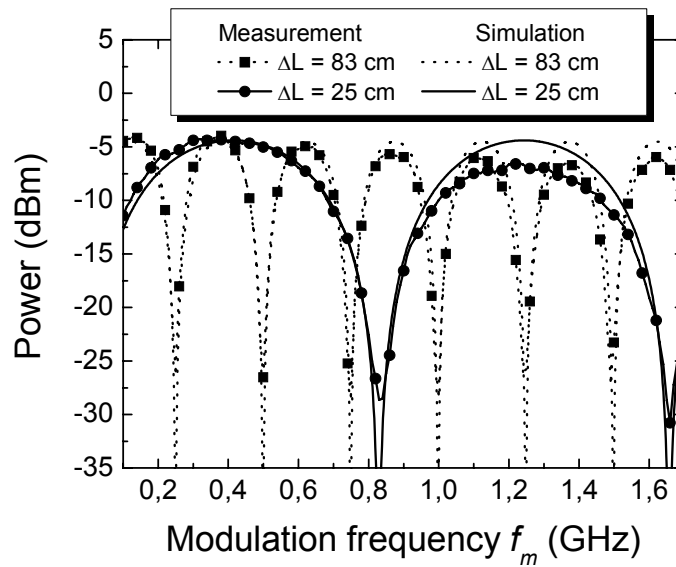


Figure 5.22: Power transfer function of the fiber loop for the spectral component at $2f_m$ for different ΔL ($P_m = 20$ dBm, $m_{ph} = 0.32$ for simulations).

If the measured values for $m_{ph}^{cw}(f_m)$ and $m_{ph}^{ccw}(f_m)$ are used in Eq. (5.21) of our model a good agreement between simulation and experiment is obtained. For a fiber loop with $\Delta L = 60$ cm the results for the spectral component $2f_m$ are shown in Figure 5.23.

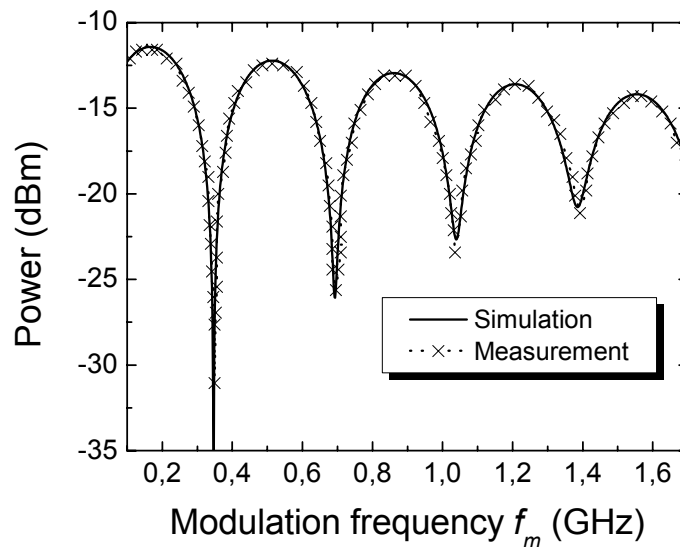


Figure 5.23: Simulated and measured power transfer function of the fiber loop for the spectral component at $2f_m$ based on the extracted phase modulation indices m_{ph} of the modulator ($P_m = 20$ dBm, $\Delta L = 60$ cm).

The measurement of the minima is straightforward from the frequency sweep and provides an estimation of ΔL . By manipulating Eq. (5.31) for two adjacent minima we obtain

$$\Delta L = \frac{c}{n\Delta f_{\min}}. \quad (5.33)$$

Moreover, to increase the bandwidth of the system, the minima should be placed farther apart. This results in ΔL being small i.e. the phase modulator should be placed slightly off the symmetry axis of the loop. For this purpose, a loop with $\Delta L = 2$ cm was realized and the results of the frequency sweep up to 10 GHz are shown in Figure 5.24 for the components f_m and $2f_m$ as well as the electrical carrier suppression when using a laser source as well as for the ASE source variant.

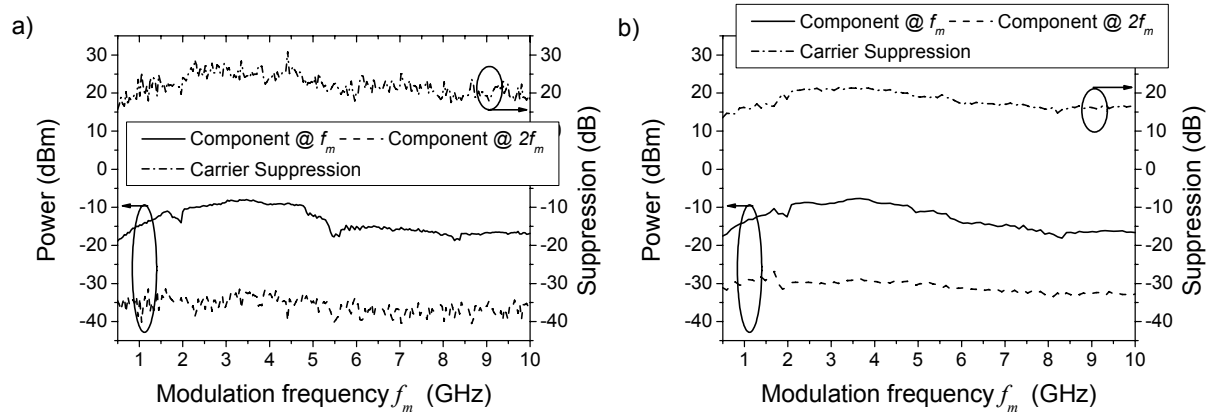


Figure 5.24: Transmission of the fiber loop as a function of modulation frequency ($P_m = 20$ dBm, $\Delta L = 2$ cm) with a) a laser source and b) ASE source.

The variations of the amplitude of the electrical carrier at f_m in Figure 5.24a are caused by random changes in the polarization of the cw and ccw waves inside the fiber loop and by the different modulation indexes that the cw and ccw waves experience at the phase modulator. Nonetheless the electrical carrier suppression (right axis in Figure 5.24a) remains more than 20 dB for most of the measurement range when using a laser source. For the ASE case depicted in Figure 5.24b, polarization effects don't play an important role as the light source can be considered unpolarized. However, the carrier suppression is not as good as in the previous case, reaching the 20 dB mark for a finite frequency band.

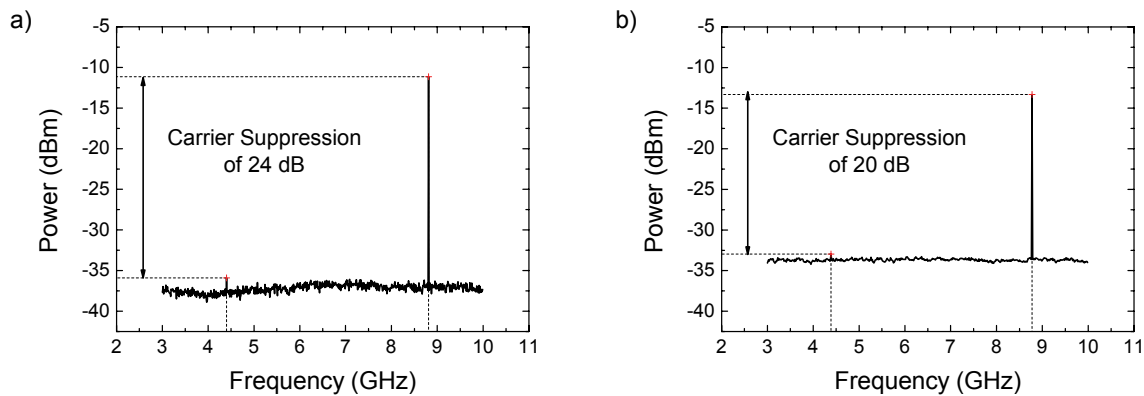


Figure 5.25: Electrical frequency spectrum of the output signal ($P_m = 20$ dBm, $f_m = 4.4$ GHz) with a) a laser source and b) an ASE source.

The electrical spectrum for a modulation frequency f_m of 4.4 GHz is shown in Figure 5.25. After tuning the polarization inside and outside the loop an electrical carrier suppression of $CS_{el} = 24$ dB was achieved. This can be calculated from Eq. (5.23). Using the data collected in Figure 5.18 for the phase modulator and the scattering matrix of the coupler used, an electrical carrier suppression of approximately 24 dB was estimated. The phase noise of an electrical carrier characterizes its stability. For the optically generated signal with $2f_m = 10$ GHz the measured single sideband phase noise is shown in Figure 5.26.

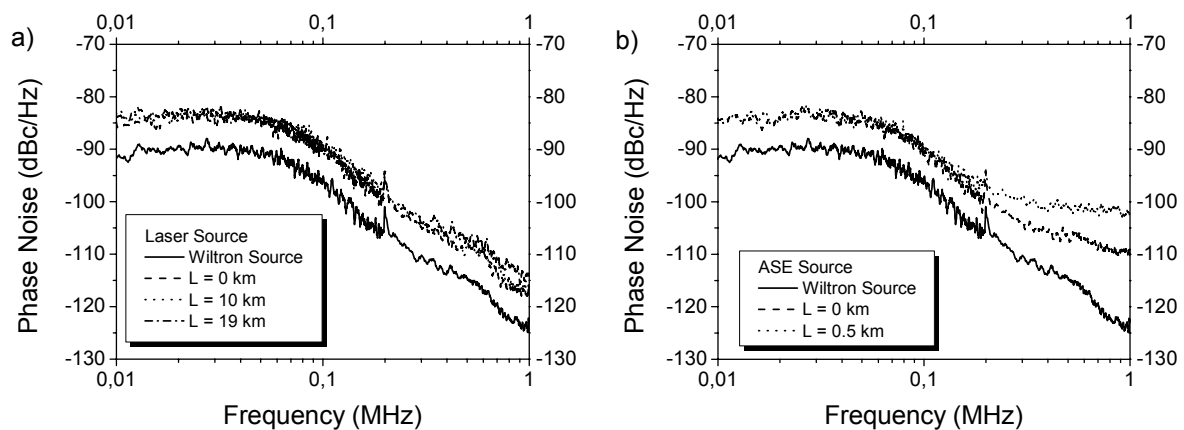


Figure 5.26: Phase noise measurement of the source synthesizer and microwave signal for different transmission lengths L with a) a laser source and b) an ASE source ($P_m = 26$ dBm, $f_m = 5$ GHz).

As a reference the phase noise of the synthesizer at $f_m = 5$ GHz is shown in the lower trace. Figure 5.26a shows the phase noise for the fiber loop using a laser source. The curves are

separated by approx. 6 dB which is the theoretical expected value for a frequency doubling scheme [115] for all transmission lengths used. In Figure 5.26b the results for a fiber loop using an ASE source are depicted. Up to an offset frequency of roughly 0.1 MHz the curves exhibit the expected 6 dB difference, but then the generated frequency component at $2f_m$ reaches a phase noise floor which increases when 500 m of single mode fiber were inserted due to decorrelation in the fiber link.

The generation of microwave signals with a fiber loop and a phase modulator has nearly no influence on the phase stability of the signal when a laser source is used. Even after transmission over $L = 19$ km of SMF there is no significant penalty observed. On the other hand, using an ASE source shows severe phase noise degradation due to decorrelation which would affect data transmission performance, especially in phase modulation formats such as PSK and multilevel formats such as QAM. Nonetheless, a link with $L = 2$ km SMF was tested and no signal was detected, so that the power fade-off of this scheme is the limiting factor, and not its phase noise performance. The efficiency of this scheme with an ASE source is strongly dependent on the optical bandwidth used, being the main limiting factor the bandwidth of the components inside the loop (i.e. the phase modulator's optical bandwidth). Tests were carried out by optically slicing the ASE spectrum with an FBG and that results in a very poor efficiency. Furthermore, the use of an ASE source hinders the utilization of this scheme in a WDM scenario, thus the application with a laser source is preferred.

5.2.2 Fiber loop with a semiconductor optical amplifier

Another way of generating the phase difference inside the loop is by using a non-linear element like a semiconductor optical amplifier (SOA). A cross-phase modulation (XPM) effect accompanies cross-gain modulation (XGM) when two optical signals are simultaneously present in a SOA [124]. XPM in SOAs applied in an interferometric configuration has been used for all-optical wavelength conversion [125]-[127], optical demultiplexing [128]-[130] and for optical clock recovery [131]. All of these schemes operate the SOA as a nonlinear element, where generally a π phase shift is desired. For our application, the XPM effect will be driven in the linear regime and thus used for the generation of a DSB-SC signal in a setup similar to the one described in the previous section.

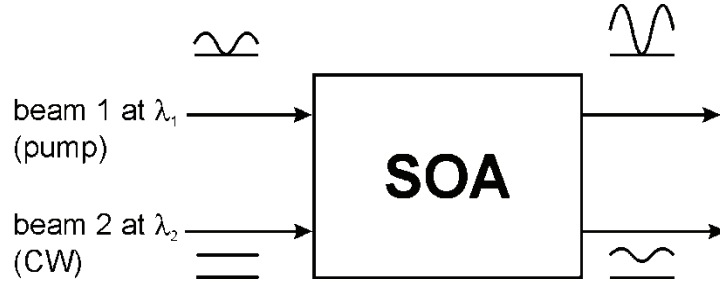


Figure 5.27: Cross-gain modulation in SOAs.

When two optical fields are incident on the same facet of a SOA, as shown in Figure 5.27, the modulation of the amplifier gain caused by optical amplification of λ_1 imparts a modulation onto the other beam at λ_2 . The carrier density $N_{cd}(z,t)$ in the SOA evolves in time as [132]

$$\frac{\partial N_{cd}}{\partial t} = \frac{J}{ed} - R(N_{cd}) - \sum_i (N_{cd} - N_{t,i}) \frac{\Pi_i}{E_{sat,i}} \quad (5.34)$$

where the summation is over the beams present in the device. Π_i are the instantaneous powers, J the injected current density, d the active layer thickness and q the electronic charge. $R(N)$ is the spontaneous recombination rate given by $R(N_{cd}) = A_{nr}N_{cd} + BN_{cd}^2 + CN_{cd}^3$, the three terms accounting for defect, radiative spontaneous and Auger recombination respectively. The gain for beam i (at wavelength λ_i) is described by $a_i(N_{cd} - N_{t,i})$ and the saturation energy E_{sat} is given by

$$E_{sat,i} = \frac{A\hbar\omega_i}{a_i\Gamma} \quad (5.35)$$

where A is the active region area and Γ the mode confinement. The propagation of optical power in the amplifier is governed by

$$\frac{\partial \Pi_i}{\partial z} = [\Gamma a_i (N_{cd} - N_{t,i}) - \alpha_{int}] \Pi_i \quad (5.36)$$

where α_{int} is the internal loss.

If there is a large saturating power in one of the optical beams and a small modulation imposed on it, then the optical power can be written as $\Pi_i = P_i + p_i$, denoting the steady state and perturbing signals respectively. The carrier density is now $N_{cd} = N_0 + n_{cd}$ and substituting in Eq. (5.34) for the steady state we have

$$0 = \frac{I}{qV} - R(N_0) - \sum_i (N_0 - N_{t,i}) \frac{P_i}{E_{sat,i}} \quad (5.37)$$

and for the small signal

$$\frac{\partial n_{cd}}{\partial t} = -\frac{n_{cd}}{\tau_c} - \sum_i \frac{(N_0 - N_{t,i}) p_i + n_{cd} P_i}{E_{sat,i}}. \quad (5.38)$$

The small signal lifetime is given by $1/\tau_c = \partial R/\partial N_{cd} \approx A_{nr} + 2BN_0 + 3CN_0^2$. For the case of sinusoidal variation with time at angular frequency ω , then

$$n_{cd} = \frac{-\sum_i (N_0 - N_{t,i}) \frac{P_i}{E_{sat,i}}}{1/\tau_c + \sum_i 1/\tau_{s,i} + j\omega} \quad (5.39)$$

where the contribution to the lifetime of the stimulated emission by each beam is given by $1/\tau_{s,i} = P_i/E_{sat,i}$ and consequently varies with z , the position inside the SOA.

The behavior of the steady-state optical power in the beams is governed by

$$\frac{\partial P_i}{\partial z} = \left[\Gamma a_i (N_0 - N_{t,i}) - \alpha_{int} \right] P_i \quad (5.40)$$

and the small signal propagation is given by

$$\frac{\partial p_i}{\partial z} = \left(\Gamma a_i (N_{cd} - N_{t,i}) - \alpha_{int} \right) p_i + \Gamma a_i n P_i. \quad (5.41)$$

The magnitude of the perturbation to the carrier density is given by n_{cd} in Eq. (5.39) and shows the response of the carriers due to the amplification of the perturbing beam which has a roll-off with a 3 dB frequency of $\sqrt{3}/2\pi\tau_{eff}$ being

$$1/\tau_{eff} = 1/\tau_c + \sum_i 1/\tau_{s,i}. \quad (5.42)$$

It would appear that this high frequency limit applies to XGM (and therefore to XPM). However, higher bandwidths than the ones imposed in Eq. (5.39) are achieved in practice due to the removal of the gain compression as the carrier population cannot follow the pump light variation [132].

The rate equations governing XGM in SOAs (i.e. Eq. (5.37)-(5.41)) can be numerically solved, but an analytic solution can be found for the case of wavelength conversion. Assuming that the CW intensity of the probe at wavelength λ_1 is smaller than the CW portion of the pump at λ_2 , then the conversion efficiency from pump (λ_2) to probe (λ_1) in the SOA is given by [132]

$$\eta_{conv} = \left| \exp \left(\frac{-g_0 L}{\tau_{s,2}/\tau_c + 1 + j\omega\tau_{s,2}} \right) - 1 \right| \quad (5.43)$$

where g_0 is the gain per unit length and L the length of the SOA. Eq. (5.43) reveals why an estimate of the bandwidth based on the carrier modulation bandwidth from Eq. (5.39) is misleading. The frequency response of the wavelength conversion mechanism (i.e. XGM) is based on a combination of the device gain and the stimulated and spontaneous lifetimes.

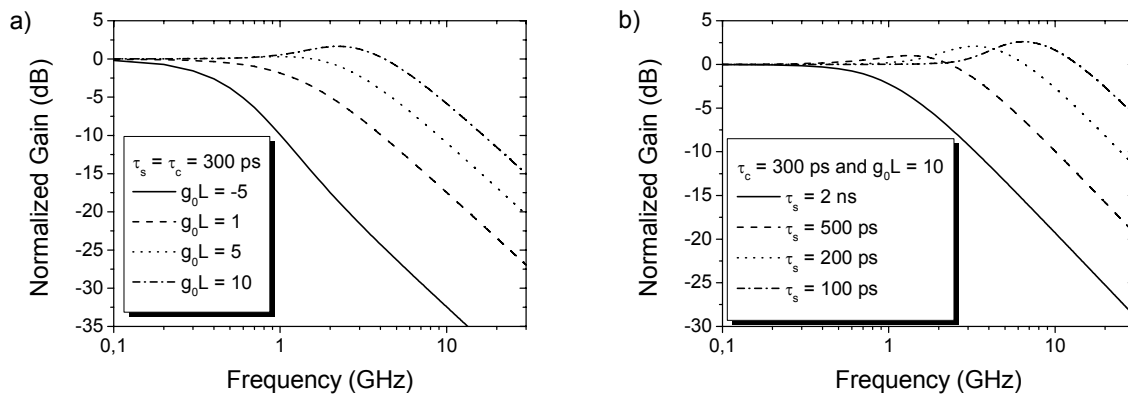


Figure 5.28: Normalized conversion efficiency of XGM versus modulation frequency f_m for a) different gains g_0L and b) stimulated carrier lifetimes $\tau_{s,2}$. Spontaneous carrier lifetime is $\tau_c = 300$ ps in all curves.

Although the parameters g_0L , τ_c and $\tau_{s,2}$ are inter-related in a real SOA, they will be set independently for illustration purposes. Figure 5.28 shows the frequency response for gain and stimulated carrier lifetime parametrization for a spontaneous carrier lifetime $\tau_c = 300$ ps. First of all, increasing the device gain g_0L or the stimulated carrier lifetime τ_s will increase the

XGM bandwidth. Furthermore, resonant peaks can be formed due to the exchange of light of the two beams, which was experimentally verified in [133].

Two SOAs were available for characterization: one commercially available from Covega and a second one custom designed from the University of Karlsruhe. More data on the SOAs can be found in Appendix C. Figure 5.29 shows the measured frequency response of the output probe beam against modulation frequency of the input pump beam. For the SOA from Covega a bias current $I_{bias} = 500$ mA was used. From CW measurements of the same amplifier, the measured saturation power is $P_{sat} = 9.4$ dBm. Using a spontaneous carrier lifetime $\tau_c = 300$ ps, the saturation energy is $E_{sat} = P_{sat} \cdot \tau_c = 2.61 \cdot 10^{-12}$ J. The optical power of the probe was -10 dBm, then the carrier lifetime due to stimulated emission is $\tau_s = 26.13$ ns. The small signal gain was 22 dB, then $g_0 L = 4$. Substituting these values into Eq. (5.43) produces the solid line in Figure 5.29. The theory matches the experimental results quite well. The 3-dB bandwidth of the XGM effect is measured to be about 1.66 GHz for this SOA.

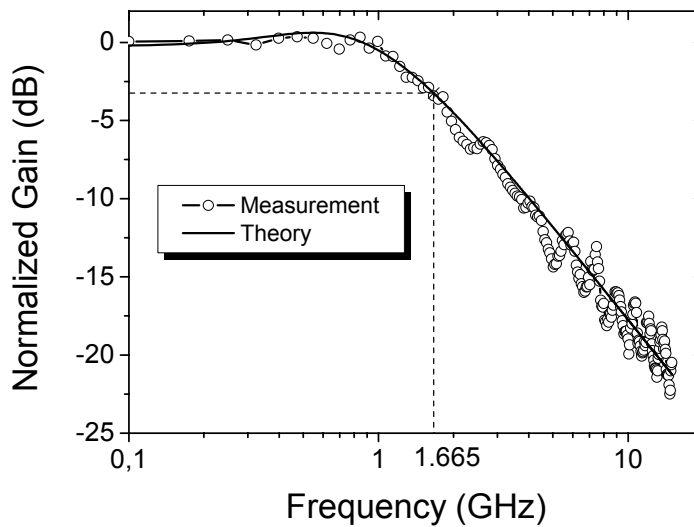


Figure 5.29: Conversion efficiency of XGM versus modulation frequency f_m for the SOA from Covega (modulation power $P_m = 17$ dBm).

A popular way to describe the refractive index behavior (and thus the phase modulation) makes use of the α -factor, also called linewidth enhancement factor. Moreover, the α -factor relates the changes of the active layer refractive index to the changes of the material gain, when the carrier density is varied. As the refractive index change depends mainly on the modulation of the carrier density in the SOA (that is why XGM and XPM are associated), it

would be interesting to have an expression linking the SOA phase to gain variations at the device output. Thus an effective α -factor (α_{eff}) is introduced in the literature as [134]

$$\alpha_{eff} = -2 \frac{\Delta\phi_{out}}{\Delta g} = -2 \frac{\Delta\phi}{\ln\left(\frac{\Delta P_{out}}{P_{in}}\right)} \quad (5.44)$$

where $\Delta\phi$ is the phase variation introduced, Δg the corresponding gain variation and ΔP_{out} the output power variation associated with Δg when the input signal power is P_{in} . The exact expression for α_{eff} is quite complicated, involving effects such as carrier heating, spectral hole burning, two photon absorption, etc. which are beyond the scope of this thesis. Eq. (5.44) is correct only when the probe beam is CW and Δg is induced by a bias current modulation or by an input power variation of a second optical beam (i.e. a pump laser). Its utility is that, for a signal whose dynamics are much slower than the carrier heating dynamics (in the ps order), the temporal phase evolution can be easily calculated using Eq. (5.44) once the gain variation at the SOA output versus time is known. But this approach has its limitations, as α_{eff} depends on parameters which vary by changing the SOA operation condition. This means that α_{eff} is practically of use when wide (some tens of ps or more) optical pulses are injected in the SOA or when its bias current is modulated. Generally the electrodes that supply the bias current to the SOA are not designed for RF performance, limiting the modulation frequencies to some MHz. That is why the setup with a pump laser is chosen as shown in Figure 5.31.

The same setup for the XGM bandwidth is used to measure the phase modulation index m_{ph} generated by XPM and is explained in detail in Appendix B. The frequency resolution of the optical spectrum analyzer dictates the minimum modulation frequency which can be resolved for the measurement. In our case, the optical resolution of the Advantest Q8384 of 10 pm would let resolve peaks which are theoretically 1.25 GHz apart but in practice we could start measuring from 2 GHz. As XPM is linked to XGM through α_{eff} as described in Eq.(5.44), which is constant for a SOA operating condition independent on the modulation frequency f_m , a similar behavior like XGM can be expected. Therefore from the previous measurements, the phase modulation index m_{ph} can be approximated as a constant value up to $f_m = 1.2$ GHz and then it rolls off as an exponential function (i.e. constant slope in the logarithmic x axis). The results for forward (cw) and backward (ccw) propagation for different bias currents are shown

in Figure 5.30 with the corresponding fit for lower frequencies. The fit curves indicate that for lower frequencies much higher modulation indexes can be achieved than with the previous phase modulator. Moreover, the forward and backward operation of the SOA produces identical modulation indexes, simplifying the model equations for the fiber loop. Nonetheless, the modulation index rolls off at higher frequencies, limiting the useful application of these scheme to values of f_m around 4-5 GHz.

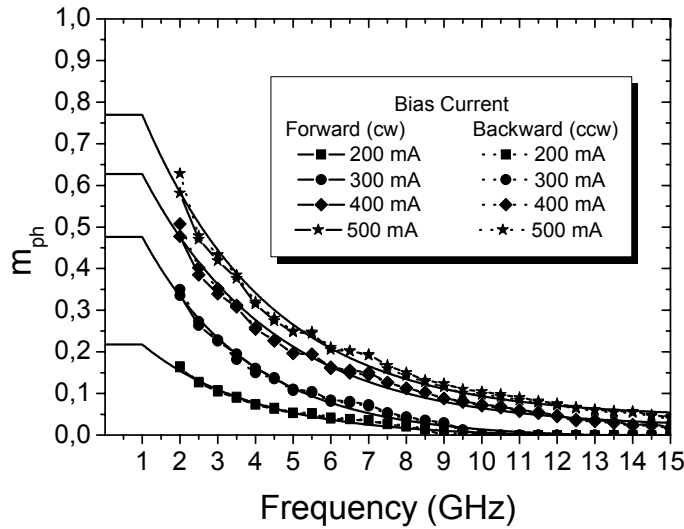


Figure 5.30: Phase modulation index m_{ph} for XPM versus modulation frequency f_m (Covega SOA, $P_m = 17$ dBm, $P_{probe} = -10$ dBm, $P_{pump} = 2.5$ dBm).

A SOA is placed $\Delta L/2$ from the symmetry axis of the fiber loop and the XPM is induced by a modulated pump laser, inserted via another coupler into the loop (Figure 5.31) and filtered out by a Fiber Bragg Grating (FBG) afterwards at the output [135]. The analysis is analogous to that in section 5.2.1, but now the counter propagating waves suffer both gain and phase changes due to XGM as well as the desired XPM effect. The complex amplitudes of the waves in (5.14) take the form

$$\begin{aligned}
 E_{cw}(t) &= S_{31} \cdot G_{cw}(t) \cdot E_0 \cdot e^{j[\omega_c t + \pi \cdot m_{ph}^{cw} \cdot \sin(\omega_m(t-\tau))]} \\
 E_{ccw}(t) &= S_{41} \cdot G_{ccw}(t) \cdot E_0 \cdot e^{j[\omega_c t + \pi \cdot m_{ph}^{ccw} \cdot \sin(\omega_m(t+\tau))]}
 \end{aligned}
 \tag{5.45}$$

where ω_c is the frequency of the probe light source, f_m is the modulation frequency applied to the the pump laser, m_{ph} is the phase modulation index, G represents the gain introduced by the SOA each different for cw and ccw propagation respectively. The phase modulation of the ccw wave is delayed by 2τ with respect to the cw wave.

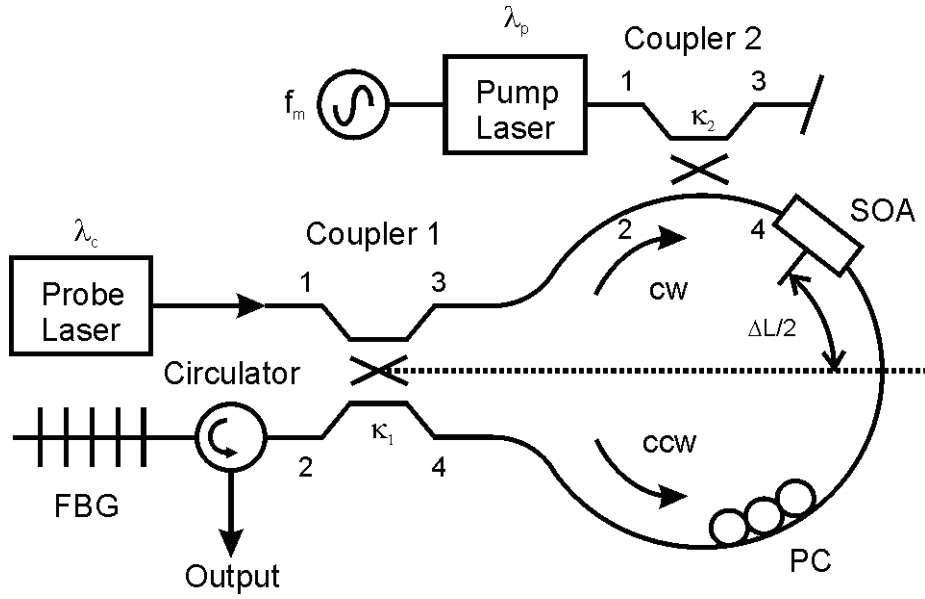


Figure 5.31: Unbalanced fiber loop mirror with SOA. PC: Polarization controller, FBG: Fiber Bragg Grating.

The transfer function of the loop for transmission now takes the form [136]

$$T(t) = \frac{1}{4} \left(G_{cw}(t-\tau) + G_{ccw}(t+\tau) - 2\sqrt{G_{cw}(t-\tau) \cdot G_{ccw}(t+\tau)} \cos(\Delta\phi(t) - \phi_0) \right) \quad (5.46)$$

where $\Delta\phi(t) = \phi_{cw}(t-\tau) - \phi_{ccw}(t+\tau) = m_{ph}^{cw} \sin(\omega_m(t-\tau)) - m_{ph}^{ccw} \sin(\omega_m(t+\tau))$. In these equations, G and ϕ are the gain and phase of the data signal, τ the loop asymmetry and ϕ_0 a static phase change. A control of the polarization states of the waves entering the SOA should be done to ensure maximum XPM of the two waves, but as the SOA used in our experiments is polarization insensitive, the only use of the polarization controllers inside the loop is to ensure maximum interference of the counter propagating waves in coupler 1. Using the Fourier series for the complex exponential from (5.16) and for the sake of simplicity we consider a symmetric 50% coupler, i.e. $\kappa = 0.5$, $S_{24} = S_{31} = \sqrt{\kappa}$ and $S_{23} = S_{41} = j \cdot S_{24}$, also $G_{cw} = G_{ccw} = G$, $\Delta g_{cw} = \Delta g_{ccw} = 0$ and $m_{ph}^{cw} = m_{ph}^{ccw} = m_{ph}$, then the complex amplitude at the output port is

$$E_{perf}(t) = G \cdot e^{j\omega t} \cdot \left(j \cdot \sum_{k=-\infty}^{\infty} \sin(k\omega_m\tau) J_k(m_{ph}) \right). \quad (5.47)$$

For $k = 0$ (i.e. the carrier) the field is zero. When $\omega_m \tau = \pi/2$ then the odd spectral components of the frequency spectrum appear at the output port and the even ones are reflected to port 1 of the loop mirror. Thus at the output of the loop a DSB-SC signal with sidebands at $f_c \pm kf_m$ is generated. The same kind of RF response is obtained for this case as in section 5.2.1. The use of a SOA has two main advantages: it generates gain inside the loop (20-25 dB optical gain) and the phase modulation index m_{ph} that can be achieved is higher than with commercial phase modulators. Popular LiNbO₃ modulators achieve a refraction index change Δn in the order of 10^{-6} to 10^{-4} caused by the Pockels-effect in the waveguide [137]. On the other hand, SOAs can achieve a $\Delta n = 2 \cdot 10^{-3}$ for $P = P_{sat}/10$ [124], that is one order of magnitude more. Higher pump powers can induce larger refractive index changes at the cost of reduced optical gain.

The experimental setup was shown in Figure 5.31 plus some additional elements, such as a variable delay line inside the loop to fine tune the delay τ between the two waves. The pump laser is externally modulated by a 10 Gbit/s modulator from JDSU which limits the modulation frequency f_m to 15 GHz. The RF spectrum corresponding to a modulation frequency f_m of 15 GHz is shown in Figure 5.32. The upconversion to $2f_m = 30$ GHz with an electrical carrier suppression of more than 25 dB is achieved.

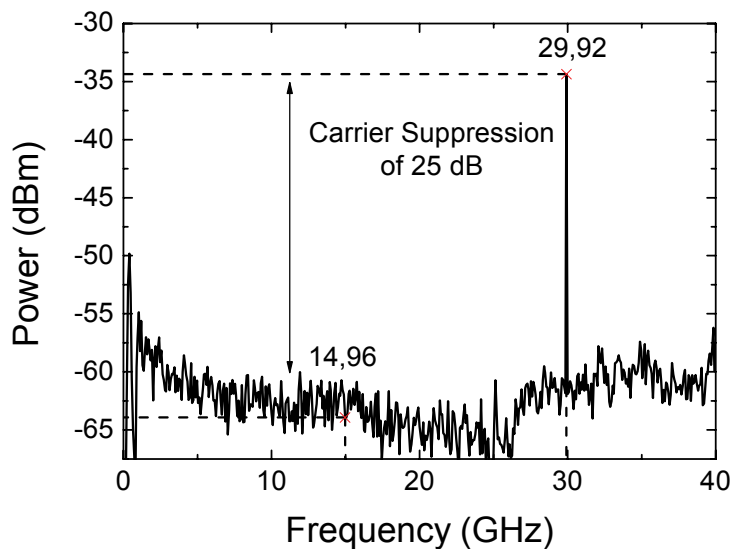


Figure 5.32: Electrical frequency spectrum of the output signal with a modulation frequency $f_m = 15$ GHz after 100 averages ($P_m = 20$ dBm, $\lambda = 1550$ nm, $\Delta L = 8$ cm).

The RF upconversion response of the setup is measured by varying the modulation frequency f_m up to 15 GHz and detecting the optical signal with a fast photodiode (NEL-KPD1510). For a fiber loop with $\Delta L = 8$ cm (i.e. $\tau = 330$ ps) and biasing the SOA from with $I_{bias} = 500$ mA, the results for the spectral component $2f_m$ are shown in Figure 5.33. Simulations were carried out in VPI for comparison purposes. The measured curves present a good agreement with the proposed fiber loop model taking into account the exponential decay of the modulation index m_{ph} due to the SOAs XPM effect. The SOA model in VPI is a transmission line model (the same used to model semiconductor lasers), being the only difference the use of anti-reflection coated facets, which is only a simple redefinition of the laser parameters.

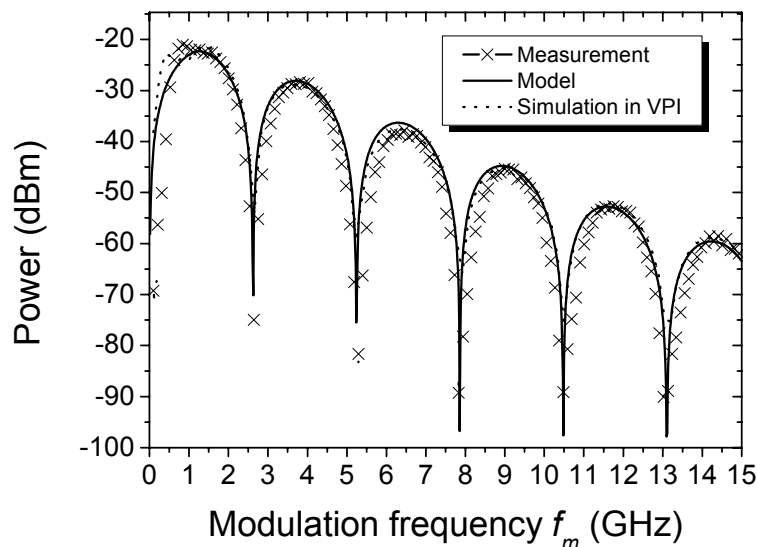


Figure 5.33: Simulated and measured power transfer function of the fiber loop for the spectral component at $2f_m$ ($P_m = 17$ dBm, $\Delta L = 8$ cm, $I_{bias} = 500$ mA).

The SOA from Covega is optimized for system performance, exhibiting a huge bandwidth of approximately 60 nm and a poor nonlinear performance as the maximum modulation index achieved was 0.76. Another SOA from the University of Karlsruhe was available for comparison. This SOA was designed for nonlinear operation and has a bandwidth of 25 nm, a small signal gain of 19 dB and a saturation power $P_{sat} = -5$ dBm. It operates with much lower bias currents, around 100 mA. For more details please refer to Appendix B and Appendix C. The measurements of the conversion efficiency and phase modulation index m_{ph} are shown in Figure 5.34. The 3dB bandwidth of the XGM is now around 2 GHz. The modulation indices achieved are much higher than with the Covega SOA, reaching m_{ph} as high as 1.08 with one quarter of the bias current for the lower frequency range (i.e. up to 1.4 GHz).

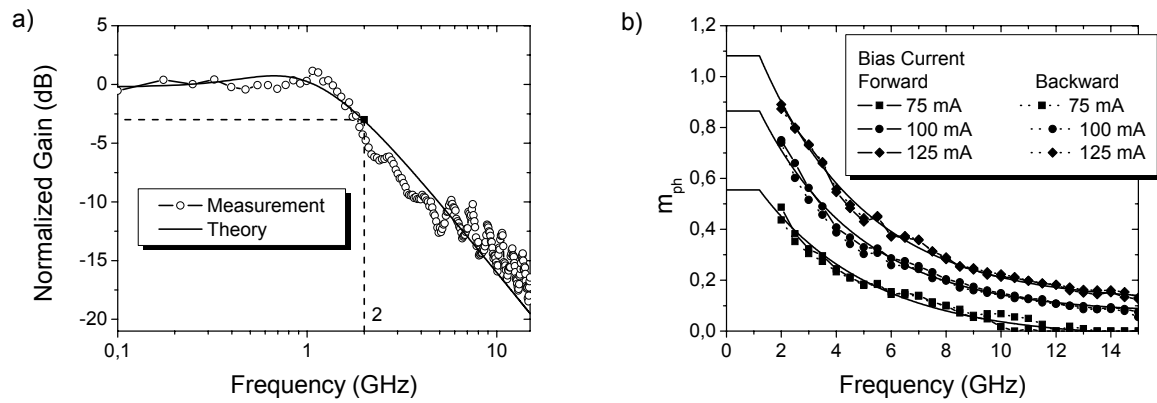


Figure 5.34: a) Conversion efficiency of XGM and b) modulation index m_{ph} versus modulation frequency f_m for the SOA from Uni Karlsruhe ($P_m = 17$ dBm, $P_{probe} = -10$ dBm, $P_{pump} = -5.5$ dBm).

This SOA was placed in another loop with $\Delta L = 6.55$ cm (i.e. $\tau = 260$ ps) and the computed simulations are shown in Figure 5.35 for $I_{bias} = 125$ mA. There is a good conformity between theory and simulations. Also as the modulation index m_{ph} increases, the transfer function suffers an overmodulation which constitutes the valley in the first period.

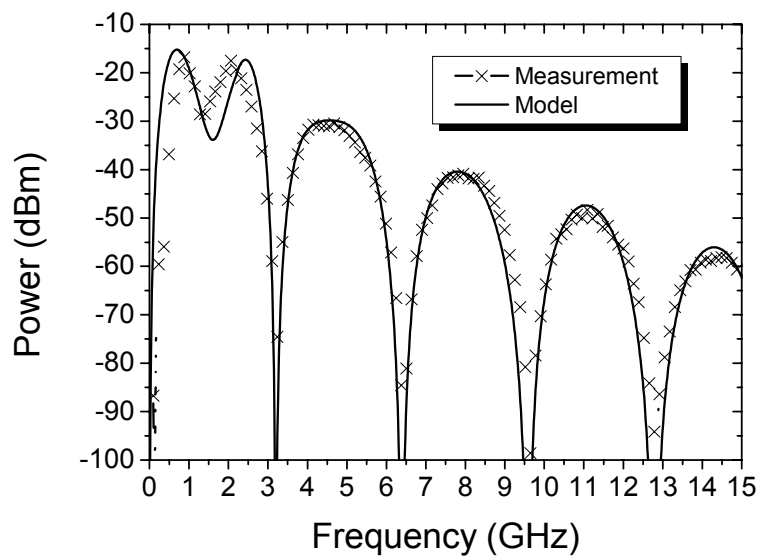


Figure 5.35: Simulated and measured power transfer function of the fiber loop for the spectral component at $2f_m$ ($P_m = 17$ dBm, $\Delta L = 6.55$ cm, $I_{bias} = 125$ mA).

The roll-off of the modulation index m_{ph} presents a problem to use this setup at high frequencies. However, the gain introduced by the SOA, the perfect bidirectional operation and the possibility to use these scheme at higher frequencies are a definite improvement over the proposal with a phase modulator. Using this frequency doubling scheme, modulating with

$f_m = 15$ GHz, a signal at 30 GHz was obtained (as shown in Figure 5.32), a 150% improvement over the 20 GHz signal obtained in section 5.2.1 with the phase modulator. The performance of both SOAs is summarized in Table 5.3, and compared with the phase modulator used in section 5.2.1.

m_{ph}	Phase modulator UTP 1-8 GHz	Covega SOA ($I_{bias} = 500$ mA)	Karlsruhe SOA ($I_{bias} = 125$ mA)
@1 GHz	0.61	0.682	1.08
@4 GHz	0.437	0.315	0.546
@8 GHz	0.188	0.15	0.29
@12 GHz	≈ 0	0.075	0.182
@15 GHz	≈ 0	0.043	0.126

Table 5.3: Phase modulation index m_{ph} for at different modulation frequencies for different SOAs and phase modulator.

The SOA especially designed for nonlinear operation (i.e. Karlsruhe SOA) exhibits a superior performance than the phase modulator and the system optimized SOA from Covega. In the frequency range for the system experiments in chapter 7 (i.e. around $f_m = 4.5$ GHz) provides the highest modulation index m_{ph} .

6 Comparison of optical heterodyne receiver architectures

The optical heterodyne receivers used in this thesis differentiate themselves with the ones used for broadband optical communications in that a wireless link is present to provide gigabit wireless access to mobile devices. Classical heterodyne receivers would use the lower path in Figure 6.1 to demodulate a signal mixed at f_{RF} by the beating of the data signal plus a local oscillator (LO). The wireless link in this case takes the role of the bandpass filter (BPF). Usually the photodiode used for heterodyning and generating the mm-wave carrier is placed at the so called base station (BS) where it receives the optical signal from a central station (CS) and broadcasts the corresponding electrical RF signal. In the mobile device the task of demodulating this broadband signal from an RF carrier remains. This is not trivial and many receiver approaches are proposed in the literature. In this chapter, some modulation formats and models for the receivers used will be presented and analysed.

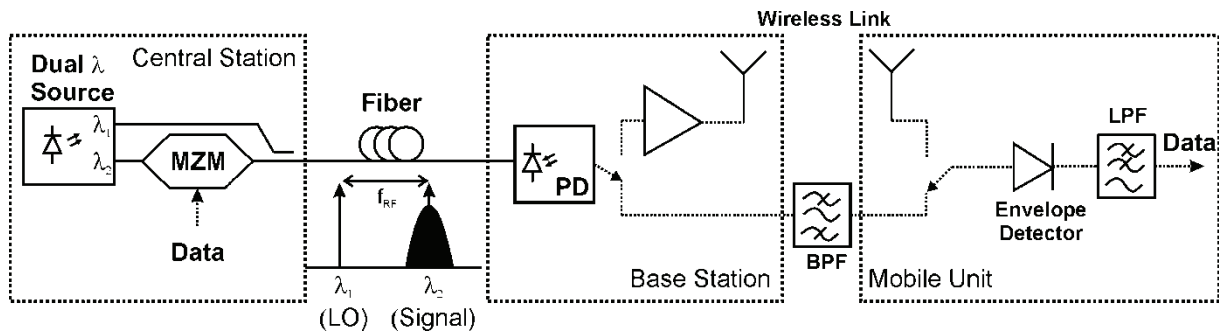


Figure 6.1: Optical heterodyne receiver example. MZM: Mach-Zehnder modulator, LO: Local oscillator, PD: Photodiode, BPF: Bandpass filter, LPF: Low pass filter.

6.1 Amplitude shift keying (ASK)

ASK is the simplest modulation format to generate. The information is modulated in the amplitude of an RF carrier and the modulated signal can be described as [138]

$$V_{sig}(t) = Z_t m(t) 2R \sqrt{P_s P_{LO}} \cos(\omega_{RF} t + \phi_{RF}(t)) + noise, \quad (6.1)$$

where $m(t)$ is the digital information, Z_t is the overall transceiver impedance, R is the photodiode responsivity, P_s is the signal power and P_{LO} the local oscillator power. The RF carrier angular frequency is ω_{RF} whereas ϕ_{RF} takes into account the phase noise present in the signal. The additive *noise* term is mainly generated by shot noise in the local oscillator laser itself when $P_{LO} > P_s$, which is generally desired in this kind of systems to approach quantum

limit efficiencies. In this so-called shot noise limit, thermal noise can be neglected and will not be considered in the following discussions.

ASK can be demodulated synchronously, by recovering the RF carrier from the signal and using it to down-convert the information to baseband in a broadband mixer as shown in Figure 6.2a. Another common method is to use an independent local oscillator at f_{RF} in the mixer, but this requires frequency and phase tracking. However, as shown in Figure 6.2b, using an envelope detector or a square-law receiver, ASK can be recovered asynchronously (i.e. no phase information is required).

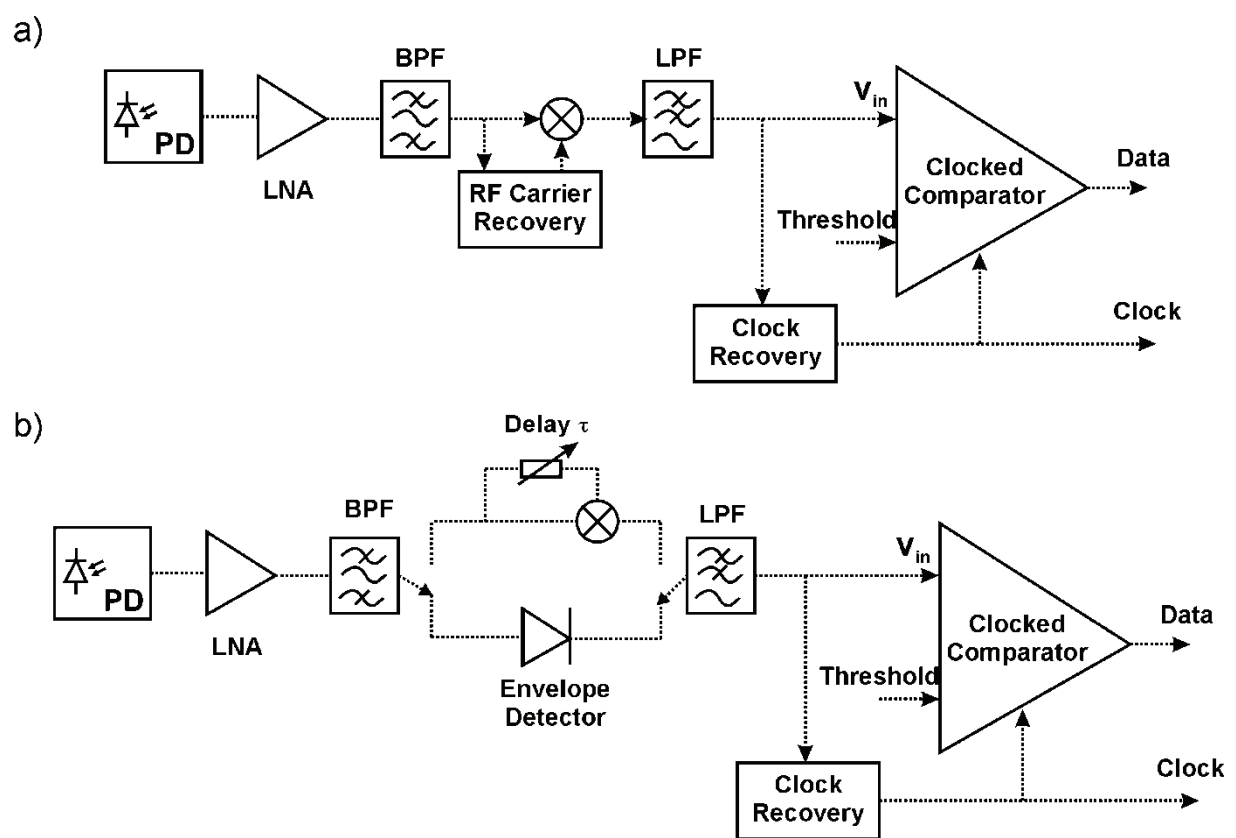


Figure 6.2: Optical heterodyne receivers for ASK with a) synchronous and b) asynchronous demodulation.

For synchronous (or coherent) demodulation as proposed in Figure 6.2a, a strong local oscillator assumption will make the system to be dominated by shot noise as a great number of photons are received per bit of information. Thus we can assume Gaussian statistics for the voltage at the decision circuit as illustrated in Figure 6.3a. The dominant LO shot noise also

allows us to assume that the noise during a “zero” is the same as the noise during a “one” so that $\sigma_0 = \sigma_1 = \sigma_n$.

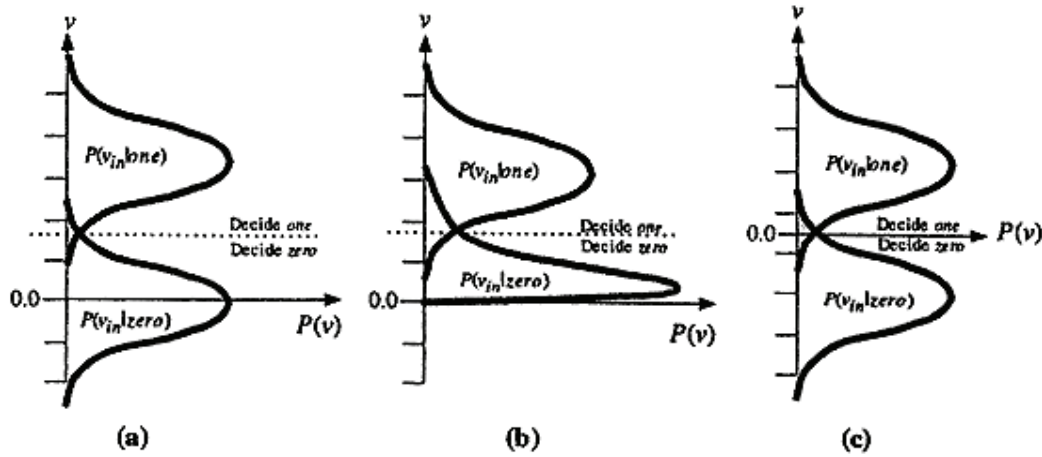


Figure 6.3: Probability densities at the input of the decision circuit in a heterodyne receiver for a) synchronous ASK, b) asynchronous ASK and c) PSK [138].

The BER performance will then be determined by solving the problem of the detection of a known pulse in Gaussian noise [139]. The maximum likelihood demodulator is a matched filter [140]. Since in the demodulators in Figure 6.2, the overall filter function is the cascade of the predetection band-pass and postdetection low-pass, either the band-pass or the low-pass filter (or a combination) could be used to approximate the ideal sinc function matched filter. The voltage obtained during a “one” is proportional to the amplitude of the RF signal, while the noise is proportional to the DC photocurrent and receiver noise bandwidth (B_n) as

$$\begin{aligned} V_{one} &= Z_t 2R \sqrt{P_{rcvdone} \cdot P_{LO}} \\ \sigma_n &= Z_t \sqrt{2qRP_{LO}B_n}. \end{aligned} \quad (6.2)$$

Here $P_{rcvdone}$ is the power in a “one”, P_{LO} the LO power, q the electron charge, R the photodiode responsivity and Z_t the overall receiver impedance. Setting the optimum threshold to half the voltage generated by the receiver during a “one” allows the calculation of the BER by using the Q function which is defined as

$$Q(a) \triangleq \frac{1}{\sqrt{2\pi}} \int_a^{\infty} e^{-\frac{x^2}{2}} dx. \quad (6.3)$$

Therefore, the BER takes the form [138],

$$BER_{ASK-coh} = Q\left(\frac{V_{one}}{2\sigma_n}\right) = Q\left(\sqrt{\frac{\eta P_{rcvd_{one}}}{2hf_c B_n}}\right) = Q\left(\sqrt{\frac{n_p}{2}}\right), \quad (6.4)$$

where $n_p = \frac{\eta P_{rcvd_{one}}}{hf_c B_n}$ is the peak number of photons required per bit of information, η the quantum efficiency of the photodiode, h Planck's constant and f_c the optical carrier frequency.

Eq. (6.4) assumes that the receiver noise bandwidth is equal to $R_b = 1/T_b$, where T_b is the symbol time. This corresponds to the case of a matched filter receiver [140]. In order to achieve a BER of 10^{-9} , the argument of the Q-function should be 6, thus requiring 72 photons in each bit that is a “one”. This translates into an average of 36 photons per bit, assuming “ones” are equally likely as “zeroes”.

The case of an asynchronous (or incoherent) receiver presents some problems, because the signal is either squared or envelope detected and now the associated statistics for the “ones” and “zeroes” are no longer Gaussian. The probability density at the output of an envelope detector with a digitally modulated sinusoidal signal under additive white-Gaussian noise is well-known to be described by a Rician distribution for a “one” and a Rayleigh distribution for a “zero” [141] as illustrated in Figure 6.3b.

To determine the BER performance for incoherent ASK demodulation now involves solving the integrals of the Rician and Rayleigh distributions. A closed formed solution with Marcum Q function can be achieved, but when the signal-to-noise ratio is high, the Marcum Q function can be approximated using the standard Q function from Eq. (6.3) [138]. Assuming that the optimum threshold level is again half the level of V_{one} , then

$$BER_{ASK-incoh} \cong \frac{1}{2} Q\left(\frac{V_{one}}{2\sigma_n}\right) + \frac{1}{2} \exp\left(-\frac{V_{one}^2}{8\sigma_n^2}\right). \quad (6.5)$$

For all practical cases the second term in Eq. (6.5) dominates the probability of error, and we can further simplify the expression to

$$BER_{ASK-incoh} \cong \frac{1}{2} \exp\left(-\frac{V_{one}^2}{8\sigma_n^2}\right) = \frac{1}{2} \exp\left(-\frac{\eta \cdot P_{rcvd_{one}}}{4hf_c B_n}\right) = \frac{1}{2} \exp\left(-\frac{n_p}{4}\right). \quad (6.6)$$

In order to achieve a BER of 10^{-9} using an incoherent ASK demodulator, 80 photons in each bit that is a “one” are required. This translates into an average of 40 photons per bit, assuming an equal symbol distribution. This represents only 4 photons more than coherent detection per bit, or a 0.5 dB optical power penalty. This is such a small degradation that incoherent demodulation is typically preferred due to its simplicity.

The task of constructing these demodulators is not trivial and several approaches are found in the literature [142]-[145]. For the system experiments both coherent and incoherent demodulation will be used, therefore the receiver architectures will be described next.

6.1.1 Receivers with coherent demodulation

To coherently demodulate an RF carrier with data on it, some kind of RF carrier recovery is needed (see Figure 6.2a) to later use it in a broadband mixer and shift the RF spectrum to baseband. Usually RF carrier recovery involves some kind of phase detector and a voltage controlled oscillator (VCO) which with the help of a phase-locked loop (PLL) tracks the frequency and the phase of the RF carrier. The receiver architecture developed in the lab is drawn in Figure 6.4.

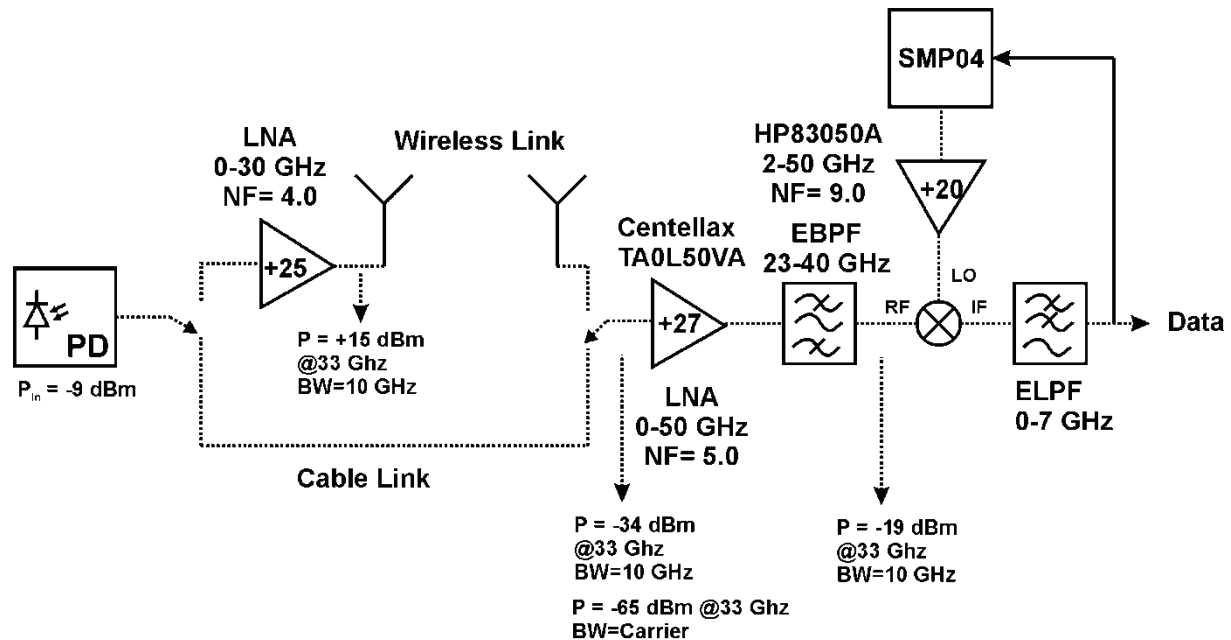


Figure 6.4: Detailed schematic of the coherent receiver.

After photodetection the RF signal can either go through a cable link for back to back (BtB) measurements or a wireless link (with added amplification). Both paths combine in the

coherent demodulator. The signal is further amplified by a Centellax low noise broadband RF amplifier (LNA). The photodetected signal also has a baseband copy due to the direct detection process in the photodiode, therefore an electrical bandpass filter is in charge of eliminating this baseband copy (mainly for the BtB case).

Instead of employing a VCO, a frequency synthesizer was used (SMP04 from Rohde & Schwarz) which generates an LO at $f_{LO} = 33$ GHz. The output signal needed to be amplified to +13 dBm which is required for the broadband mixer (Miteq M2640W) to operate. To obtain coherent demodulation, two issues needed to be addressed: frequency and phase tracking of the RF carrier. The frequency stability was achieved by synchronizing the SMP04 with the source synthesizer used to generate the optical DSB-SC signal at the central station via its 10 MHz reference port. Otherwise, a frequency mismatch which varies in time is observed. Secondly, the phase mismatch of both synthesizers causes amplitude variations in the recovered data. To solve this issue, a slow PLL was implemented in Labview. The DC component of the recovered data signal was used as an input and the program changed the electrical phase of the local oscillator (SMP04) to achieve maximum amplitude. Not only was this vital, but the phase noise of the source synthesizer needs to be quite good too. The first experiments involving a WILTRON synthesizer couldn't be carried out. By changing the source synthesizer with an Agilent PSG04, the signals could be locked during the experiments time frame.

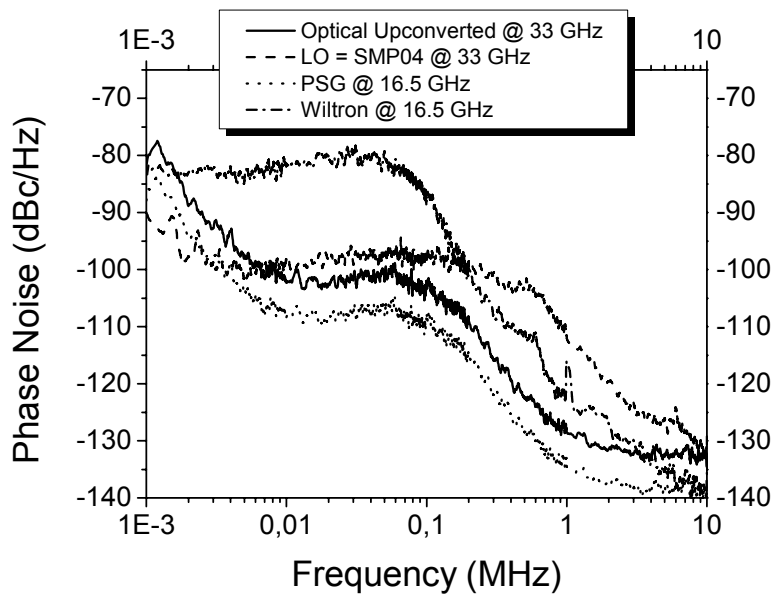


Figure 6.5: Phase noise of the synthesizers used.

Figure 6.5 shows the phase noise measurements of three synthesizers involved in the experiments demonstrating that the WILTRON synthesizer provides much higher phase noise than the PSG. The optimal combination is to use the PSG as the source synthesizer for the DSB-SC optical signal and the SMP04 as local oscillator in the receiver unit.

From Eq. (2.4) in section 2.3 we can solve for the implementation loss (IL) of our proposed receiver, which is rewritten as

$$IL = P_{TX} + G_{TX} + G_{RX} - PL(d) - L_{shad} - (10 \cdot \log_{10}(k_B T B_n) + NF_{RX}) \quad (6.7)$$

Considering the BtB case (i.e. no wireless link), then $G_{TX} = G_{RX} = PL(d) = 0$. Moreover, no shadowing is considered, so $L_{shad} = 0$ too. To obtain a BER = 10^{-9} a Q factor of 6 is needed, which translates in $SNR = 10 \cdot \log_{10}(Q^2) = 15.6$ dB [146]. The cascaded noise figure of the receiver was calculated using Friis formula [147] and results in $NF_{RX} = 5.04$ dB which is expected due to the low noise amplifier (LNA) as the first stage of the receiver. The remaining parameters are $B_n = 7$ GHz and $P_{TX} = -34$ dBm (the measured electrical power for BER = 10^{-9} in the lab). Solving Eq. (6.7) results in $IL_{coh} = 20.91$ dB for this receiver, which demonstrates there is sufficient margin for improvement. Typical values of IL considered in chapter 2 for the simulations were around 6 dB. One of the key issues when dealing with huge bandwidths is the group delay response of all the components involved. As the bit slot is 100 ps for 10 Gbps, the group delay ripple of the amplifiers and mixer combined should be kept below this value. Also the use of a transimpedance amplifier directly after the photodiode will improve the sensitivity of the proposed receiver.

However, the biggest drawback of this scheme is the requirement to lock both source and receiver synthesizers which is unrealistic at best due to the fiber link plus the wireless link to the mobile unit. Moreover, some kind of phase tracking is also needed, increasing the complexity of the receiver, which should be incorporated in the mobile devices plus a carrier recovery circuit. To avoid RF carrier recovery we move on to receivers using incoherent demodulation, which will be explained in the next section.

6.1.2 Receivers with incoherent demodulation

In order to have mm-wave carrier independence, receivers with incoherent demodulation such as square-law detection or envelope detection are used. As the theoretical penalty in

comparison with coherent demodulation techniques is quite small (40 photons per bit compared to 36 for coherent detection, only 0.5 dB), these methods are preferred due to the costs savings of not having a local oscillator. Two approaches will be described, one involving square-law detection (i.e. the self homodyne receiver) and one using envelope detection.

6.1.2.1 Self-homodyne receiver

The self-homodyne receiver is based on the principle of mixing the incoming RF signal with itself to produce baseband demodulation. The RF signal is actually squared, producing harmonic products at baseband and twice the RF carrier frequency. Due to bandwidth limitations of the electrical components and low pass filtering, the higher order components are removed. Therefore demodulation takes place with no local oscillator, providing mm-wave carrier independence as long the RF carrier is within the square-law device's bandwidth (usually a broadband mixer is used for this purpose). A detailed setup of the self homodyne receiver is shown in Figure 6.6.

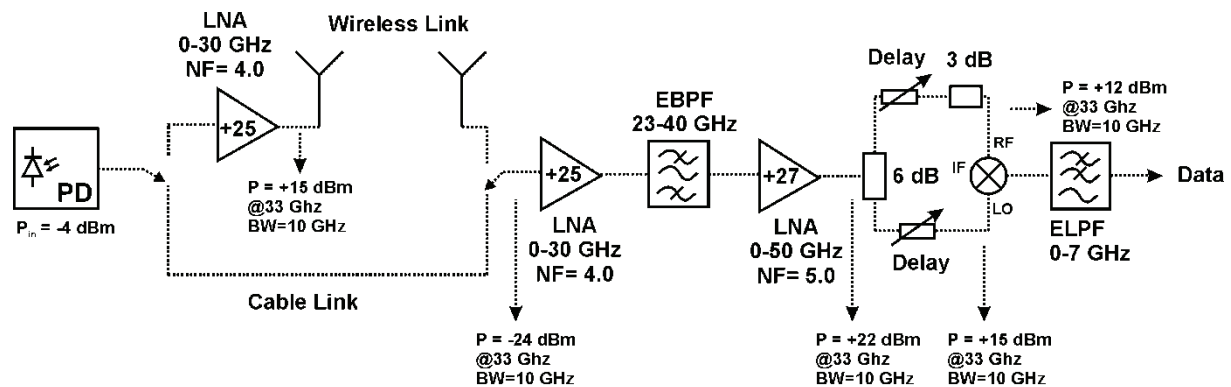


Figure 6.6: Detailed schematic of the self-homodyne receiver.

After the O/E conversion in a broadband photodiode, the signal can travel through two paths: a cable link for BtB measurements or a wireless link. Both paths reunite in the self-homodyne receiver consisting of a low noise preamplifier with gain $G_1 = 25$ dB and noise figure $NF_1 = 4$ dB, a bandpass filter in the 23-40 GHz band, another low noise amplifier with gain $G_2 = 27$ dB and noise figure $NF_2 = 5$ dB. A 6 dB broadband coupler splits the signal into two paths, which are adjusted through broadband delay lines, and recombine in an electrical broadband mixer (Miteq 2640W which operates in the 26-40 GHz region). The mixer needs high powers in the LO port to operate correctly (i.e. light up the diodes in the mixer). From

the manufacturer's datasheet, at least +13 dBm RF power is required in the LO port of the Miteq mixer. Transforming this power requirement to the input port of the self-homodyne receiver gives us a sensitivity of -24 dBm for $\text{BER} = 10^{-9}$ at 10 Gbps. After self mixing, the signal is low-pass filtered (ELPF, $B = 7$ GHz) to remove the unwanted high frequency images after the mixing process.

This type of receiver is quite straight forward and doesn't require a local oscillator with PLL like the coherent receiver from the previous section. However, it needs a large amount of RF amplification to operate. An improvement to reduce the high power requirements could be by using active mixers (with power supply), however none were available in the desired frequency range during the development of this thesis. For our case then, two broadband low noise amplifiers (LNA) just give a sensitivity of -24 dBm for $\text{BER}=10^{-9}$, which is much worse than the coherent case. The calculated equivalent noise figure is now $NF_{RX} = 4.02$ dB, which is 1 dB better than before, but the power needed to be increased to $P_{TX} = -24$ dBm. Using Eq. (6.7) results in $IL_{SH} = 33.93$ dB, roughly 13 dB worse than the coherent demodulator. For this reason, instead of using a square-law type of receiver, the next step would be to simply do an envelope detection of the incoming RF signal.

6.1.2.2 Envelope detection receiver

By detecting the envelope of the RF signal, all its amplitude information can be recovered linearly. For this purpose, a broadband diode detector already in a WR28 waveguide was available from Spacek Labs (model DKa-2P in Figure 6.7a).

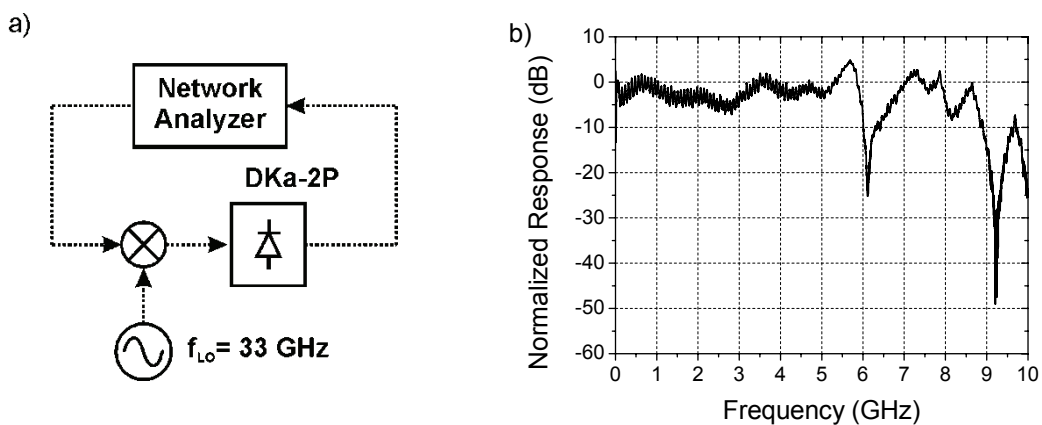


Figure 6.7: a) Setup used to measure the IF bandwidth of DKa-2P diode detector and b) corresponding frequency response.

The waveguide specifications allows it to operate in the 26-40 GHz region but its IF bandwidth was never characterized for this application. Usually these kind of diodes are used as video receivers for CATV systems where an IF bandwidth of only a couple of MHz is required [148]. Using the setup depicted in Figure 6.7a, the IF bandwidth could be estimated and the results are shown in Figure 6.7b. Surprisingly, the IF bandwidth of the diode detector can be estimated to be 5.5 GHz even though in the “pass band” there is much ripple present. This would allow the detector to operate with data rates as high as 7.5 Gbps (i.e. 3 dB bandwidth at least 75% of the bitrate). The following receiver depicted in Figure 6.8 was constructed around the DKa-2P. The setup is very similar to the self-homodyne one, but instead of dividing the signal into two paths for self mixing, the RF signal can be directly fed to the diode detector (DKa-2P). As a consequence, much less RF amplification is needed in comparison with the self-homodyne receiver, i.e. only one mm-wave amplifier with gain $G = 25$ dB and $NF = 4$ dB. In this case a Centellax UAL130VM LNA was used due to its flat group delay response. After the broadband detector a 10 Gbps baseband amplifier from Picosecond Pulselabs (PSPL 5828) was used and a 1 dB attenuator was required to match impedances. The low pass filter is in charge of reshaping the pulses to a raised cosine form as well as filtering unwanted high frequency components. The sensitivity for $BER = 10^{-9}$ and a data rate of 7.5 Gbps was measured to be -34 dBm, a 10 dB improvement over the self homodyne case with one less RF amplifier used. The cascaded noise figure was calculated to be $NF_{RX} = 4.04$ dB, comparable to the self-homodyne receiver.

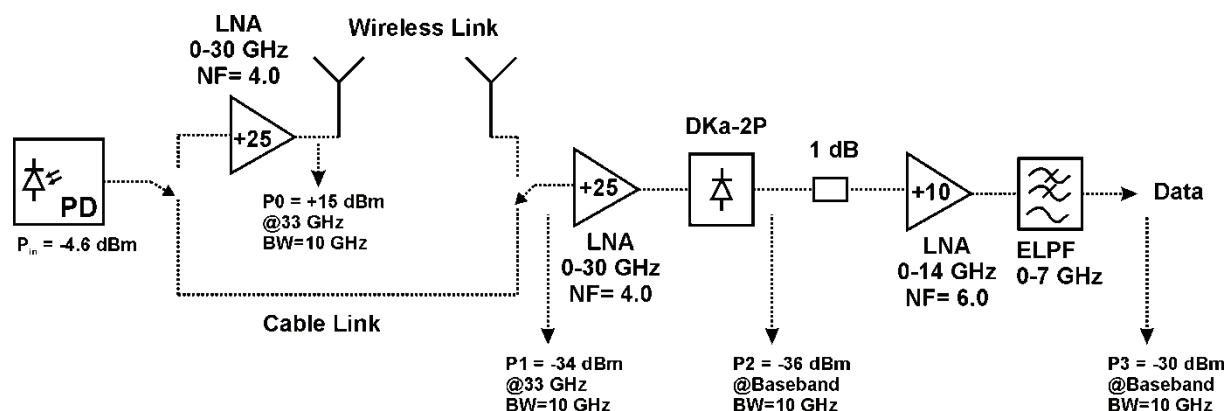


Figure 6.8: Detailed schematic of the diode envelope detector receiver.

The low pass filter used was designed for 10 Gbps systems, therefore it is not a matched filter for other data rates. This means that for lower data rates, specially 2.5 Gbps and lower, the

recovered data could exhibit spurious responses within the filters bandwidth. The sensitivity varies then with the data rate and they are summarized in Table 6.1.

Data Rate	2.5 Gbps	5 Gbps	7.5 Gbps	10 Gbps
Opt. Power (dBm)	-3.3	-4.6	-4.6	+8.5
P ₁ (dBm)	-33.85	-34.14	-34.20	-22.40
P ₂ (dBm)	-32.52	-36.89	-36.02	-4.6
P ₃ (dBm)	-26.08	-30.26	-30.30	2.21

Table 6.1: Measured envelope detector sensitivities for BER = 10⁻⁹ and different data rates.

Eventhough the previous analysis for the IL is not quite correct for lower data rates (as we stop using a matched filter), using Eq. (6.7) for comparison purposes results in $IL_{env} = 21.91$ dB, only 1 dB worse than the coherent demodulator. This receiver architecture combines simplicity and a sensitivity of -34 dBm comparable with that of coherent detection, which makes it the best choice for gigabit wireless systems. The main drawback is the reduced bandwidth (i.e. $B = 5.5$ GHz due to the detector response plus low-pass filtering afterwards), allowing a maximum error free data rate of 7.5 Gbps. Higher data rates such as 10 Gbps were also tested but suffered severely from intersymbol interference and thus were not error free despite the higher optical powers used. A more detailed explanation is carried out in chapter 7 for the system experiments.

6.2 Phase shift keying (PSK)

In PSK systems, the transmitted signal's envelope is held constant while the phase of the RF signal is varied by the information being transmitted. The form of the recovered RF signal is

$$V_{sig}(t) = Z_t 2R \sqrt{P_s P_{LO}} \cos(\omega_{RF} t + m(t)\pi + \phi_{RF}(t)) + noise, \quad (6.8)$$

where $m(t)$ takes the values of 0 or 1 depending on the information. In conventional PSK systems $m(t)$ corresponds directly to the data. This type of system requires absolute phase knowledge either through a homodyne receiver or a synchronous demodulator in a heterodyne receiver.

In a homodyne receiver the LO is phase-locked to the received signal, then the RF frequency is zero, which makes this case not very interesting for wireless transmission. In the case of coherent demodulation in a heterodyne PSK system, the signal appears at an RF frequency instead of at baseband. Under the assumption of a sufficiently high RF frequency, the BER is given by [144]

$$BER_{coh-PSK} = Q\left(\sqrt{2n_p}\right). \quad (6.9)$$

This requires 18 photons per bit for a BER = 10⁻⁹. This is a little more than 3 dB better than the ASK receivers previously mentioned.

An alternative to PSK is to differentially encode the data being transmitted, called differential PSK (DPSK). In this scheme, a “zero” is transmitted as a change in phase, while a “one” is sent as no change in phase. Since the information is encoded into the relative phase from symbol to symbol, a simple heterodyne receiver with a one-bit delay and multiply as shown in Figure 6.9 will demodulate the signal.

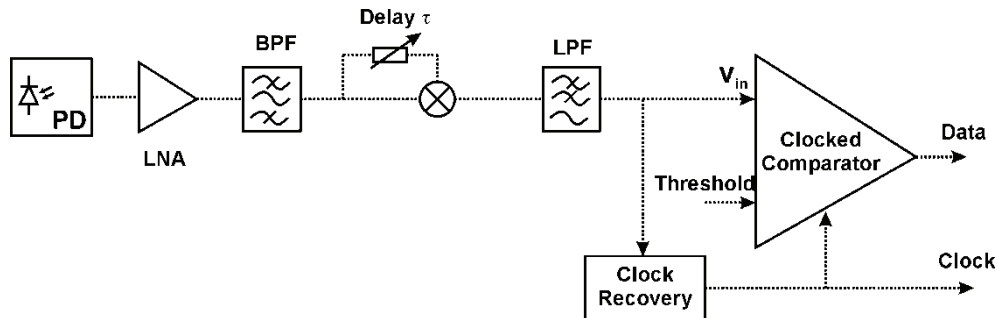


Figure 6.9: Schematic of a DPSK receiver.

The relative-phase comparison used in DPSK implies that DPSK will have less exacting requirements on the laser phase noise. The receiver in Figure 6.9 can be implemented with the same components as the self-homodyne receiver in Figure 6.6 but changing the delay lines settings to have a one bit delay between both paths.

Under the strong LO and zero-linewidth assumptions, the expression for the BER is [144]

$$BER_{DPSK} = \frac{1}{2} \exp(-n_p). \quad (6.10)$$

This requires 20 photons per bit for BER = 10⁻⁹. The small difference with heterodyne PSK makes this scheme usually favoured. This is exactly 3 dB better than the ASK receivers

mentioned in section 6.1. As a matter of fact, phase modulation is usually the preferred modulation format for wireless communications as the effect of amplitude variations is minimized. This type of receiver will be used in the systems experiments with a fiber loop, described in the next section, using an intermediate frequency of $f_{IF} = 2$ GHz and working with data rates of 155 Mbps. Using this low data rates requires smaller RF bandwidths, which make the noise contributions smaller, and thus an implementation loss of $IL_{DPSK} = 6.5$ dB was achieved, much better than the previous ASK receivers, but for lower data rates.

6.3 Linewidth effects

Linewidth is a major factor in determining the performance of an optical receiver. In contrast to microwave sources which can have a linewidth as low as 1 Hz, usually DFB lasers exhibit linewidths in the order of 10 MHz, which is a substantial percentage of the bit rate, even for Gbps data rates. The resulting mm-wave linewidth depends on how this signal is optically generated, but it strongly depends on the type of lasers used.

The most notorious observable effect of a finite mm-wave linewidth is an increase in the observed BER for a given amount of received signal power. This is effectively a reduction in receiver sensitivity and is demonstrated in Figure 6.10 when using two uncorrelated laser sources to generate a 10 Gbps ASK mm-wave signal (setup details in Appendix D, Figure D.6).

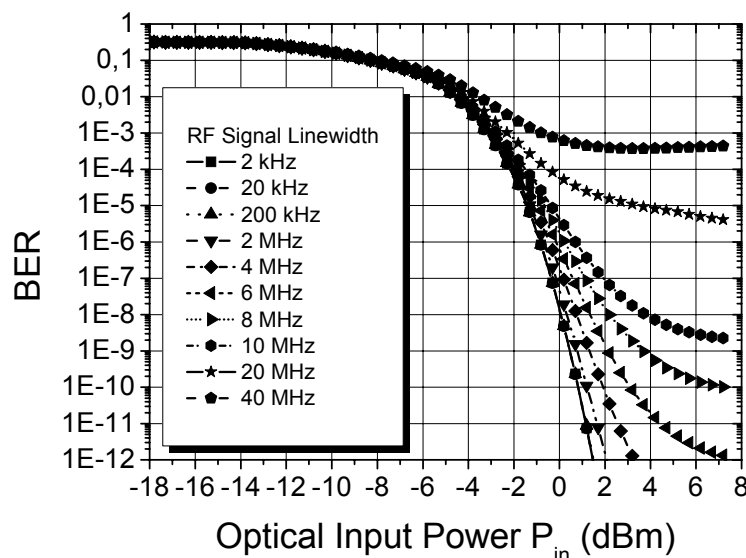


Figure 6.10: Effect of mm-wave linewidth in receiver performance.

For a given modulation format, the ideal BER curve is calculated using the assumption that the RF linewidth is zero. As the linewidth is increased the slope of the BER curve dramatically changes and a BER floor may be observed [143].

A non-zero RF linewidth spreads the RF signal energy over a broader bandwidth than is expected just from the modulation of the signal. This causes fluctuations in signal power and introduces cross-talk. The precise impact of linewidth on communications performance is difficult to predict in analytic form, therefore numerical techniques are used to estimate the performance, such as simulation suites like VPI TransmissionMaker 8.0.

The tolerance to linewidth varies depending on the modulation format used. Table 6.2 shows the ideal sensitivities and the approximate amount of RF linewidth ($\Delta\nu$) that results in 1 dB degradation receiver sensitivity for the conventional demodulators described in the previous sections.

The methods used to combat the effects of a large RF linewidth depend on the type of signaling used. ASK uses a wideband RF filter, envelope detector, and narrowband postdetection low-pass filter, for example. A wideband predetection filter is used instead of a matched filter so that most of the signal energy, which was spread in frequency due to phase noise, is captured. The postdetector filter substantially reduces the effects of the additional noise bandwidth of the wide predetection filter. The sum of the two filter time constants is usually equal to the symbol time [149].

6.4 Overview

The most important parameters of all the previously discussed receivers are gathered in Table 6.2, along with the theoretical quantum limit sensitivities (i.e. photons per bit for $\text{BER} = 10^{-9}$), linewidth requirements (i.e. $\Delta\nu$ as a percentage of the bit rate R_b), implementation losses (i.e. IL in dB) and noise figures (NF in dB) of the constructed demodulators. A comparison of the theoretical receiver performance is drawn in Figure 6.11. for an ideal quantum efficiency $\eta = 1$ and $B_n = 10$ GHz. As usual, the PSK formats exhibit a 3 dB improvement in performance in regard to amplitude modulation. As previously discussed, incoherent demodulation is only 0.5 dB worse than the coherent case (both for ASK and PSK). Adding the simplicity of incoherent demodulation plus this low penalty makes this type of receivers the optimum choice.

Demodulator	n_p for BER = 10^{-9}	$\Delta\nu$ (% of R_b)	IL (dB)	NF (dB)	BER
ASK – Coherent	72	~ 0.5 %	20.91	5.04	$Q\left(\sqrt{\frac{n_p}{2}}\right)$
ASK – Square Law	80	~ 10 %	33.93	4.02	$\frac{1}{2}\exp\left(-\frac{n_p}{4}\right)$
ASK – Envelope	80	~ 10 %	21.91	4.04	$\frac{1}{2}\exp\left(-\frac{n_p}{4}\right)$
PSK - Coherent	18	~ 0.5 %	Not available	Not available	$Q\left(\sqrt{2n_p}\right)$
DPSK	20	~ 1 %	6.5	4.03	$\frac{1}{2}\exp(-n_p)$

Table 6.2: Receivers key parameters.

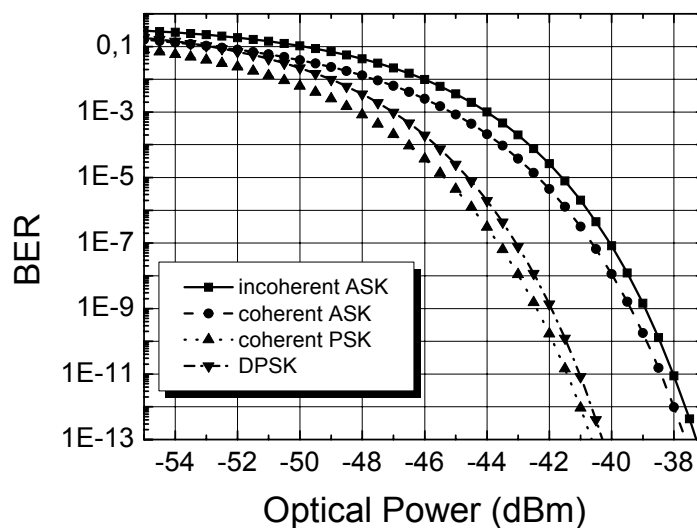


Figure 6.11: Theoretical BER vs received optical power for heterodyne receivers.

For later broadband system experiments two types of antennas will be used: a Vivaldi DRH40 and a horn SGH, both of them already characterized in section 2.4.2. Returning to the channel capacity calculations from section 2.3, we can recalculate Shannon's maximum channel capacity C as a function of transmission distance d using Eq. (2.3) and Eq. (2.4) for all the constructed receivers. Implementation loss (IL) and noise figure (NF) can be taken from Table 6.2 and we set the transmitted power to $P_{TX} = 15$ dBm. For this calculations the antenna gains are considered constant at $G_{Vivaldi} = 15$ dB and $G_{Horn} = 24$ dB, even though both exhibit a major tilt in the frequency response (see section 2.4.2). The results for a wireless link at

$f_{RF} = 33$ GHz and $B_n = 10$ GHz are shown in Figure 6.12 for all broadband receivers (i.e. for the DPSK receiver no wireless experiments were carried out).

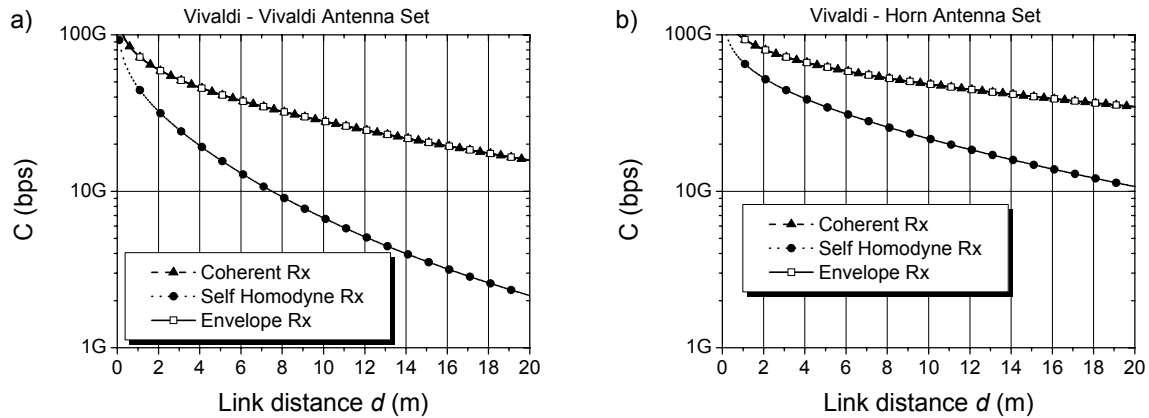


Figure 6.12: Shannon's theoretical maximum capacities for ASK broadband receivers for a) Vivaldi-Vivaldi antenna set and b) Vivaldi-Horn antenna set.

The coherent and envelope receivers show the same performance due to the fact that the 1 dB less IL from the coherent receiver is compensated with a 1 dB higher NF (see Table 6.2). From Figure 6.12a, using the self-homodyne receiver, a 10 Gbps link can be realized only up to 8 m. The coherent receiver would have no problem extending the distance more than 20 m. The case of the envelope receiver is a bit misleading. Theoretically it has the same performance as the coherent receiver, but due to the bandwidth limitation of the broadband detector, an error free 10 Gbps link could not be realized. The advantage of using a horn antenna as a receiver is clear from Figure 6.12b as it increases dramatically the theoretical maximum channel capacity and reach.

7 System experiments

This chapter is concerned with system experiments involving the before mentioned mm-wave signal generation methods. The scheme using a fiber loop (both with phase modulator and SOA) will be tested in section 7.1 for relatively low RF frequencies (i.e. $f_{RF} = 11$ GHz) due to the phase modulator limitations, this also limiting the data rates to be transmitted (in this case 155 Mbps will be used). Increasing the RF frequency to $f_{RF} = 33$ GHz allows the transmission of broadband data up to 10 Gbps. Two broadband setups for wireless transmission of 10 Gbps will be explained: Optical double sideband (ODSB) will be described in section 7.2.1 whereas optical single sideband (OSSB) is portrayed in section 7.2.2. Lastly, heterodyning of two uncorrelated lasers will be investigated in section 7.3 as a possible in-house solution in fiber to the home systems.

7.1 Fiber loop setup

Two configurations regarding the fiber loop setup mentioned in section 5.2 were carried out. The principle of operation is the same for both, but what changes is the non-reciprocal phase changing element inside the loop. The first setup is the one using a phase modulator inside the fiber loop while the other one uses XPM in SOAs to achieve the same results.

7.1.1 Fiber loop with phase modulator

In order to demonstrate the upconversion of an intermediate frequency signal (IF) carrying a digital base band signal, the setup shown in Figure 7.1 is used. As the phase modulator used operates only up to frequencies as high as 8 GHz, this limits the available bandwidth of the system. The fiber loop is tuned to have a $\Delta L = 2$ cm (as described in section 5.2.1, Figure 5.24). A subcarrier of 2 GHz is DPSK modulated with a 155 MBit/s NRZ pseudo random ($2^{31}-1$) base band signal. The light source can be either a DFB laser or an ASE source which is modulated in its intensity with a modulation index $m_a=0.6$ to guarantee linearity. The phase modulator in the unbalanced fiber loop is modulated with $f_m = 4.5$ GHz. This results in a maximum transmission of the loop at 9 GHz. At port 2 of the loop the spectrum consists of two sidebands $f_c \pm 4.5$ GHz each one modulated with the 2 GHz IF signal containing the baseband information. After photodetection we obtain two signals at 9 ± 2 GHz from which the one at 11 GHz is demodulated.

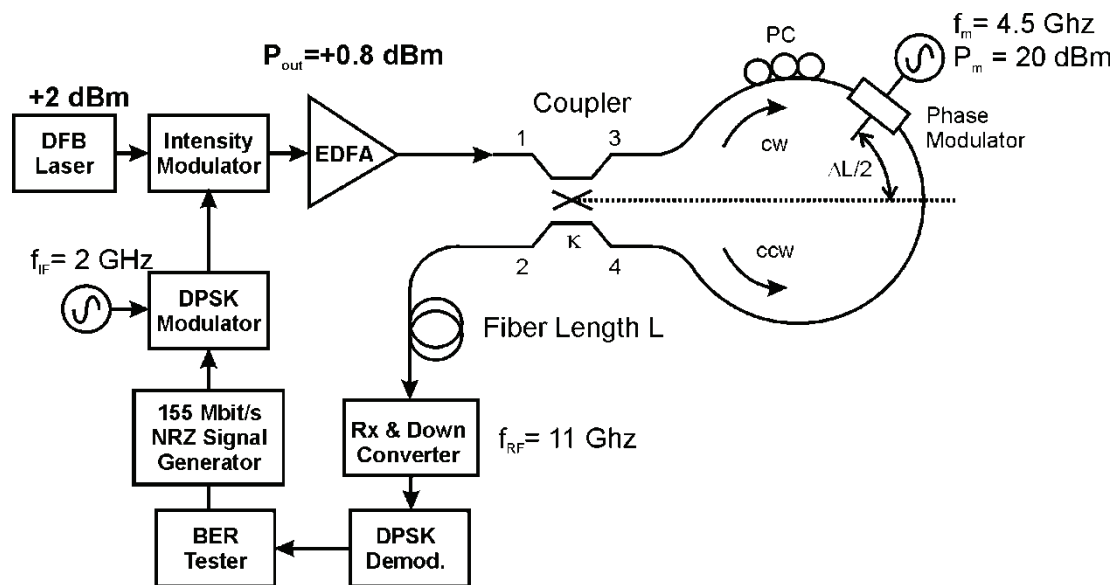


Figure 7.1: Setup for the upconversion of an IF signal at 2 GHz modulated with a 155 Mbit/s baseband signal using a fiber loop with a phase modulator (PC: Polarization Controller).

Figure 7.2 shows the Bit Error Rate (BER) for four different lengths of fiber ($L = 0.5, 2, 12.8$ and 19.2 km) and an optical back-to-back measurement as a function of optical power at the photodiode. Within the experimental uncertainties all measured curves are showing the same slope. No influence of fiber chromatic dispersion was observed. The experimental setup is limited in its transmission length due to the attenuation of the fiber link and the available amplification devices at the time of the measurements.

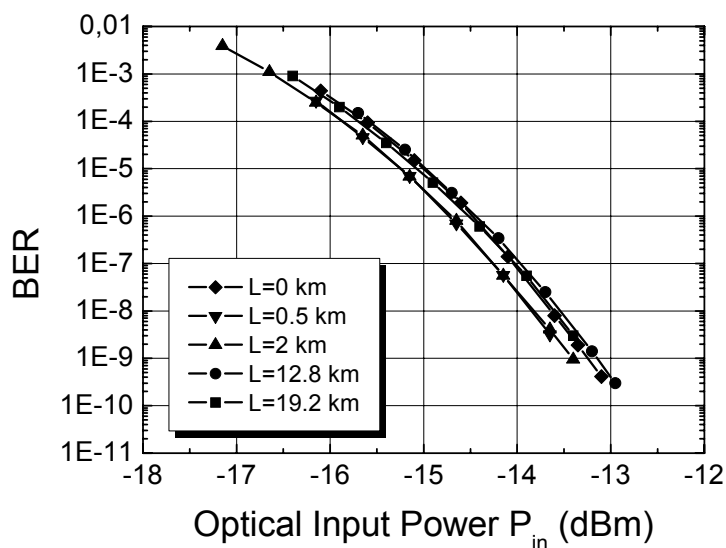


Figure 7.2: BER vs optical power at photodiode for different fiber lengths L using a laser source.

According to the theory developed in Section 4.2.2 and using the values of $f_{RF} = 9$ GHz and $f_{IF} = 2$ GHz from our experiments, the carrier to noise penalty as a function of fiber length L is plotted in Figure 7.3. The first transmission zero occurs at $L_0 = 204$ km and for $L = 20$ km the C/N penalty is only 0.1 dB and can be considered negligible for our experiments. If sufficient amplification were available, transmission distances of up to 120 km with a penalty of only 4.4 dB due to chromatic dispersion could be achieved.

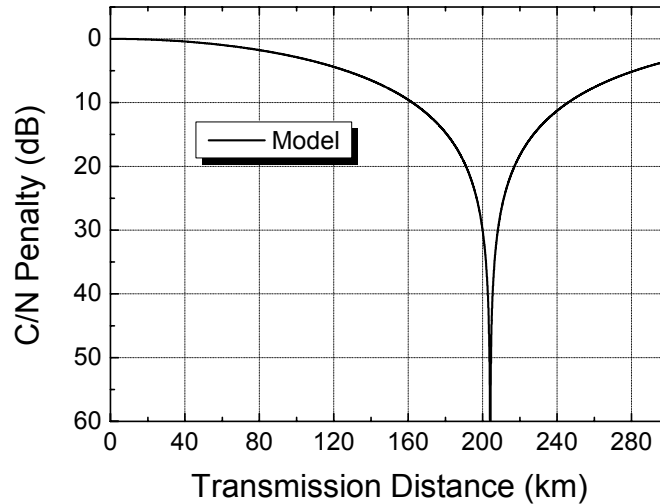


Figure 7.3: Dispersion induced C/N penalty as a function of transmission distance for DSB-SC method. Calculations with $D = 17$ ps/nm·km, $\lambda_c = 1550$ nm, $f_{RF} = 9$ GHz and $f_{IF} = 2$ GHz.

In Figure 7.4 the BER curves for two configurations with an incoherent source (e.g. the amplified spontaneous emission of an EDFA), one with the stand alone fiber loop and the other with a fiber length $L = 0.5$ km are shown. In the first case ($L = 0$ km) the slope is similar to the previous case with a laser source. As a short span of Corning SMF 28 is introduced ($L = 0.5$ km) it can be evidently seen that more power (6 dB at $\text{BER} = 10^{-9}$) is needed to obtain the same BER performance and also a deterioration in the BER slope occurs. These effects are attributed to the fiber chromatic dispersion. As each spectral line experiences different dispersion values through the whole ASE spectrum (30 nm or more), the interference of all these spectral lines is out of phase in the photodiode and a stronger power fade-off effect occurs. Therefore to achieve the same BER performance, more power is needed. As the fiber length was increased to 2 km, no detection was anymore possible.

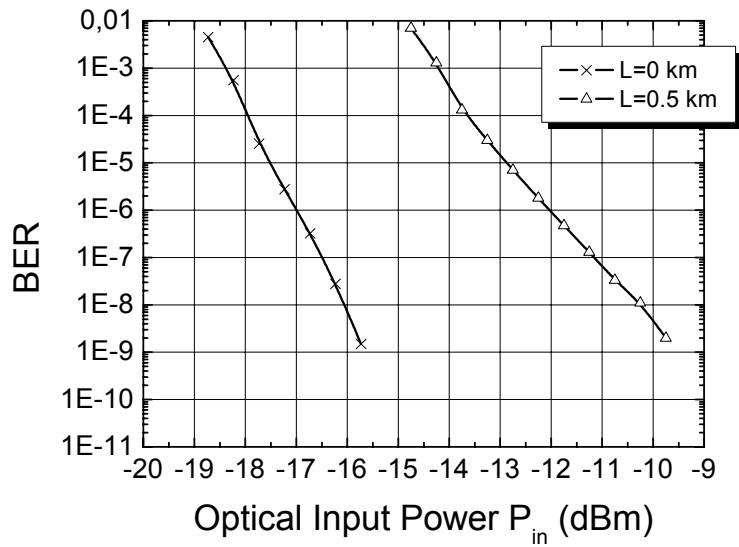


Figure 7.4: BER vs optical power at photodiode for different fiber lengths L using an ASE source.

Simulations were carried out in VPI TransmissionMaker 8.0 for the setup with an ASE source and the results of the C/N penalty are shown in Figure 7.5. For $L = 500$ m a penalty of 13 dB is reached which agrees with our expected penalty of 6 dB in the optical domain. For $L = 2$ km the penalty is 22.5 dB approx. which is out of the dynamic range of our receiver.

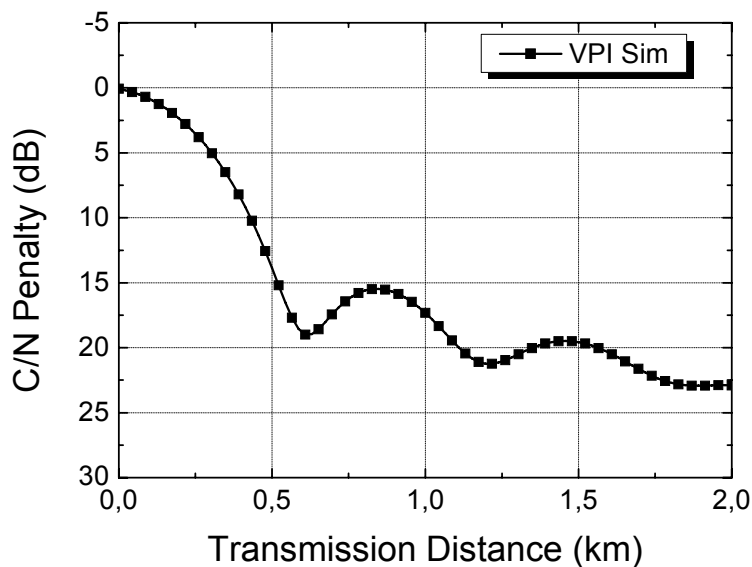


Figure 7.5: Dispersion induced C/N penalty as a function of transmission distance for DSB-SC method with an ASE source. Calculations with $D = 17$ ps/nm·km, $\lambda_c = 1550$ nm, $f_{RF} = 9$ GHz and $f_{IF} = 2$ GHz.

7.1.2 Fiber loop with SOA

The setup for a fiber loop with a SOA is shown in Figure 7.6. A subcarrier of 2.3 GHz is DPSK modulated with a 155 Mbit/s NRZ pseudo random ($2^{31}-1$) base band signal. The data laser is directly modulated in its intensity with a modulation index $m_a = 0.6$ to guarantee linearity. The pump laser is externally modulated by an AT&T Mach-Zehnder modulator with $f_m = 4.2$ GHz and a modulation index $m_a = 0.84$ due to electrical amplification limitations (corresponding to $P_m = 20$ dBm and $V_\pi = 7.5$ V). The length difference ΔL in the fiber loop is adjusted to 4 cm to ensure maximum transmission of the loop at 8.4 GHz and the SOA used is the one from Covega. At the output of the loop the spectrum consists of two sidebands $f_c \pm 4.2$ GHz each one modulated with the 2.3 GHz IF signal containing the baseband information plus the pump laser. Therefore, a FBG is used to filter out the unwanted pump signal. After photodetection two signals at 8.4 ± 2.3 GHz are obtained from which the one at 10.7 GHz is filtered for demodulation.

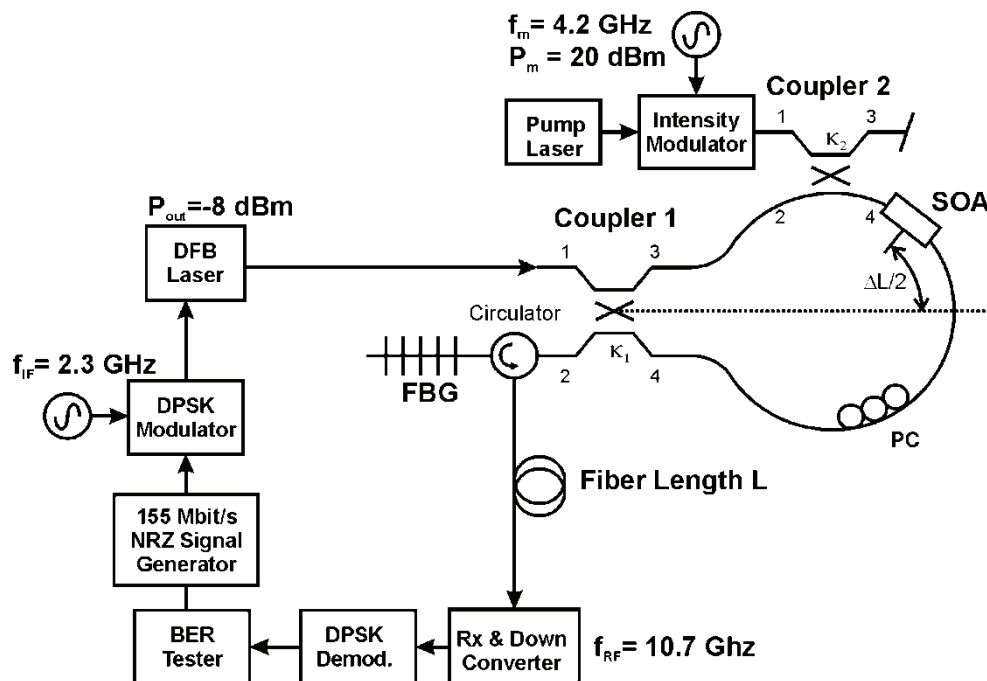


Figure 7.6: Setup for the upconversion of an IF signal at 2.3 GHz modulated with a 155 Mbit/s baseband signal using a fiber loop with Covega SOA (PC: Polarization Controller).

Figure 7.7 shows the BER for different lengths of fiber and an optical back-to-back measurement as a function of optical power at the photodiode. Considering small empirical deviations, all measured curves are showing the same slope indicating that no influence of the chromatic dispersion was observed as expected from [150].

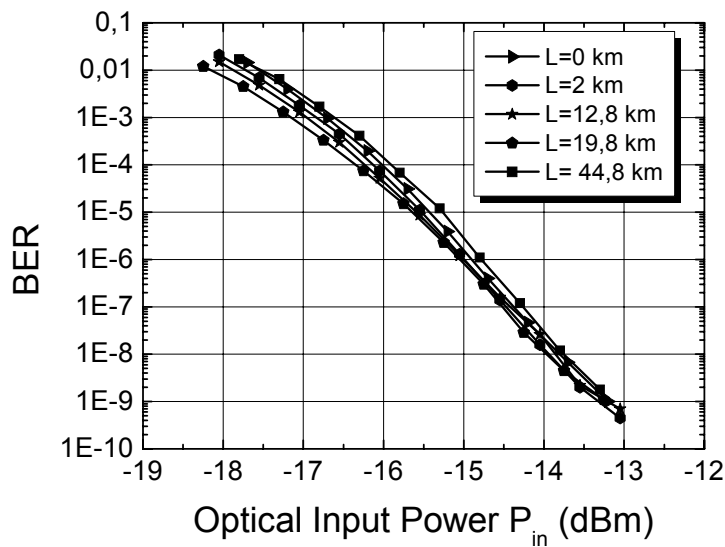


Figure 7.7: BER vs optical power at photodiode for different fiber lengths L using a fiber loop with Covega SOA.

The spans of fiber that can be used are limited mainly due to the attenuation of the fiber link and the available amplifiers. However, transmission over spans up to 44 km of SMF 28 was achieved, doubling the reach obtained with the fiber loop and a phase modulator in section 7.1.1 with no use of extra optical amplification. This makes evident the advantage of the gain introduced by the SOA inside the loop which extends the transmission distance without need of pre- and/or post-link amplification.

When using XPM of SOAs to transmit data in this scheme, there are plenty of variables which influence XPM and thus the effective transmission of the signal. To mention some there are the pump and probe powers (P_{pump} and P_{probe} respectively), wavelength separation of the pump and probe ($\Delta\lambda$), SOA temperature (T) and so on. In the next graphs the effect on the BER curves of varying these parameters will be studied.

The first parameter to be tested will be the probe power required for optimum performance. As the probe doesn't need to have high powers, generally an optical amplifier can be spared in comparison to the setup using a phase modulator. The results of varying the probe power in the range -12 to 0 dBm can be observed in Figure 7.8. The fiber length was set to $L = 0$ km, so it is an optical back-to-back measurement. Figure 7.8a shows the "high power" range. Here we can notice that high probe powers are not convenient, as the probe starts working as a pump, and thus the XPM efficiency decreases (see Appendix B.1). Optimum values for the probe power lie between -4 and -9 dBm where all the BER curves lie together. As the probe power

continues to decrease (see Figure 7.8b), the BER curve deteriorates and a BER floor is reached. This could be due to the small power of the probe signal reaching the receiver.

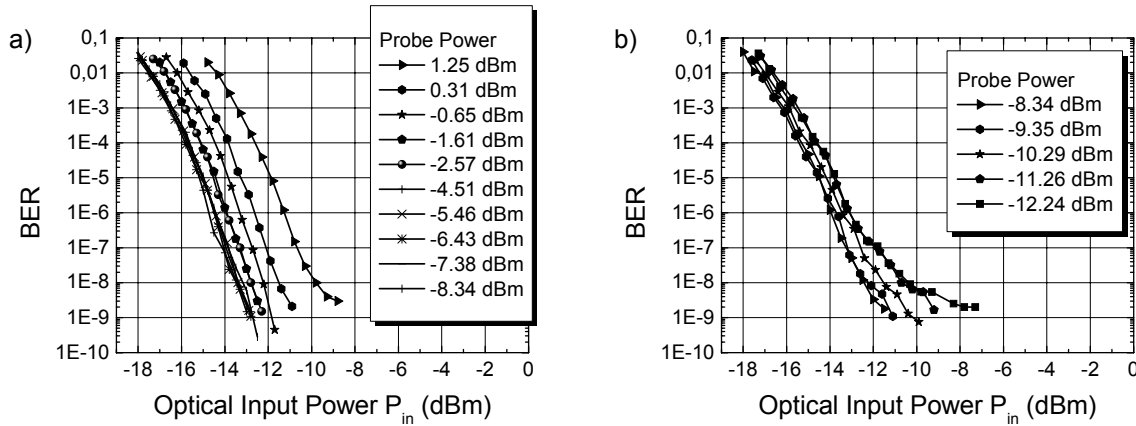


Figure 7.8: BER vs optical power at photodiode for different probe powers P_{probe} using a fiber loop with Covega SOA and fiber length $L = 0$ km.

Another parameter of interest is the pump power. Usually high pump powers (in the order of +5 dBm) are needed to have a high XPM efficiency, which is crucial in this setup. The BER curves for different pump powers can be observed in Figure 7.9. As long as the pump power remains over -1 dBm there is no distinct BER penalty to be seen. As the pump power decreases, the BER curves worsen; being the minimum pump power required -4 dBm to obtain decent results.

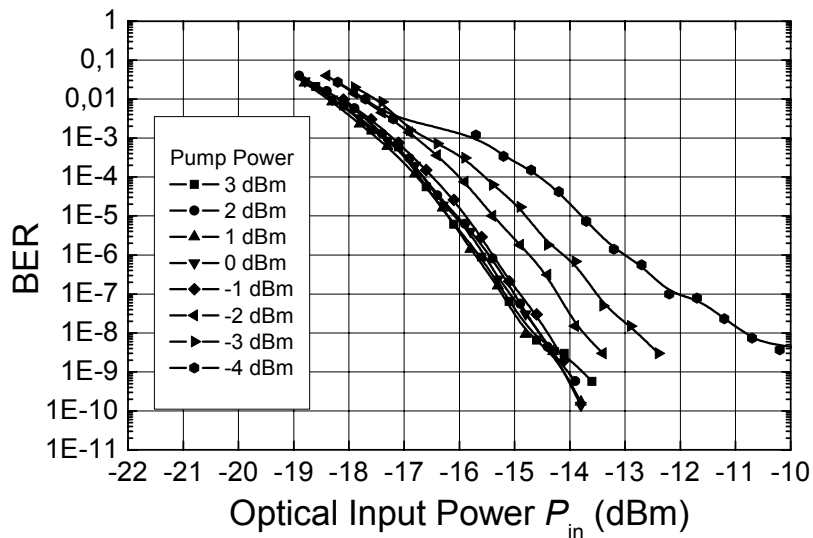


Figure 7.9: BER vs optical power at photodiode for different pump powers P_{pump} into the SOA using a fiber loop with Covega SOA and fiber length $L = 0$ km.

The next parameter of interest is the wavelength separation between the pump and the probe. The further apart they are, the less efficient the XPM effect is. The result on the BER curves can be appreciated in Figure 7.10. For this experiment, the probe was fixed at $\lambda_{probe} = 1549$ nm whereas the pump wavelength λ_{pump} was varied in the 1545 to 1554 nm range. Powers for the pump and probe were taken from the best cases of the previous tests to be $P_{pump} = +3$ dBm and $P_{probe} = -10$ dBm. As shown in Appendix B.3, varying the wavelength of the probe didn't have much influence in the modulation index. As the pump wavelength is increased to the maximum allowed by the available laser, no significant penalty could be observed for high values such as $\lambda_{pump} = 1553$ nm. The same behavior is observed for the lower wavelength range (i.e. 1545 nm). As this test could only be done around the FBG tunability of only 10 nm, this seems not to be enough wavelength separation to produce a significant difference in modulation index m_{ph} .

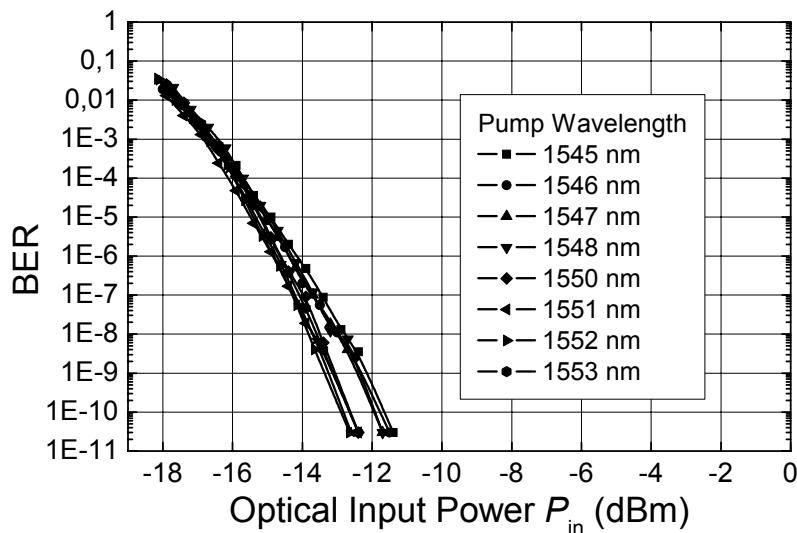


Figure 7.10: BER vs optical power at photodiode for different pump wavelengths λ_{pump} using a fiber loop with Covega SOA, $\lambda_{probe} = 1549$ nm and fiber length $L = 0$ km.

The last parameter of interest is the SOAs temperature. In all of the setups the SOA is stabilized by a temperature controller (ILX Lightwave - LDC 3722) which also provides the SOA with the injection current (to allow the SOA to operate in the inversion regime). The effects of maintaining the injection current at $I_{bias} = 500$ mA but varying the desired working temperature can be seen in Figure 7.11.

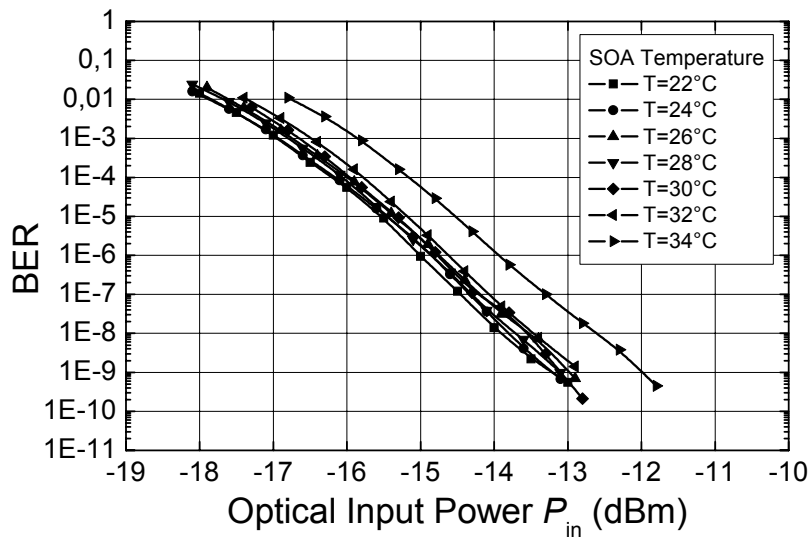


Figure 7.11: BER vs optical power at photodiode for different SOA temperatures T using a fiber loop with Covega SOA and fiber length $L = 0$ km.

As long as the SOA is cooled below 32°C the performance is optimal. For higher temperature values a BER penalty is obtained. The maximum working temperature of the SOA used (Covega) was specified to be no higher than 35°C . As shown in Appendix B.4, varying the operating temperature has no significant effects on the modulation index m_{ph} as long as the threshold temperature is not reached. Once near this temperature (in this case $T = 34^{\circ}\text{C}$) a lower m_{ph} was measured, causing the penalty observed in the BER curve.

7.2 Broadband radio over fiber wireless access

In order to transmit wireless broadband signals such as 10 Gbps of data, high mm-wave carriers are needed. Recent research is focused on transmitting on the free designated bands around 60 GHz (these vary for different countries as already described in section 2.1 and Table 2.1). In this scenario, a relative bandwidth of 10% is generally set to allow the electronics to cope with this high frequency.

From the proposed electrooptical upconversion methods described in section 5, the most efficient, stable and able to achieve high frequencies is the one using a MZM biased at the minimum transmission point. Then the next task is to modulate the broadband data optically so that it is upconverted in the base station (BS) to the desired mm-wave frequency.

7.2.1 Optical double sideband data modulation

The simplest setup is shown in Figure 7.12. It is straightforward in the fact that both generated laser lines are modulated in their amplitude by MZM₂. This method was already used in [151] with excellent wireless transmission experiments and broadband data rates as high as 12.5 Gbps at 60 GHz.

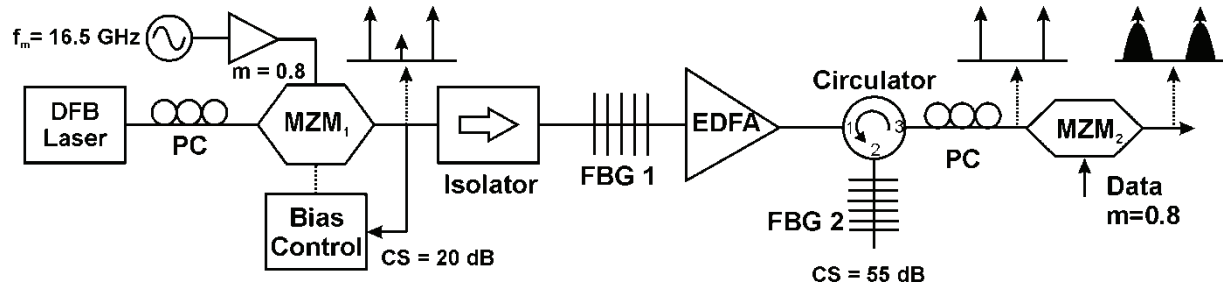


Figure 7.12: Setup I (ODSB) to transmit broadband signals with double sideband suppressed carrier data modulation.

This approach provides easy mm-wave tunability but its greatest disadvantage is the poor resilience to chromatic dispersion. As both broadband optical signals mix in the photodiode, the resulting upconverted signal is not very tolerant to dispersion. The mm-wave carrier was set to a low value of $f_{RF} = 33$ GHz to cope with the instruments available in our lab.

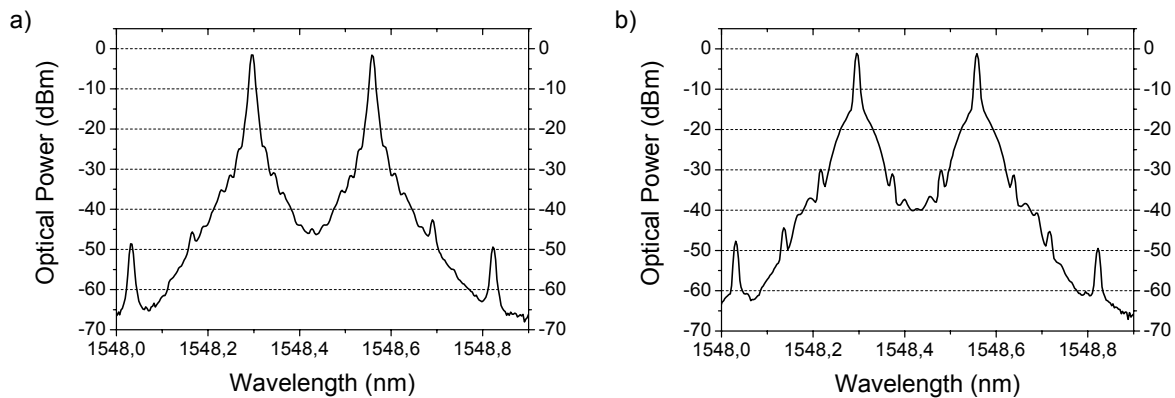


Figure 7.13: Measured optical spectra at the output of setup I for a) 2.5 Gbps and b) 10 Gbps. Resolution bandwidth = 10 pm.

The corresponding measured optical spectra for 2.5 Gbps and 10 Gbps are depicted in Figure 7.13. It is evident that both laser lines are modulated with the broadband data. For the case of 2.5 Gbps the low mm-wave carrier gives enough spacing so that the spectra do not overlap. The case of 10 Gbps is more critical, as can be observed from Figure 7.13b. The mm-wave separation is the same in both cases $f_{RF} = 33$ GHz = 0.264 nm. The suppression of the carrier is of utmost importance, as it generates an interfering spectrum. From mode partition noise

theory in DFB lasers, [152] demonstrated that a mode suppression ratio of more than 20 dB was needed to maintain the BER penalties below 0.1 dB. Taking a rough analogy, a carrier suppression of more than 20 dB would also make the interference effects negligible.

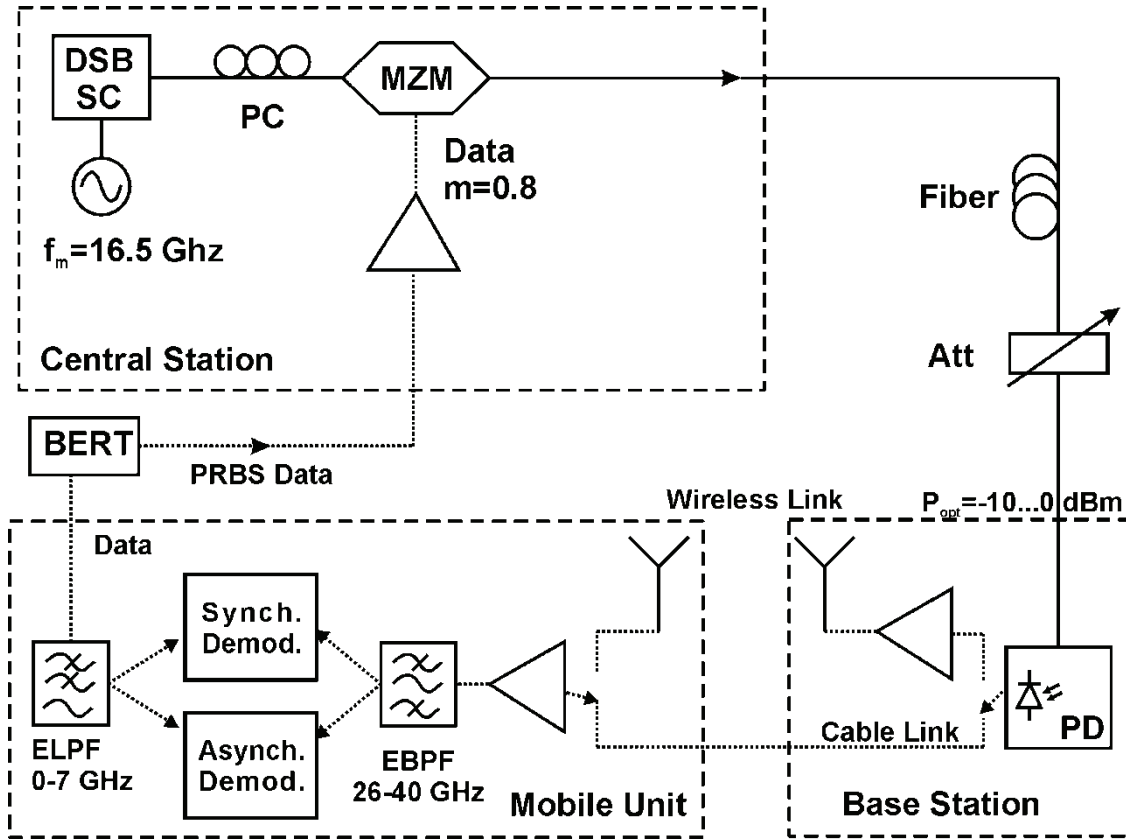


Figure 7.14: System experiments setup I to transmit broadband signals.

The system experiment for setup I is shown in Figure 7.14. Generation of the DSB-SC signal and subsequent data modulation is performed at the Central Station (CS). Then the signal is transmitted via a Single Mode Fiber (SMF) link to the Base Station (BS). In the BS the optical signal heterodynes in a broadband photodiode (NEL KEPD2525VPG, $B \approx 100$ GHz) to produce a mm-wave carrier at $f_{RF} = 33$ GHz with the broadband data modulated on it. To reach the Mobile Unit (MU) the signal is transmitted through a wireless link. Also a cable link is available for back-to-back measurements. The received RF signal is bandwidth limited by an electrical bandpass filter (EBPF) to the Ka band (i.e. 26-40 GHz). In the MU the downmixing of the RF signal can be done either synchronously with a local oscillator or asynchronously via square law detection (i.e. self-homodyne principle) or a broadband diode envelope detector. The three receivers were already introduced in chapter 6. The demodulated

data is low pass filtered (ELPF) to $B_{LP} = 7$ GHz and compared with the original transmitted data in a Bit Error Rate Tester (Advantest D3286) with a clock recovery unit from Maxim (MAX 3991) which only works for data rates between 9.95 and 11.1 Gbps.

Setting the bitrate to $R_b = 2.5$ Gbps, the back-to-back measurement (i.e. cable link) results are shown in Figure 7.15 for synchronous and asynchronous demodulation with the fiber link length L as a parameter. Using a self-homodyne receiver (see Figure 7.15b) provides mm-wave carrier independence at the cost of poor receiver sensitivity (-24 dBm electrical power for $\text{BER} = 10^{-9}$ as measured in section 6.1.2.1). Nonetheless, fiber lengths up to $L = 65$ km could be tested. By using a local oscillator (LO) in the receiver and thus using synchronous demodulation, the sensitivity is improved by 10 dB (-34 dBm electrical for $\text{BER} = 10^{-9}$ as demonstrated in section 6.1.1) and now longer fiber lengths can be tested (see Figure 7.15a). In this case an error floor is observed for $L = 70$ km at $\text{BER} = 10^{-10}$.

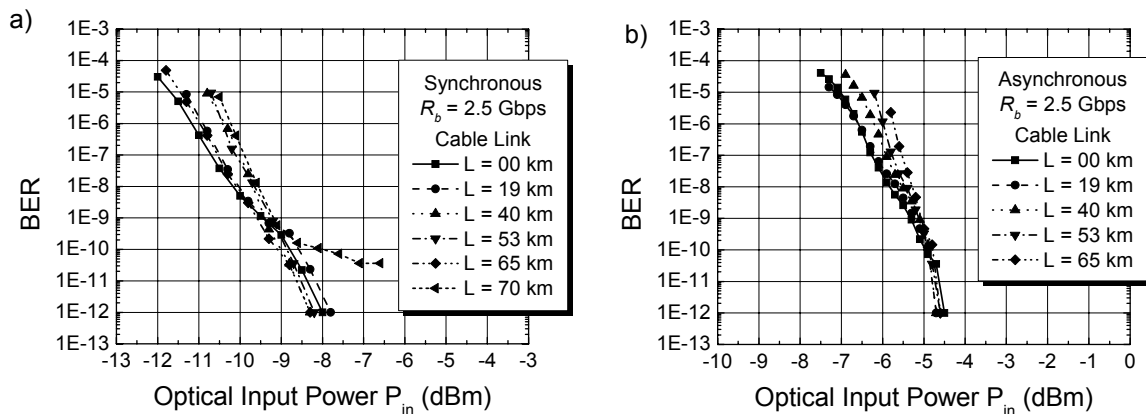


Figure 7.15: BtB BER curves for the system experiments with $R_b = 2.5$ Gbps using setup I with fiber length L as a parameter for a) synchronous and b) asynchronous demodulation.

The error floor can be better described with the eye diagrams of the recovered data shown in Figure 7.16 for the synchronous demodulation case. For $L = 0$ km the eye is open, but as the fiber link length L is increased, a closure of the eye due to fiber dispersion becomes apparent, indicated by the arrows in the figures. At the extreme case of $L = 70$ km, the eye appears totally closed at this power level, causing intersymbol interference and the error floor observed in Figure 7.15a.

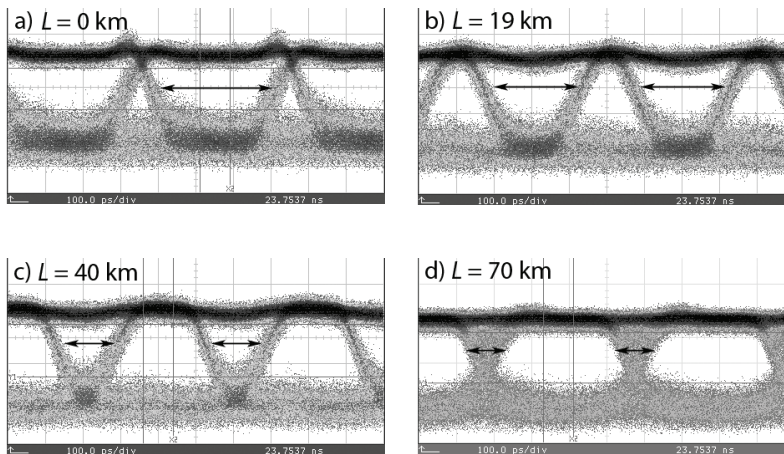


Figure 7.16: Eye diagrams for synchronous demodulation at $R_b = 2.5$ Gbps for a) $L = 0$ km, b) $L = 19$ km, c) $L = 40$ km and d) $L = 70$ km. Optical power = -8 dBm, time base = 100 ps/div and amplitude scale = 50 mV/div for all cases.

Increasing the data rate to $R_b = 10$ Gbps will be discussed next. The BER curves for this case are shown in Figure 7.17 for both demodulation techniques and the length of the fiber link L is varied. After only $L = 2$ km of SMF the effects of chromatic dispersion are evident. There is a penalty of 0.2 dB in comparison to the BtB case. Due to the RF carrier at $f_{RF} = 33$ GHz, both modulated spectral lines experience different chromatic dispersion values, which when demodulated cause intersymbol interference. This effect is expected to be worse at higher RF frequencies such as 60 GHz. As the fiber length L is increased, the penalty increases, almost 0.6 dB for $L = 5$ km. Now the curves differ for each demodulation scheme. For synchronous demodulation and $L = 7$ km error free operation is achieved, albeit with a penalty of 1 dB. However with asynchronous demodulation, for $L = 7$ km an error floor is reached at $\text{BER} = 10^{-10}$ with an optical power of $P_{opt} = -11.5$ dBm. This means that even increasing the optical power doesn't achieve lower error rates or error free transmission. As the asynchronous demodulation uses the self-homodyne principle (i.e. square law detection), saturation effects cause evidently nonlinearity penalties which make the system operate worse with higher optical powers. Nonetheless, in the synchronous demodulator scheme in Figure 7.17a also an error floor is reached at $\text{BER} = 10^{-11}$ for $L = 10$ km and $\text{BER} = 3 \cdot 10^{-9}$ for $L = 12$ km. For a fiber length of $L = 13$ km no data could be retrieved.

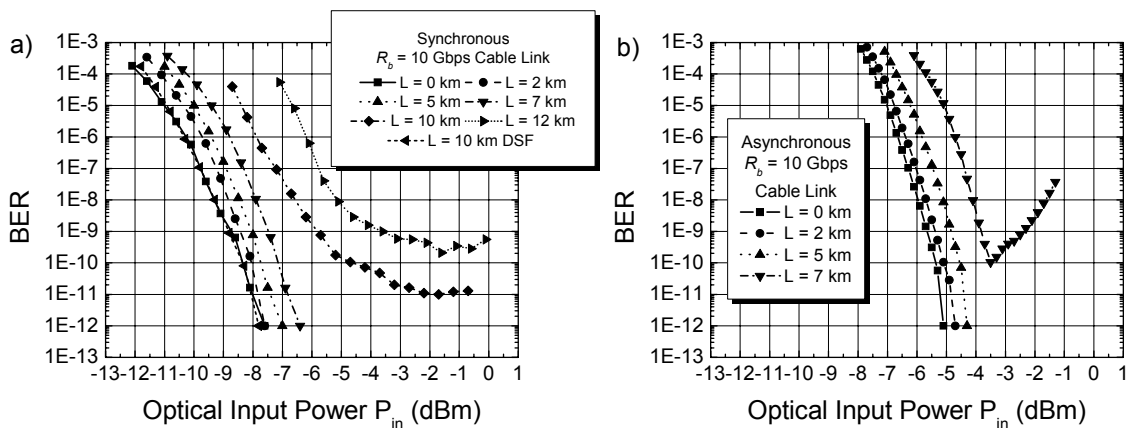


Figure 7.17: BtB BER curves for the system experiments with $R_b = 10$ Gbps using setup I with fiber length L as a parameter for a) synchronous and b) asynchronous demodulation.

The corresponding eye diagrams can be observed in Figure 7.18 for the asynchronous receiver. In Figure 7.18d, corresponding to $L = 13$ km, the eye is completely closed, indicating strong intersymbol interference effects. To test if the system is extremely impaired by chromatic dispersion, a dispersion shifted fiber (DSF) with $L = 10$ km and a dispersion value of $D = -2$ ps/nm·km at $\lambda = 1549$ nm was used for the synchronous demodulation case. The results show the same behavior as the optical BtB case of $L = 0$ km.

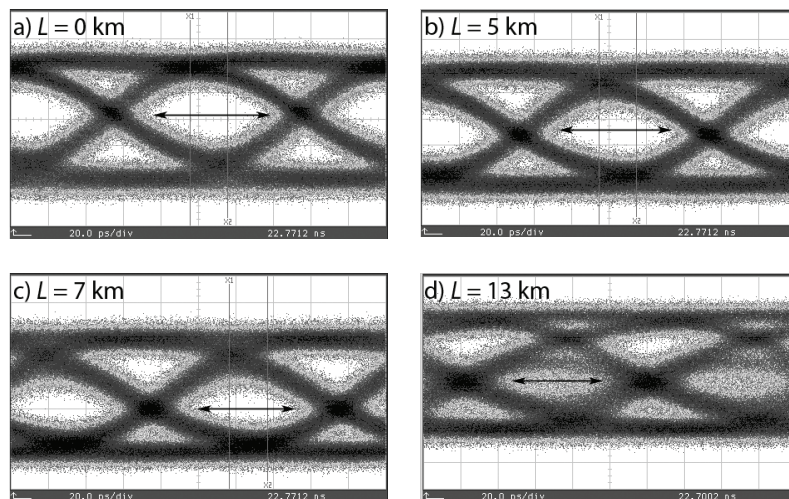


Figure 7.18: Eye diagrams at $R_b = 10$ Gbps for a) $L = 0$ km, b) $L = 5$ km, c) $L = 7$ km and d) $L = 13$ km. Optical power = -8 dBm, time base = 20 ps/div and amplitude scale = 50 mV/div for all cases.

System simulations were carried out in the commercial software VPI TransmissionMaker 8.0 using an ideal heterodyne receiver (a detailed schematic can be found in Appendix D, Figure D.3). The BER curves for setup I are shown in Figure 7.19a using an RF bandwidth of $B_{RF} = 14$ GHz (which is available in the lab but not in the international regulations) and a low pass filter with $B_{LP} = 7.5$ GHz. The curves exhibit approximately the same behavior as the measurements besides the fact that using an ideal receiver reduces the optical power needed drastically. Nonetheless, the same error floors due to fiber dispersion as in the measurements are observed for $L = 10$ km and $L = 12$ km. Simulating for $L = 15$ km shows an even higher error floor which could not be achieved in the laboratory (the eye closes completely for $L = 13$ km, as seen in Figure 7.18d).

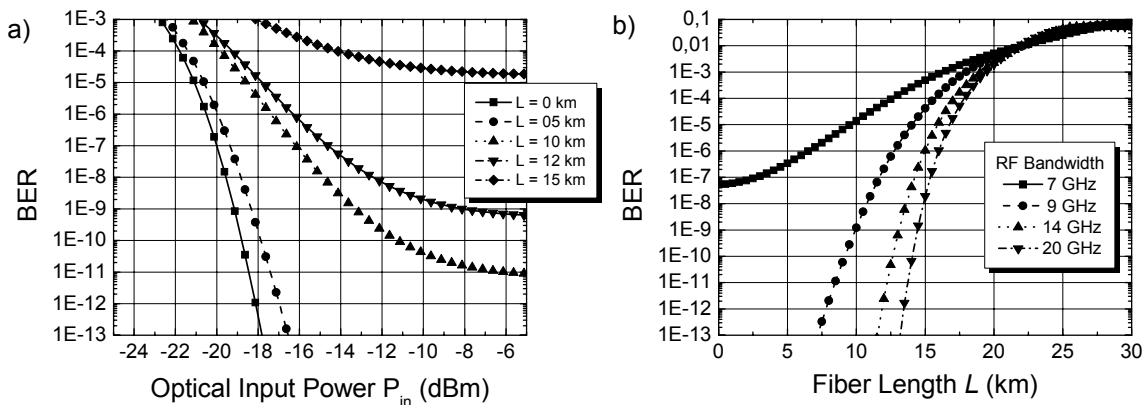


Figure 7.19: System simulations with $R_b = 10$ Gbps using setup I. a) BER curves with fiber length L as a parameter and b) BER as a function of fiber length L for different RF bandwidths.

Figure 7.19b depicts the influence of the RF bandwidth on the BER as a function of fiber length. It is evident that higher RF bandwidths accommodate larger signal power and thus, lower BER. However, increasing the bandwidth past 14 GHz doesn't provide a large improvement. Moreover, the regulations in the 60 GHz spectrum dictate a bandwidth limit of 7 GHz in USA and 9 GHz in Europe, meaning a more efficient way of using the limited spectrum is vital in achieving high data rates for decent fiber transmission lengths.

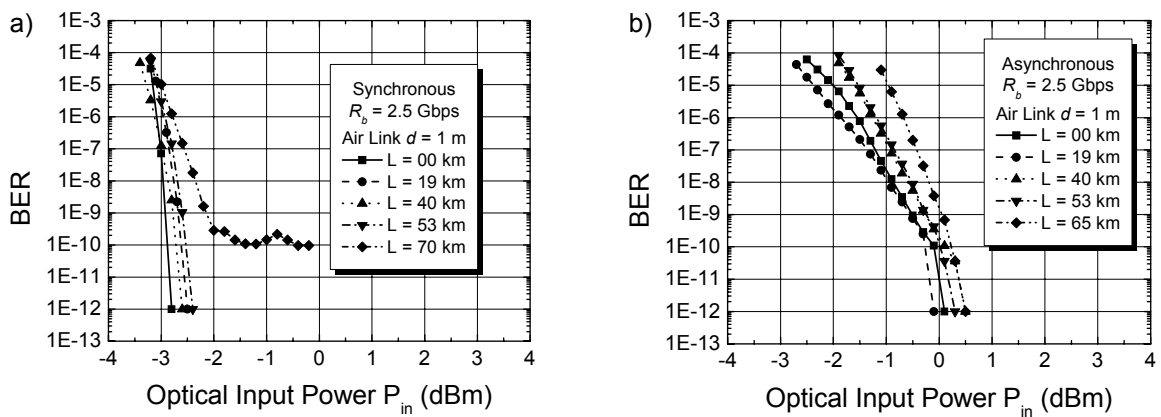


Figure 7.20: BER curves for the system experiments with $R_b = 2.5$ Gbps using setup I and transmission over a wireless link of $d = 1$ m for a) synchronous and b) asynchronous demodulation.

For the first wireless link, two broadband (4-40 GHz) Vivaldi antennas (DRH40) with nominal gains at the transmitter and receiver of $G_{TX} = G_{RX} = 15$ dB were used. The link loss of our system is $LL = 33$ dB at $f_{RF} = 33$ GHz and for $d = 1$ m. The results of a wireless link with $d = 1$ m are shown in Figure 7.20 for $R_b = 2.5$ Gbps and both demodulation schemes. The results are similar to the cable link case but with a higher optical power requirement. Nonetheless, this indicates negligible influence of the wireless link at this short distance.

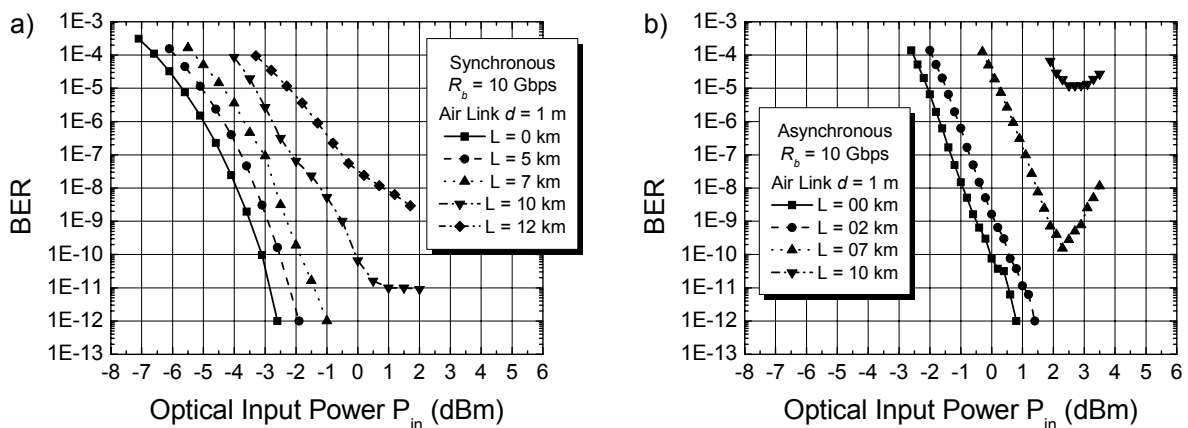


Figure 7.21: BER curves for the system experiments with $R_b = 10$ Gbps using setup I and transmission over a wireless link of $d = 1$ m for a) synchronous and b) asynchronous demodulation.

The case for $R_b = 10$ Gbps is shown in Figure 7.21. Again, the short wireless link doesn't play an important role, as the curves are analogous to the cable link case. The same error floors are reached at the same fiber link lengths. Moreover, the same saturation effects and nonlinear

penalties are observed for asynchronous demodulation. Worth of notice is the high penalty and error floor at $\text{BER} = 10^{-5}$ in Figure 7.21b for $L = 10$ km.

7.2.2 Optical single sideband data modulation

As opposed to the previous section, the idea behind setup II is to modulate only one optical line with the broadband data. In this way, a superior dispersion tolerance can be achieved. There are plenty of ways of separating phase correlated optical lines to transmit broadband signals, as demonstrated in [108],[153]-[156]. Our setup is based on [108] so that a custom made optical Mach Zehnder Interferometer (MZI) with a Free Spectral Range (FSR) of twice the mm-wave frequency used is employed (see Figure 7.22).

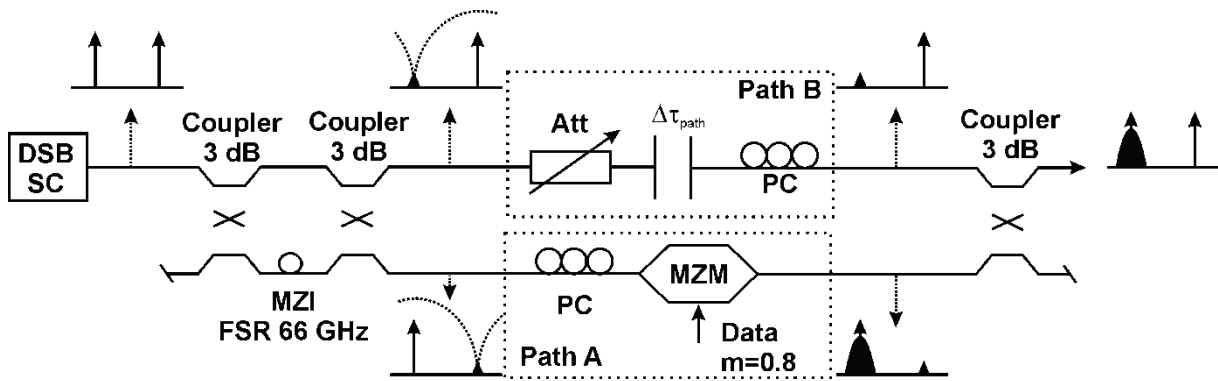


Figure 7.22: Setup II to transmit broadband signals with single sideband data modulation.

The two phase correlated spectral lines are generated in the same way as in section 7.2.1, with a MZM biased at minimum transmission and an extra carrier suppression FBG (optical spectrum shown in Figure 7.23a). As depicted in Figure 7.22, the FSR of our MZI is set to $\text{FSR} = 66$ GHz. In this way, both spectral lines are separated into two different optical paths (path A and B) with more than 30 dB suppression (see Figure 7.23b). Path A is NRZ modulated with the broadband data (i.e. $2^{31}-1$ PRBS sequence) by using a MZM with a modulation index $m_a = 0.8$ to ensure no overmodulation, as in the previous section (see Figure 7.23c). On the other hand, path B is only attenuated, delayed τ seconds and tuned in its polarization to obtain maximum coupling at the last coupler. By adjusting the path imbalance delay $\Delta\tau_{\text{path}}$ between path A and B, the tolerance to dispersion can be controlled [96]. However, for the upcoming experiments, the delay τ was adjusted so that path A and B are of equal length (i.e. $\Delta\tau_{\text{path}} = 0$). After reuniting the signals in a 3 dB coupler, an optical single

sideband (OSSB) signal with the desired mm-wave frequency separation is obtained (see Figure 7.23d).

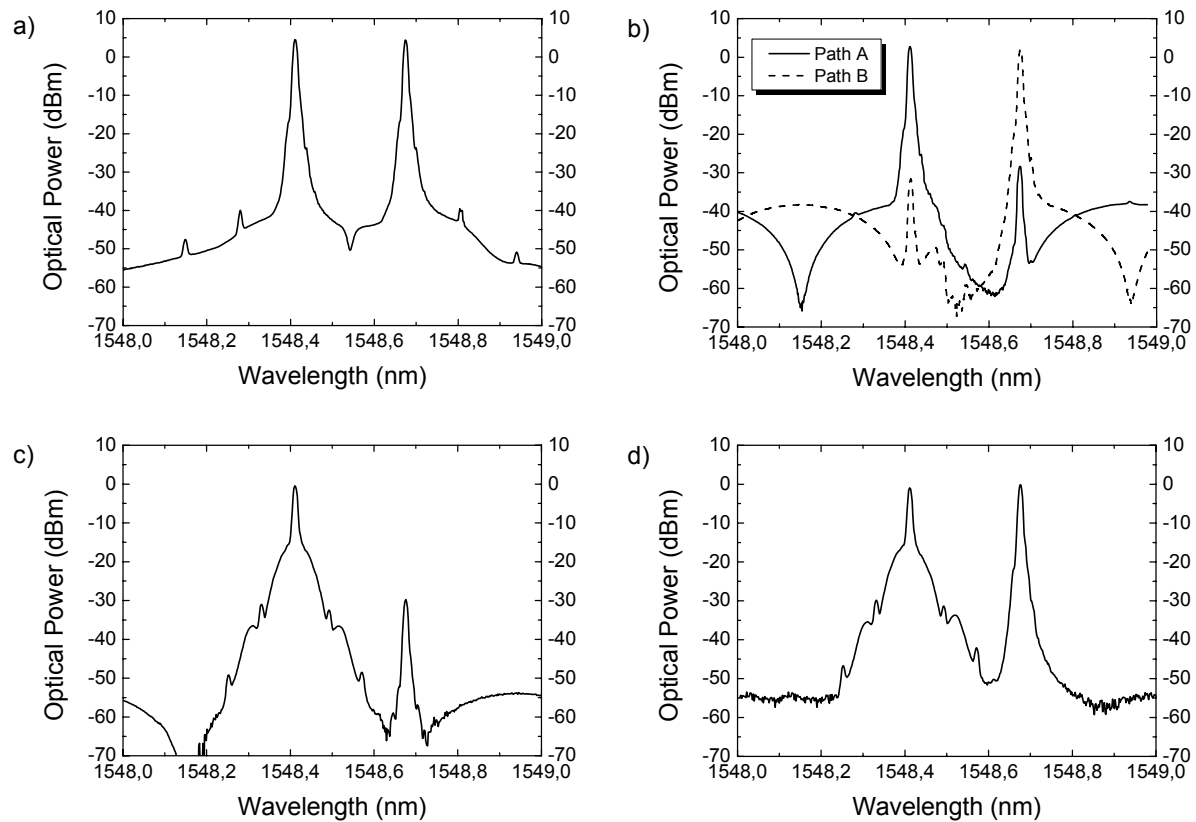


Figure 7.23: Optical spectra for setup II at a) DSB-SC, b) after MZI, c) path B after data modulation and d) OSSB signal. $R_b = 10$ Gbps, resolution bandwidth = 10 pm.

The system experiments setup is the same as in the previous section but now using OSSB data modulation. Nonetheless, a setup schematic is shown in Figure 7.24. An extra EDFA is used to amplify the signals before photodetection. As usual, an optical bandpass filter (OPBF) with bandwidth $B = 1$ nm is used to limit the ASE from the EDFA (see optical spectrum in Figure 7.23d). The system allows multigigabit transmission with data rates up to 10 Gbps. At the receiver end, a synchronous receiver (i.e. with a local oscillator) presents some major problems as the path separation of the signal in the MZI and subsequent combining after data modulation creates a stringent requirement on the phase tracking of the mm-wave signal. Therefore a phase-locked loop is needed to match the phase of the mm-wave carrier and the local oscillator. Even though they are locked in frequency through the 10 MHz reference port, the phase mismatch results in amplitude variations of the recovered data. At the time of the experiments no PLL was available (nor designed) and the resulting phase divergence varied

too quickly to obtain realistic measurements. For this reason, the self-homodyne receiver was preferred in this case.

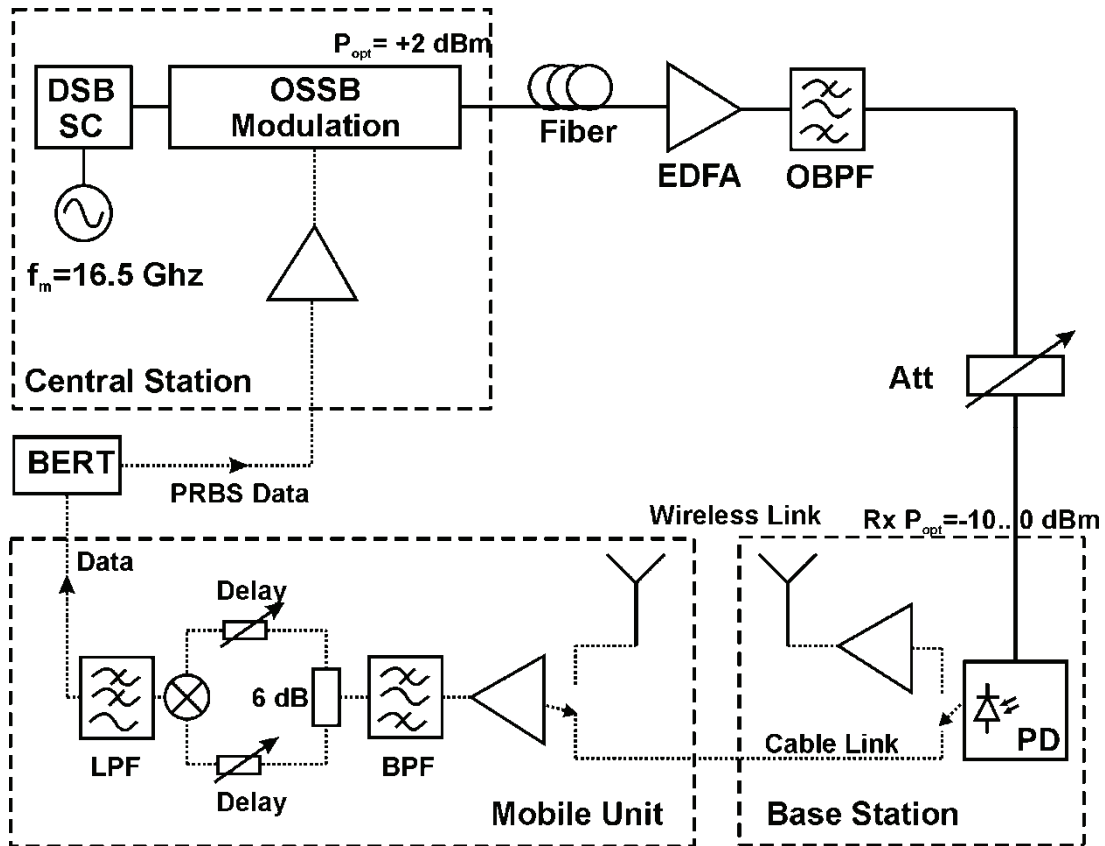


Figure 7.24: System experiments setup II to transmit broadband signals using OSSB data modulation.

Transmission of 2.5 Gbps was already demonstrated in [153] but with a different setup using Fiber Bragg Gratings to carry out the optical spectral line separation. In this context, the first experiments will be carried out with a data rate of 2.5 Gbps to test and compare the proposed system. The BER curves for the 2.5 Gbps cable link case are shown in Figure 7.25a for different fiber lengths L . The curves show all the same slope indicating a good tolerance to chromatic dispersion up to 69 km. Even after 69 km of SMF there is no significant penalty due to chromatic dispersion. Theory from section 4.4 predicts negligible C/N penalties for this approach, and from Figure 4.19 and using a laser linewidth of $\Delta\nu = 10$ MHz (typical values for the DFB lasers used) even after 100 km fiber transmission the penalty is only 0.12 dB. Simulations neglecting fiber attenuation for this kind of system are shown in Figure 7.25b (a detailed schematic can be found in Appendix D, Figure D.4). The dispersion penalty after

120 km SMF is only 1 dB at $\text{BER} = 10^{-9}$, indicating the system would be attenuation limited before dispersion starts playing an important role. Using longer fiber lengths such as $L = 90$ km, the effects of amplification limit start showing. For this long distance, the gain of the EDFA is maximized, and thus its noise contribution. The BER curve has a different slope, reaching error free operation but with a penalty of 1 dB compared to the optical back to back case. This is can also be caused by the lack of a matched filter for $R_b = 2.5$ Gbps. The low pass filter (LPF in Figure 7.24) was designed for $R_b = 10$ Gbps and thus doesn't shape the lower data rate pulses into a raised cosine form, which is the optimum pulse form for demodulation [140].

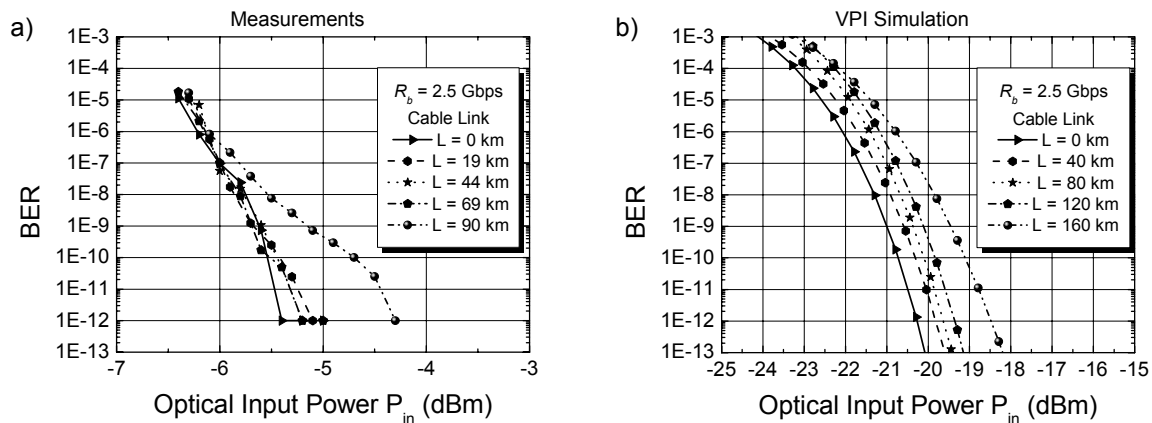


Figure 7.25: 2.5 Gbps BER curves for a) the system experiments setup II for the cable link case and different fiber lengths L and b) simulations in VPI.

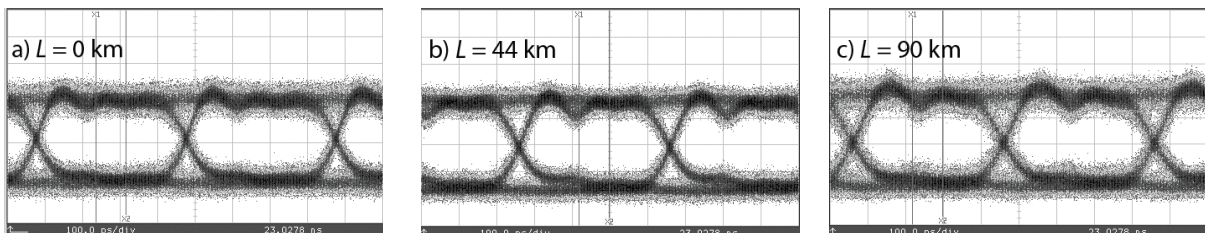


Figure 7.26: Eye diagrams at $R_b = 2.5$ Gbps for setup II cable link case for a) $L = 0$ km, b) $L = 44$ km and c) $L = 90$ km of SMF and optical power at the photodiode = -3 dBm. Time base = 100 ps/div, amplitude scale = 50 mV/div.

The corresponding eye diagrams were measured with a sampling scope after recovery and are shown in Figure 7.26. Some ringing effects are evident, but this may be due to the low pass filter used, which has a bandwidth $B = 7$ GHz, which is designed for 10 Gbps signals according to ITU-T specifications. Nonetheless, the distortions increase with longer fiber

length L and by $L = 90$ km the signal is much noisier, leading to a change in BER slope and the 1 dB penalty at $\text{BER} = 10^{-12}$.

The next data rate of interest would be 10 Gbps. For this case, a clock recovery circuit from MAXIM was available. The MAX 3991 recovers and reshapes the data and extracts the clock out of it for BER measurements. It operates for data rates ranging from 9 to 11.1 Gbps according to the manufacturer. The data and clock recovery unit is placed right after the LPF, before entering the BER tester. In this way, the clock reference is the same for all measurements, independent of the fiber length L tested. For the optical back-to-back case and a data rate of 10 Gbps, the BER curves are shown in Figure 7.27a.

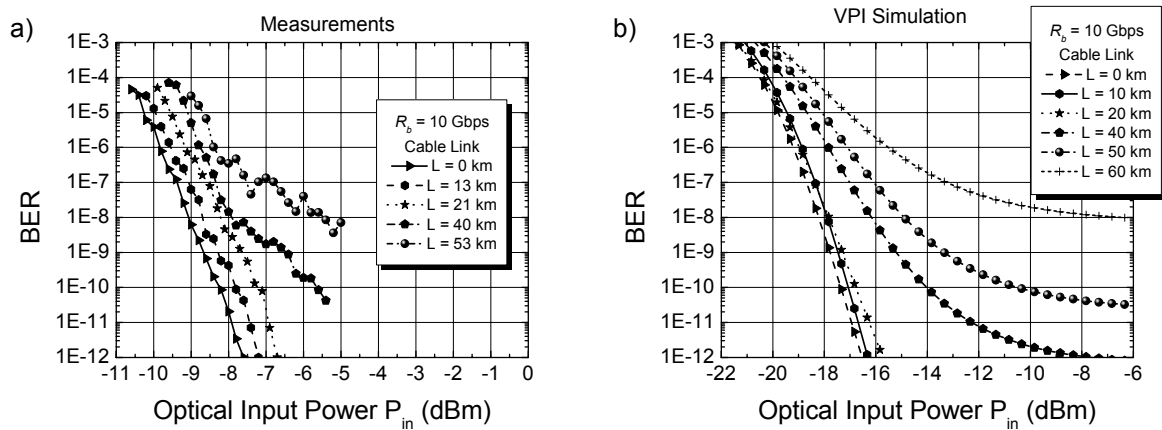


Figure 7.27: 10 Gbps BER curves for a) the system experiments and b) simulations in VPI for setup II cable link case and different fiber lengths L .

All the curves up to $L = 21$ km show the same slope, the penalty due to fiber chromatic dispersion are measured to be 0.4 dB, 1 dB and 2.2 dB for $L = 13$, 21 and 40 km and $\text{BER} = 10^{-9}$. For $L = 40$ km chromatic dispersion starts to influence the signal with its characteristic change in slope. The case of $L = 53$ km is much more critical, not even reaching $\text{BER} = 10^{-9}$. Figure 7.27b shows system simulations in VPI using the schematic depicted in Figure D.5 and increasing the data rate to 10 Gbps. It demonstrates that chromatic dispersion starts affecting the system for $L = 40$ km even using an ideal heterodyne receiver. As a rule of thumb, the maximum distance for 10 Gbps NRZ and $\text{BER} = 10^{-9}$ is around 60 km in a real system, where not even $\text{BER} = 10^{-9}$ can be reached as expressed in the simulations. Nonetheless, much longer distances could be achieved than with setup I, where by $L = 13$ km

no data could be retrieved. Moreover, a small penalty in comparison to an ideal baseband transmission of optical broadband signals could be achieved.

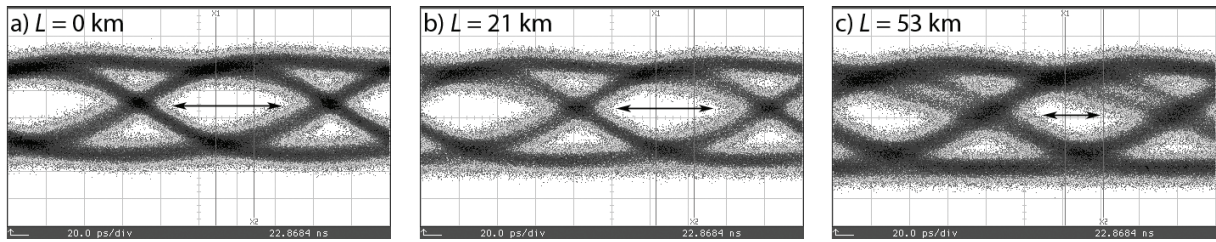


Figure 7.28: Eye diagrams at $R_b = 10$ Gbps for setup II cable link case for a) $L = 0$ km, b) $L = 21$ km and c) $L = 53$ km of SMF and optical power at the photodiode = -1.6 dBm. Time base = 20 ps/div, amplitude scale = 50 mV/div.

The corresponding eye diagrams are shown in Figure 7.28. The eye appears undistorted even after 21 km of SMF transmission. For $L = 53$ km, the eye closure leading to an increased BER is evident.

For the wireless experiments the same Vivaldi DRH40 antennas as the previous section were used. The link loss is still 33 dB for $d = 1$ m. In defining the wireless reach of the system, one key parameter is the photodiode used. As the amount of electrical amplification of the system is limited due to group delay response, especially for high data rates as 10 Gbps, a high power photodiode with a decent responsivity R provides a longer reach. The first available photodiode is a broadband one from the company NEL (KEPD2525VPG, $B > 100$ GHz, $R = 0.9$ A/W) but its main drawback is that it allows operation with low input optical powers ($P_{max} = 0$ dBm). Using this photodiode, the maximum wireless reach for error free operation was experimentally demonstrated for $d = 1$ m and a data rate of 10 Gbps over 21 km of SMF [157]. To increase the wireless reach either a greater responsivity R is required or a photodiode capable of handling high optical input powers. The company u2t provides such a photodiode with its XPDV3120R with a lower bandwidth (i.e. $B = 70$ GHz), but it can handle optical input powers up to $P_{opt} = +13$ dBm and has a responsivity $R = 0.6$ A/W. The reduced responsivity is more than compensated by the 13 dB more optical power which can be delivered to the photodiode. Figure 7.29 shows the BER curves for a data rate of 2.5 Gbps and a wireless link of $d = 1.1$ m using this high power photodiode from u2t.

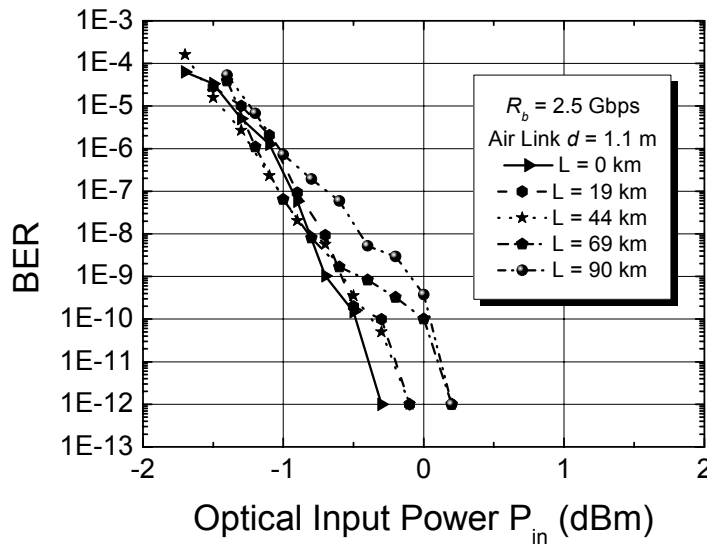


Figure 7.29: BER curves for the system experiments with $R_b = 2.5$ Gbps and setup II for a wireless link of $d = 1.1$ m and different fiber lengths L .

The BER curves behave comparable to the cable link case showing the same slope up to $L = 69$ km. A small deviation at $L = 69$ km can be seen, attributed to the wireless channel. As in the cable case, for $L = 90$ km, the slope changes, making evident the limits of this approach due to chromatic dispersion in the fiber.

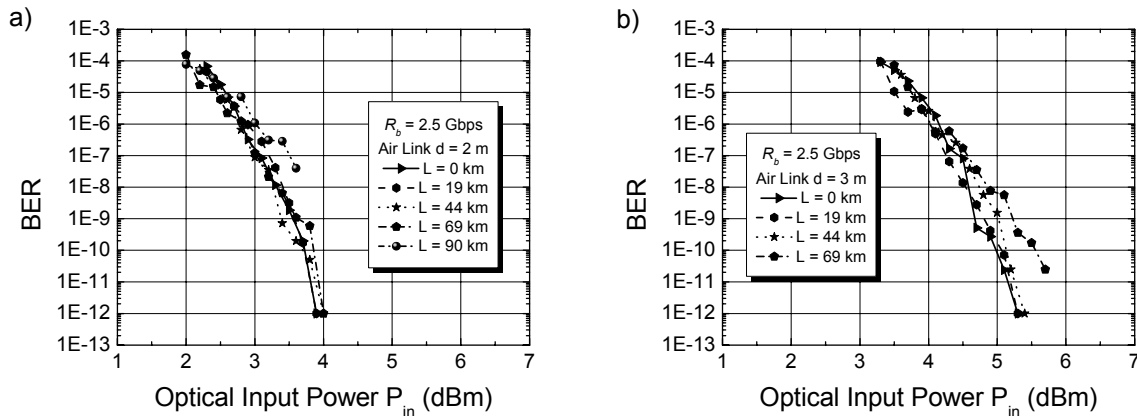


Figure 7.30: BER curves for the system experiments with $R_b = 2.5$ Gbps and setup II for a wireless link of a) $d = 2$ m and b) $d = 3$ m for different fiber lengths L .

Increasing the wireless distance to $d = 2$ m and $d = 3$ m result in the curves shown in Figure 7.30. No significant change in performance is observed despite the change in wireless reach. As the optical power was limited, for $L = 90$ km SMF the power budget was at the limit of the labs capacity. That is why for $d = 2$ m the curve starts with $\text{BER} = 10^{-8}$ and for $d = 3$ m this

link could not be tested. Nonetheless, with sufficient optical amplification the same performance as for the $d = 1.1$ m link can be expected.

In Figure 7.31 the results with a data rate of 10 Gbps are presented for a wireless link with $d = 1.1$ m. The curves exhibit the same slope as the optical BtB case and error free transmission is achieved even after 21 km of SMF. As in the cable case, for $L = 40$ km, an error floor is reached at $\text{BER} = 10^{-10}$ due to chromatic dispersion. The change in slope is also evident, as well as in the $L = 50$ km case, where the error floor is now $\text{BER} = 10^{-9}$, barely reaching the BER requirements for access networks. The penalties for $\text{BER} = 10^{-9}$ are now 0.4 dB for $L = 21$ km and 1.4 dB for $L = 40$ km, much lower than in the cable case. Even the performance for $L = 50$ km is improved, reaching $\text{BER} = 10^{-9}$, meaning that the bandwidth limitation imposed by the antennas (4-40 GHz) proves helpful for the system performance.

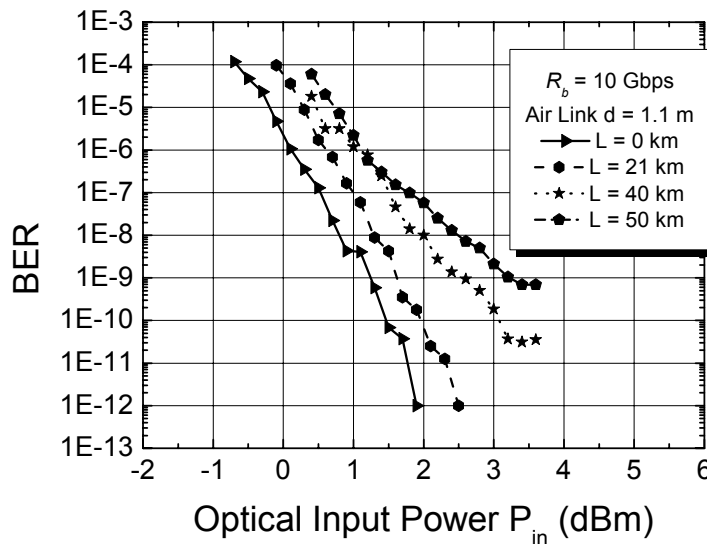


Figure 7.31: BER curves for the system experiments with $R_b = 10$ Gbps and setup II for a wireless link of $d = 1.1$ m for different fiber lengths L .

For $d = 2$ m the link loss increases in 6 dB, and is now $LL_{2m} = 38.8 \pm 2.5$ dB. Respectively, $LL_{3m} = 42.3 \pm 2.5$ dB for $d = 3$ m. Both wireless links are depicted in Figure 7.32. For $d = 2$ m, the performance degrades significantly. Although error free operation was achieved up to 21 km SMF transmission, for 40 and 50 km the BER is one order of magnitude worse as the previous case. Similar behavior happens for $d = 3$ m, where not even the optical BtB is error free. It seems that for our system, 1 m increase in wireless link length degrades to one order of magnitude in BER.

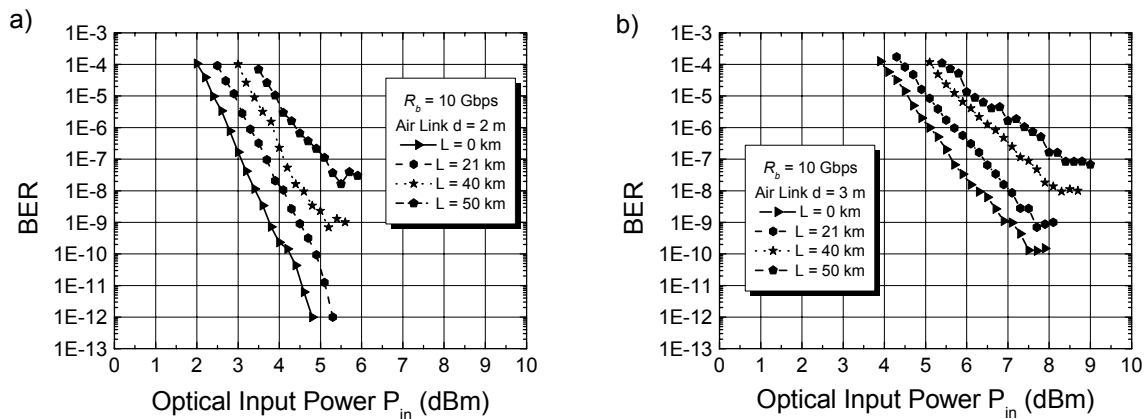


Figure 7.32: BER curves for the system experiments with $R_b = 10$ Gbps and setup II for a wireless link of a) $d = 2$ m and b) $d = 3$ m for different fiber lengths L .

By changing the receiver Vivaldi antenna with a Horn antenna with $G_{RX} = 24$ dB, the link loss is reduced in 9 dB, meaning greater distances can be achieved. Pushing the limits of amplification and lab space, the results for $d = 5$ m and $d = 7$ m are shown in Figure 7.33, corresponding to $LL_{5m} = 37.8$ dB and $LL_{7m} = 40.7$ dB, respectively.

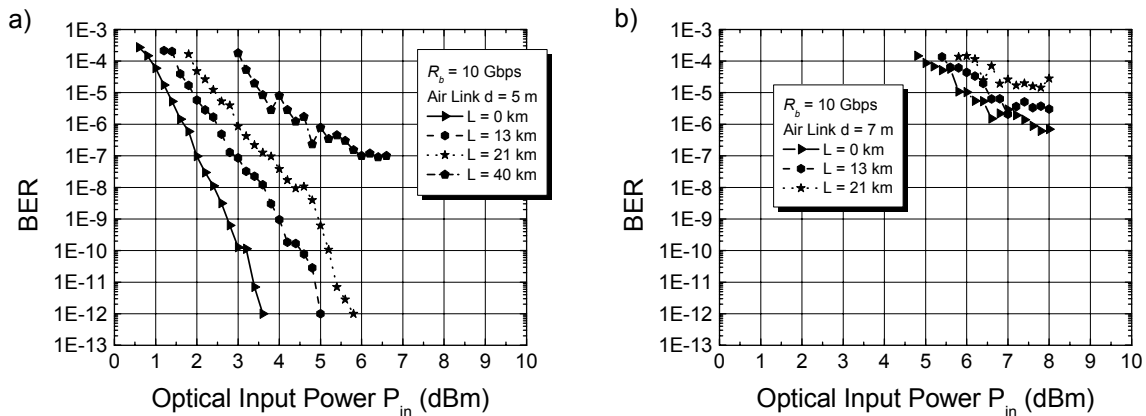


Figure 7.33: BER curves for the system experiments with $R_b = 10$ Gbps and setup II for a wireless link with a horn receiver for a) $d = 5$ m and b) $d = 7$ m for different fiber lengths L .

Although the link loss LL is comparable to the previous measurements with $d = 2$, for $d = 5$ m the performance starts deteriorating significantly for $L = 40$ km, but is error free up to $L = 21$ km, showing the same slope as the previous cases. In the case of $d = 7$ m, no special care was taken with regard to multipath effects, and the link was operated across the lab, with plenty of metal and interference objects. Even though the line of sight was clear, BER not better than 10^{-6} could be achieved. This is sufficient for a femtocell network distribution

system but not good enough for wireless access, which require at least a $BER = 10^{-9}$. The penalties for $BER = 10^{-9}$ and the different configurations as a function of fiber length L are summarized in Table 7.1 for the 10 Gbps system experiments.

	BtB	Wireless 1.1 m	Wireless 2m	Wireless 3m
21 km	1	0.4	0.8	0.8
40 km	2.2	1.4	1.2	N/A

Table 7.1: 10 Gbps system penalties in dB for $BER = 10^{-9}$.

Surprisingly the penalties for the BtB case are higher than for the wireless transmission experiments. This can be attributed to the higher powers available in the BtB case which drive the amplifiers into saturation, producing distortions and this, higher penalties. The loss introduced through the wireless link lets the amplifiers work in a linear regime, minimizing nonlinear distortions.

To increase the wireless distance, the receiver in the mobile unit presents plenty of improvement opportunities. The self-homodyne receiver provides mm-wave carrier independence at the cost of a poor sensitivity (in our case, -24 dBm for $BER = 10^{-9}$) and requires plenty of RF amplification. By using classic LO downconverting schemes, the sensitivity can be improved up to -45 dBm and wireless links were demonstrated up to 20 m for 10 Gbps [151]. The main drawback from this scheme is the requirement of synchronization of the LO and RF signals, usually through a PLL or coupling of the transmitter and receiver mm-wave oscillators, to achieve stable operation.

7.2.3 Comparison ODSB vs OSSB

To better compare the performance of the ODSB method from section 7.2.1 and the OSSB method from section 7.2.2, a sampling scope measurement right after the photodiode is quite useful. Here the baseband data and the mm-wave carrier with the broadband data are detected, and one can infer the effects of fiber dispersion on the baseband signal from the corresponding eye diagrams. However, this kind of measurement poses some triggering problems. The setup used for these measurements is shown in Figure 7.34, with the mm-wave carrier remaining at $f_{RF} = 33$ GHz, but the data rate has to be a fraction of the modulation

frequency f_m , thus the clock for the PRBS generator is driven with $f_R = f_m/2$ setting the data rate to $R_b = 8.25$ Gbps (1/4 from f_{RF}).

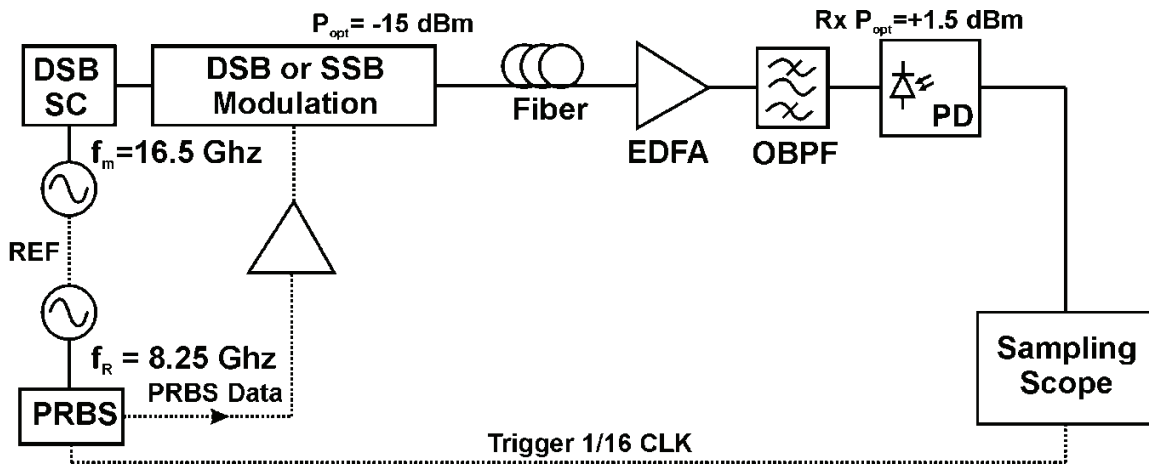


Figure 7.34: Setup to measure the mm-wave plus baseband signal.

First of all, for a clear picture, all microwave sources have to be synchronized. That means that the generator modulating the DSB-SC subsystem and the clock for the PRBS generator need to have the same electrical reference, which is the link marked as REF in Figure 7.34. Second, the selection of the data rate is not trivial, as it needs to be an exact divisor of the resulting mm-wave frequency. That is why $R_b = \frac{1}{4} f_{RF} = 8.25$ Gbps was chosen and taken from the coupled generator with $f_R = 8.25$ GHz. Finally, the trigger signal for the sampling scope is taken from the PRBS generators CLK/16 output which in this case is approximately 515 MHz.

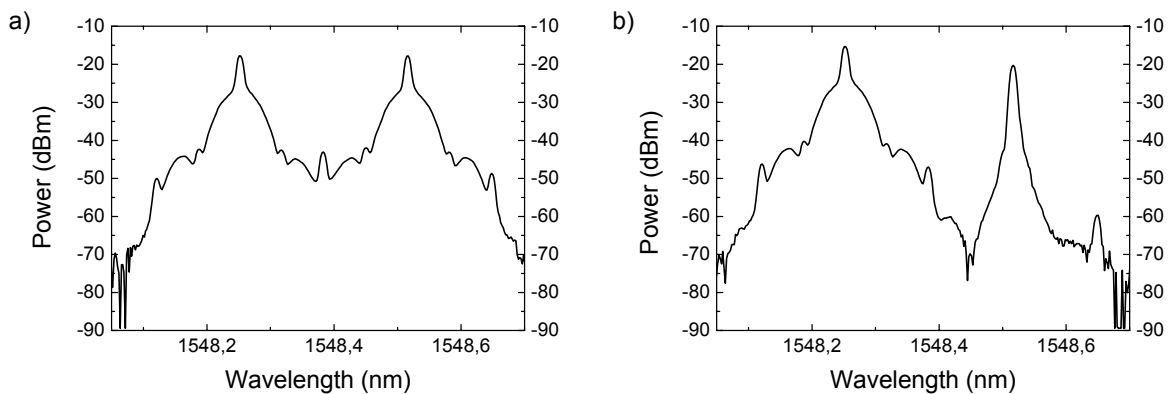


Figure 7.35: Optical spectra for a) the ODSB and b) OSSB setup both with $m_a = 0.8$. Data rate $R_b = 8.25$ Gbps. Resolution bandwidth = 10 pm.

The power spectrum for both setups is shown in Figure 7.35. Figure 7.35a depicts the ODSB signal with the data rate $R_b = 8.25$ Gbps. A small spectral overlap is present, as the mm-wave frequency is relatively small. The relative bandwidth of the system is 25%. Figure 7.35b on the other hand, shows the OSSB power spectrum, with a modulated signal and unmodulated LO signal for the mm-wave upconversion. The whole bandwidth of the baseband signal is undistorted.

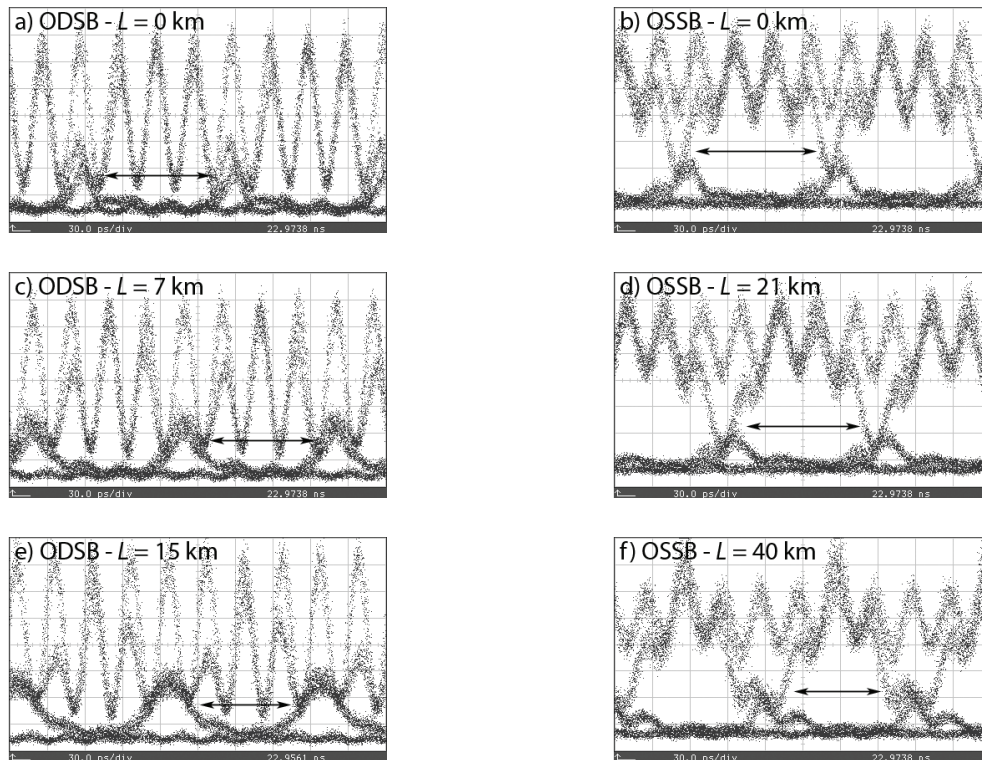


Figure 7.36: Eye diagrams with mm-wave signal plus baseband for the ODSB and OSSB setups. Fiber lengths a) $L = 0$ km, b) $L = 0$ km, c) $L = 7$ km, d) $L = 21$ km, e) $L = 15$ km and f) $L = 40$ km. Optical power = 1.5 dBm, time base = 30 ps/div and amplitude scale = 10 mV/div for all cases.

The resulting eye diagrams measured with the sampling scope are displayed in Figure 7.36 as a function of the transmission fiber length L . It is evident that for the ODSB case, the baseband signal is much more dispersion compromised, as the eye starts closing for $L = 7$ km and even more for $L = 15$ km. As the two sidebands experience different group delays, this causes the distortion when mixed with each other at the mixer. In the OSSB case, however, even after $L = 40$ km transmission over SMF, the baseband eye remains open. Testing the limits of the OSSB system with regard to optical amplification is shown in Figure 7.37 where

the transmission length was extended to 65 and even 90 km. Even though the signal is pretty much distorted, the baseband eye remains open, finally proving the superior dispersion immunity of the OSSB method in comparison with the easy to setup ODSB approach.

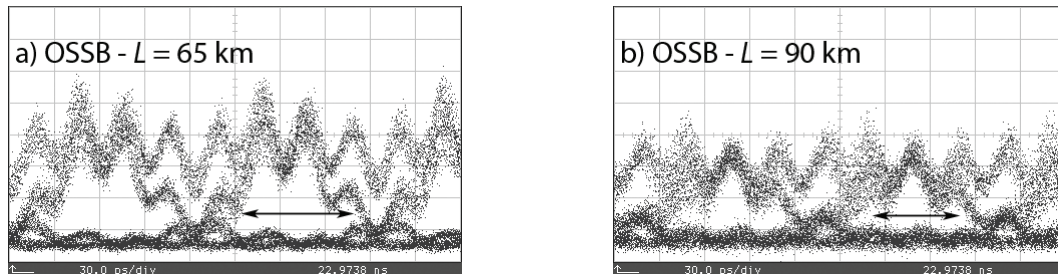


Figure 7.37: Eye diagrams with mm-wave signal plus baseband for the OSSB setups. Fiber lengths a) $L = 65$ km and b) $L = 90$ km. Optical power = 1.5 dBm, time base = 30 ps/div. Amplitude scale = 10 mV/div in a) and 5 mV/div in b).

7.3 Heterodyned uncorrelated lasers

The simplest method to generate mm-wave signals would be to heterodyne two uncorrelated laser sources. This method produces higher phase noise mm-wave signals and is thus discarded as an efficient mm-wave generation scheme also due to the small laser wavelength variations which cause mm-wave jitter. On the other hand, depending on the application, this idea can prove beneficial. For example, this could be used to benefit from existing 10 Gigabit Ethernet (10 GbE) connections from Fiber to the Home (FTTH) architectures. In this way, the 10 GbE signal could be coupled with a local oscillator laser which provides the mm-wave frequency upconversion of the broadband baseband signal. This is an easy method to implement for the downlink in femtocell networks, where the number of cells is greater than 100. Some other considerations have to be taken for the case of the uplink, as it will require an E/O conversion. Much research was done in this field in the early stages of long haul optical communications and heterodyne receivers [158]-[159] albeit for lower data rates. The requirements on laser linewidth and other parameters were deeply studied in [160] and experimentally demonstrated in [161]. A basic schematic of a heterodyne receiver is shown in Figure 7.38. The receiver architecture with square envelope detections is basically the same as the self-homodyne receiver described in previous sections.

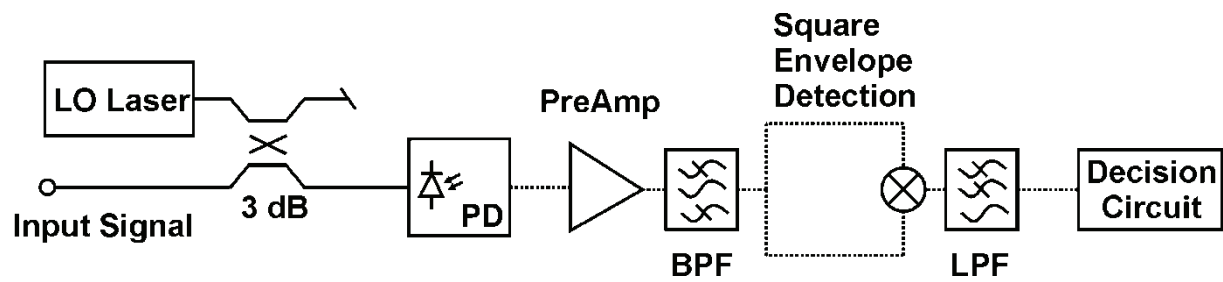


Figure 7.38: Optical heterodyne receiver.

The bandwidths of the bandpass filter and low pass filter play an important role in the system performance. Also the linewidth of the local oscillator (LO) laser proves to be a critical factor, as well as the decision threshold level. For the system experiments the following setup shown in Figure 7.39 was used. The RF receiver architecture chosen is the self-homodyne receiver which provides mm-wave carrier independence and thus is tolerant to the carrier jitter. The optical SSB signal is now formed by heterodyning two uncorrelated laser sources in a 3 dB fiber coupler. The 10 GET connection is emulated by an externally modulated laser source. A polarization controller (PC) is in charge of obtaining maximum coupling of the two waves. After optical amplification and bandpass filtering to reduce ASE, the signal is launched via an SMF link into the receiver at the base station.

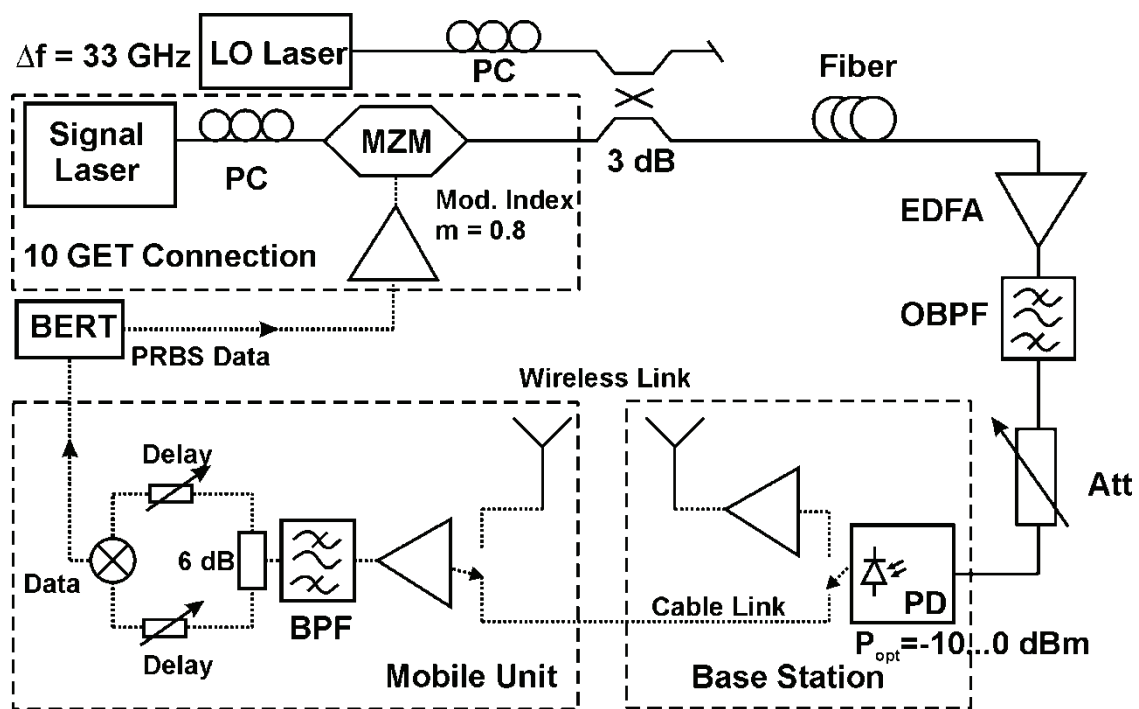


Figure 7.39: System experiments setup III to transmit broadband signals using OSSB data modulation.

7.3.1 RF bandwidth

The effects of the RF bandwidth were already studied in [162] showing that using IF bandwidths smaller than two times the bit rate R_b resulted in asymptotically high sensitivity penalties. The previous system depicted in Figure 7.39 was simulated in VPI (for a more complete schematic refer to Appendix D, Figure D.6) and the RF bandwidth was varied by using an electrical bandpass filter with variable bandwidth. The rest of the parameters for the simulation were LO laser power $P_{LO} = 10$ dBm, signal laser power $P_s = 0$ dBm, combined laser linewidth $\Delta\nu = 200$ kHz (i.e. simulating two ECLs with $\Delta\nu = 100$ kHz each), $\Delta f = 33$ GHz and using an ideal square law detection receiver with $R = 1$ A/W, a preamplifier with $G = 20$ dB and a post detection filter with $B_{LPF} = 0.75 \cdot R_b$ (in our case $B_{LPF} = 7.5$ GHz as $R_b = 10$ Gbps). The results for the BER curves for $L = 0$ km are shown in Figure 7.40a.

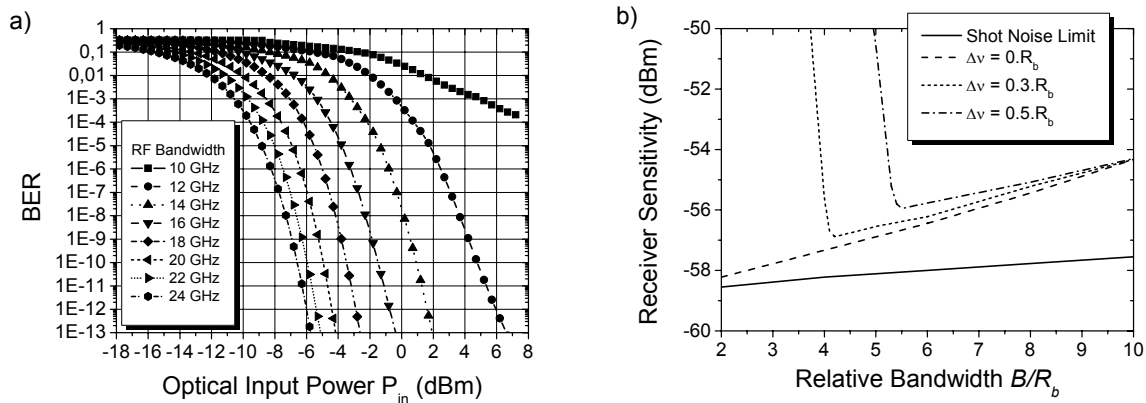


Figure 7.40: a) Simulation BER curves for the system experiments with $R_b = 10$ Gbps and setup III for the cable link and for different RF bandwidths. b) Receiver sensitivity versus relative bandwidth for $\text{BER} = 10^{-9}$ and optimum threshold setting from [162].

It is evident that higher bandwidths accommodate higher RF power and thus the performance is improved. Even using $B = 10$ GHz RF bandwidth is not enough to achieve decent data rates without FEC, so this scheme would not be useful for 60 GHz systems due to bandwidth limit regulations. Apart from using narrower linewidth lasers (which would increase the costs), there are two ways of lowering the error floor: lowering the decision threshold or increase the RF passband. Lowering the threshold would reduce the systems sensitivity so increasing the RF passband is preferred, as it can be partially compensated by the post-detection filter. Nevertheless, increasing the bandwidth indefinitely doesn't always achieve better results, as the performance improves meagerly from $B = 20$ GHz (i.e. a system with a huge 60% relative

bandwidth). This is due to the fact that at some point, more noise than data is collected by the increased RF bandwidth.

The receiver sensitivity for $\text{BER} = 10^{-9}$ for a 140 Mbps-ASK receiver with square-law detection was calculated in [162] as a function of the RF bandwidth relative to the bit rate R_b and the results are shown in Figure 7.40b. The shot noise limit curve was calculated under the assumption of a strong local oscillator and zero linewidth lasers. It demonstrates the ultimate sensitivity achievable. For all other curves, a local oscillator with $P_{LO} = 10$ dBm was used and the resulting linewidths were varied relative to the bit rate R_b . Even for zero linewidth, the curve deviates steeply from the shot noise limit. Increasing the linewidth shows an asymptotical behavior for small RF bandwidths. If the RF bandwidth is large enough, then the curves follow the zero linewidth one. However, for small RF bandwidths, the error rate floor may rise above 10^{-9} and the receiver performance degrades disastrously. The minimum sensitivities are reached at $4.2 \cdot R_b$ and $5.5 \cdot R_b$ for linewidths $0.3 \cdot R_b$ and $0.5 \cdot R_b$ respectively. In [162] the RF bandwidth was assumed to be greater than two times the bit rate (i.e. $B > 2 \cdot R_b$) to simplify the calculations. In our case, however, we are using at most $B = 1.4 \cdot R_b$ meaning that a small linewidth may be critical for achieving error free performance.

7.3.2 Laser linewidth

As already studied in [160], the lasers linewidth proves to be a critical factor in system performance. In remote heterodyne systems, the product laser linewidth x system bandwidth limits the transmission distance as already demonstrated in section 4.4 for phase modulation formats (refer to Figure 4.22). To test our system under different conditions, the lasers linewidth was varied by using different laser sources. One is a distributed feedback (DFB) laser with a linewidth of $\Delta \nu_{DFB} = 10$ MHz. These are the laser typically employed in 10 GET systems. On the other hand, narrower laser sources such as external cavity lasers (ECL) can be employed, with laser linewidths of $\Delta \nu_{ECL} = 100$ kHz.

In the case of uncorrelated heterodyning of two laser sources, the resulting mm-wave signal will have a linewidth $\Delta \nu_{RF}$ equivalent to the sum of each lasers linewidth [149]. Mathematically,

$$\Delta \nu_{RF} = \Delta \nu_{sig} + \Delta \nu_{LO} \quad (6.11)$$

where $\Delta\nu_{sig}$ and $\Delta\nu_{LO}$ are the signal lasers and LO lasers linewidth respectively. By using different combinations of signal and LO laser, the resulting mm-wave linewidth can be varied.

Figure 7.41a shows the BER curves by using two DFB lasers with a resulting linewidth of approximately $\Delta\nu_{RF} = 20$ MHz. Only the optical BtB link could be tested, and the error rate is not better than $BER = 10^{-6}$. For longer transmission distances, the BER deteriorates, being almost a flat line at $BER = 10^{-4}$ for $L = 25$ km. For the wireless link only $BER = 10^{-4}$ could be achieved (not shown in Figure 7.41a).

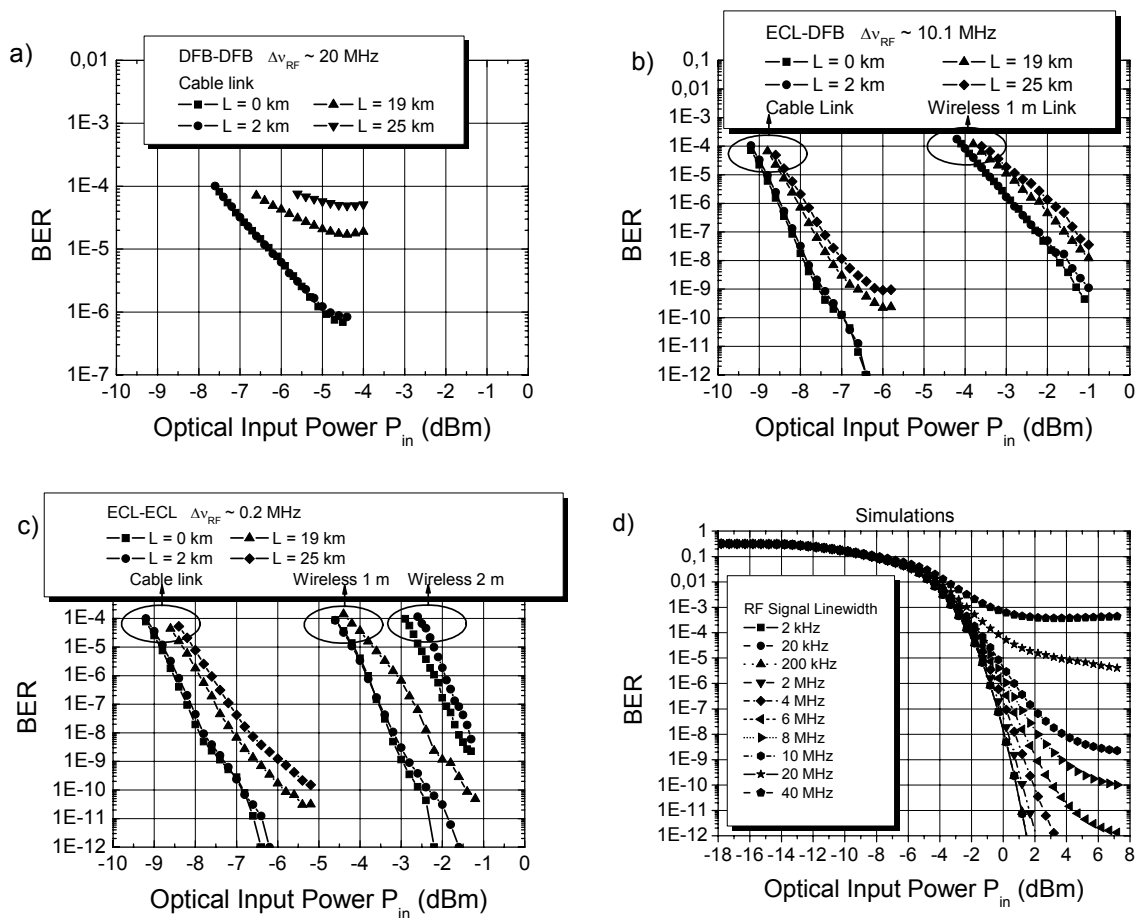


Figure 7.41: BER curves for setup III with resulting linewidth a) $\Delta\nu_{RF} = 20$ MHz, b) $\Delta\nu_{RF} = 10.1$ MHz and c) $\Delta\nu_{RF} = 0.2$ MHz. d) System simulations. Data rate $R_b = 10$ Gbps for all cases.

By changing the LO laser to a narrow linewidth ECL ($\Delta\nu_{ECL} = 0.1$ MHz), the resulting linewidth is reduced to $\Delta\nu_{RF} = 10.1$ MHz. This improvement is significantly shown in Figure 7.41b as some BER curves now reach error free operation in the optical BtB case. The

penalties for longer transmission distances such as 19 and 25 km are less, although an error floor is reached at $\text{BER} = 10^{-10}$ and $\text{BER} = 10^{-9}$ respectively. A wireless link of $d = 1$ m was tested and the BER curves show all the same slope, with small penalties for the longer fiber distances.

To obtain the smallest resulting linewidth of $\Delta\nu_{RF} = 0.2$ MHz, two ECL lasers were employed. The results shown in Figure 7.41c confirm that the narrower the linewidth the better the system performance. Almost error free operation was achieved even under long fiber transmission distances for the cable case. A wireless links with $d = 1$ m also demonstrates error free operation after $L = 2$ km but a significant penalty of 1 dB for $L = 19$ km. Duplicating the link distance to $d = 2$ m results in decent operation with $\text{BER} = 10^{-9}$.

With the same simulation set as in section 7.3.1, now the linewidth of both lasers was simultaneously varied and the BER curves calculated. The parameters remain the same: $P_{LO} = 10$ dBm, $P_s = 0$ dBm, $B_{LPF} = 7.5$ GHz, $R = 1$ A/W, $G = 20$ dB and $L = 0$ km. The RF bandwidth was set to $B_{RF} = 14$ GHz. The results are shown in Figure 7.41d with the resulting RF linewidth as a parameter. For RF linewidths up to 2 MHz the curves show little penalty, but when two standard uncooled DFB lasers are used (i.e. $\Delta\nu_{DFB} = 10$ MHz each), the performance degrades abruptly, reaching an error floor at 10^{-6} . These results agree with our experimental data, where only using narrow linewidth ECLs resulted in error free performance.

7.3.3 Simple remote heterodyne with diode detector

An improvement based on the previous setup to use two uncorrelated lasers would be to use envelope detection to achieve better sensitivities (see section 6.1.2.2). The receiver consists now of a low noise mm-wave amplifier (LNA) and a broadband diode detector (DKa-2P) in WR28 waveguide from Spacek Labs Inc. The diode detector is used as an envelope detector providing mm-wave carrier independence. It is specified to operate in the 26-40 GHz region with a sensitivity of 2000 mV/mW throughout the Ka band, but the IF frequency response is not specified as it is usually not used for this kind of application. The tangential sensitivity is specified to be -45 dBm in a 2 MHz video bandwidth [163]. The response was already measured in section 6.1.2.2 providing a bandwidth of $B = 5.5$ GHz. This would mean that data rates as high as $R_b = 7.5$ Gbps can be detected without distortion. Higher data rates like

10 Gbps suffer the notch at 6 GHz but in principle could also be demodulated with this diode detector. The setup for the system experiments is schematically shown in Figure 7.42.

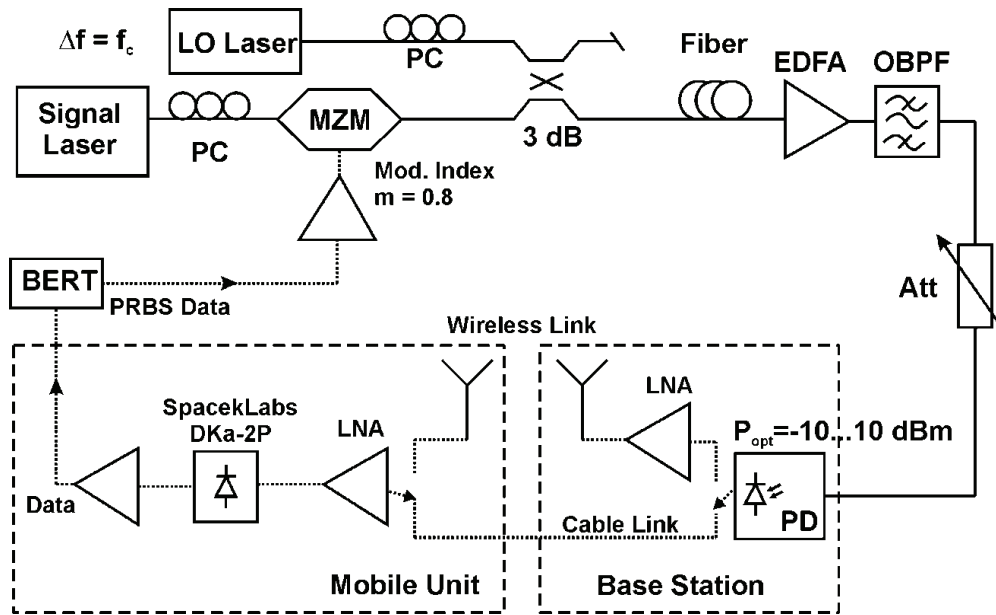


Figure 7.42: System experiments setup IV to transmit broadband signals using OSSB data modulation.

With the setup described in Figure 7.42, the carrier frequency f_{RF} can be adjusted, so that the behavior of the broadband detector can be characterized in the Ka band (i.e. 26-40 GHz). The first data rate chosen was $R_b = 5$ Gbps to test if a multi channel configuration could be possible. The bit error ratio (BER) was measured for different carrier frequencies and only a small fiber link (i.e. $L \approx 0$ km). The results are plotted in Figure 7.43 for the cable link case.

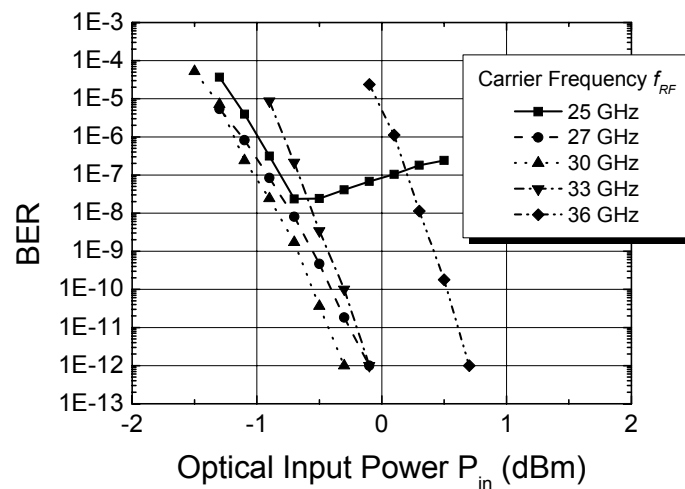


Figure 7.43: BER curves for the system experiments with $R_b = 5$ Gbps and setup IV for the cable link and for different carrier frequencies f_{RF} .

The best operation was obtained for $f_{RF} = 30$ GHz, but also 27 and 33 GHz have small penalties (0.2 dB). For $f_{RF} = 25$ GHz an error floor is observed which can be explained due to the cutoff frequency of the WR28 waveguide at 25.5 GHz. For $f_{RF} = 36$ GHz a bigger penalty is incurred (1 dB). A carrier frequencies of 39 GHz provided too much distortion and no data could be recovered. The most important result of this experiment is that the broadband detector could be used in a multi channel environment provided extra filtering in each receiver for channel selection is available.

The Q-factors corresponding to the measurements in Figure 7.43 are listed in Table 7.2. The optical power was maintained constant for all the measurements at 2.2 dBm. The optimum carrier frequency is then $f_{RF} = 30$ GHz with $Q = 7.5$ and the largest eye opening.

	Carrier Frequency f_{RF}				
	25 GHz	27 GHz	30 GHz	33 GHz	36 GHz
Q-factor	4.86	5.6	7.45	6.54	5.99
Eye opening (mV)	21.4	37.5	43	33.8	25

Table 7.2: Measured Q-factors for $R_b = 5$ Gbps and different carrier frequencies f_c .

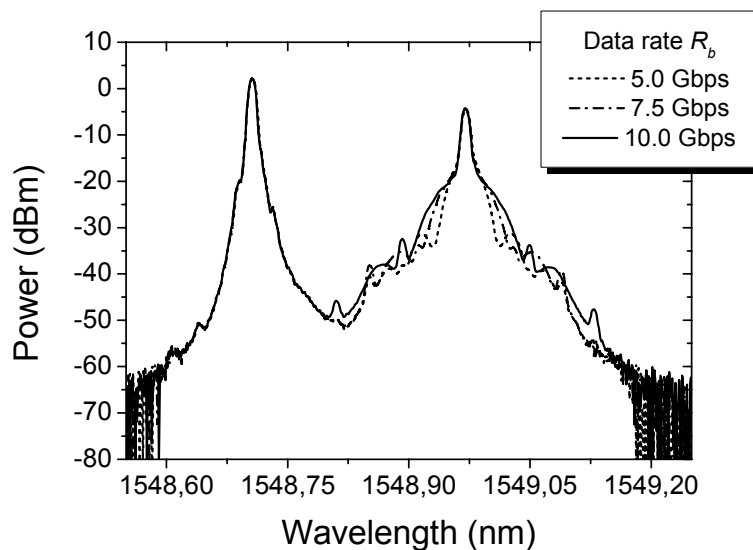


Figure 7.44: Optical SSB spectra for different data rates R_b .

Using the optimum $f_{RF} = 30$ GHz, the data rate R_b was varied from 5 to 10 Gbps and the optical spectrum is plotted in Figure 7.44. This type of OSSB modulation causes no optical spectrum overlap and provides enough chromatic dispersion tolerance so that transmission over huge spans of SMF is possible. Usually in heterodyne receivers the LO laser power

should be high, but due to saturation effects in our receiver it was optimized for the best possible Q factor of the recovered signal. This resulted in $P_{LO} = 2$ dBm, roughly 6.4 dB higher than the signal power.

In the system experiments, the receiver front end has a sensitivity of -34 dBm for $\text{BER} = 10^{-9}$ and a noise figure $NF = 4.04$ dB (as measured in section 6.1.2.2). The broadband photodiode from u²t operates up to 70 GHz with a responsivity $R = 0.6$ A/W and can handle large optical powers (max $P_{in} = 13$ dBm). Due to the response of the diode detector up to 6 GHz, it acts as a natural matched filter for $R_b = 7.5$ Gbps. That is, the noise equivalent bandwidth B_n is equal to the data rate R_b and proves to be the maximum likelihood demodulator [138].

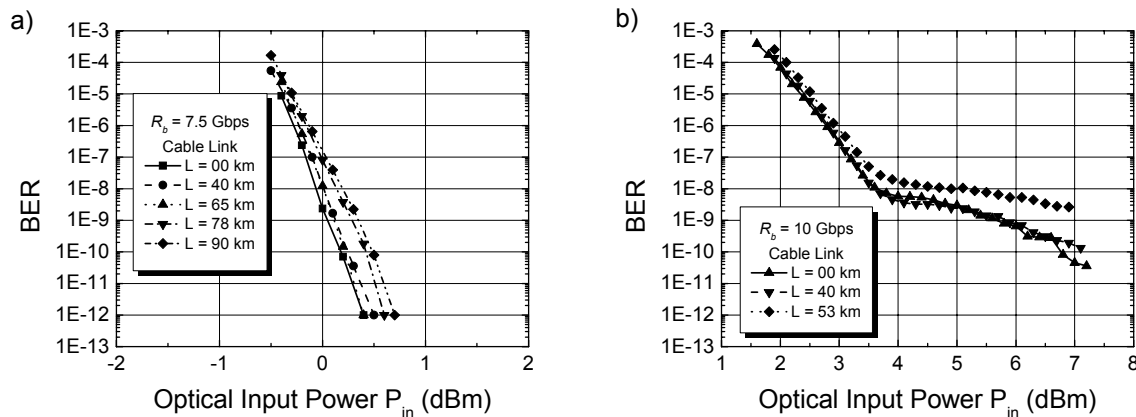


Figure 7.45: BER curves for the system experiments setup IV for the cable link for a) $R_b = 7.5$ Gbps and b) $R_b = 10$ Gbps for different fiber lengths L .

The BER versus received optical power for the cable link connection is shown in Figure 7.45 for two different data rates: 7.5 and 10 Gbps. The curves shown in Figure 7.45a prove that even after 90 km of SMF transmission the power penalties are negligible. A longer span of $L = 103$ km was tested but could not be measured due to power budget problems with a single optical preamplifier and the 8 dB insertion loss of the optical attenuator used. Moving to higher data rates such as 10 Gbps (see Figure 7.45b) confirms that the bandwidth limitation imposed by the diode detector ($B = 6$ GHz, refer to section 6.1.2.2 and Figure 6.7b) causes massive intersymbol interference as no error free performance can be achieved. Moreover, after $L = 53$ km of SMF an error floor is reached with $\text{BER} = 3.10^{-9}$. Nonetheless, this is acceptable for wireless access systems even though the optical power required to operate in the low error region is quite high. The recovered eye diagrams at $R_b = 7.5$ Gbps are shown in

Figure 7.46 for an optical input power of 2.5 dBm. There is some distortion after 90 km SMF but the eye remains open.

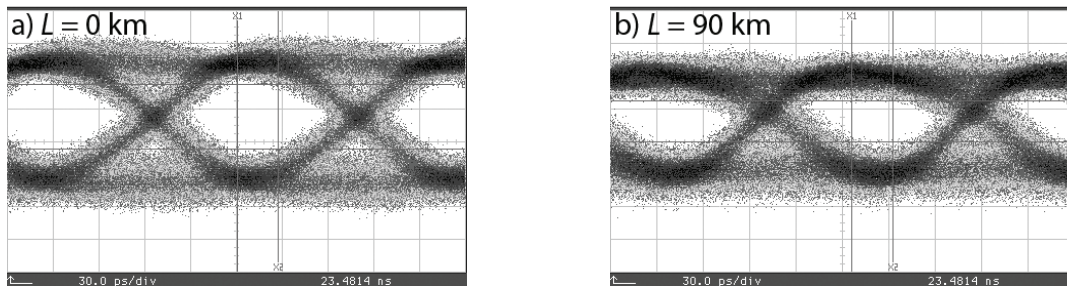


Figure 7.46: Eye diagrams for $R_b = 7.5$ Gbps and cable link. Fiber lengths a) $L = 0$ km and b) $L = 90$ km. Optical power = 2.5 dBm, time base = 30 ps/div. Amplitude scale = 50 mV/div.

A wireless link of $d = 1.5$ m was chosen to carry out the wireless experiments. At the transmitter end a Vivaldi antenna working in the 4-40 GHz range and having a gain $G_{TX} = 15$ dB was employed. Extra amplification was needed to overcome the free space path loss, which at $f_{RF} = 30$ GHz is $PL_{\text{freespace}} = 62$ dB. The receiver antenna was a horn antenna working from 26-40 GHz and having a gain $G_{RX} = 24$ dB. With this in mind, the link loss is only $LL = 23$ dB.

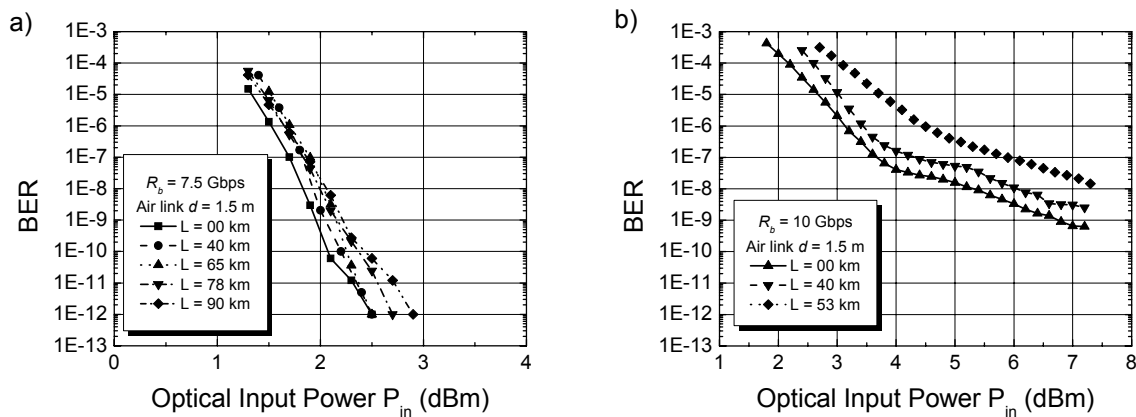


Figure 7.47: BER curves for the system experiments setup IV for a wireless link of $d = 1.5$ m for a) $R_b = 7.5$ Gbps and b) $R_b = 10$ Gbps for different fiber lengths L .

Clearly wireless transmission requires higher optical power, but the curves in Figure 7.47a show no significant degradation due to the wireless channel for $R_b = 7.5$ Gbps. Transmitting at $R_b = 10$ Gbps suffers from more distortion effects which result in a slight change of slope in the BER curves and one order of magnitude worse performance in Figure 7.47b. Nonetheless,

fiber transmission distances up to 53 km were achieved and the use of forward error correction (FEC) would allow such a system to operate error free at the expense of signal processing in the mobile unit.

7.4 Overview

To summarize the wireless experiments carried out in one diagram, the theoretical maximum capacities for each receiver were calculated with the theory developed in chapters 2 and 6, and the results are shown in Figure 7.48. The receivers are denoted by “Demodulation type – Tx antenna – Rx antenna”, being ‘V’ for Vivaldi and ‘H’ for Horn antenna. The different setups (denoted by points according to the bit rate achieved and distance transmitted) are divided into:

- Setup I: Optical Double Sideband from section 7.2.1.
- Setup II: Optical Single Sideband from section 7.2.2.
- Setup III and IV: heterodyning of two uncorrelated lasers from section 7.3.

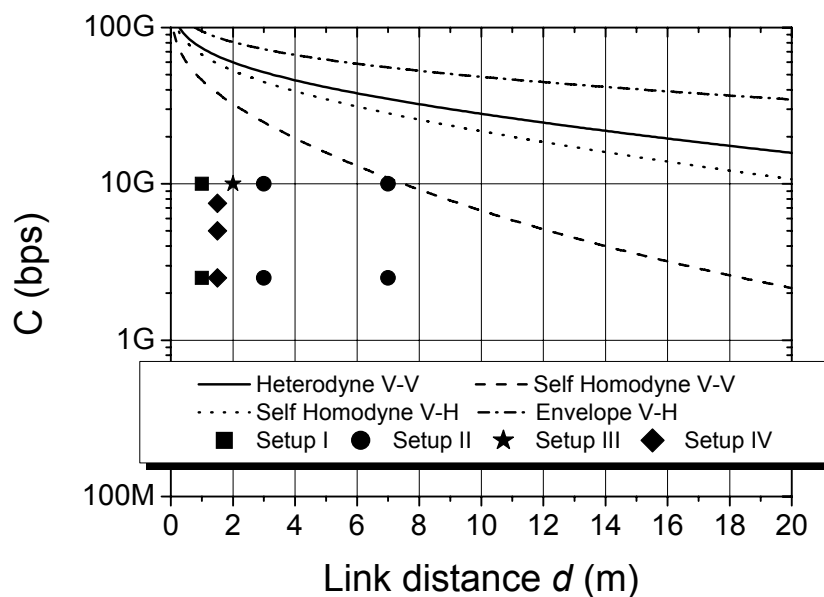


Figure 7.48: Overview of wireless system experiments.

The line types correspond to the different receivers tested. From Figure 7.48, the best receiver available would be the envelope detector, but its bandwidth limitation makes it possible to transmit error free only up to 7.5 Gbps using ASK modulation. 10 Gbps was also tested and $\text{BER} = 10^{-9}$ were achieved, which is enough for broadband wireless access.

The second best receiver would be the heterodyne demodulator. In this case only a proof of concept link with $d = 1$ m was tested eventhough the capabilities of the system would allow transmission distances of more than 20 m. The main drawback of this scheme is the need of a carrier recovery unit to use as local oscillator (LO) in the receiver. This was carried out in the lab by synchronizing the signal generator in the central station with the LO signal generator in the receiver, which is only a proof of concept setup and not a real scenario.

The self homodyne receiver is the worst of all due to its high power requirements, which results in an implementation loss $IL_{SH} = 33.93$ dB. Therefore, the distances that can be achieved with such receiver are severely limited. Nevertheless, its stability allows the use of any of the setups and the maximum reach of 7 m for 10 Gbps was in this way obtained in the lab.

One general requirement for all receivers is the group delay response of all its components. As the bit slot is 100 ps for a 10 Gbps signal, if the overall group delay ripple of the receiver is in this order of magnitude, then intersymbol interference will inevitably occur. Therefore special care should be taken when choosing amplifiers, delay lines and mixers in this kind of receivers. Moreover, linewidth requirements discussed in section 6.3 prove to be another system limitation. The experiments in section 7.3.2 show that narrower linewidths as expected from theory are needed. The linewidths in Table 6.2 are expressed as a percentage of the data rate, and since demodulators can be implemented in a variety of ways for a given modulation format, they are only estimates of the required linewidth. Nonetheless, from the experimental results, ASK with incoherent demodulation required linewidths in the order of 10 MHz or less to operate error freely for a 10 Gbps signal ($\Delta\nu/R_b = 0.001$ %).

In chapter 2 the focus on 60 GHz systems was mentioned, mainly due to its huge unregulated bandwidth availability worldwide. All the proposed optical setups located in the central station are easily scalable to this higher frequency by changing the separation of the spectral lines to $f_{RF} = 60$ GHz by using a MZM with sufficient RF bandwidth ($BW > 30$ GHz). For the OSSB case, the MZI has to be desgined with an $FSR = 120$ GHz instead. The components of the different receivers in the mobile unit have to be completely changed for the corresponding frequency range. This is also not a major issue and shifting to higher frequencies provides the benefit of a smaller system relative bandwidth, where the RF components can cope with the bandwidth demands of high bitrates such as 10 Gbps.

8 Summary

The main focus of this work has been the optical generation of mm-wave signals for future gigabit wireless networks. The main motivation resides in the use of radio over fiber (RoF) systems as a distribution medium of broadband multimedia content. The advantages of a fiber distribution system include low loss (i.e. longer transmission distances), immunity to electromagnetic interference, ease of deployment, light weight and the immense available bandwidth (i.e. the possibility of multichannel capability through DWDM). The efforts by different providers to supply fiber connections to each end user (i.e. FTTH networks) make RoF an attractive future technology.

From this point of view, the characteristics of gigabit wireless networks were generally described in chapter 2. The choice of the mm-wave band is strongly backed up by the huge worldwide unregulated bandwidth in the 60 GHz region. Due to high free space path losses at this frequency, plus oxygen absorption losses, the reach of 60 GHz mobile systems is severely distance limited. This is a disadvantage for fixed wireless links but a big advantage for picocell and femtocell systems due to frequency reuse. The key aspect in extending the reach would be to use high gain directional antennas. For a fixed wireless link, Cassegrain antennas can be used to reach a couple of kms of wireless transmission. In a mobile environment, however, such huge antennas are impractical, which makes the need of smart antennas with adaptive directional capabilities imperative. The theoretical maximum achievable capacities were calculated in section 2.3 demonstrating the large influence of the antennas in both achievable data rate and reach.

To simplify the base stations architecture in a RoF network requires the need of some kind of mm-wave signal distribution. These can be accomplished through different optical methods briefly described in chapter 3. Another advantage of a fiber distribution system is the ability to optically upconvert lower frequency signals. The properties of transmission of radio signals through optical fiber are developed in chapter 4. The chromatic dispersion (CD) of the fiber proves to be a key impediment in achieving long fiber transmission distances. Due to the phase shift produced by CD on the different spectral lines and depending on how the mm-wave signal is transmitted optically, the link can be limited to some kms. In order to extend this to some tenths of kms, the use of double sideband with suppressed carrier (DSB-SC) is

proposed. By eliminating the optical carrier, chromatic dispersion induced penalties are harshly reduced.

The novel concept in this thesis is the use of a fiber loop mirror (FLM) with a phase modulation element inside it to generate an optical DSB-SC signal. The inherent stability of the FLM and the reduction of acousto-optic effects due to the bidirectional nature of the loop make this approach theoretically quite attractive in comparison to the more simple method of using a Mach-Zehnder modulator biased at minimum. Several FLMs were constructed during the development of this thesis, some used a phase modulator (PM) and others employed a semiconductor optical amplifier (SOA). The carrier suppression of all the setups was well over the required 20 dB. However, the FLM transmission behavior is extremely dependent on the position of the phase modulation element inside the loop and its bidirectional behavior. Commercial phase modulators up to 30 GHz are available; however, to reach such high frequency performance, the RF electrodes are of the traveling wave type, meaning that the efficiency is maximized in one operation direction, as demonstrated in Appendix A.

By means of cross-phase modulation (XPM) effect in SOAs, the FLM becomes more complicated, requiring an optical pump to be spliced inside the loop. However, the phase modulation indices m_{ph} achieved in this way are much higher (see Appendix B) meaning a more efficient electro-optical upconversion. On the other hand, the frequency response of this mechanism is quite slow, limiting the achievable frequencies to a couple of GHz. This is advantageous for WLAN and UWB systems, but not for 60 GHz applications.

Independently of the phase inducing element used, the FLM has a periodic frequency behavior dependent on the position of this element inside the loop (see Figure 5.22). To maximize the usable RF bandwidth, the phase inducing element has to be placed near the symmetry axis of the loop. This is quite difficult to achieve by splicing and requires complete control on all the devices inside the loop. Using a phase modulator specified to work up to 8 GHz and modulated at $f_m = 4.5$ GHz, proof of concept system experiments were carried out at $f_{RF} = 11$ GHz with data rates as high as 155 Mbps (as described in section 5.2.1). Exploiting the same test bed, the FLM with a SOA was also used to carry out the same system experiments with decent results (see section 5.2.2). The broad optical bandwidth of the fiber loop, limited only by the bandwidth of the phase inducing element, makes this approach suitable to address multiple users through DWDM.

To reach higher mm-wave frequencies (i.e. 60 GHz), and thus transmit higher data rates, the FLM setup was limited due to the phase modulator employed. Moreover, SOAs also exhibit a reduced efficiency as the modulation frequency f_m is increased (see Figure 5.33). For these reasons, the generation of a DSB-SC signal at higher frequencies was carried out by a Mach-Zehnder modulator (MZM) biased at its minimum transmission point. Utilizing a standard 10 Gbps OC-192 MZM, mm-wave signals up to 33 GHz were generated with $f_m = 16.5$ GHz. Due to mismatches in the MZM construction and polarization issues, there is always a remnant optical carrier. Different configurations of this approach were presented in section 5.1 with special interest in the carrier suppression capabilities. The best solution resulted in suppressing the optical carrier via optical filtering through a Fiber Bragg grating (FBG). In this fashion, by tuning the FBG via stress, the carrier was attenuated more than 60 dB and two spectral lines separated by $f_{RF} = 33$ GHz were produced (as shown in Figure 5.14). By optical mixing in a fast photodiode, the resulting mm-wave signal is obtained. The choice of this f_{RF} was driven by the limitations of the equipment in the lab but using a more broadband MZM, a 60 GHz RF signal can be easily generated in this way.

Concerning broadband data modulation, two options are available using a DSB-SC signal: optical double sideband (ODSB) and optical single sideband (OSSB). ODSB means the modulation of both spectral lines with the broadband data takes place and is described in section 7.2.1. It is a simple method, requiring only a second MZM and no extra optical components resulting in high stability. The main drawback is the poor immunity to fiber chromatic dispersion. Working with $R_b = 10$ Gbps, a maximum fiber transmission distance of $L = 10$ km with standard singlemode fiber (SMF) was achieved.

On the other hand, OSSB is more complex and is fully described in section 7.2.2. The phase-correlated spectral lines are separated by a Mach-Zehnder Interferometer (MZI) with a free spectral range (FSR) equal to twice the desired RF frequency. In this way, one of the spectral lines can be modulated with the broadband data while the other remains unchanged. After recombination in a 3 dB coupler, an optical single sideband signal is obtained as shown in Figure 7.22. Chromatic dispersion tolerance is extremely improved with this method, reaching fiber transmission distances as far as $L = 53$ km of SMF at $R_b = 10$ Gbps.

To demonstrate the feasibility of both approaches in a FTTH scenario like the one depicted in Figure 1.2, a wireless link was setup and several receivers for the mobile units were tested.

The modulation format chosen was amplitude shift keying (ASK) due to its simplicity to implement. Therefore, three options were available to demodulate an ASK signal: heterodyne downmixing with a local oscillator, self homodyne and envelope detection.

Heterodyne downmixing with a local oscillator (LO) is a coherent form of demodulation (see section 6.1.1) which requires complete phase and frequency control of the LO signal. This translates in the need of a carrier recovery unit with a phase locked loop (PLL) to track the signals phase, making the receiver more complex. The sensitivity for $\text{BER} = 10^{-9}$ was measured to be -34 dBm with a noise figure $\text{NF} = 5.04$ dB. However, the implementation loss of this receiver was calculated to be $IL_{coh} = 20.91$ dB which leaves plenty of room for improvement. A proof of concept link with $d = 1$ m was constructed and error free transmission of 10 Gbps was achieved.

Moving to incoherent demodulators relaxes the need of frequency and phase tracking, but increases the implementation loss and in some cases reduces the sensitivity. The self-homodyne receiver described in section 6.1.2.1 is a simple scheme which mixes the incoming signal with itself. Though simple, it requires high electrical power in the mixer to light up the diodes, making its measured sensitivity to be -24 dBm (as measured in section 6.1.1). Therefore, its implementation loss is the highest of all at $IL_{sh} = 33.93$ dB. Nevertheless, a wireless link with $d = 7$ m and 10 Gbps was constructed and operated error free. Another variation is the use of envelope detection. The key issue in this method is the availability of broadband diode detectors. A diode detector from Spacek Labs with a bandwidth $B \approx 6$ GHz was used in the proposed experiments, limiting the bitrate to $R_b = 7.5$ Gbps. The implementation loss for this approach was $IL_{env} = 21.91$ dB, comparable to the coherent receiver and offering the same sensitivity at -34 dBm for $\text{BER} = 10^{-9}$. A proof of concept link with $d = 1.5$ m and 7.5 Gbps operated error free. Increasing the data rate to 10 Gbps proved that the bandwidth limitation causes massive intersymbol interference. Nevertheless, the system operated with $\text{BER} = 10^{-9}$, which meets the requirements for broadband wireless access.

Apart from using two phase-correlated spectral lines such as the ones emerging from a DSB-SC signal, the mixing of two completely uncorrelated lasers is another low-cost option. For this method, described in section 7.3, an incoherent demodulator is needed as the RF frequency is unstable when both lasers are free running and unlocked. This approach is the

simplest to implement if an already deployed 10 Gigabit Ethernet connection is to be used, such as is available in the wired FTTH connections. However, the performance is severely influenced by two parameters: the lasers linewidth and the RF bandwidth available. In the experiments at $f_{RF} = 33$ GHz, a reduced laser linewidth improved performance strongly (see Figure 7.41d). When the resulting RF signal linewidth approaches $\Delta\nu_{RF} = 10$ MHz (e.g. by using two DFB lasers with $\Delta\nu = 5$ MHz each) an error floor at $BER = 10^{-9}$ is reached. The other vital parameter is the RF bandwidth. Larger RF bandwidths can accommodate more signal power and thus improve the performance as demonstrated by the system simulations in Figure 7.40a. This proves to be the major issue as the bandwidth is limited to 9 GHz at the most in the 60 GHz band and thus is a compromise solution between bandwidth available and laser linewidth.

To summarize, this thesis encompasses a complete and comprehensive working system for the wireless distribution of high definition multimedia content, with data rates as high as 10 Gbps, operating error free with wireless links up to 7 m. The construction of the proof of concept system, although lab-limited to $f_{RF} = 33$ GHz, proved quite challenging as a relative bandwidth of 30% was realized where usually 10% is the design limit in real RF systems. Moreover, proficiency in multiple fields was required (e.g. fiber optic communications, RF component and system design and wireless propagation theory). Over the scope of one PhD thesis this includes an ample amount of research and energy. Technically, the optical generation of mm-wave signals is a mature technology, meaning that efficient methods for LO generation and distribution are already available. Depending on the system requirements, a simple method such as optical double sideband (ODSB) can be employed, limiting the fiber transmission distance to some kms for 10 Gbps. However, if longer fiber links are required, such as in future broadband access networks, optical single sideband (OSSB) is the way to go due to its resilience to chromatic dispersion. With fiber links up to 53 kms for OSSB with a data rate of 10 Gbps already demonstrated, the ultimate limit lies in the chromatic dispersion distortions on the baseband data itself. If fiber links longer than 100 km will be required, then dispersion compensation is mandatory. In my opinion, the key aspects that need to be further developed in gigabit wireless links are located in the RF domain. First of all, the influence of the antenna gain is enormous to develop high capacity links, thus the requirement of high gain and smart directional antennas is a necessity. Second, another area of improvement is the

receivers in the mobile units. The receivers used during this work were built with the available components in the laboratory and only as a proof of concept. Therefore, its implementation loss (IL) is quite high (e.g. 21-33 dB). Monolithic integration and careful design can reduce the IL and thus provide more signal to noise ratio (SNR) to reach longer wireless transmission distances by improving receiver sensitivity. Lastly, the use of higher modulation formats such as M-ary PSK can provide a capacity boost as well as a better use of the limited spectrum in the worldwide unlicensed 60 GHz band, which in the end is the goal of this type of systems.

Literature

- [1] Henry, P. S., "Alternative Broadband Access: Wired and Wireless Technologies for the Last Mile", Short Course SC-262, *OFC 2009*, San Diego, USA, 22.03.2009.
- [2] Rick Merritt, "New Tech Breaks into Network SpecsWar", *EE Times*, December 2006.
- [3] S. K. Yong and C.-C. Chong, "An Overview of Multigigabit Wireless through Millimetre Wave Technology: Potentials and Technical Challenges", *EURASIP Journal on Wireless Communications and Networking*, Article ID 78907, vol 2007 (2007), DOI:10.1155/2007/78907.
- [4] H. T. Friis, "A Note on a Simple Transmission Formula", *Proceedings of the IRE*, vol. 34, no.5, pp. 254-256, 1946.
- [5] M. Marcus and B. Pattan, "MillimetreWave Propagation; Spectrum Management Implications", *IEEE Microwave Magazine*, vol. 6, no.2, pp. 54-62, 2005.
- [6] C. E. Shannon, "Communication in the Presence of Noise", *Proceedings of the IEEE*, vol. 86, no.2, pp. 447-457, 1998.
- [7] M. K. Simon and M. S. Alouini, "Digital Communication over Fading Channels", 2nd edition, Wiley-IEEE Press, New York, 2004.
- [8] M. Fiaco and S. Saunders, "Final report for OFCOM - Indoor propagation factors at 17 GHz and 60 GHz", 1998.
- [9] C. C. Chong et al., "A new statistical wideband spatio-temporal channel model for 5-GHz band WLAN systems", *IEEE Journal on Selected Areas in Communications*, vol. 21, no.2, pp. 139-150, 2003.
- [10] C. C. Chong et al., "A novel wideband dynamic directional indoor channel model based on a Markov process", *IEEE Transactions on Wireless Communications*, vol. 4, no.4, pp. 1539-1552, 2005.
- [11] R. J. Cramer, R. A. Scholtz and M. Z. Win, "An evaluation of the ultra-wideband propagation channel", *IEEE Transactions on Antennas and Propagation*, vol. 50, no.5, pp. 561-570, 2002.
- [12] C. C. Chong, Y. E. Kim, S. K. Yong and S. S. Lee, "Statistical characterization of the UWB propagation channel in indoor residential environment", *Wireless Communications and Mobile Computing*, vol. 5, no.5, pp. 503-512, 2005.
- [13] A. F. Molisch, D. Cassioli and C. C. Chong, "A comprehensive standardized model for ultrawideband propagation channels", *IEEE Transactions on Antennas and Propagation*, vol. 54, no.11, pp. 3151-3166, 2006.
- [14] M. Steinbauer, A. F. Molisch and E. Bonek, "The double directional radio channel", *IEEE Antennas and Propagation Magazine*, vol. 43, no.4, pp. 51-63, 2001.
- [15] S. Geng, J. Kivinen, X. Zhao and P. Vainikainen, "Millimeter-Wave Propagation Channel Characterization for Short-Range Wireless Communications", *IEEE Transactions on Vehicular Technology*, vol. 58, no.1, pp. 3-13, 2009.

- [16] B. Langen, G. Lober and W. Herzig, "Reflection and transmission behaviour of building materials at 60 GHz", *PIMRC '94*, The Hague, Netherlands, 18-23.09.1994.
- [17] K. Huang and Z. Wang, "Millimeter-wave circular polarized beam-steering antenna array for gigabit wireless communications", *IEEE Transactions on Antennas and Propagation*, vol. 54, no.2, pp. 743–746, 2006.
- [18] G. Grosskopf et al., "Photonic 60-GHz maximum directivity beam former for smart antennas in mobile broad-band communications", *IEEE Photonics Technology Letters*, vol. 14, no.8, pp. 1169-1171, 2002.
- [19] G. Grosskopf et al., "Photonic beam forming of mm-wave smart antennas", *International Topical Meeting on Microwave Photonics (MWP 03)*, Budapest, Hungary, 10-12.09.2003.
- [20] B. Kuhlow et al., "Optical beam forming of MM-wave array antennas in a 60 GHz radio over fiber system", *OFC 2003*, San Diego, California, USA, 23-28.03.2003.
- [21] R. Emrick et al., "Technology for emerging commercial applications at millimeter-wave frequencies", *Wireless Communications and Applied Computational Electromagnetics 2005*, Honolulu, Hawaii, USA, 3-7.4.2005.
- [22] B. Gaucher, "Completely Integrated 60 GHz ISM Band Front End Chip Set and Test Results", IEEE 802.15-15-06-0003-00-003c, Big Island, Hawaii, USA, January 2006.
- [23] C. H. Doan, S. Emami, A. M. Niknejad and R. W. Broderon, "Millimeter-wave CMOS design", *IEEE Journal of Solid-State Circuits*, vol. 40, no. 1, pp. 144–155, 2005.
- [24] A. Behravan et al., "System Implications in Designing a 60 GHz WLAN RF Front End", *GigaHertz 2001 Symposium on Gigahertz Electronics*, 2001.
- [25] J. Oetting, "A Comparison of Modulation Techniques for Digital Radio", *IEEE Transactions on Communications*, vol. 27, no.12, pp. 1752 - 1762, 1979.
- [26] D. Wake, L. Johansson and D. G. Moodie, "Passive picocell: a new concept in wireless network infrastructure", *Electronics Letters*, vol. 33, no.5, pp. 404-406, 1997.
- [27] A. Stöhr, K. Kitayama and D. Jäger, "Full-duplex fiber-optic RF subcarrier transmission using a dual-function modulator/photodetector", *IEEE Transactions on Microwave Theory and Techniques*, vol. 47, no.2, pp. 1338-1341, 1999.
- [28] E. Wong, K. L. Lee and T. B. Anderson, "Directly Modulated Self-Seeding Reflective Semiconductor Optical Amplifiers as Colorless Transmitters in Wavelength Division Multiplexed Passive Optical Networks", *IEEE Journal of Lightwave Technology*, vol. 25, no.1, pp. 67-74, 2007.
- [29] D. H. Kim et al., "Bidirectional 1.25Gb/s colorless RSOA based WDM-PON using Suppressed Optical Carrier and Polarization Beam Splitter", *OFC 2008*, paper JThA97, San Diego, California, USA, 24-28.02.2008.
- [30] K. Y. Cho, Y. Takushima and Y. C. Chung, "10-Gb/s Operation of RSOA for WDM PON", *IEEE Photonics Technology Letters*, vol. 20, no.18, pp. 1533-1535, 2008.
- [31] W. S. C. Chang, "RF Photonic Technology in Optical Fiber Links", Cambridge University Press, Cambridge, UK, 2002.

-
- [32] Z. Ahmed et al., "Locking characteristics of a passively mode-locked monolithic DBR laser stabilized by optical injection", *IEEE Photonics Technology Letters*, vol. 8, no.1, pp. 37-39, 1996.
- [33] J. Park, L.A. Buckman and K.Y. Lau, "A broad-band millimeter-wave optical modulator using a passively modelocked laser with phase noise compensation", *IEEE Photonics Technology Letters*, vol. 9, no.5, pp. 619-621, 1997.
- [34] Z. Ahmed et al., "Optically-fed millimetre-wave (37 GHz) transmission system incorporating a hybrid mode-locked semiconductor laser", *Electronics Letters*, vol. 32, no.19, pp. 1790-1792, 1996.
- [35] R. Ludwig and A. Ehrhardt, "Turn-key-ready wavelength-, repetition rate- nad pulsewidth-tunable femtosecond hybrid modelocked semiconductor laser", *Electronics Letters*, vol. 31, no.14, pp. 1165-1167, 1995.
- [36] W. H. Loh et al., "40 GHz optical-millimetre wave generation with a dual polarisation distributed feedback fibre laser", *Electronics Letters*, vol. 33, no.7, pp. 594-595, 1997.
- [37] D. Wake, C. R. Lima and P. A. Davies, "Optical generation of millimeter-wave signals for fiber-radio systems using a dual-mode DFB semiconductor laser", *IEEE Transactions on Microwave Theory and Techniques*, vol. 43, no.9, pp. 2270-2276, 1995.
- [38] C. R. Lima, D. Wake and P. A. Davies, "Compact optical millimetre-wave source using a dual-mode semiconductor laser", *Electronics Letters*, vol. 31, no.5, pp. 364-365, 1995.
- [39] S. Pajarola, G. Guekos, P. Nizzola and H. Kawaguchi, "Dual-polarization external-cavity diode laser transmitter for fiber-optic antenna remote feeding", *IEEE Transactions on Microwave Theory and Techniques*, vol. 47, no.7, pp. 1234-1240, 1999.
- [40] D. Novak, Z. Ahmed, R. B. Waterhouse and R. S. Tucker, "Signal generation using pulsed semiconductor lasers for application in millimeter-wave wireless links", *IEEE Transactions on Microwave Theory and Techniques*, vol. 43, no.9, pp. 2257-2262, 1995.
- [41] D. Y. Kim et al., "Ultrastable millimetre-wave signal generation using hybrid modelocking of a monolithic DBR laser", *Electronics Letters*, vol. 31, no.9, pp. 733-734, 1995.
- [42] R. P. Braun, G. Grosskopf, D. Rohde and F. Schmidt, "Low-phase-noise millimeter-wave generation at 64 GHz and data transmission using optical sideband injection locking", *IEEE Photonics Technology Letters*, vol. 10, no.5, pp. 728-730, 1998.
- [43] L. Goldberg et al., "Microwave signal generation with injection-locked laser diodes", *Electronics Letters*, vol. 19, no.13, pp. 491-493, 1983.
- [44] L. Goldberg et al., "35 GHz microwave signal generation with an injection-locked laser diode", *Electronics Letters*, vol. 21, no.18, pp. 814-815, 1985.
- [45] L. Goldberg et al., "Generation and control of microwave signals by optical techniques", *IEE Proc. Optoelectronics*, vol. 139, no.4, pp. 288-295, 1992.
-

- [46] R. P. Braun et al., "Microwave generation for bidirectional broadband mobile communications using optical sideband injection locking", *Electronics Letters*, vol. 33, no.16, pp. 1395-1396, 1997.
- [47] A. Bordonalli, C. Walton and A. Seeds, "High-performance phase locking of wide linewidth semiconductor lasers by combined use of optical injection locking and optical phase-lock loop", *IEEE Journal of Lightwave Technology*, vol. 17, no.2, pp. 328-342, 1999.
- [48] C. Laperle et al., "Frequency multiplication of microwave signals by sideband optical injection locking using a monolithic dual-wavelength DFB laser device", *IEEE Transactions on Microwave Theory and Techniques*, vol. 47, no.7, pp. 1219-1224, 1999.
- [49] C. Schaffer et al., "Microwave multichannel system with a sideband injection locking scheme in the 60 GHz-band", *International Topical Meeting on Microwave Photonics (MWP) 1998*, Princeton, New Jersey, USA, 12-14.10.1998.
- [50] R. C. Steele, "Optical phase-locked loop using semiconductor laser diodes", *Electronics Letters*, vol. 19, no.2, pp. 69-71, 1983.
- [51] J. Harrison and A. Mooradian, "Linewidth and offset frequency locking of external cavity GaAlAs lasers", *IEEE Journal of Quantum Electronics*, vol. 25, no.6, pp. 1152-1155, 1989.
- [52] K. J. Williams et al., "6-34 GHz offset phase-locking of Nd:YAG 1319 nm nonplanar ring lasers", *Electronics Letters*, vol. 25, no.18, pp. 1242-1243, 1989.
- [53] G. Simonis and K. Purchase, "Optical generation, distribution, and control of microwaves using laser heterodyne", *IEEE Transactions on Microwave Theory and Techniques*, vol. 38, no.5, pp. 667-669, 1990.
- [54] R. T. Ramos and A. J. Seeds, "Fast heterodyne optical phase-lock loop using double quantum well laser diodes", *Electronics Letters*, vol. 28, no.1, pp. 82-83, 1992.
- [55] U. Gliese et al., "A wideband heterodyne optical phase-locked loop for generation of 3-18 GHz microwave carriers", *IEEE Photonics Technology Letters*, vol. 4, no.8, pp. 936-938, 1992.
- [56] R. P. Braun, G. Grosskopf, D. Rohde and F. Schmidt, "Optical millimetre-wave generation and transmission experiments for mobile 60 GHz band communications", *Electronics Letters*, vol. 32, no.7, pp. 626-628, 1996.
- [57] Z. F. Fan, P. J. S. Heim and M. Dagenais, "Highly coherent RF signal generation by heterodyne optical phase locking of external cavity semiconductor lasers", *IEEE Photonics Technology Letters*, vol. 10, no.5, pp. 719-721, 1998.
- [58] A. C. Davidson, F. W. Wise and R. C. Compton, "Low phase noise 33-40-GHz signal generation using multilaser phase-locked loops", *IEEE Photonics Technology Letters*, vol. 10, no.9, pp. 1304-1306, 1998.
- [59] R. T. Ramos et al., "Optical injection locking and phase-lock loop combined systems", *Optics Letters*, vol. 19, no.1, pp. 4-6, 1994.

-
- [60] M. Jarrahi, T. H. Lee and D. A. B. Miller, "Wideband, low driving voltage traveling wave Mach Zehnder modulator for RF photonics", *IEEE Photonics Technology Letters*, vol. 20, pp. 517-519, 2008.
- [61] H. N. Klein et al., "1.55 μm Mach Zehnder modulators on InP for optical 40/80 bit/s transmission networks", *Indium Phosphide and Related Materials Conference Proceedings*, pp. 171-173, 2006.
- [62] D. A. B. Miller et al., "Electric field dependence of optical absorption near the bandgap of quantum well structures", *Phys. Rev. B, Condens. Matter*, vol. 32, no.2, pp. 1043-1060, 1985.
- [63] T. H. Wu, Y. J. Chiu and F. Z. Lin, "High speed (60 GHz) and low voltage driving electroabsorption modulator using two consecutive steps selective undercut wet etching waveguide", *IEEE Photonics Technology Letters*, vol. 20, pp. 1261-1263, 2008.
- [64] J. J. O'Reilly, P. M. Lane, R. Heidemann and R. Hofstetter, "Optical generation of very narrow linewidth millimetre wave signals", *Electronics Letters*, vol. 28, no.25, pp. 2309-2311, 1992.
- [65] J. J. O'Reilly and P. M. Lane, "Fibre-supported optical generation and delivery of 60 GHz signals", *Electronics Letters*, vol. 30, no.16, pp. 1329-1330, 1994.
- [66] J. J. O'Reilly and P. M. Lane, "Remote Delivery of Video Services Using mm-Waves and Optics", *Journal of Lightwave Technology*, vol. 12, no.2, pp. 369-375, 1994.
- [67] C. K. Sun, R. J. Orazi, S. A. Pappert and W. K. Burns, "A photonic-link millimeter-wave mixer using cascaded optical modulators and harmonic carrier generation", *IEEE Photonics Technology Letters*, vol. 8, no.9, pp. 1166-1168, 1996.
- [68] M. Sauer et al., "Simultaneous electro-optical upconversion to 60 GHz of uncoded OFDM signals", *International Topical Meeting on Microwave Photonics (MWP'98)*, pp. 219-222, Princeton, USA, 1998.
- [69] M. Sauer et al., "Comparison of different IF band modulation techniques for electro-optical upconversion and fiber transmission at 60 GHz", *International Topical Meeting on Microwave Photonics (MWP) 1999*, Melbourne, Australia, 17-19 Nov 1999.
- [70] C. Lim et al., "Millimeter-Wave Broad-Band Fiber-Wireless System Incorporating Baseband Data Transmission over Fiber and Remote LO Delivery", *IEEE Journal of Lightwave Technology*, vol. 18, no.10, pp. 1355-1363, 2000.
- [71] G. P. Agrawal, "Fiber-Optic Communication Systems", Wiley, New York, 1997.
- [72] B. E. A. Saleh and M. C. Teich, "Fundamentals of Photonics", John Wiley & Sons, New York, 1991.
- [73] E.-G. Neumann, "Single Mode Fibers", Springer Verlag, Berlin, 1988.
- [74] L. H. Malitson, "Interspecimen Comparison of the Refractive Index of Fused Silica", *Journal of the Optical Society of America*, vol. 55, no.10, pp. 1205, 1965.
- [75] M. J. Adams, "An introduction to optical waveguides", Wiley, New York, 1981.
-

- [76] J. Sánchez García, A. Galindo González and M. Larraz Iribas, "Polarization Mode Dispersion Power Penalty; Influence of Rise/Fall Times, Receiver Q and Amplifier Noise", *IEEE Journal of Lightwave Technology*, vol. 8, no.12, pp. 1719-1721, 1996.
- [77] A. F. Elrefaie et al., "Chromatic dispersion limitations in coherent lightwave transmission systems", *IEEE Journal of Lightwave Technology*, vol. 6, no.5, pp. 704-709, 1988.
- [78] H. Schmuck, "Comparison of optical millimetre-wave system concepts with regard to chromatic dispersion", *Electronics Letters*, vol. 32, no.21, pp. 1848-1849, 1995.
- [79] F. Devaux, Y. Sorel and J.F. Kerdiles, "Simple measurement of fiber dispersion and of chirp parameter of intensity modulated light emitter", *IEEE Journal of Lightwave Technology*, vol. 11, no.12, pp. 1937-1940, 1993.
- [80] Y. Le Guennec, G. Maury, B. Cabon and J. Yao, "Up-Conversion of IQ Modulated Subcarriers with Dispersive Fiber for 60 GHz Radio-Over-Fiber Networks", *International Topical Meeting on Microwave Photonics (MWP) 2006*, Paper W1.3, Grenoble, France, 3-6.10.2006.
- [81] M. Sauer, "Elektro-optische Aufwärtskonversion zur Erzeugung von Millimeterwellen-Signalen", PhD thesis, Shaker Verlag, Aachen, 2001.
- [82] G. H. Smith, D. Novak and Z. Ahmed, "Technique for optical SSB generation to overcome dispersion penalties in fibre-radio systems", *Electronics Letters*, vol. 33, no.1, pp. 74-75, 1997.
- [83] J. M. Fuster, J. Marti and J. L. Corral, "Chromatic dispersion effects in electro-optical upconverted millimetre-wave fiber optic links", *Electronics Letters*, vol. 33, no.23, pp. 1969-1970, 1997.
- [84] K. Petermann, "Laser diode modulation and noise", Kluwer Academic Publishers, Dordrecht, 1991.
- [85] F. Koyama and K. Iga, "Frequency chirping in external modulators", *IEEE Journal of Lightwave Technology*, vol. 6, no.1, pp. 87-93, 1988.
- [86] T. L. Koch, R. A. Linke, "Effect of nonlinear gain reduction on semiconductor laser wavelength chirping", *Applied Physics Letters*, vol. 48, pp. 613-615, 1986.
- [87] M. McAdams et al., "Improved laser modulation response by frequency modulation to amplitude modulation conversion in transmission through a fiber grating", *Applied Physics Letters*, vol. 71, pp. 879-881, 1997.
- [88] C. G. Schaeffer and M. Sauer, "Fiber transmission behavior of millimeter-wave electro-optical upconversion systems with transmitter chirp", *Proceedings of the European Microwave Association*, vol. 3, no.3, pp. 190-200, 2007.
- [89] S. K. Korotky et al., "High-speed, low power optical modulator with adjustable chirp parameter," *Proc. Integrated Photon. Res.*, paper TuG2, 1991.
- [90] A. Djupsjobacka, "Residual chirp in integrated-optic modulators", *IEEE Photonics Technology Letters*, vol. 4, no.1, pp. 41-43, 1992.

-
- [91] A.H. Gnauck et al., "Dispersion penalty reduction using an optical modulator with adjustable chirp", *IEEE Photonics Technology Letters*, vol. 3, no. 10, pp. 916-918, 1991.
- [92] N. G. Walker, D. Wake and I. C. Smith, "Efficient millimetre-wave signal generation through FM-IM conversion in dispersive optical fibre links", *Electronics Letters*, vol. 28, no.21, pp. 2027-2028, 1991.
- [93] M. Schiess and H. Carldén, "Evaluation of the Chirp Parameter of a Mach-Zehnder Intensity Modulator", *Electronics Letters*, vol. 30, no. 18, pp. 1524-1525, 1994.
- [94] F. Devaux, Y. Sorel and J.F. Kerdiles, "Simple measurement of fiber dispersion and of chirp parameter of intensity modulated light emitter", *IEEE Journal of Lightwave Technology*, vol. 11, no. 12, pp. 1937-1940, 1993.
- [95] G. H. Smith, D. Novak and Z. Ahmed, "Overcoming Chromatic-Dispersion Effects in Fiber-Wireless Systems Incorporating External Modulators", *IEEE Transactions on Microwave Theory and Techniques*, vol. 45, no.8, pp. 1410-1415, 1997.
- [96] C. Schäffer, R. Braun, G. Grosskopf, F. Schmidt, "Compensation of Fiber Dispersion in an Optical mm-Wave System in the 60 GHz-Band", *International Microwave Symposium (IMS) 1998*, Paper TH3C-6, Baltimore, USA, 7-12 June 1998.
- [97] P. Gallion, F. J. Mendieta and R. Leconte, "Single-frequency laser phase-noise limitation in single-mode optical-fiber coherent-detection systems with correlated fields", *Journal Optical Society of America*, vol. 72, no.9, pp. 1167-1170, 1982.
- [98] P. B. Gallion and G. Debarge, "Quantum phase noise and field correlation in single frequency semiconductor laser systems", *IEEE Journal of Quantum Electronics*, vol. 20, no.4, pp. 343-349, 1984.
- [99] H. E. Rowe, "Signals and Noise in Communication Systems", Van Nostrand, 1965.
- [100] U. Gliese, E. L. Christensen and K. Stubkjaer, "Laser linewidth requirements and improvements for coherent optical beam-forming networks in satellites", *IEEE Journal of Lightwave Technology*, vol. 9, no.6, pp. 779-790, 1991.
- [101] Intelsat earth station standards (IESS), "QPSK/FDMA performance characterization for Intelsat business services (IBS) ", Document IESS-309 (Rev.2), Approval date: Mar. 9, 1990, pp. 14.
- [102] H. Schmuck, "Carrier-to-noise limitations in optical mm-wave links due to phase-induced-intensity noise", *Electronics Letters*, vol. 33, no.14, pp. 1236-1237, 1997.
- [103] D. A. Atlas, "Fibre induced distortion and phase noise to intensity noise conversion in external modulated CATV systems", *NCTA Technical papers*, pp. 289, 1996.
- [104] S. Yamamoto et al., "Analysis of Laser Phase Noise to Intensity Noise Conversion by Chromatic Dispersion in Intensity Modulation and Direct Detection Optical-Fiber Transmission", *IEEE Journal of Lightwave Technology*, vol. 8, no.11, pp. 1716-1722, 1990.
- [105] E. Iannone et al., "Effect of polarization dispersion on the performance of IM-DD communication systems", *IEEE Photonics Technology Letters*, vol. 5, no.10, pp. 1247-1249, 1993.
-

- [106] H. Bülow, "Operation of a digital optical transmission system with minimal degradation due to polarization mode dispersion (PMD)", *Electronics Letters*, vol. 31, no.3, pp. 214-215, 1995.
- [107] H. Schmuck, "Effect of polarization-mode dispersion in fiber-optic millimeter-wave systems", *Electronics Letters*, vol. 30, no.18, pp. 1503-1504, 1994.
- [108] R. Hofstetter, H. Schmuck and R. Heidemann, "Dispersion Effects in Optical Millimeter-Wave Systems Using Self-Heterodyne Method for Transport and Generation", *IEEE Transactions on Microwave Theory and Techniques*, vol. 43, no.9, pp. 2263-2269, 1995.
- [109] C.K. Sun, R.J. Orazi and S.A. Pappert, "Efficient microwave frequency conversion using photonic link signal mixing", *IEEE Photonics Technology Letters*, vol. 8, no.1, pp. 154-156, 1996.
- [110] M. Sugiyama et al., "Low-drive-voltage and compact RZ-DQPSK LiNbO₃ Modulator," *ECOC 2007*, Berlin, Germany, 17-19.09.2007.
- [111] T. Kawanishi et al., "70 dB Extinction-Ratio LiNbO₃ Optical Intensity Modulator for Two-Tone Lightwave Generation," *OFC 2006*, Anaheim, USA, 2006.
- [112] S. Aisawa et al., "Dc Drift Compensation Method Using Low Frequency Perturbation For LiNbO₃ Intensity Modulator", *CLEO/Pacific Rim '97*, pp. 123-124, Baltimore, USA, 14-18 July 1997.
- [113] A. Wiberg, B. E. Olsson, P. O. Hedekvist and P. A. Andrekson, "Dispersion-Tolerant Millimeter-Wave Photonic Link Using Polarization-Dependent Modulation", *IEEE Journal of Lightwave Technology*, vol. 25, no.10, pp. 2984-2991, 2007.
- [114] R. Kashyap, "Fiber Bragg Gratings", Academic Press, San Diego, USA, 1999.
- [115] W. P. Robins, "Phase Noise in Signal Sources", *IEE Telecommunications Series 9*, Peter Peregrinus Ltd., pp. 78, 1984.
- [116] G. Qi et al., "Phase-Noise Analysis of Optically Generated Millimeter-Wave Signals With External Optical Modulation Techniques", *IEEE Journal of Lightwave Technology*, vol. 24, no.12, pp. 4861-4875, 2006.
- [117] D. B. Mortimore, "Fiber loop reflectors", *IEEE Journal of Lightwave Technology*, vol. 6, No. 7, pp. 1217-1224, July 1988.
- [118] X. Chen, "Application of refractive index changing effects in fiber structures for optical signal processing", *Diplomarbeit*, TU Dresden, June 2002.
- [119] G. K. Gopalakrishnan et al., "Performance and Modeling of Broadband LiNbO₃ Traveling Wave Optical Intensity Modulators", *IEEE Journal of Lightwave Technology*, vol. 12, no. 10, 1994, pp. 1807-1819, 1994.
- [120] E. D. Wooten et al., "A Review of Lithium Niobate Modulators for Fiber-Optic Communications Systems", *IEEE Selected Topics in Quantum Electron.*, vol. 6, pp. 69-82, 2000.
- [121] U. Gliese, S. Norskov and T. N. Nielsen, "Chromatic dispersion in fiber-optic microwave and millimetre-wave links", *IEEE Trans. Microwave Theory Tech.*, vol.44, pp. 1716-1724, Oct. 1996.

-
- [122] N. A. Olsson, "Lightwave systems with optical amplifiers", *IEEE Journal of Lightwave Technology*, vol. 7, No. 7, pp. 1071-1082, July 1989.
- [123] I. González Insua, K. Kojucharow and C. G. Schäffer, "Optical generation of microwave signals with ASE", *International Topical Meeting on Microwave Photonics (MWP) 2004*, Ogunquit, USA, 4.-6.10.2004.
- [124] E. Voges and K. Peterman, "Optische Kommunikationstechnik", Chapter 16.3.5, pp. 573-574, Springer Verlag, Berlin, 2002.
- [125] J. Leuthold et al., "100 Gbit/s all-optical wavelength conversion with integrated SOA delayed-interference configuration", *Electronic Letters*, vol. 36, no.13, pp. 1129-1130, 2000.
- [126] Y. Ueno et al., "168 Gb/s OTDM wavelength conversion using an SMZ-type all-optical switch," *ECOC 2000*, Munich, Germany, September 2000.
- [127] M. Dülk et al., "Efficient and robust regenerative all-optical wavelength converter for C- and L-band (80 nm span) and for data rates up to 40 Gbit/s", *CLEO 2000*, San Francisco, USA, May 2000.
- [128] M. Tsurusawa, K. Nishimura and M. Usami, "First demonstration of simultaneous demultiplexing from 80 Gb/s to 2x40 Gb/s by SOA-based all-optical polarization switch," *ECOC 2001*, Amsterdam, Holland, October 2001.
- [129] S. Nakamura, Y. Ueno and K. Tajima, "Error-free all-optical demultiplexing at 336 Gb/s with hybrid-integrate symmetric-Mach-Zehnder switch", *OFC 2002*, Anaheim, USA, March 2002.
- [130] T. Tekin et al., "Ultrafast all-optical demultiplexing performance of monolithically integrated band gap shifted Mach-Zehnder interferometer", *ECOC 2001*, Amsterdam, Holland, October 2001.
- [131] T. Yamamoto et al., "160 Gbit/s demultiplexer with clock recovery using SOA-based interferometric switches and its application to 120 km fiber transmission", *ECOC '01*, Amsterdam, Holland, October 2001.
- [132] D. A. O. Davies, "Small-signal analysis of wavelength conversion in semiconductor laser amplifiers via gain saturation", *IEEE Photonics Technology Letters*, vol. 7, no.6, pp. 617-619, 1995.
- [133] T. Durhuus et al., "All-optical wavelength conversion by semiconductor optical amplifiers", *IEEE Journal of Lightwave Technology*, vol. 14, no.6, pp. 942-954, 1996.
- [134] L. Occhi, L. Schares and G. Guekos, "Phase modeling based on the a-factor in bulk semiconductor optical amplifiers", *Selected Topics in Quantum Electronics*, vol. 9, no.3, pp. 788-797, 2003.
- [135] I. González Insua and C. G. Schäffer, "Optical generation of microwave signals based on XPM of SOAs in a fiber loop", *International Topical Meeting on Microwave Photonics (MWP) 2006*, Grenoble, France, 3.-6.10.2006.
- [136] L. Schares et al., "Phase Dynamics of Semiconductor Optical Amplifiers at 10-40 Ghz", *IEEE Journal of Quantum Electronics*, vol. 39, no.11, pp. 1394-1408, 2003.
-

- [137] B. E. A. Saleh and M. C. Teich, "Fundamentals of Photonics", Chapter 18.1, pp. 698-699, Wiley, 1991.
- [138] S. B. Alexander, "Optical Communication Receiver Design", SPIE, 1997.
- [139] H. Van Trees, "Detection Estimation and Modulation Theory - Part 1", Wiley & Sons, Inc., New York, 1968.
- [140] J. M. Wozencraft, I. M. Jacobs, "Principles of Communication Engineering", Wiley & Sons, New York, 1965.
- [141] C. W. Helstrom, "Probability and Stochastic Processes for Engineers", Macmillan Publishing Company, New York, 1984.
- [142] R. S. Vodhanel et al., "Performance of directly modulated DFB lasers in 10-Gb/s ASK, FSK, and DPSK lightwave systems", *IEEE Journal of Lightwave Technology*, vol. 8, no.9, pp. 1379-1386, 1990.
- [143] P. S. Henry, S. D. Personick, "Coherent Lightwave Communications", IEEE Press, New York, 1990.
- [144] T. Okoshi and K. Kikuchi, "Coherent Optical Fiber Communications", Kluwer Academic Publishers, Boston, 1988.
- [145] A. H. Gnauck et al., "4-Gb/s heterodyne transmission experiments using ASK, FSK and DPSK modulation", *IEEE Photonics Technology Letters*, vol. 2, no.12, pp. 908-910, 1990.
- [146] S. Ramachandran, "Fiber Based Dispersion Compensation", Springer, 2007.
- [147] J. J. Carr, "The technician EMI handbook: clues and solutions", Newnes, 2000.
- [148] Hewlett Packard Application Note 923, "Schottky Barrier Diode Video Detectors", 1986.
- [149] G. Foschini, L. Greenstein and G. Vannucci, "Noncoherent detection of coherent lightwave signals corrupted by phase noise", *IEEE Transactions on Communications*, vol. 36, no.3, pp. 306-314, 1988.
- [150] M. Sauer, K. Kojucharow, H. Kaluzni, M. Otto and C. G. Schäffer, "Millimeter-Wave Wireless LAN Based on Simultaneous Upconversion Technique of Optical WDM Channels", *European Microwave Conference*, paper G-TuF2, München, 4.-8.10.1999.
- [151] M. Weiss et al., "60 GHz Radio-over-Fibre Wireless System for Bridging 10 Gb/s Ethernet Links", *European Conference on Optical Communications (ECOC) 2008*, paper Tu.3.F.6, Brussels, Belgium, 21-25.09.2008.
- [152] R. Linke et al., "Mode power partition events in nearly single-frequency lasers," *IEEE Journal of Lightwave Technology*, vol. 3, no. 3, pp. 706-712, 1985.
- [153] A. Wiberg et al., "Fiber-Optic 40-GHz mm-Wave Link With 2.5 Gb/s Data Transmission", *IEEE Photonics Technology Letters*, vol. 17, no.9, pp. 1938-1940, 2005.
- [154] L. Chen et al., "A Novel Radio-Over-Fiber System with Wavelength Reuse for Upstream Data Connection", *IEEE Photonics Technology Letters*, vol. 19, no.6, pp. 387-389, 2007.

-
- [155] L. Chen, H. Wen and S. Wen, "A Radio-Over-Fiber System With a Novel Scheme for Millimeter-Wave Generation and Wavelength Reuse for Up-Link Connection", *IEEE Photonics Technology Letters*, vol. 18, no.19, pp. 2056-2058, 2006.
- [156] J. Yu et al., "Optical millimeter-wave generation or up-conversion using external modulators", *IEEE Photonics Technology Letters*, vol. 18, no.1, pp. 265-267, 2006.
- [157] I. Gonzalez Insua and C. G. Schäffer, "Broadband Wireless Access", 9. ITG Fachtagung "Photonische Netze", Leipzig, Germany, 28-29.04.2008.
- [158] S. B. Alexander, "Design of wide-band optical heterodyne balanced mixer receivers", *IEEE Journal of Lightwave Technology*, vol. 5, no.4, pp. 523-537, 1987.
- [159] G. Jacobsen and I. Garrett, "Optical ASK heterodyne receiver: comparison of a theoretical model with experiment", *Electronics Letters*, vol. 22, no.3, pp. 170-171, 1986.
- [160] I. Garrett and G. Jacobsen, "The effect of laser linewidth on coherent optical receivers with nonsynchronous demodulation", *IEEE Journal of Lightwave Technology*, vol. 5, no.4, pp. 551-560, 1987.
- [161] Y. Park et al., "Performance of ASK heterodyne detection for various laser linewidths", *Electronics Letters*, vol. 22, no.5, pp. 283-284, 1986.
- [162] G. Jacobsen and I. Garrett, "Theory for heterodyne optical ASK receivers using square-law detection and postdetection filtering", *IEE Proceedings J Optoelectronics*, vol. 134, no.5, pp. 303-312, 1987.
- [163] http://www.spaceklabs.com/Products/Broadband_Detectors/broadband_detectors.html
- [164] D. Zhou et al., "A simple method to characterize dynamic parameters of semiconductor waveguide amplifiers", *LEOS '98*, Orlando, USA, December 1998.
- [165] L. Occhi, "Semiconductor optical amplifiers made of ridge waveguide bulk InGaAsP/Inp", ETH Zurich, 2002.

Acknowledgments

The results of this thesis have been realized thanks to the help and support of a large number of people in numerous ways. Most of the technical help was provided by my colleagues at the chair for RF & Photonics at Dresden University of Technology (TUD) whereas emotional support came mostly from family and friends, old ones from Argentina and new ones made along the way. I hope not to forget anyone involved, but since erring is human, please forgive me if I missed somebody.

The first special thanks go to Prof. Dr. Ing. Schäffer who gave me the opportunity to work in this very exciting field and supervised my work. I especially appreciate the scientific freedom he let me, his continuous support, his readiness to let me cooperate with other research groups, and his patience and availability in correcting my manuscripts.

Further I would like to thank Prof. Dr. rer. nat. habil. Dieter Jäger for having devoted part of his time to co-examine this thesis and Dr. Andreas Stöhr who was originally going to be one of my co-examiners but due to University regulations could finally not participate in the process.

During the first half of my stay in Dresden University of Technology I had the pleasure to work with kind persons such as Thomas Duthel, Michael Otto, Falk Michael, Maik Spaarschuh, Klaus Wolf, Konstantin Kojukarow and Jens Peupelmann, who helped me take my first steps in the experimental laboratory and university life. From this group I want to specially thank Thomas for all his advice and additional help regarding bureaucracy issues as well as for always being there as a good friend.

The second part of my stay added new PhD students who helped me along the way, namely Michael Haas, Niels Neumann, Tobias Schuster and Reinhold Herschel; as well as a new head of staff in Dr. Plettemeier who was always available and ready to help me in everyway. Further thanks go to Angela Schober who was in charge of endlessly filling university forms and organizing all of the trips to conferences and congresses.

I would like to particularly thank my family, who sustained me emotionally as well as economically during my stay in Germany. Special thanks go to my parents, Jose Antonio and

Silvia, as well as to my brothers Fernando, Mariana and Guillermo. Their support and company at times were always a great help and heartily welcomed.

To my best friends from Argentina: Manu, Marce, Seba, Pato, Yepu, Negrito, Kevin, Sergio, Otto, German, Luis, Mathias and many college colleagues. Thanks for all the support during my career and specially my life.

During my seven year residence in Dresden I made many friends, mostly Erasmus exchange students, which are too many to mention, but I will try it anyway. My biggest gratitude goes to Eugenio and Susi, who were always there for me and besides being my best friends in Dresden I also consider them part of my family already. Even though they work on a totally different field, their insight as researchers and their experience as PhDs helped me to carry on even in the most difficult of times. Many thanks go to Llanos, who was kind of a sidekick for me during her stay at the chair for RF & Photonics. Her company made everyday less cumbersome.

From my first “Erasmus year”, I would like to acknowledge the companionship of Txapy, Isaac, Noel, Edu, Rafa, Dani, César, Marisa, Gonzalo and many more. They introduced me to the Erasmus way of life, and there is no going back now.

The second Erasmus season provided some good friends in Borja, Victor, Amaia and David, with whom I shared many quality times, such as Borja’s wedding in Burgos, Spain, which I will never forget.

The third year meant meeting wonderful and uncomplicated persons such as Manu, Hernan, Sara, Fabian, Maru, Bjorn, Borja, Sheila, Märy and many more which deserve my special thanks.

My fourth Erasmus period (and probably the best one) deserves the special mention to Sakito, Joan, Fernando, Hector, Angel, Javi, Mario, Alex, Carles, Laura, Isa, Märy (again), Llanos, Butombo, Roberto, Angela, Bea, Fran, Selvan, Guillermo Santander, Guillermo Murcia, Gabi, Quique, Koki, Yoda and I hope I am not forgetting anyone, because we had such a really good time, with plenty of parties and awesome trips. Their friendship still lasts today and I hope not to lose contact with any of them.

During my fifth year I met some more amazing persons, such as Pablet, Fran (again) Antonia, Inma, Ana, Marta, and Maria. This was kind of a farewell Erasmus year.

During my sixth year I couldn't participate much in the Erasmus life due to the finishing of this thesis. Nonetheless I met some incredible friends in Javi, Carlos, Esther, Miguel, Jose, Jesus, Rebeca, Oscar, Gloria, Michela, Bibi and Edu. Thank you very much for all the fun times.

Now finally at the end of this long journey, I would like to mention the last people who help me make everyday worthwhile: Sergio, Paloma, Felix, Flamenquinma, Miguel (again), Diego, Fernando and Daniela.

It has been a long way since leaving Argentina to pursue a higher education and survive the economical crisis my country still lies in. Many thanks go to Prof. Roxana Saintnom in Argentina who encouraged me to stay in this path.

Dresden, September 2009.

Appendix A Phase modulation index measurements of PM

The modulation of the phase of an optical signal is usually quite difficult to measure directly, as the phase information of an optical carrier is lost after photodetection. Generally an indirect measurement takes place in which the phase modulation is converted to intensity modulation. The electric field of an optical carrier modulated in its phase takes the form

$$E(t) = E_0 \cdot e^{j[\omega_c t + \pi \cdot m_{ph} \cdot \sin(\omega_m t)]} \quad (\text{A.1})$$

where ω_c is the angular frequency of the optical carrier, $m_{ph} = V_{RF} / V_\pi$ is the phase modulation index, V_π is the modulators half-wave voltage and ω_m is the modulation angular frequency. Expanding Eq. (A.1) as a series of Bessel functions of the first order k results in

$$E(t) = E_0 \cdot e^{j\omega_c t} \sum_{k=-\infty}^{\infty} [J_k(\pi \cdot m_{ph})] \cdot e^{jk\omega_m t}. \quad (\text{A.2})$$

From Eq. (A.2) it is evident that the spectrum consists of infinite harmonics $k\omega_m$ around ω_c . The amplitude and phase of the harmonics are governed in such a way that after photodetection they all cancel out. Figure A.1 shows a simulation of the generated harmonics for $k = \pm 5$ with their corresponding phase.

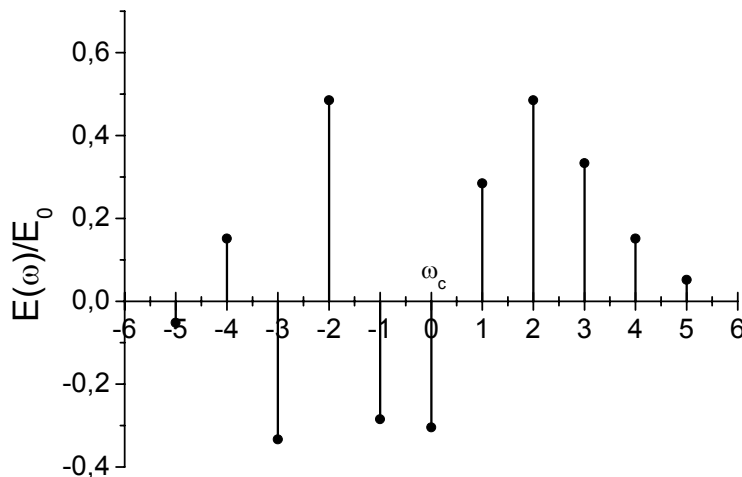


Figure A.1: Phase modulation harmonics of ω_m around ω_c .

In order to measure the phase modulation index m_{ph} of the UDT PM-1.5-8.0, the setup shown in Figure A.2 was used. A dual wavelength source is in charge of generating two phase correlated spectral lines which in our case are $\Delta f_c = 33$ GHz apart. They are then separated in two different optical paths by a Mach-Zehnder Interferometer. The spectral line in path A is modulated in its phase by the phase modulator (PM) under test, whereas the other spectral line remains unchanged. After recombination in a 50% coupler, the phase modulation is turned into intensity modulation and therefore detected by the broadband photodiode.

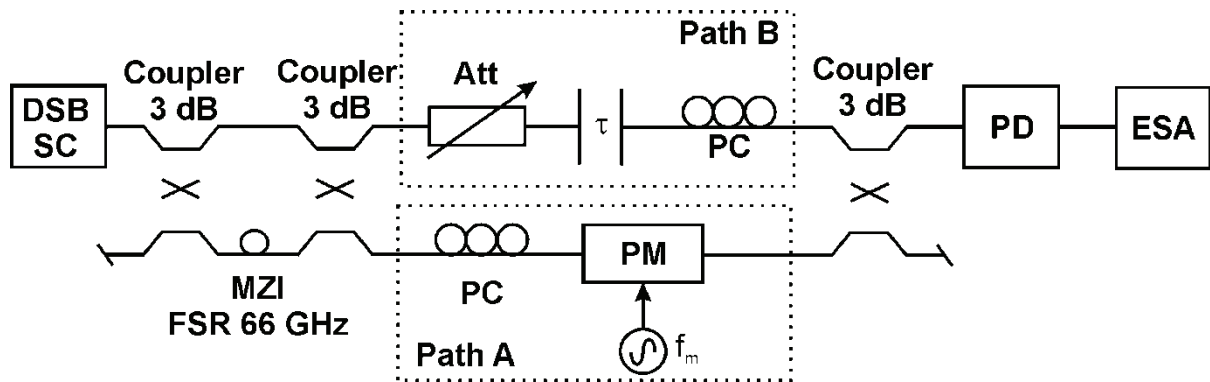


Figure A.2: Setup to measure the phase modulation index m_{ph} . MZI: Mach-Zehnder interferometer, PM: Phase modulator, PC: Polarization controller, PD: Photodiode, ESA: Electrical spectrum analyzer.

Mathematically, the signals in path A and B take the form

$$E_A(t) = E_0 \sin \left[\left(\omega_c + \frac{\Delta\omega_c}{2} \right) t + \pi \cdot m_{ph} \cdot \sin(\omega_m t) \right] \quad (\text{A.3})$$

$$E_B(t) = E_0 \sin \left(\left(\omega_c - \frac{\Delta\omega_c}{2} \right) t \right) \quad (\text{A.4})$$

where ω_c is the central frequency of the dual-wavelength source, $\Delta\omega_c = 2\pi\Delta f_c \ll \omega_c$ and $\omega_m = 2\pi f_m$, being f_m the modulation frequency applied to the phase modulator. The signal entering the photodiode is the sum of both electrical fields and after some algebraic manipulation takes the form

$$E_{out}(t) = E_A(t) + E_B(t) = 2E_0 \sin \left[\omega_c t + \frac{\pi m_{ph}}{2} \sin(\omega_m t) \right] \cos \left[\frac{\Delta\omega_c t}{2} + \frac{\pi m_{ph}}{2} \sin(\omega_m t) \right] \quad (\text{A.5})$$

As the photodiode acts as a squaring device, the current I_{PD} is then proportional to

$$I_{PD}(t) \propto |E_{out}(t)|^2 = E_0^2 \left\{ 1 - \cos[2\omega_c t + \pi \cdot m_{ph} \sin(\omega_m t)] \right\} \cdot \left\{ 1 + \cos[\Delta\omega_c t + \pi \cdot m_{ph} \sin(\omega_m t)] \right\}. \quad (\text{A.6})$$

As the photodiode has a finite bandwidth, all high frequency components will be filtered out, in this case the first term of Eq. (A.6). Neglecting all the high frequency components of I_{PD} such as $2\omega_c$, I_{PD} takes the form

$$I_{PD} \approx A \left\{ 1 + \cos[\Delta\omega_c t + \pi \cdot m_{ph} \sin(\omega_m t)] \right\}. \quad (\text{A.7})$$

I_{PD} is a phase modulated signal with the frequency $\Delta\omega_c$, and can be expanded in a series of Bessel functions of the first order as

$$I_{PD}(t) \approx A \left[1 + \sum_{k=-\infty}^{\infty} J_k(\pi \cdot m_{ph}) \cdot \cos(\Delta\omega_c t + k\omega_m t) \right] \quad (\text{A.8})$$

The power spectrum now has harmonics of $k\omega_m$ around the GHz band frequency $\Delta\omega_c$. The ratio of the power in the center harmonic to the first sideband is a function of m_{ph} and is given by

$$\frac{P_1}{P_0} = P_r = \frac{J_1(\pi \cdot m_{ph})}{J_0(\pi \cdot m_{ph})}. \quad (\text{A.9})$$

The power ratio from Eq. (A.9) is calculated and plotted in Figure A.3. It is clearly a monotonic increasing function up to the first zero of $J_0(\pi m_{ph})$ which occurs for $m_{ph} = 0.76$.

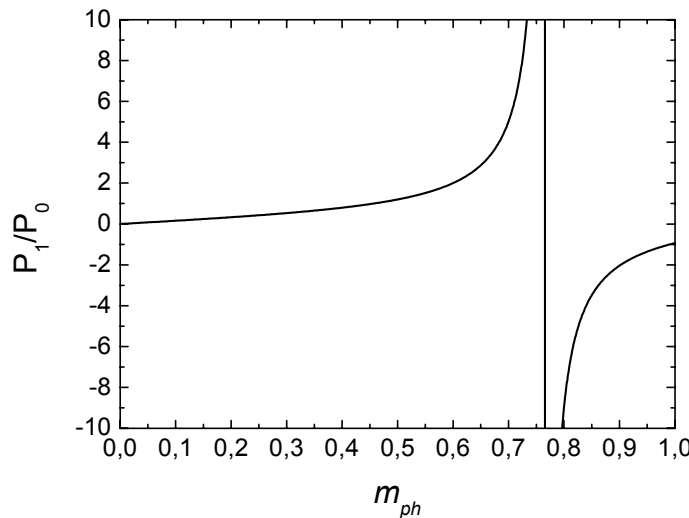


Figure A.3: Power ratio as a function of the phase modulation index m_{ph} .

As long as the phase modulation index $m_{ph} < 0.76$, the inverse function can be calculated and thus the value of m_{ph} retrieved. Mathematically

$$m_{ph} = f^{-1}[P_r] = f^{-1}\left[\frac{J_1(\pi \cdot m_{ph})}{J_0(\pi \cdot m_{ph})}\right] \quad (\text{A.10})$$

and expanding it in a Taylor series of order 4 results in

$$m_{ph} = 0.0151 - 0.006 \cdot P_r - 0.2453 \cdot (P_r)^2 + 0.6973 \cdot (P_r)^3 - 0.0033 \cdot (P_r)^4. \quad (\text{A.11})$$

This approximation works best for modulation index values $m_{ph} < 0.6$. For phase modulation index values approaching $m_{ph} = 0.76$ a higher order polynomial would be needed to maintain the same accuracy.

Figure A.4 shows the measurements of the modulation index m_{ph} for both operation directions, forward and backward, as a function of the modulation frequency f_m . The power was controlled and set to be $P_m = 26$ dBm throughout the whole measurement. It is evident that the phase modulator under test has a travelling wave electrode, as the phase modulation index m_{ph} for the forward and backward direction differ greatly as the frequency increases. In the forward direction, the phase modulation index m_{ph} decreases with a slope of $-0.057/\text{GHz}$. For backward operation, the phase modulation index m_{ph} decreases more abruptly with a slope of $-0.19/\text{GHz}$ up to 4 GHz. From there onwards, the modulation index remains approximately zero.

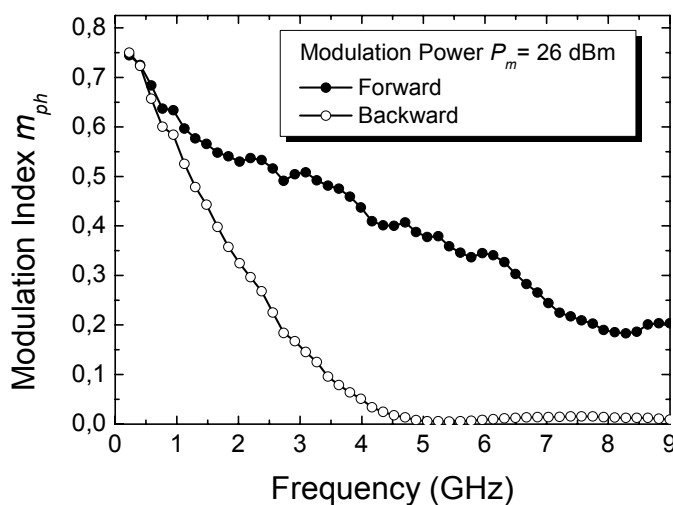


Figure A.4: Phase modulation index m_{ph} as a function of modulation frequency f_m for forward and backward modulation ($P_m = 26$ dBm).

The response to variations in the modulation power P_m are depicted in Figure A.5 for different modulation frequencies f_m . Figure A.5a shows the response in the forward direction whereas the results of backward operation are described in Figure A.5b. First of all, although V_π of the phase modulator used is specified from the datasheet to be $V_\pi = 14$ V, from the graphs in Figure A.5 it is clear that this value is never reached (i.e. $m_{ph} = 1$) even for high RF swing voltages such as $V_{pp} = 14$ V. Second, the curves have different slopes according to the modulation frequency f_m . For the forward case, up to 6 GHz the results are acceptable, but then a much lower efficiency occurs even for $f_m = 8$ GHz which is within the phase modulators reported bandwidth. Last but not least, backward operation is extremely inefficient, as already shown in Figure A.4. Even for high RF powers, the backward response is negligible from 4 GHz onwards. This is explained due to the fact that high speed phase modulators employ travelling wave electrodes to achieve this kind of high frequency response. The downside is that this works only on one direction of propagation, where the optical signal and the RF signal copropagate. On the opposite direction, the response is thus hampered.

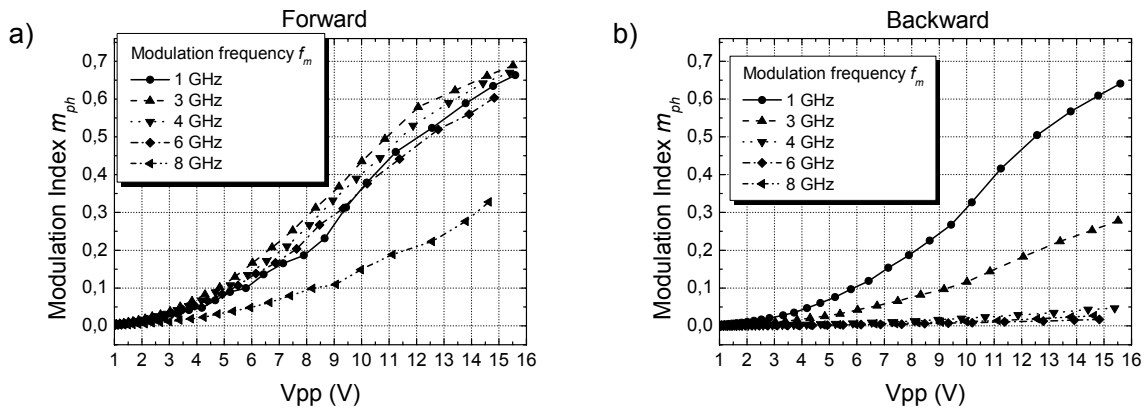


Figure A.5: Phase modulation index m_{ph} as a function of modulation power P_m for a) forward and b) backward operation with modulation frequency f_m as a parameter.

To better compare the differences between forward and backward operation, Figure A.6 shows both modes for selected frequencies f_m . As expected, at lower frequencies such as $f_m = 0.5$ GHz, the difference between forward and backward operation is minimal. At the other end of the phase modulators bandwidth, at $f_m = 8$ GHz, the differences are greater, as the modulation efficiency decreases, for backward operation there is practically no modulation.

And even in forward operation the modulation index achieved is less than half for lower frequencies.

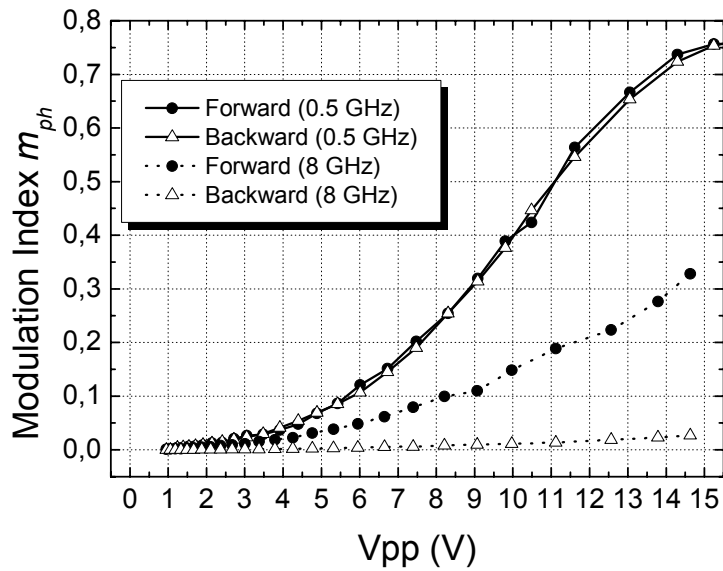


Figure A.6: Phase modulation index m_{ph} as a function of modulation power P_m with modulation frequency f_m as a parameter.

Appendix B Phase modulation index measurement of SOAs

Semiconductor optical amplifiers (SOAs) are used throughout this work to generate mm-wave signals via cross-phase modulation (XPM) in a fiber loop configuration. The measurement of the modulation index m_{ph} generated by XPM in SOAs is not so easy to measure with the setup described in Appendix A, as there is also an inherent cross-gain modulation (XGM) associated with it. Therefore the setup shown in Figure B.1 is proposed in the literature [164]-[165]. By injecting two optical signals into the SOA, the low power probe laser will exhibit a XGM and XPM effect due to the high power pump laser which modulates the carrier density inside the SOA. After filtering out the pump with a fiber Bragg grating (FBG), the desired probe beam is available to process.

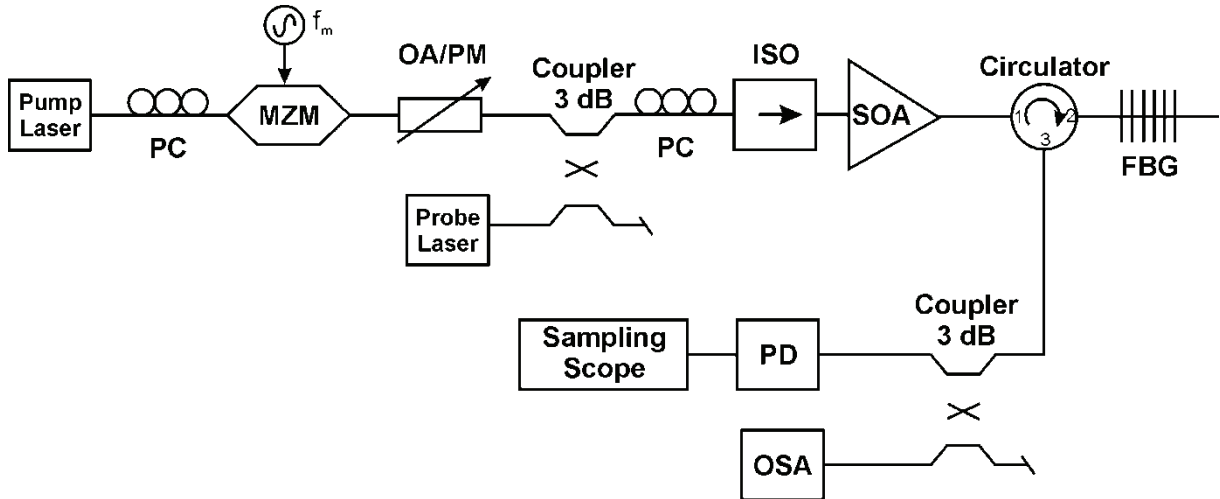


Figure B.1: Setup to measure the phase modulation index m_{ph} generated by XPM in SOAs. MZM: Mach-Zehnder modulator, OA/PM: Optical attenuator/power monitor, PC: Polarization controller, ISO: isolator, FBG: Fiber Bragg grating, PD: Photodiode, OSA: Optical spectrum analyzer.

The amplitude modulation index m_a can be directly measured with a calibrated photodiode (PD) and a sampling scope in the time domain as shown in Figure B.2a. Mathematically,

$$m_a = \frac{V_{\max} - V_{AVG}}{V_{AVG}} \quad (\text{B.1})$$

where V_{\max} is the maximum voltage and V_{AVG} the average voltage of the waveform. The phase modulation index can be calculated from the optical spectrum by measuring the optical carrier

power $|C_0|^2$ and the first sideband power $|C_1|^2$ as shown in Figure B.2b. The relationship between the ratio optical carrier to sideband is [165]

$$\frac{|C_1|^2}{|C_0|^2} = \frac{4 \cdot J_1(\beta)^2 + m_a^2 (J_1(\beta)/\beta - J_2(\beta))^2}{4 \cdot J_0(\beta) + m_a^2 \cdot J_1(\beta)^2} \quad (\text{B.2})$$

where $\beta = \pi m_{ph}$ and J_n are the Bessel functions of order n . Once m_a is known, β is calculated numerically from Eq. (B.2) thus providing a way of calculating m_{ph} due to XPM in SOAs.

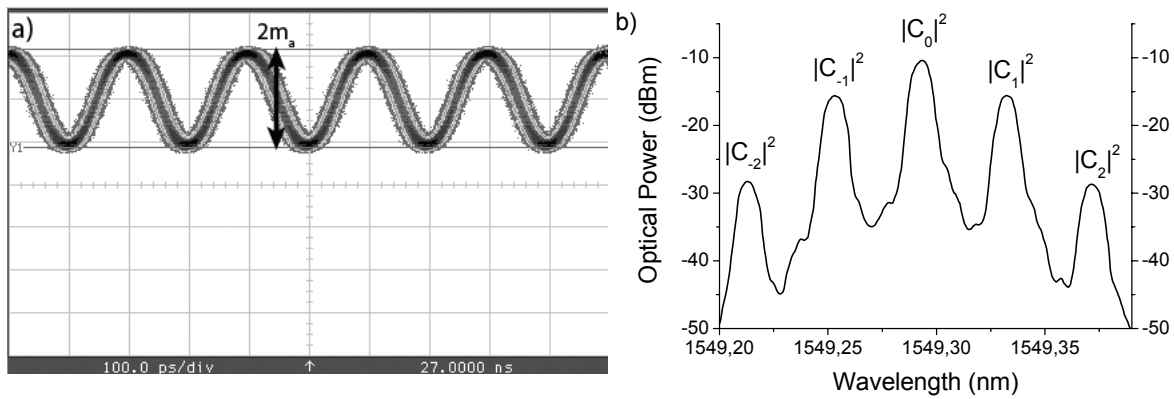


Figure B.2: a) Output power versus time and b) output power spectrum from OSA ($f_m = 5$ GHz). Resolution bandwidth 10 pm.

For the phase modulation index measurements two SOAs were available. A commercial one from COVEGA and a custom made one from University of Karlsruhe. The most important parameters of both SOAs are summarized in Table B.1, for more measurements and data refer to Appendix C.

	Length (mm)	G (dB)	Gain Ripple (dB)	Psat (dBm)	Operating Current (mA)	ASE Peak Wavelength (nm)	Optical 3-dB BW (nm)
COVEGA	1	22	0.13	9.4	500	1535.1	59.4
Uni Karlsruhe	0.7	19	2	-5	150	1555.7	25.4

Table B.1: Basic parameters of the tested SOAs.

The SOA from COVEGA is designed for DWDM system performance, therefore it presents high gain ($G = 22$ dB) over a broad optical bandwidth ($B = 59.4$ nm) with a decent saturation power $P_{sat} = 9.4$ dBm to provide linear operation. On the other hand, the SOA from Uni

Karlsruhe was specially designed for nonlinear operation. Consequently, the saturation power is quite low at $P_{sat} = -5$ dBm, it has a smaller optical bandwidth with $B = 25.4$ nm and comparable gain with $G = 19$ dB. An important factor is that it requires less current to bias with $I_{op} = 150$ mA.

A sample measurement is shown in Figure B.3 for both SOAs for different bias currents I_{bias} and for both forward and backward operation. As was explained in section 5.2.2, the XPM bandwidth can be approximated with the XGM bandwidth and then an estimation of the phase modulation index m_{ph} outside the measurement range can be predicted. One important result is that higher modulation indices than with a phase modulator can be achieved in the low frequency range and that the device operates bidirectionally.

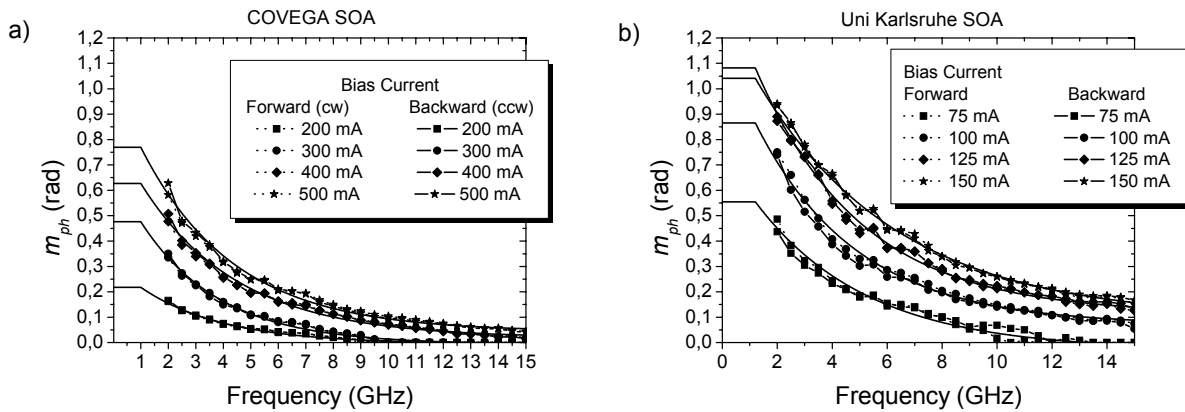


Figure B.3: Phase modulation index m_{ph} for XPM versus modulation frequency f_m . a) Covega SOA, $P_m = 17$ dBm, $P_{probe} = -10$ dBm, $P_{pump} = 2.5$ dBm and b) Uni Karlsruhe SOA, $P_m = 17$ dBm, $P_{probe} = -10$ dBm, $P_{pump} = -5.5$ dBm.

The dependence on the phase modulation index m_{ph} on different SOA parameters will be investigated in the next sections for the SOA from Covega only.

B.1 Probe power dependency

The probe power is varied from $P_{probe} = -12$ to 0 dBm and the results are shown in Figure B.4. As the probe power increases, the modulation index m_{ph} decreases because the probe starts acting as a new pump. So theoretically, low probe powers prove beneficial to obtain a high modulation index m_{ph} , but there is a tradeoff in signal power, as the gain of the device is limited.

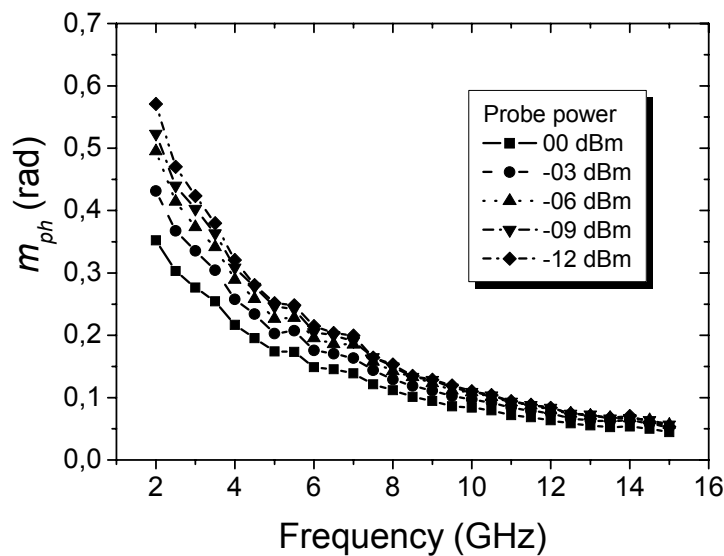


Figure B.4: Phase modulation index m_{ph} for XPM versus modulation frequency f_m for different probe powers P_{probe} (Covega SOA, $P_m = 17$ dBm, $P_{pump} = 2.5$ dBm).

B.2 Pump power dependency

Now the pump power is varied from $P_{pump} = -7.5$ dBm to $+2.5$ dBm. The results are plotted in Figure B.5. As expected from theory, the stronger the pump power, the higher the modulation index m_{ph} that can be achieved.

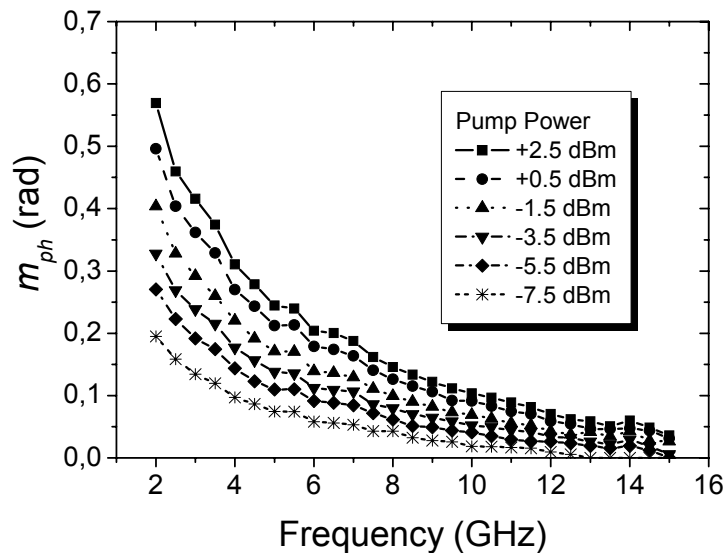


Figure B.5: Phase modulation index m_{ph} for XPM versus modulation frequency f_m for different pump powers P_{pump} (Covega SOA, $P_m = 17$ dBm, $P_{probe} = -10$ dBm).

B.3 Wavelength dependency

In this section the wavelength separation of pump and probe will be varied, and the optical filters tuned accordingly, to measure the dependency of the XGM effect with regards to wavelength separation. As the tuning range of the FBG was limited to 8 nm and the pump laser could also be tuned but only 2 nm around 1549 nm, then the pump laser was set fix at $\lambda_{pump} = 1549.6$ nm and the probe beam was swept through the 8 nm tunable range of the FBG. The results are shown in Figure B.6.

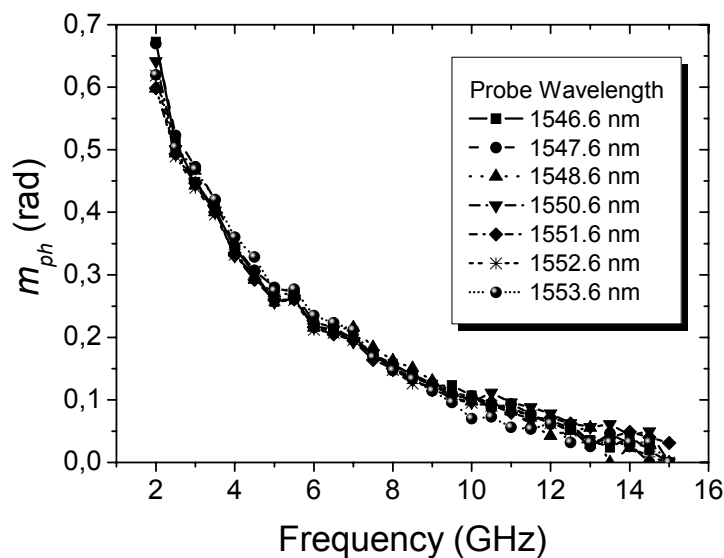


Figure B.6: Phase modulation index m_{ph} for XPM versus modulation frequency f_m for different wavelength separations of pump and probe. (Covega SOA, $P_m = 17$ dBm, $P_{probe} = -10$ dBm, $P_{pump} = 2$ dBm).

No significant variation is observed through the swept wavelength range probably due to the limited tuning range of the FBG which could only be varied 8 nm.

B.4 Temperature dependency

The dependency of the modulation index m_{ph} with regards to operation temperature will be the last test. The operating temperature can be controlled via the biasing and temperature controller from ILX LDC-3722. The range tested was from $T = 22^\circ\text{C}$ to 34°C and the results are shown in Figure B.7.

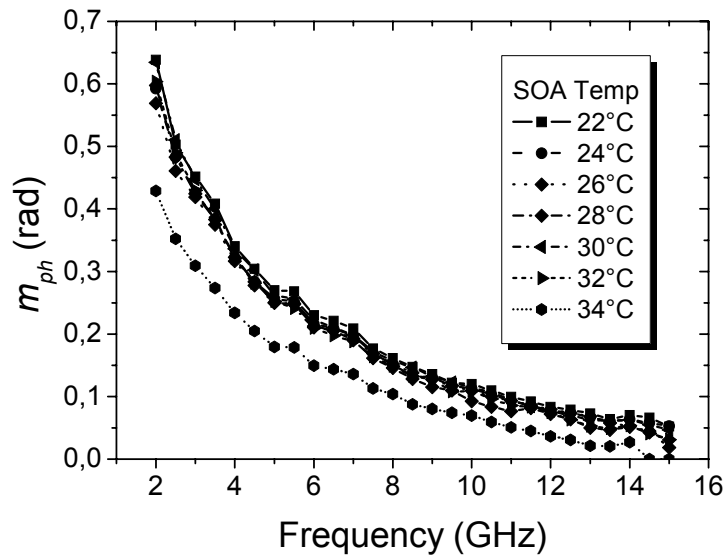


Figure B.7: Phase modulation index m_{ph} for XPM versus modulation frequency f_m for different operating temperatures. (Covega SOA, $P_m = 17$ dBm, $P_{probe} = -10$ dBm, $P_{pump} = 2$ dBm).

The increase in temperature has no predominant effect on the modulation index m_{ph} as long as the threshold temperature is not reached. This states that the temperature of the active region has no appreciable influence on the device operation as long as the injection current is maintained constant. In the case of the SOA from Covega, the operating temperature was specified to be no higher than 35°C. As this temperature is approached (i.e. $T = 34^\circ\text{C}$) then a lower m_{ph} is observed which could be due to problems with the injection current distribution at this operating temperatures.

Appendix C SOA datasheets



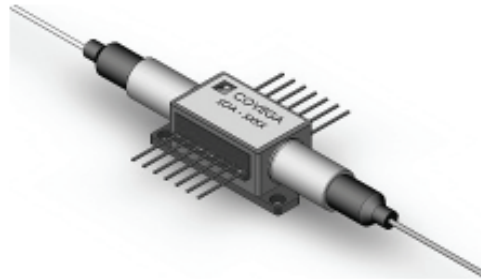
SOA 1117: 1550nm Semiconductor Optical Amplifier, Non-Linear

Limited Availability

Description

COVEGA's 1117 SOA is a polarization insensitive optical amplifier housed in a standard 14-pin butterfly package. Advanced epitaxial wafer growth and opto-electronic packaging techniques enable high output saturation power, low noise figure, and large gain across a broad spectral bandwidth.

Packaging options include input and output isolators, SMF and PMF fiber tails and choice of connectors.



Applications

- ✓ Optical Booster and In-line Amplification in WDM Metro Network Systems
- ✓ Optical Loss Compensator
 - Channel Launch (Modulator)
 - Mid-Stage (Add/Drop)
- ✓ Pre-Amplifier
- ✓ Non-Linear Applications such as 2R / 3R Regeneration, Four Wave Mixing, Wavelength Conversion

Features

- High Fiber-to-Fiber Gain
- Broad Spectral Bandwidth
- Optimized for Non-Linear Applications

Specifications

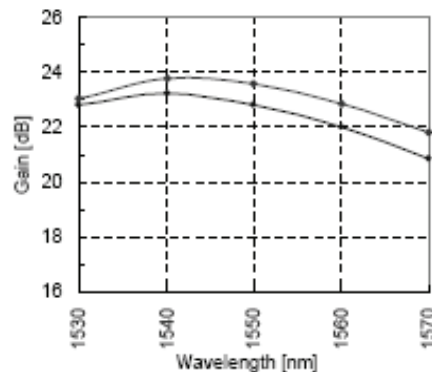
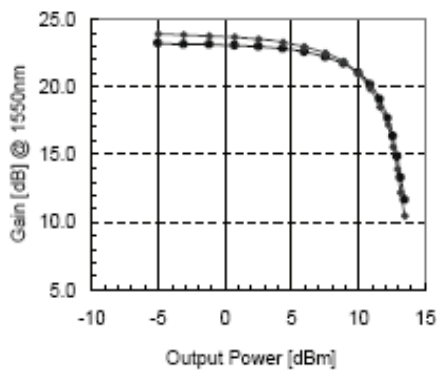
CW; T (Chip) = 25°C, T (Case) = 0 - 70°C

Parameter		Min	Typ	Max	
Operating Current	I_{OP}		500		mA
Operating Wavelength Range: C-band	Δ	1528		1568	nm
Central Wavelength	λ_C		1550		nm
Optical 3 dB Bandwidth	BW		60		nm
Saturation Output Power @ -3 dB	P_{SAT}		10		dBm
Small Signal Gain across BW @ $P_{in} = -20$ dBm	G		20		dB
Gain Flatness	ΔG		2		
Gain Ripple (p-p) @ I_{OP}	δG		0.5		dB
Polarization Dependent Gain	PDG		1		dB
Noise Figure	NF		9		dB
Forward Voltage	V_F		1.6		V
TEC Operation (typ / max @ $T_{CASE} = 25^\circ C / 70^\circ C$)					
- TEC Current	I_{TEC}		0.23	1.2	A
- TEC Voltage	V_{TEC}		0.6	3.5	V
- Thermistor Resistance	R_{TH}		10K		Ω

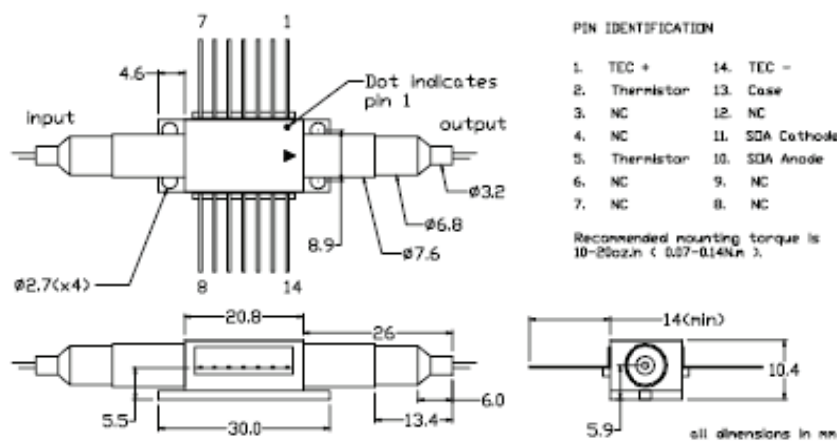


SOA 1117

Performance



Packaging



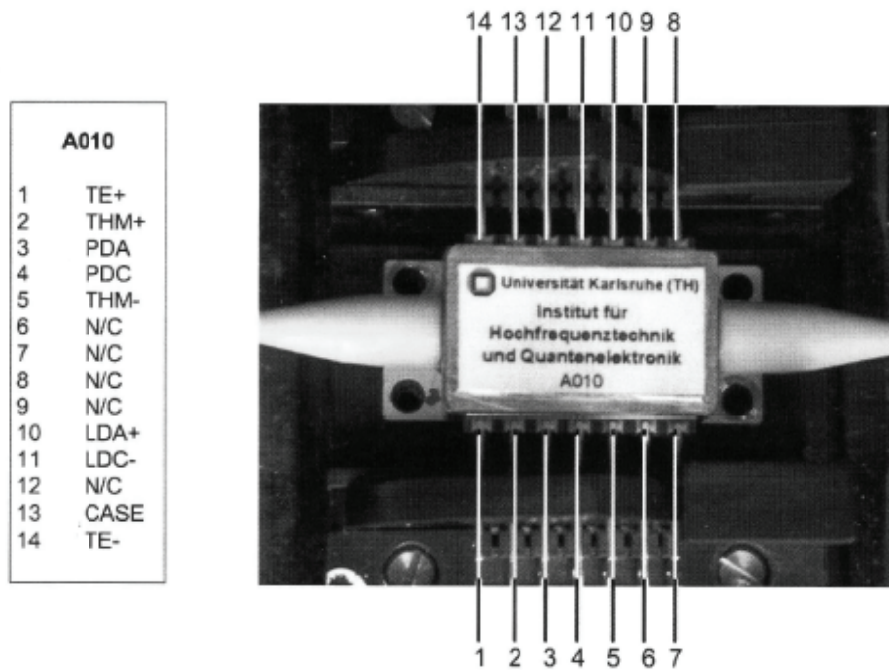
Ordering Information

SOA 1117 - X - 0 - X - X - X - X - X						
X	0	X	X	X	X	X
Isolator	Photodiode	Fibertail [†]	Input Fiber	Output Fiber	Input Connector	Output Connector
0 = none	0 = N/A	B	S = SMF	S = SMF	B = Bare Fiber	B = Bare Fiber
1 = input only		N	P = PMF	P = PMF	A = FC/APC	A = FC/APC
2 = output only		S			O = Other	O = Other
3 = input & output						

[†] see separate fibertail options datasheet

Covega Corporation
 10335 Guilford Road, Jessup, MD 20794, USA
 Phone: +1 877.226.8342 Fax: +1 240.456.7200 Email: sales@covega.com Web: <http://www.covega.com>

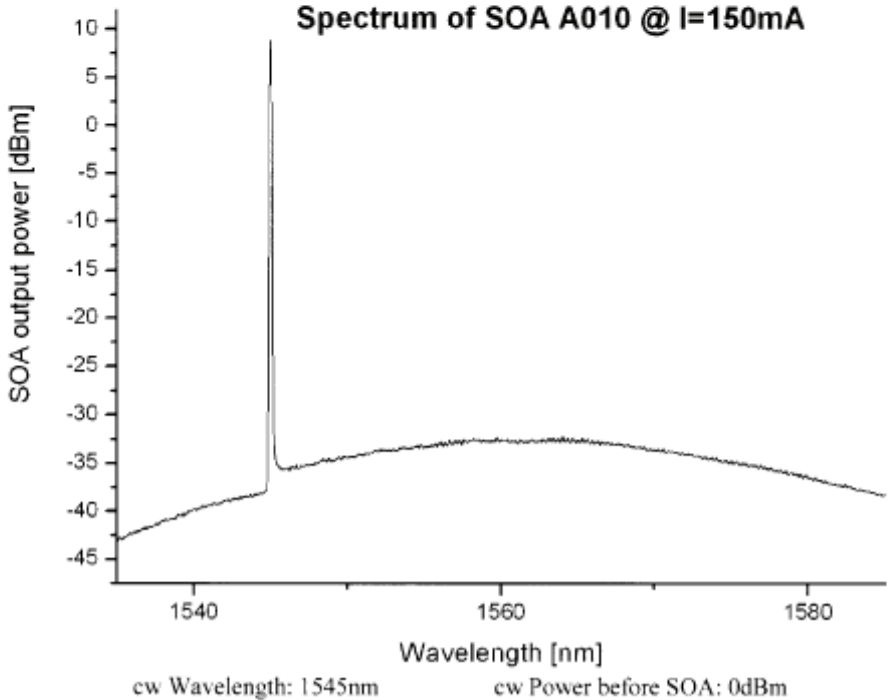
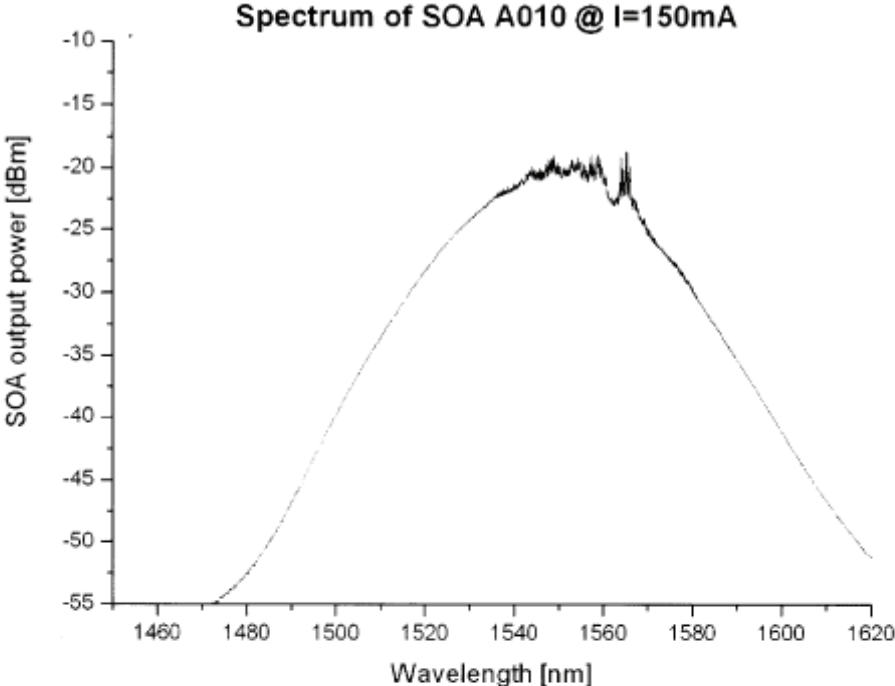
Packaged SOA – pin settings & data



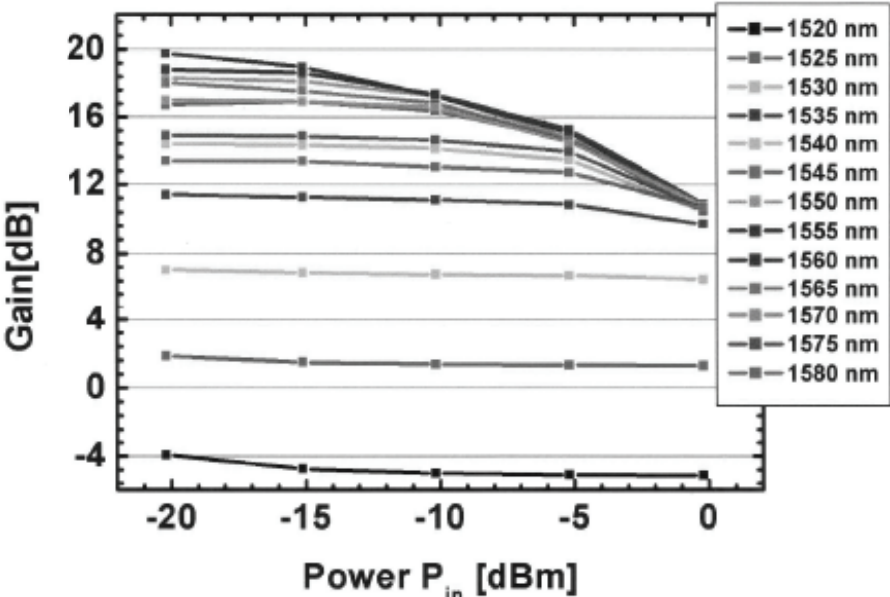
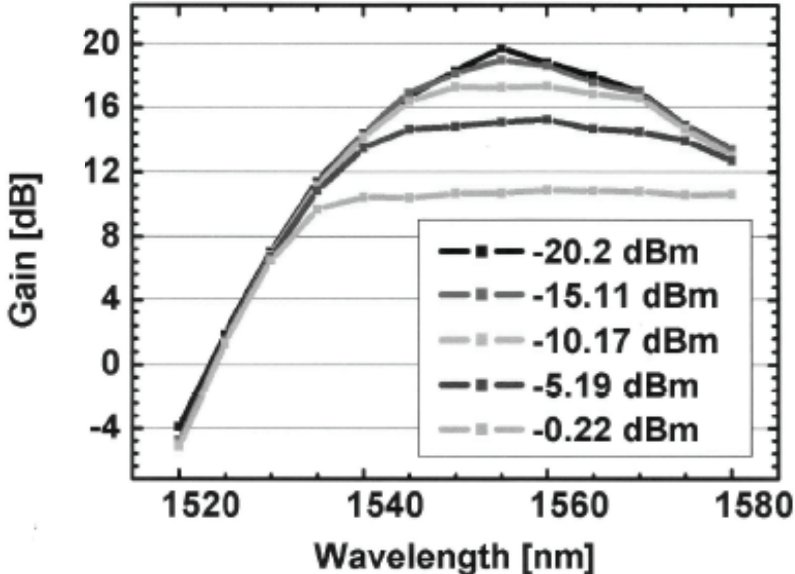
Typical values used during testing:

Device ID: A010
Current range: 100mA – 500mA
Temperature: 20°C

Max. Peltier Current @ 500mA: 0.6A



Packaged SOA – steady state measurements



Appendix D VPI simulation schematics

D.1 Fiber loop mirror simulations

For the different fiber loop mirrors explained throughout chapter 5, the schematics used for the simulations in VPI are shown in Figure D.1 and Figure D.2.

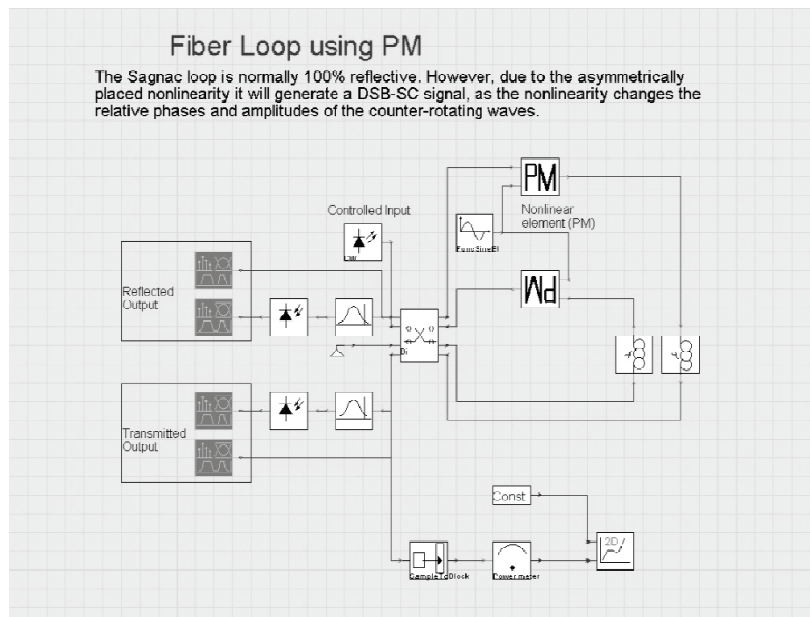


Figure D.1: VPI schematic for the fiber loop mirror with a phase modulator.

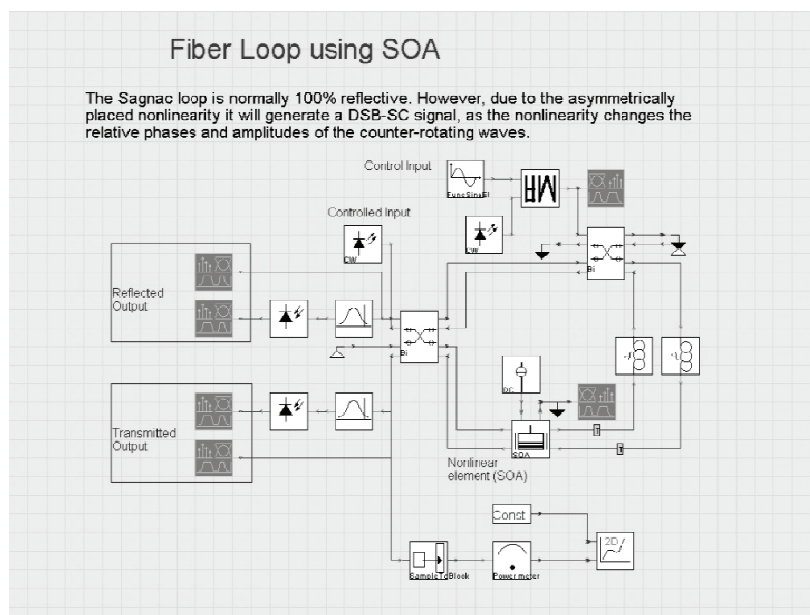


Figure D.2: VPI schematic for the fiber loop mirror with a semiconductor optical amplifier (SOA).

D.2 System simulations

The different schematics for the system simulations are depicted in Figure D.3 to Figure D.6.

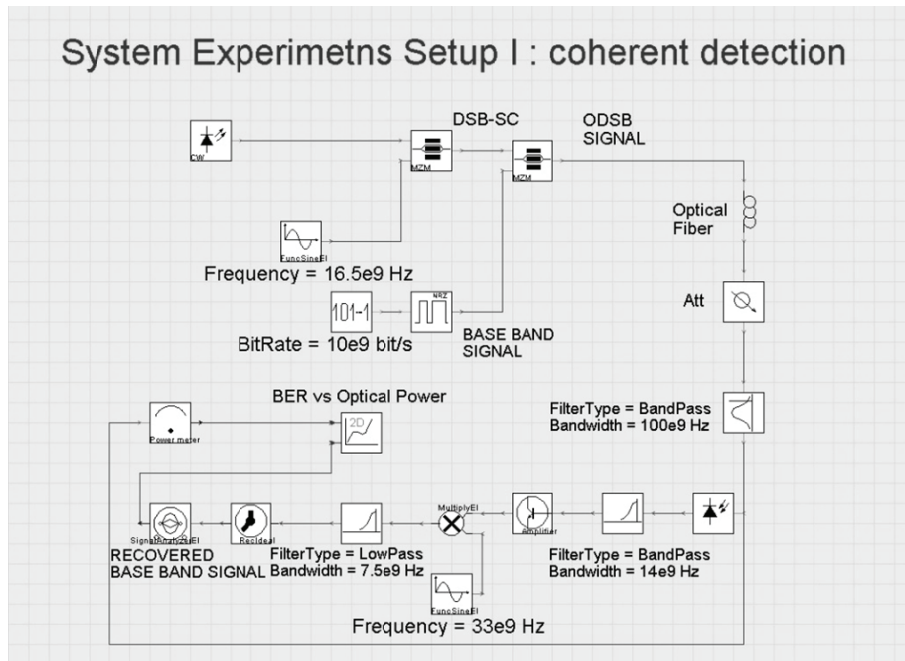


Figure D.3: VPI schematic for the system simulations with setup I (ODSB and coherent detection).

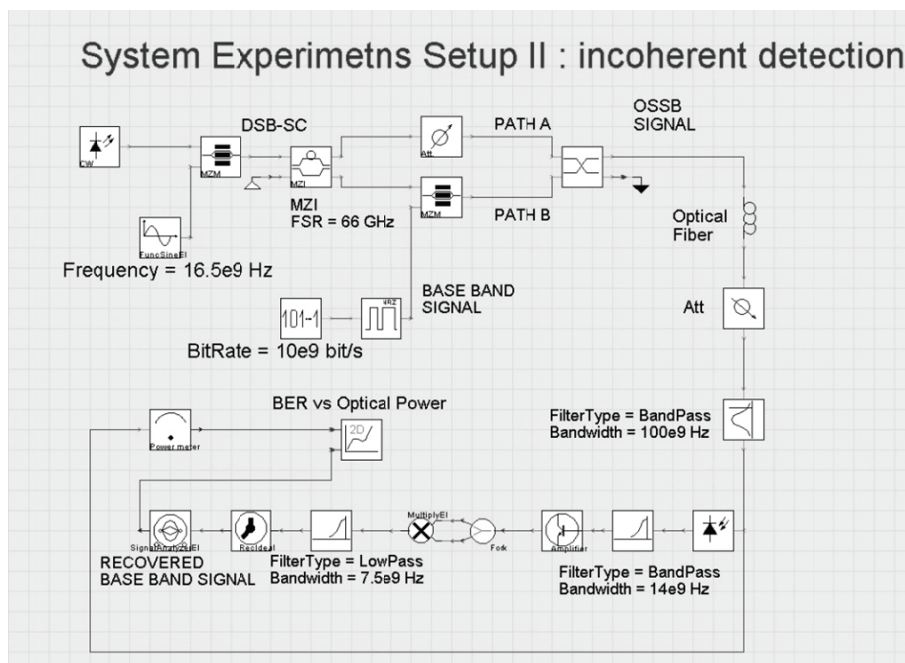


Figure D.4: VPI schematic for the system simulations with setup II (OSSB and incoherent detection).

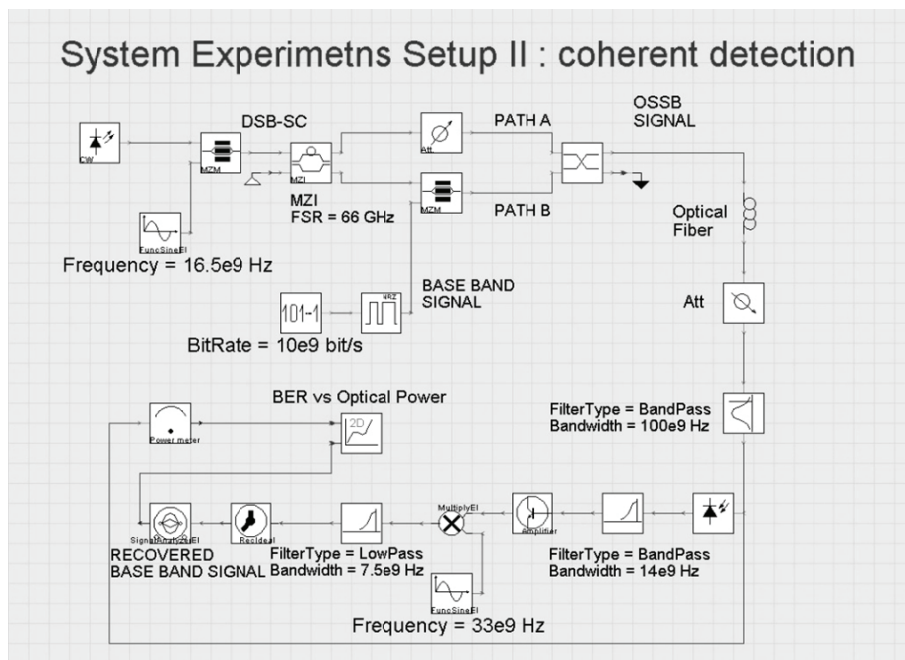


Figure D.5: VPI schematic for the system simulations with setup II (OSSB and coherent detection).

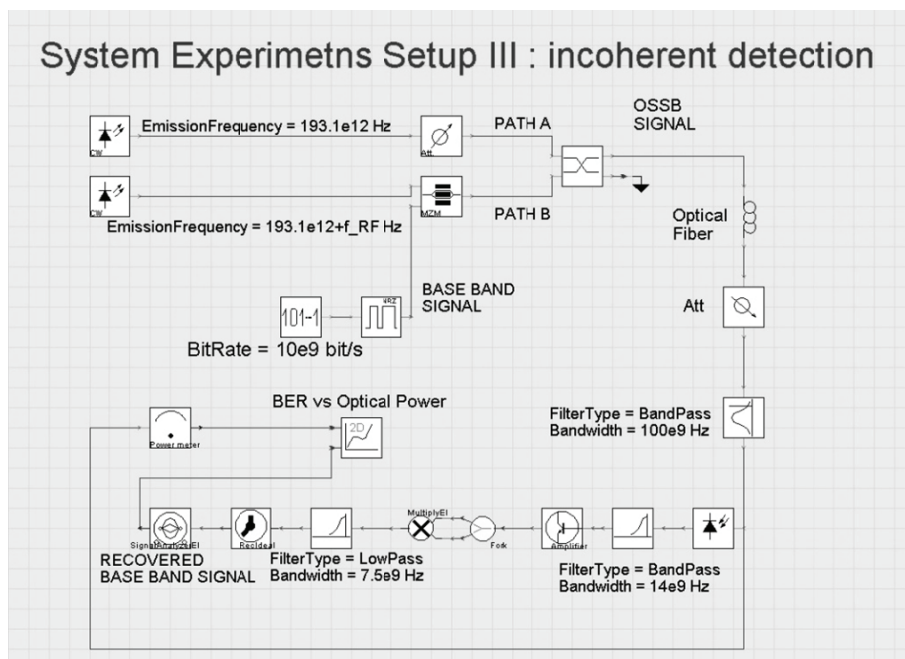


Figure D.6: VPI schematic for the system simulations with setup III (uncorrelated heterodyning and incoherent detection).

Curriculum Vitae

PERSONAL DATA



Name	Ignacio González Insua
Date of birth	19/04/1979
Place of birth	Buenos Aires, Argentina
Nationality	Argentine
Address	Bodenbacher Strasse 20, 01277 Dresden, Germany
Telephone	0049 351 463 32119
E-Mail	gonzalez@ifn.et.tu-dresden.de

EDUCATION

- 1985-1996 High School: Instituto Privado “San Brendano”, Buenos Aires, Argentina. Bachillerato Bilingüe Castellano-Inglés (Bilingual Bachelor Spanish-English)
- 1997-2002 Electronic Engineer Studies in Instituto Tecnológico de Buenos Aires “ITBA”. Degree: Ingeniero Electrónico (Electronic Engineer).
Career Average: 7.6/10.

WORK EXPERIENCE AND PRACTICAL TRAINING

- 2000-2001 Lab assistant in the electronics laboratory of the university (ITBA).
- 2002 Practical training in the RF & Photonics chair in Dresden University of Technology.
- 2003-2010 PhD student and research assistant in the RF & Photonics chair in Dresden University of Technology.

SPECIAL KNOWLEDGE AND ABILITIES

- Foreign Languages Spanish (Mother language)
English: “Test of English for International Communication” (TOEIC) 930/1000, 03/1997.
“First Language English”, IGCSE: grade B, 11/1996.
German: „ZdaF“ (Zertifikat Deutsch als Fremdsprache) 100.25/120 Goethe Institut, Buenos Aires 12/1995
- Software Windows, MS-Office, C++, ABEL, Photoshop, CorelDraw, Microsim Design Center, Mathcad, Matlab, Labview, VPI Photonics.

LIST OF PUBLICATIONS

M. Otto, I. González Insua, T. Duthel, F. Michael, C. G. Schäffer: **"Fiber optical structure for tunable dispersion compensation using cascaded long-period gratings"**, OSA Topical Meeting on Bragg Gratings Photosensitivity and Poling in Glass Waveguides, September 1-3, 2003, Monterey, California, USA

M. Otto, I. González Insua, T. Duthel, F. Michael, C. G. Schäffer: **"Fiber Optical Tunable Dispersion Compensator based on cascaded Long Period Gratings"**, European Conference on Optical Communication (ECOC'03), 21.-25.9.03, Rimini, Italien

C. G. Schäffer, I. González Insua, K. Kojucharow: **"Optical Generation of Microwave Signals based on an unbalanced Fiber Loop Mirror"**, IEEE MTT-S International Microwave Symposium, TU6C_3, Fort Worth, USA, 6.-11.6.2004.

T. Duthel, F. Michael, M. Otto, I. González Insua, C. G. Schäffer: **"Properties of optical delay-line filters for group delay dispersion compensation"**, 5. ITG-Fachtagung "Photonische Netze", pp. 25 - 28, May 2004.

C. G. Schäffer, I. González Insua, K. Kojucharow: **"Optical Generation of Microwave Signals with ASE"**, International Topical Meeting on Microwave Photonics (MWP'04), Ogunquit, USA, 4.-6.10.2004

I. González Insua, C. G. Schäffer: **"Generation of advanced modulation formats with a fiber loop"**, International Students and Young Scientists Workshop "Photonics and Microsystems", 7.-8.07.2005 Dresden.

I. González Insua, C. G. Schäffer: **"Optical Generation of Microwave Signals based on XPM of SOAs in a Fiber Loop"**, International Topical Meeting on Microwave Photonics (MWP'06), 3-6.10.2006 in Grenoble, France.

I. González Insua, C. G. Schäffer: **"Optical Microwave Signal Generation using a Fiber Loop"**, Journal of Lightwave Technology, vol. 25, issue 11, pp. 3341-3349, Nov. 2007.

I. González Insua, C. G. Schäffer: **"Broadband Wireless Access"**, 9. ITG Fachtagung Photonische Netze, Leipzig 28.04.-29.04.2008.

I. González Insua, K. Kojucharow, C. G. Schäffer: "**MultiGbit/s transmission over a fiber optic mm-wave link**", International Microwave Symposium 2008 in Atlanta, USA, 15.06.-20.06.2008, Paper WE3D-02.

I. González Insua, D. Plettemeier, C. G. Schäffer: "**Broadband radio-over-fiber-based wireless access with 10 Gbits/s data rates**", Journal of Optical Networking, vol. 8, issue 1, pp. 77-83, Jan. 2009.

I. González Insua, G. Schäffer: "**Heterodyne Radio over Fiber System with 10 Gbps Data Rates**", OFC 2009 in San Diego, USA, 22-26.03.2009, Poster JWA52.

I. González Insua, C. G. Schäffer: "**Experimental Comparison of 10 Gbit in Radio over Fiber Systems**", International Microwave Symposium 2009 in Boston, USA, 7-11.06.2009, Paper TU4D-03.

I. González Insua, D. Plettemeier, C. G. Schäffer: "**Simple In-house Millimeter Wave Radio Over Fiber System for Gbps Wireless Networks**", 12th International Symposium on Wireless Personal Multimedia Communications (WPMC) 2009 in Sendai, Japan, 7-10.09.2009.

I. González Insua, D. Plettemeier, C. G. Schäffer: "**Simple Remote Heterodyne RoF System for Gbps Wireless Access**", International Topical Meeting on Microwave Photonics (MWP'09), 14-16.10.2009 in Valencia, Spain.

I. Gonzalez Insua, D. Plettemeier, C. G. Schäffer, "**Simple Remote Heterodyne Radio over Fiber System for Gbps Wireless Access**", IEEE Journal of Lightwave Technology, accepted for publication.